



**HAL**  
open science

# Hydrodynamics of semi-submersible floater for offshore wind turbines in highly nonlinear waves using Computational Fluid Dynamics (CFD), and validation of overset meshing technique in a numerical wave tank

Romain Pinguet

► **To cite this version:**

Romain Pinguet. Hydrodynamics of semi-submersible floater for offshore wind turbines in highly nonlinear waves using Computational Fluid Dynamics (CFD), and validation of overset meshing technique in a numerical wave tank. Fluids mechanics [physics.class-ph]. Ecole Centrale Marseille, 2021. English. NNT : 2021ECDM0004 . tel-03512872

**HAL Id: tel-03512872**

**<https://theses.hal.science/tel-03512872v1>**

Submitted on 5 Jan 2022

**HAL** is a multi-disciplinary open access archive for the deposit and dissemination of scientific research documents, whether they are published or not. The documents may come from teaching and research institutions in France or abroad, or from public or private research centers.

L'archive ouverte pluridisciplinaire **HAL**, est destinée au dépôt et à la diffusion de documents scientifiques de niveau recherche, publiés ou non, émanant des établissements d'enseignement et de recherche français ou étrangers, des laboratoires publics ou privés.



## DISSERTATION

submitted in fulfillment of the requirements for the degree of Doctorate of  
Philosophy of ECOLE CENTRALE de MARSEILLE

Speciality: Mechanics and Physics of Fluids

Doctoral school: ED353 - Engineering sciences: Mechanics, Physics, Micro  
and Nano-electronics

Prepared at the Institut de Recherche sur les Phénomènes Hors-Equilibre  
(IRPHE) (UMR 7342 - Aix Marseille Univ., CNRS, Centrale Marseille)

by **Romain PINGUET**

---

# Hydrodynamics of semi-submersible floater for offshore wind turbines in highly nonlinear waves using Computational Fluid Dynamics (CFD), and validation of overset meshing technique in a numerical wave tank

---

Presented and publicly defended on June 15th, 2021

### PhD Examination Committee:

Pr. David R. FUHRMAN	Technical University of Denmark	Referee
Pr. Antonio SOUTO-IGLESIAS	Universidad Politecnica de Madrid, Spain	Referee
Pr. David LE TOUZE	Ecole Centrale Nantes & LHEEA, France	Examiner
Dr. Amy ROBERTSON	National Renewable Energy Laboratory, USA	Examiner
Dr. Daewoong SON	Principle Power Inc., USA	Examiner
Pr. Michel BENOIT	Ecole Centrale Marseille & Irphé, France	Supervisor
Pr. Bernard MOLIN	Ecole Centrale Marseille & Irphé, France	Co-Supervisor





THÈSE  
pour obtenir le grade de  
Docteur de L'ÉCOLE CENTRALE de MARSEILLE

Specialité: Mécanique et Physique des Fluides  
Ecole doctorale: ED353 - Sciences pour l'Ingénieur : Mécanique, Physique,  
Micro et Nanoélectronique

Préparée à l'Institut de Recherche sur les Phénomènes Hors-Equilibre  
(IRPHE) (UMR 7342 - Aix Marseille Univ., CNRS, Centrale Marseille)

par **Romain PINGUET**

---

**Hydrodynamique des éoliennes flottantes de type  
semi-submersible soumises à des vagues  
fortement non-linéaires en utilisant la Mécanique  
des Fluides Numérique (MFN), et validation  
d'une méthode overset appliquée à un canal à  
houle numérique**

---

Présentée et soutenue publiquement le 15 Juin 2021

Jury de thèse :

Pr. David R. FUHRMAN	Technical University of Denmark	Rapporteur
Pr. Antonio SOUTO-IGLESIAS	Universidad Politecnica de Madrid, Spain	Rapporteur
Pr. David LE TOUZE	Ecole Centrale Nantes & LHEEA, France	Examinateur
Dr. Amy ROBERTSON	National Renewable Energy Laboratory, USA	Examinateur
Dr. Daewoong SON	Principle Power Inc., USA	Examinateur
Pr. Michel BENOIT	Ecole Centrale Marseille & Irphé, France	Directeur
Pr. Bernard MOLIN	Ecole Centrale Marseille & Irphé, France	Co-Directeur



## Declaration of Authorship

I, Romain PINGUET, declare that this thesis titled, “Hydrodynamics of semi-submersible floater for offshore wind turbines in highly nonlinear waves using Computational Fluid Dynamics (CFD), and validation of overset meshing technique in a numerical wave tank ” and the work presented in it are my own. I confirm that:

- This work was done wholly or mainly while in candidature for a PhD degree at Ecole Centrale Marseille.
- Where any part of this thesis has previously been submitted for a degree or any other qualification at Ecole Centrale Marseille or any other institution, this has been clearly stated.
- Where I have consulted the published work of others, this is always clearly attributed.
- Where I have quoted from the work of others, the source is always given. With the exception of such quotations, this thesis is entirely my own work.
- I have acknowledged all main sources of help.
- Where the thesis is based on work done by myself jointly with others, I have made clear exactly what was done by others and what I have contributed myself.

Signed:



---

Date: June 15<sup>th</sup> 2021

---



# Hydrodynamics of semi-submersible floater for offshore wind turbines in highly nonlinear waves using Computational Fluid Dynamics (CFD), and validation of overset meshing technique in a numerical wave tank

Romain Pinguet

## Abstract

The rapid emergence of Floating Offshore Wind Turbines (FOWT) has brought a strong demand for high-fidelity numerical methods to better predict the response of such structures under severe metocean conditions. In these scenarios, design standards suggest simplified approaches, but their applicability is limited, especially when considering complex geometries and/or nonlinear events. Moreover, experimental campaigns are expensive, and few field data are available. So, Computational Fluid Dynamics (CFD) could be a key asset in the design process of FOWT. This thesis aims to assess the ability of a CFD approach to model critical hydrodynamic aspects of semi-submersible FOWT. The overset meshing method built in the open-source software OpenFOAM® is used to handle the body motions. The wave generation and absorption toolbox waves2Foam is coupled with the overset solver to model the interaction between waves and the structure. The results are validated against experimental and numerical data from the literature. Convergence analysis and meshing methodologies of a 2D Numerical Wave Tank (NWT), with fixed and freely floating structures subjected to waves, are considered. Non-linearities are emphasized. The NWT is then extended in 3D to investigate the hydrodynamic response of the Deep-CWind semi-submersible FOWT, designed by NREL. Forces and run-up are analyzed for fixed and anchored moving platforms. Wave induced motion and free decay tests are presented. The overset mesh method is also used to estimate the hydrodynamic coefficients resulting from the vertical forced motion of heave damping plate, widely used in FOWT designs.

# Hydrodynamique des éoliennes flottantes de type semi-submersible soumises à des vagues fortement non-linéaires en utilisant la Mécanique des Fluides Numérique (MFN), et validation d'une méthode overset appliquée à un canal à houle numérique.

Romain Pinguet

## Résumé

L'émergence rapide des éoliennes flottantes a entraîné une forte demande de méthodes numériques haute-fidélité afin de mieux prédire le comportement de telles structures dans des conditions météorologiques sévères. Dans ces scénarios, les standards de conception suggèrent des approches simplifiées, mais leur applicabilité est limitée, en particulier lorsque l'on considère des géométries complexes et / ou des événements non-linéaires. De plus, les campagnes expérimentales sont coûteuses et peu de données réelles sont disponibles. Ainsi, la Mécanique des Fluides Numérique (MFN) pourrait être un atout clé dans le processus de conception des éoliennes flottantes. Cette thèse vise à évaluer la capacité d'une approche de MFN à modéliser certains aspects hydrodynamiques critiques des éoliennes flottantes de type semi-submersible. La méthode des maillages superposés (overset), intégrée dans le logiciel open-source OpenFOAM<sup>®</sup>, est utilisée pour modéliser les mouvements de la structure. La méthode numérique de génération et d'absorption de vagues de l'outil waves2Foam est couplée au solveur de maillages superposés pour modéliser les interactions entre les vagues et la structure. Les résultats sont validés par comparaison avec des données expérimentales et numériques issues de la littérature. Des analyses de convergence numérique sont réalisées, et les méthodologies de maillage d'un Canal à Houle Numérique 2D (CHN) sont analysées, pour des structures fixes ou flottantes soumises aux vagues. Les non-linéarités sont mises en évidence. Le CHN est ensuite étendu en 3D pour étudier la réponse hydrodynamique du flotteur semi-submersible DeepCWind, conçu par NREL. Les forces et le run-up le long des parois sont analysés pour des plateformes fixes ou flottantes. L'étude des mouvements de la structure dans les vagues, ainsi que des cas d'extinction libre, sont présentés. La méthode des maillages superposés est également utilisée pour étudier les coefficients hydrodynamiques résultant du mouvement forcé vertical de plaques d'amortissement en pilonnement, largement utilisées dans la conception d'éoliennes flottantes.

## *Acknowledgements*

I would like to express my sincere gratitude to the following people, who all contributed to the success of my PhD research:

To my supervisors Michel Benoit and Bernard Molin, for providing me with unique knowledge, methods, and guidance throughout these three years. I am extremely grateful for their patience, efficiency, and support. It was truly an honor to work with such brilliant Professors.

To researchers from Centrale Marseille and Irphé. I learned a lot from all the projects that were conducted while I was working in Marseille. Special thanks to the other PhDs of the team: Paul Pergler, Jie Zhang, Paul Milesi, and Fabien Robaux with whom I shared great discussions on CFD, wave modeling, Python, and so many other fun topics. Many thanks to Guillaume Dupont, who guided me for my first steps with OpenFOAM®.

To the rest of the "plot 4" building at Centrale Marseille, for the warm welcome and the great moments of conviviality.

To all my colleagues and friends at Principle Power, in Europe, and in California for giving me the chance to benefit from their expertise in floating offshore wind and for the great off-work events. To Dominique Roddier for initiating this research project and giving me a chance in the first place. To Sam Kanner and Flavia Rezende for supervising my work, and for sharing their valuable knowledge. Their support and time were extremely helpful. To Seth Price for being a great manager and making me feel part of the team.

To all the participants of the OC6 project from whom I learned considerably during project meetings. Special thanks to Lu Wang and Amy Robertson from NREL for leading the project, sharing advice, methods, codes, and results that were crucial added value to my research.

To the Centre de Calcul Intensif d'Aix-Marseille, for granting access to its high-performance computing resources.

To the InnoEnergy PhD School Program and the European Institute of Technology (EIT), for supporting this research and co-funding the PhD thesis. The PhD school providing me with exciting training in several European universities, where I met interesting PhD students from all over the world, some of whom are now my friends.



*Dedicated to my parents Eliane and Philippe, as well as my sisters  
Clémence and Marie-Camille, who, in their way, brought me the  
support and motivation I needed to succeed in my PhD.*



# Contents

<b>Declaration of Authorship</b>	<b>iii</b>
<b>Acknowledgements</b>	<b>vii</b>
<b>1 Introduction</b>	<b>1</b>
1.1 An overview of the floating offshore wind industry . . . . .	1
1.1.1 General Context . . . . .	1
1.1.2 The main technologies of FOWT . . . . .	3
1.1.2.1 Spar concept . . . . .	3
1.1.2.2 Barge . . . . .	4
1.1.2.3 TLP . . . . .	4
1.1.2.4 Semi-submersible . . . . .	4
1.1.2.5 Hybrid concepts . . . . .	6
1.2 State of the art of the modeling of FOWT with current engineering models . . . . .	6
1.3 Modeling of Floating wind with CFD . . . . .	8
1.3.1 Most popular CFD software tools for maritime purposes . . . . .	8
1.3.2 Wave Modeling in OpenFOAM® . . . . .	9
1.3.3 Modeling of Dynamic Structures in CFD . . . . .	10
1.3.3.1 Meshing methods for moving structures . . . . .	10
1.3.3.2 Remeshing and Mesh Morphing methods for FOWT modeling . . . . .	10
1.3.3.3 Overset mesh method for floating structure in CFD . . . . .	12
1.4 Experimental research on Semi-submersible FOWT . . . . .	13
1.5 Objectives and outline of the Ph.D. thesis . . . . .	15
1.6 Publications . . . . .	16
<b>2 Theory</b>	<b>19</b>
2.1 Introduction of parameters of interest . . . . .	19
2.2 Governing Equations . . . . .	19
2.2.1 Navier-Stokes equations . . . . .	19
2.2.2 Multiphase Modeling: Volume of Fluid (VOF) Model . . . . .	20
2.2.3 Turbulence Closure Model . . . . .	20
2.3 Wave generation and absorption with Waves2Foam . . . . .	21
2.3.1 Wave theories . . . . .	21
2.3.2 Wave relaxation . . . . .	21
2.3.3 Dynamic Solver and Restraint Forces . . . . .	22
2.4 Overset Grid Method . . . . .	23
2.5 Boundary conditions . . . . .	25
2.6 Finite Volume Method (FVM) . . . . .	25
2.7 Solution and Algorithm Control . . . . .	26
2.8 Summary . . . . .	27

<b>3</b>	<b>Meshing method and convergence analysis of wave modeling in the NWT</b>	<b>29</b>
3.1	Description of the NWT	29
3.1.1	Geometry of the NWT	29
3.1.2	Boundaries of the NWT	30
3.2	Global Meshing Process	30
3.3	Incident Wave Calibration	31
3.3.1	Mesh convergence	31
3.3.1.1	Global mesh refinement	31
3.3.1.2	Impact of the cell size expansion ratio	32
3.3.1.3	Impact of the relaxation zone length	33
3.3.2	Convergence of key numerical parameters	34
3.3.2.1	Relaxation coefficient in the damping zone	34
3.3.2.2	Time step	35
3.3.2.3	Maximum residual in the Poisson iterative solution for pressure	36
3.4	Conclusion	37
<b>4</b>	<b>2D simulations of inverted T-sections in nonlinear waves</b>	<b>39</b>
4.1	Wave induced forces on a fixed structure	39
4.1.1	Description of the selected test-case	39
4.1.2	Numerical Models	40
4.1.2.1	Potential models	40
4.1.2.2	CFD Numerical model	42
4.1.3	Numerical simulations with regular waves	43
4.1.3.1	Influence of wave period (at constant wave steepness)	43
4.1.3.2	Analysis of the test case $T = 12.1$ s	45
4.2	Wave Induced Motion of a T-shape structure	48
4.2.1	Description of the experimental set-up	48
4.2.2	Description of the numerical case	49
4.2.2.1	Geometry	49
4.2.2.2	Numerical Schemes	49
4.2.2.3	Boundary Conditions	50
4.2.3	Mesh convergence analysis	50
4.2.3.1	Global Meshing method	50
4.2.3.2	Influence of the global mesh refinement	52
4.2.3.3	Influence of the Refined Box in the background mesh	53
4.2.4	Solver stability	55
4.2.4.1	Influence of the Courant number	55
4.2.4.2	Influence of the acceleration relaxation coefficient	56
4.2.5	Comparison with experimental results	57
4.2.5.1	Results and discussion	58
4.3	Conclusions	60
<b>5</b>	<b>CFD analysis of added mass, damping and induced flow of isolated and cylinder-mounted heave plates at various submergence depths using an overset mesh method</b>	<b>61</b>
5.0.1	Overview of heave plates for offshore structures	61
5.0.2	Physical analysis of the problem of interest	63
5.0.3	Objectives of this study and lay-out of the article	65
5.1	Numerical Methods	65

5.1.1	Prescribed dynamics of the structure . . . . .	65
5.1.2	CFD Numerical model . . . . .	65
5.1.2.1	Governing equations and boundary conditions . . . . .	65
5.1.2.2	Numerical inputs . . . . .	66
5.1.3	Overset mesh method . . . . .	67
5.1.4	Representation of a cylinder with a wedge section . . . . .	68
5.1.5	Wave relaxation with waves2Foam . . . . .	68
5.1.6	Computation of hydrodynamic coefficients . . . . .	68
5.2	Case of an isolated disk . . . . .	70
5.2.1	Experimental model . . . . .	70
5.2.2	Mesh generation of the CFD model . . . . .	71
5.2.3	Immersion $d = 0.05$ m ( $d/D = 1/12$ ) . . . . .	74
5.2.3.1	Comparison of time series of vertical load on the disk and radiated waves . . . . .	74
5.2.3.2	Comparison of the hydrodynamic coefficients . . . . .	76
5.2.3.3	Comparisons of the RAOs of the free surface elevation . . . . .	78
5.2.3.4	Interactions between vortices and free surface . . . . .	79
5.2.4	Immersion $d = 0.25$ m ( $d/D = 5/12$ ) . . . . .	82
5.3	Case of disk at the bottom of a vertical cylindrical column . . . . .	84
5.3.1	Description of the case . . . . .	85
5.3.2	Results . . . . .	85
5.3.2.1	Hydrodynamic coefficients . . . . .	85
5.3.2.2	Vorticity . . . . .	86
5.4	Conclusion . . . . .	86
<b>6</b>	<b>3D simulations of fixed FOWT in waves: the OC6 project</b> . . . . .	<b>89</b>
6.1	Introduction to the static analysis of the DeepCWind FOWT within the OC6 project . . . . .	89
6.2	Monochromatic wave case . . . . .	89
6.2.1	Model 1 of the static DeepCWind FOWT . . . . .	90
6.2.1.1	Description of the fluid domain . . . . .	90
6.2.1.2	Mesh description of the model . . . . .	90
6.2.1.3	Physics and Solver of the model 1 . . . . .	91
6.2.1.4	Results of model 1 . . . . .	91
6.2.2	Model 2 of the DeepCWind FOWT based on OC6 project . . . . .	93
6.2.2.1	Imposed numerical inputs and mesh . . . . .	94
6.2.2.2	Results . . . . .	95
6.3	Bichromatic wave cases . . . . .	96
6.3.1	Set up of the numerical model . . . . .	97
6.3.2	Wave Calibration . . . . .	99
6.3.3	Results of the bichromatic wave loads on the structure . . . . .	100
6.4	Conclusions . . . . .	103
<b>7</b>	<b>3D simulations of freely-floating FOWT</b> . . . . .	<b>105</b>
7.1	Validation of the overset mesh method using free-decay tests of floating offshore wind turbines . . . . .	105
7.1.1	Case of a vertical cylinder . . . . .	105
7.1.1.1	Settings of the case . . . . .	105
7.1.1.2	Results . . . . .	109
7.1.2	Case of the DeepCWind FOWT . . . . .	112
7.1.2.1	Settings of the case . . . . .	112

	7.1.2.2	Results	115
7.2		Wave Induced Motion	117
	7.2.1	Validation with a small scale model	117
		7.2.1.1 Description of the case	118
		7.2.1.2 Results	121
	7.2.2	Hydrodynamic response of FOWT in regular waves for different values of wave steepness	126
		7.2.2.1 Description of the case	126
		7.2.2.2 Wave Calibration	127
		7.2.2.3 Results of motions of the FOWT	128
7.3		Conclusions	134
<b>8</b>		<b>General conclusions and perspectives</b>	<b>137</b>
	8.1	Summary of the main results	137
	8.2	Main achievements of the thesis	139
	8.3	Perspectives and future work	139
<b>A</b>		<b>Comparison of the free surface of the experimental tests with the surface computed in CFD for forced oscillations of a disk</b>	<b>143</b>
<b>B</b>		<b>Wave loads on the freely-floating DeepCwind FOWT</b>	<b>145</b>
	B.1	Forces and moment from the small scale model based on the experimental results presented in the work of Rivera-Arreba et al. [56]	145

# List of Figures

1.1	Average capacity factor for offshore wind around the World [3] . . . . .	2
1.2	Overview of offshore structures in the Oil and Gas industry [4] . . . . .	2
1.3	BoB buoy, installed on the site of the future floating wind project: Eoliennes Flottantes du Golfe du Lion (France), to study the biodiversity. Credits : ECOCEAN / Remy Dubas . . . . .	3
1.4	Hywind design (Equinor) [6] . . . . .	3
1.5	Examples of barge and TLP types of FOWT . . . . .	4
1.6	Semi-submersible concepts for Floating offshore wind turbines . . . . .	5
1.7	Hexafloat technology (Saipem) [13] . . . . .	6
1.8	Different wave force regimes [15] $D$ is the characteristic dimension, $H$ is the wave height, and $\lambda$ is the wave length . . . . .	6
1.9	Experimental model of the DeepCWind floater tested in a wave basin at MARIN (The Netherlands) [100] . . . . .	13
1.10	Main dimensions of the DeepCWind FOWT at full scale . . . . .	14
1.11	Experimental model of the semi-submersible from Lacaze [101] tested in the wind-wave tank facility at Marseille-Luminy (France) . . . . .	15
1.12	Experimental model of the WindFLoat design at UC Berkeley (CA, USA) [11] . . . . .	15
2.1	Sketch of the mooring model including a resting state . . . . .	23
2.2	Background mesh (green) and body-fitted mesh (orange) in the overset mesh method. Description of the location of the receptor and hole cells. The grey box is the body of the fitted mesh . . . . .	24
2.3	Description of the interpolation between donor and receptor cells at the internal and external boundaries. Adapted from [85]. . . . .	24
2.4	Information flow in the overset mesh method . . . . .	25
2.5	Flow chart of the solver coupling free surface flow solver, overset mesh method and the PISO algorithm for velocity-pressure coupling . . . . .	28
3.1	General description of the NWT and its boundaries . . . . .	29
3.2	Description of the refinement zones of the mesh . . . . .	30
3.3	Convergence analysis as a function of the global refinement . . . . .	32
3.4	Convergence analysis as a function of the expansion ratio . . . . .	33
3.5	Convergence analysis as a function of the relaxation zones lengths . . . . .	34
3.6	Convergence analysis as a function of the relaxation exponent . . . . .	35
3.7	Convergence analysis as a function of the time step . . . . .	36
3.8	Convergence analysis as a function of the maximum residual of pressure. The second value is considered for the last iteration . . . . .	37
4.1	Geometry of the inverted T-section, corresponding to a vertical slice of a DeepCWind floater column [113] . . . . .	40
4.2	Sub-domain decomposition used with the linear potential flow model developed by Pr. Molin . . . . .	41

4.3	Typical shape of a 2D cell used with the HPC method . . . . .	41
4.4	Decomposition of the OpenFOAM® mesh and cell size criteria . . . . .	42
4.5	Partial view of the NWT and column meshing in OpenFOAM® . . . . .	43
4.6	Overview of OpenFOAM® global computational domain . . . . .	43
4.7	First harmonic amplitude of normalized $F_x$ , $F_z$ and run-up compared to the linear results . . . . .	44
4.8	Maximum and minimum values of the RAO of $F_x$ and $F_z$ and run-up compared to the linear case . . . . .	45
4.9	HPC and OpenFOAM® forces ( $F_x$ , $F_z$ ) and run-up compared to the linear model - case $T = 12.1$ s, steepness $H/\lambda = 3.1$ . . . . .	46
4.10	Harmonics 1, 2 and 3 of $F_x$ , $F_z$ and run-up from the HPC model and CFD computation. $T = 12.1$ s. Linear amplitude is also superimposed to compare the first harmonics. . . . .	47
4.11	Description of the experimental set up (adapted from [116]) . . . . .	48
4.12	Sketch of the numerical 2D model with main dimensions . . . . .	49
4.13	Global meshing process of the 2D case with the overset mesh method . . . . .	51
4.14	Time series of free surface elevation, heave and pitch motions. Influence of the global refinement of the meshes . . . . .	52
4.15	Refined box in the background mesh and zoom at the bottom left corner of the overset mesh – Box 1: level 4 of refinement – Box 2: level 2 of refinement – Box 3: no refinement box . . . . .	53
4.16	Time series of free surface elevation, heave and pitch motions. Influence of the refinement of the background box . . . . .	54
4.17	Time series of free surface elevation, heave and pitch motions. Influence of the maximum Courant number $Co$ . . . . .	55
4.18	Time series of free surface elevation, heave and pitch motions. Influence of the acceleration relaxation coefficient $f_a$ . . . . .	57
4.19	Comparison of the numerical results (case 1) with the experimental measurements from [116] . . . . .	58
4.20	Comparison of the green water event on the platform and the position of the floater. Left: present numerical CFD simulations, right: experimental pictures from [116] . . . . .	59
5.1	Definition sketches of the two considered cases (not on scale) . . . . .	62
5.2	global domain . . . . .	67
5.3	disk expe . . . . .	68
5.4	disk expe . . . . .	71
5.5	disk expe . . . . .	72
5.6	Global mesh refinement. The cell size is defined by a number of cells per amplitude of vertical motion, considering the minimum value of this amplitude namely $A_{min} = 0.005$ m. . . . .	72
5.7	cellperamp . . . . .	73
5.8	Level refinement at the disk vicinity . . . . .	73
5.9	vicinity . . . . .	74
5.10	Time series of the position normalized by the amplitude of motion (top), $C_F$ , and the free surface elevation $\eta$ normalized by $A$ at 0.20 m from the edge of the disk (bottom) for two amplitudes of oscillation. The red line is the experimental result [118] and the blue line is the CFD result. $T = 1.1$ s, $d = 0.05$ m ( $d/D = 1/12$ , $kR = 1.06$ ) . . . . .	75

5.11	Time series of the position normalized by the amplitude of motion (top), $C_F$ , and the free surface elevation $\eta$ normalized by $A$ at 0.20 m from the edge of the disk (bottom) for two amplitudes of oscillation. The red line is the experimental result [118] and the blue line is the CFD result. $T = 1.6$ s, $d = 0.05$ m ( $d/D = 1/12$ , $kR = 0.61$ ) . . . . .	75
5.12	Time series of the position normalized by the amplitude of motion (top), $C_F$ , and the free surface elevation $\eta$ normalized by $A$ at 0.20 m from the edge of the disk (bottom) for two amplitudes of oscillation. The red line is the experimental result [118] and the blue line is the CFD result $T = 2$ s, $d = 0.05$ m ( $d/D = 1/12$ , $kR = 0.47$ ) . . . . .	76
5.13	Added mass coefficients for two amplitudes of oscillation at different value of $kR$ (modifying $T$ ). The black line is the theoretical result of the LPFM [118], the red crosses are the experimental results [118] and the blue dots are the CFD results. $d = 0.05$ m ( $d/D = 1/12$ ) . . . . .	77
5.14	Damping coefficients for two amplitudes of oscillation at different value of $kR$ (modifying $T$ ). The black line is the theoretical result of the LPFM [118], the red crosses are the experimental results [118] and the blue dots are the CFD results. $d = 0.05$ m ( $d/D = 1/12$ ) . . . . .	78
5.15	Modulus of the RAO of the free surface, 0.20 m from the edge of the disk, for two amplitudes of oscillation, at different value of $kR$ (modifying $T$ ). The black line is the theoretical result of the LPFM [118], the red crosses are the experimental results [118] and the blue dots are the CFD results. $d = 0.05$ m ( $d/D = 1/12$ ) . . . . .	79
5.16	Phase of the RAO of the free surface, 0.20 m from the edge of the disk, for two amplitudes of oscillation, at different values of $kR$ (modifying $T$ ). The black line is the theoretical result of the LPFM [118], the red crosses are the experimental results [118] and the blue dots are the CFD results. $d = 0.05$ m ( $d/D = 1/12$ ) . . . . .	79
5.17	vorticity/ $\omega$ induced by the vertical motion of the disk only (left : downward, right upward). $A = 0.015$ m, $T = 1.6$ s, $d = 0.05$ m ( $d/D = 1/12$ , $kR = 0.61$ , $KC = 0.157$ ) . . . . .	81
5.18	Ca i25 . . . . .	83
5.19	Cb i25 . . . . .	84
5.20	Hydrodynamic coefficients $C_a$ (left) and $C_b$ (right) for different $KC$ . The red crosses are the experimental results and the blue dots are the CFD results. $T = 1$ s ( $kR = 1.22$ ) . . . . .	85
5.21	vorticity/ $\omega$ induced by the vertical motion of the disk+column (left : downward, right upward). $A = 0.036$ m, $T = 1$ s, ( $kR = 1.22$ , $KC = 0.9$ ) . . . . .	86
6.1	Description of the NWT of the model 1 for the static DeepCWind FOWT	90
6.2	Description of the mesh of the model 1 of the static DeepCWind case .	91
6.3	Time series of the forces acting on the global structure. The purple line is the amplitude of the linear model from G. Dupont. The red line are the experimental results from the OC6 project, The blue line are the CFD results of the present work. Model 1 - full scale: $T = 12.1$ s, $A = 3.5$ m . . . . .	92
6.4	Time series of the forces acting on the upstream column. The purple line is the amplitude of the linear model from G. Dupont, the blue line are the CFD results of the present work. Model 1 - full scale: $T = 12.1$ s, $A = 3.5$ m . . . . .	92

6.5	Time series of the forces acting on the central column. The purple line is the amplitude of the linear model from G. Dupont, the blue line are the CFD results of the present work. Model 1 - full scale: $T = 12.1$ s, $A = 3.5$ m . . . . .	93
6.6	Time series of the run-up acting on the upstream column. The purple line is the amplitude of the linear model from G. Dupont, the blue line are the CFD results of the present work. Model 1 - full scale: $T = 12.1$ s, $A = 3.5$ m . . . . .	93
6.7	Domain description of the model 2 prescribed by the OC6 project . . . . .	94
6.8	Vertical slice of the mesh prescribed by the OC6 project . . . . .	94
6.9	Vertical force ( $F_x$ ) acting on the global structure. Comparison between the present work (in orange), experimental measurements (in black), and CFD results of other participants of the OC6 project. Model 2 - small scale: $T = 12.1$ s, $A = 3.5$ m . . . . .	95
6.10	Horizontal force ( $F_z$ ) acting on the global structure. Comparison between the present work (in orange), experimental measurements (in black), and CFD results of other participants of the OC6 project. Model 2 - small scale: $T = 12.1$ s, $A = 3.5$ m . . . . .	96
6.11	Pitch moment ( $M_y$ ) acting on the global structure. Comparison between the present work (in orange), experimental measurements (in black), and CFD results of other participants of the OC6 project. Model 2 - small scale: $T = 12.1$ s, $A = 3.5$ m . . . . .	96
6.12	Geometry of the DeepCWind without braces and central column (dimensions are given at full scale) . . . . .	97
6.13	Mesh used for the bichromatic wave analysis. Credit for the mesh : Adria Borrás Nadal (IFPEN) . . . . .	98
6.14	Dimensions of the NWT and boundary conditions for the bichromatic wave case of OC6 . . . . .	98
6.15	Amplitude of the primary waves (left scale) and the difference-frequency wave (right scale) along the NWT . . . . .	99
6.16	Amplitude of the primary waves (left scale) and the difference-frequency wave (right scale) at $x = 0$ m over time. . . . .	100
6.17	Amplitude of the surge force ( $F_x$ ) at difference-frequency ( $f_d$ ) and primary wave frequencies ( $f_1$ and $f_2$ ). The darkest bars are the results from the present thesis, the hatched bars are the results from QTF method [150] . . . . .	101
6.18	Amplitude of the heave force ( $F_z$ ) at difference-frequency ( $f_d$ ) and primary wave frequencies ( $f_1$ and $f_2$ ). The darkest bars are the results from the present thesis, the hatched bars are the results from QTF method [150] . . . . .	102
6.19	Amplitude of the pitch moment ( $M_y$ ) at difference-frequency ( $f_d$ ) and primary wave frequencies ( $f_1$ and $f_2$ ). The darkest bars are the results from the present thesis, the hatched bars are the results from QTF method [150] . . . . .	102
7.1	Overview of the computational domain for the vertical cylinder case . . . . .	106
7.2	Description of the mesh sizing for the vertical cylinder case . . . . .	106
7.3	Sketch of the catenary mooring lines of the cylinder . . . . .	108
7.4	Initial vertical displacement of the floating cylinder for the heave decay test . . . . .	109

7.5	Comparison of the time series for the heave decay test of the simple cylinder . . . . .	110
7.6	Comparison of the time series for the pitch decay test of the simple cylinder . . . . .	110
7.7	Comparison of the time series for the surge decay test of the simple cylinder . . . . .	111
7.8	Overall mesh of the model for the free-decay tests of the deepCWind FOWT . . . . .	113
7.9	Mesh on the boundaries of the deepCWind FOWT . . . . .	114
7.10	Mooring distribution for the DeepCWind FOWT based on the experimental model presented in [56] . . . . .	114
7.11	Initial position of the free-decay tests. The orange mesh is the background mesh, the green mesh is the overset mesh . . . . .	115
7.12	Comparison of the time series for the heave decay test of the FOWT normalized in time by the experimental natural period $T = 2.47$ s and by the initial displacement $z_{init} = 0.027$ m . . . . .	116
7.13	Comparison of the time series for the pitch decay test of the FOWT normalized in time by the experimental natural period $T = 4.68$ s and by the initial tilt angle $angle_{init} = 3.34^\circ$ . . . . .	117
7.14	Global mesh of the FOWT numerical wave tank. The red cells are the overset mesh and the dark blue cells are in the background mesh. The light blue represents the free surface . . . . .	119
7.15	Vertical slice of the mesh of the FOWT. Blue cells are in the background mesh and red cells are in the overset mesh. The red lines are the catenary mooring lines . . . . .	120
7.16	First order wave amplitude of the Fourier analysis on a sliding time window using overWaveDyMFoam solver . . . . .	121
7.17	Time series of free surface elevation, heave pitch and surge positions. The blue lines are the results from the present CFD model, the red lines are the experimental results from [56]. Small scale: $T = 1.71$ s $A = 0.07$ m . . . . .	122
7.18	Modulus of the RAO for free surface elevation, heave, pitch, and surge motions. The blue bars correspond to the present CFD model and the red bars correspond to the experimental results from [56]. Small scale: $T = 1.71$ s $A = 0.07$ m . . . . .	123
7.19	Run-up around the upstream column during one wave period. Fore side view. Small scale: $T = 1.71$ s $A = 0.07$ m . . . . .	123
7.20	Run up around the upstream column during one wave period. Port side view. Small scale: $T = 1.71$ s $A = 0.07$ m . . . . .	124
7.21	Velocity magnitude of the flow at the free surface near the structure. Small scale: $T = 1.71$ s $A = 0.07$ m . . . . .	125
7.22	Catenary mooring positions on the floater based on the experimental campaign of [98] . . . . .	127
7.23	First order wave amplitude of the Fourier analysis on a sliding time window using overWaveDyMFoam solver. Initial and tuned wave conditions . . . . .	128
7.24	Modulus of the RAO for surge, heave, and pitch motions. The blue bars correspond to the present CFD model, the red and grey bars correspond to the experimental and FAST results respectively, taken from [98]. . . . .	129

7.25	Modulus of the RAO for surge, heave, and pitch motions. the stars correspond to the regular wave cases, the blue and orange lines are the experimental and FAST results of Coulling [98] from an irregular wave spectrum. . . . .	131
7.26	Time series of surge heave and pitch positions for 3 wave amplitudes. $T = 12.1$ s . . . . .	132
7.27	Time series of surge heave and pitch positions for the 2 wave amplitudes. $T = 14.1$ s . . . . .	133
7.28	Time series of surge heave and pitch positions for the 2 wave amplitudes. $T = 20.0$ s . . . . .	133
7.29	Run-up around the upstream column during one wave period. Port side view. Case 4: $T = 14.3$ s $A = 3.57$ m . . . . .	134
7.30	Run-up around the upstream column during one wave period. Port side view. Case 5: $T = 14.3$ s $A = 5.37$ m . . . . .	134
A.1	Comparison of the free surface of the experimental tests (left [118] and the 3D projection of the 2D CFD results $A = 0.015$ m, $T = 1.6$ s, $d = 0.05$ m, $KC = 0.157$ . part 1/2 . . . . .	143
A.2	Comparison of the free surface of the experimental tests (left) [118] and the 3D projection of the 2D CFD results (right) $A = 0.015$ m, $T = 1.6$ s, $d = 0.05$ m, $KC = 0.157$ . part 2/2 . . . . .	144
B.1	Time series of the horizontal and vertical forces and the moment. The blue lines correspond to the global structure, the red and black lines to the upstream and starboard columns respectively. Small scale: $T = 1.71$ s $A = 0.07$ m . . . . .	145
B.2	Modulus of the RAO for the horizontal and vertical forces and the CoG moment. The blue lines correspond to the global structure, the red and black lines to the upstream and starboard columns respectively. Small scale: $T = 1.71$ s $A = 0.07$ m . . . . .	146
B.3	Time series of the horizontal and vertical forces and the CoG moment on the whole structure for the cases 1, 2 and 3 . . . . .	147
B.4	Time series of the horizontal and vertical forces and the CoG moment on the whole structure for the cases 4 and 5 . . . . .	147
B.5	Time series of the horizontal and vertical forces and the CoG moment on the whole structure for the cases 6 and 7 . . . . .	148
B.6	Modulus of the RAO for the horizontal and vertical forces and the CoG moment on the whole structure for the 7 cases . . . . .	148

# List of Tables

3.1	Description of the boundary conditions used by default for the simulations of this thesis (unless otherwise stated) for volume fraction, pressure and velocity . . . . .	30
3.2	Cases for the convergence analysis of the global refinement . . . . .	31
3.3	Cases for the convergence analysis of the expansion ratio . . . . .	32
3.4	Cases for the convergence analysis of the relaxation zones lengths . . . . .	33
3.5	Cases for the convergence analysis of the relaxation exponent . . . . .	34
3.6	Cases for the convergence analysis of the time step . . . . .	35
3.7	Cases for the convergence analysis of the maximum residual of pressure. . . . .	36
4.1	Numerical schemes used in the CFD model . . . . .	49
4.2	Description of the boundary condition for volume fraction, pressure and velocity . . . . .	50
4.3	Comparison of the input parameters and the computational outputs for the convergence analysis of the global refinement of the mesh . . . . .	53
4.4	Comparison of the input parameters and the computational outputs for the refined box convergence analysis . . . . .	54
4.5	Comparison of the computational times for three values of the maximum Courant number $Co$ . . . . .	56
4.6	Comparison of the computational times for four values of the acceleration relaxation coefficient . . . . .	57
5.1	Description of the boundary conditions for volume fraction, pressure and velocity . . . . .	66
5.2	Numerical schemes used in the CFD model . . . . .	66
6.1	Cell dimensions for the mesh imposed in the OC6 project . . . . .	95
6.2	Numerical parameters and settings for CFD solver imposed in OC6 project . . . . .	95
6.3	Numerical settings for CFD solver imposed in OC6 project for the bichromatic wave case . . . . .	98
6.4	Description of the parameters of the bichromatic wave case . . . . .	99
6.5	Normalization factors for the wave loads [150] . . . . .	100
7.1	Description of the boundary conditions for volume fraction, pressure and velocity . . . . .	107
7.2	Numerical schemes used in the CFD model for the vertical cylinder case . . . . .	107
7.3	Position of the anchors and the fairleads of the mooring lines (in meters) . . . . .	108
7.4	Natural periods and damping coefficients of the free-decay tests of the vertical cylinder . . . . .	112
7.5	Main characteristics of the FOWT at model scale [53] . . . . .	113
7.6	Mooring characteristics for the DeepCWind FOWT based on the experimental model presented in [56] . . . . .	115

7.7	Natural periods and damping coefficients of the free-decay tests for the DeepCWind cases . . . . .	117
7.8	Main characteristics of the FOWT at model scale [53] . . . . .	118
7.9	General characteristics of the FOWT [65] . . . . .	126
7.10	Mooring lines characteristics [65] . . . . .	127
7.11	Parameters of the simulated wave cases . . . . .	128

# List of Abbreviations

<b>BEM</b>	<b>B</b> oundary <b>E</b> lement <b>M</b> ethod
<b>CAD</b>	<b>C</b> omputer <b>A</b> ided <b>D</b> esign
<b>CFD</b>	<b>C</b> omputational <b>F</b> luid <b>D</b> ynamics
<b>CFL</b>	<b>C</b> ourant <b>F</b> riedrichs <b>L</b> ewy number
<b>CoG</b>	<b>C</b> entre of <b>G</b> ravity
<b>DoF</b>	<b>D</b> egree of <b>F</b> reedom
<b>FDM</b>	<b>F</b> inite <b>D</b> ifference <b>M</b> ethod
<b>FEM</b>	<b>F</b> inite <b>E</b> lement <b>M</b> ethod
<b>FOWT</b>	<b>F</b> loating <b>O</b> ffshore <b>W</b> ind <b>T</b> urbine
<b>FSI</b>	<b>F</b> luid- <b>S</b> tructure <b>I</b> nteractions
<b>FVM</b>	<b>F</b> inite <b>V</b> olume <b>M</b> ethod
<b>HPC</b>	<b>H</b> armonic <b>P</b> olynomial <b>C</b> ell
<b>IEA</b>	<b>I</b> nternational <b>E</b> nergy <b>A</b> gency
<b>IRENA</b>	<b>I</b> nternational <b>R</b> enewable <b>A</b> gency
<b>LCOE</b>	<b>L</b> evelized <b>C</b> ost <b>O</b> f <b>E</b> nergy
<b>LPFM</b>	<b>L</b> inear <b>P</b> otential <b>F</b> low <b>M</b> odel
<b>NREL</b>	<b>N</b> ational <b>R</b> enewable <b>E</b> nergy <b>L</b> aboratory
<b>NWT</b>	<b>N</b> umerical <b>W</b> ave <b>T</b> ank
<b>QTF</b>	<b>Q</b> uadratic <b>T</b> ransfer <b>F</b> unction
<b>RANS</b>	<b>R</b> eynolds <b>A</b> veraged <b>N</b> avier- <b>S</b> tokes equations
<b>SWL</b>	<b>S</b> till <b>W</b> ater <b>L</b> evel
<b>TLP</b>	<b>T</b> ension <b>L</b> eg <b>P</b> latform
<b>VOF</b>	<b>V</b> olume of <b>F</b> luid
<b>WEC</b>	<b>W</b> ave <b>E</b> nergy <b>C</b> onverter



# 1 Introduction

## 1.1 An overview of the floating offshore wind industry

### 1.1.1 General Context

According to the International Renewable Energy Agency (IRENA), the production of energy is responsible for two-thirds of the global greenhouse gas emissions [1], mostly because of the massive use of fossil fuels (about 84% of energy use at the global scale). The electricity generation is the most CO<sub>2</sub>-emitting sector. The decarbonization of energy production will have a crucial impact to meet the so-called Paris agreements and maintain the temperature rise below 2°C. According to IRENA, renewable electricity could reach 80% of the World demand by 2050 whereas it represents only 25% today [1]. There is thus an unquestionable need to develop new technologies for green energy production to reach the goals of the Paris agreements. The success of this endeavor lies in the diversification of the sources. The development of solar power and onshore wind has already shown significant results for power generation, and those sources of energies are now competitive with traditional sources of production such as coal, gas, fuel or nuclear power [2]. More recently, even though it represents only 0.3% of the global power production [3], the expansion of offshore wind energy has become a true added value to the energy mix.

The fixed foundation wind turbine farms have been largely developed in northern Europe (80% of the global market [3]) and in Asia, and have grown rapidly (30% per year for the last 10 years [3]). Offshore wind energy enables larger turbines than onshore with a wind resource higher and more constant in time, reaching a capacity factor of 40-50% [3].

As reported by the International Energy Agency (IEA), the offshore wind itself could cover 11 times the global energy demand by 2040. To reach this capacity, it is necessary to expand the deployment to larger water depths. Fixed offshore foundations have a limit of water depth, usually around 60 m. Therefore, areas where these turbines can be deployed are limited to coastal shelves, or these turbines need to be installed very close to the shore. The solution, to benefit from the large wind resource of the oceans with larger water depth, is to move from fixed foundations to floating structures.

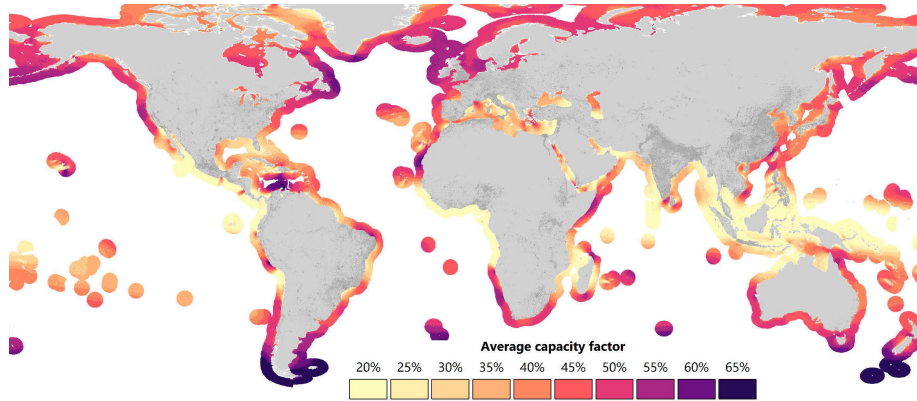


FIGURE 1.1: Average capacity factor for offshore wind around the World [3]

The basic idea is to install the wind turbine on a floating platform anchored to the ocean bottom and to bring the electricity back to shore with a submarine cable. The use of a massive floating platform for energy production is not new. It has largely been developed in the oil and gas industry over the past decades, and many solutions for wind energy can be inspired by these existing technologies, some of them being illustrated in figure 1.2.

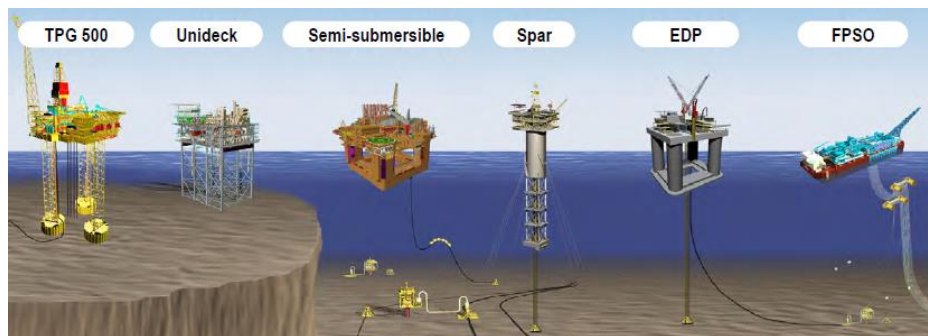


FIGURE 1.2: Overview of offshore structures in the Oil and Gas industry [4]

However, several new challenges are specific to the integration of wind turbines such as the coupling between hydro and aerodynamics loads or the export of electricity. The Floating Offshore Wind Turbines (FOWT) industry is still at an early stage with over 30 concepts in development [4]. By now, only a few pilot projects have been deployed in the World. The first evaluations are very promising, and the market is expected to grow rapidly in the coming years. These pilot farms are the cornerstone enabling a wider diffusion into commercial farms of 60+ wind turbines with a Levelized Cost Of Energy (LCOE) expected to reach around \$130/MWh (£85-95/MWh, estimated in 2015 for the 2020s [4]).

The acceptability of the technology is an important factor to consider and will be improved compared to other wind energy solutions because the turbines are installed far offshore, and the visual impact is therefore limited. Studies have been done to mitigate the impact on the ecosystem, and many others are still under investigation. The first results have been promising with limited negative impact observed. It has even shown positive impacts on biodiversity by creating artificial reefs and protected

areas. For example, the company ECOCEAN, in partnership with the Centre de Recherche sur les Ecosystèmes Marins, installed an artificial reef on the location of a future floating wind farm to investigate the development of the biodiversity around these structures (figure 1.3).

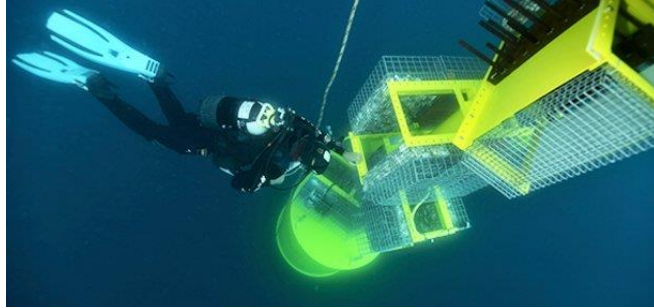


FIGURE 1.3: BoB buoy, installed on the site of the future floating wind project: Eoliennes Flottantes du Golfe du Lion (France), to study the biodiversity. Credits : ECOCEAN / Remy Dubas

### 1.1.2 The main technologies of FOWT

Nowadays, floating wind turbines can be categorized into four main types: Spar-buoy, Tension-Leg Platform (TLP), Semi-submersible, and Barge. Each of these types uses three methods to achieve static stability: the ballasting, the mooring lines, the buoyancy, or any combination of these methods. A few of the most advanced concepts are presented in this section. One may refer to [5] for a more detailed overview of that industry sector.

#### 1.1.2.1 Spar concept

The spar type concept uses mainly the ballasting stability principle. It usually has a vertical cylindrical column shape with a large draft. A large portion of the global mass is located at the bottom of the structure to lower the center of mass as much as possible. The rest of the structure provides adequate buoyancy. The most advanced project of Spar in FOWT is the Hywind design [6] (see figure 1.4). A pilot farm of five 6 MW turbines has been installed in 2017 and is currently in operation in Scotland. This technology has a great advantage to have a good stability and is relatively easy to fabricate. However, the installation of such structures with wind turbines is complex and usually requires large water depth.



FIGURE 1.4: Hywind design (Equinor) [6]

### 1.1.2.2 Barge

On the contrary, the barge design has a very shallow draft compared to spar. The stability of such structures is ensured by their large waterplane area that provides a high level of buoyancy. This solutions has been used for instance in the Floatgen project developed by Ideol in France [7] (see figure 1.5a). A first 2 MW prototype has been installed off the coast of Le Croisic (France) and is currently under operation. The advantage of this technology is its simple geometry that enables the use of different types of materials for its construction, such as steel or concrete.

### 1.1.2.3 TLP

The TLP have great stability thanks to their taut mooring lines that counteract the platform's motions. A TLP type concept is being developed by IFPEN and SBM offshore [8] (see figure 1.5b), and should be deployed in the French seas in the coming years. This technology has the great advantage of being compact with a reduced structural mass, compared to other technologies. However, the platform installation can be challenging since the platform is naturally unstable when disconnected from its mooring system.



(A) FloatGen design (Ideol) [7]



(B) TLP design (IFPEN and SBM offshore)  
[8]

FIGURE 1.5: Examples of barge and TLP types of FOWT

### 1.1.2.4 Semi-submersible

The semi-submersible concept has been largely implemented in the Oil and Gas industry and seems to be slightly ahead in the FOWT market with several projects developing this solution. This technology gains its stability mostly from its buoyancy. These types of platforms have the great advantage of being relatively easy to install. The turbine can be mounted on the quayside, and the floater can be towed to its

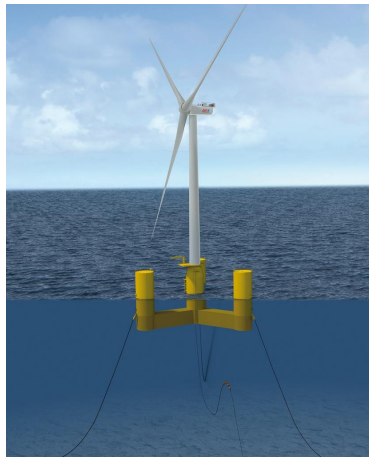
location or brought back to shore for repair or decommissioning. It requires catenary mooring lines that are cheaper than the taut lines of TLP platforms. Its main constraint is its complex geometry that makes its fabrication more difficult. It also requires a significant amount of structural mass [4].



(A) WindFloat (Principle Power).  
credit: Principle Power/A. Aula



(B) Tri-Floater (GustoMSC) [9]



(C) Naval Energies Technology ([www.naval-energies.com](http://www.naval-energies.com))



(D) Maine University Technology [10]

FIGURE 1.6: Semi-submersible concepts for Floating offshore wind turbines

The most advanced project of this family is the WindFloat concept designed by the company Principle Power (PP) [11] (figure 1.6a). A prototype has been successfully installed in Portugal in 2011, has operated for 4 years, has been decommissioned, and has been reinstalled in Scotland in 2018. Recently, PP successfully connected to the Portuguese electricity grid, a pilot wind farm of 3 turbines for a total of 25 MW. Many projects using the Windfloat technology are under development in the World, including commercial-size wind farms. Other companies, at a lower stage of development, have also presented semi-submersible concepts ([9], [10], [12]). Few of them are presented in figure 1.6. An open-source semi-submersible design named DeepCWind is widely used by the research community to better understand the physics of FOWT and share the results.

### 1.1.2.5 Hybrid concepts

Hybrid concepts of these technologies have also been imagined to benefit from the advantages of different technologies. The most famous is the truss spar that has already been used in the Oil and Gas industry. It is a mix between a semi-submersible platform and a spar. The stability is obtained with the combination of a low center of gravity (CoG) and a large water plane to increase the buoyancy. The idea is to have a lower draft than a spar, but a smaller structural mass than a semi-submersible platform. More recently, an innovative concept has been developed for FOWT. The idea is to reach stability by lowering the CoG, but unlike the spar, the ballast mass is connected to the main floater with connectors. It allows more flexibility for installation. Thanks to this ballast, the main floater structural mass is largely reduced. Three companies (Esteyco, Stiesdal A/S [14], and Saipem [13]) have been developing this idea, and a prototype is expected to be launched soon. Saipem's concept is presented on figure 1.7.



FIGURE 1.7: Hexafloat technology (Saipem) [13]

## 1.2 State of the art of the modeling of FOWT with current engineering models

No matter the FOWT concept, the challenge for engineering teams that develop these structures is to anticipate the performance of the platform in all expected metocean conditions, during its entire lifetime. The hydrodynamic stability is the first criterion to consider to prevent the platform from capsizing or sinking. The amplitude of motion and the acceleration in the 6 Degrees of Freedom (DoF) are also a key-driven aspect of the design. These motion amplitudes are mostly constrained by the mooring system (for the linear motions) and the wind turbine performances (for the rotations). At the same time, the mass of the structure or its installation and construction process have the largest impact on the cost of a project. So it is crucial to find an optimum solution that will provide survivability and efficiency at the lowest possible cost. To study so many scenarios in a

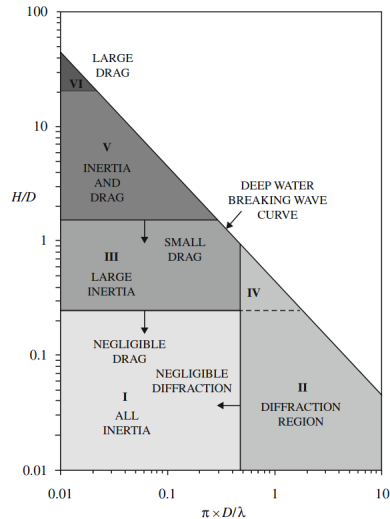


FIGURE 1.8: Different wave force regimes [15]  $D$  is the characteristic dimension,  $H$  is the wave height, and  $\lambda$  is the wave length

reasonable amount of time, several engineering tools based on simplified assumptions are available.

Figure 1.8 shows the different force regimes induced by the interaction between waves and a body. When the structure dimensions are large compared to the wave height, the inertia forces dominate, and when the structure is large compared to the wavelength, the diffraction forces prevail. On the contrary, as the structure dimensions become small compared to the characteristic dimensions of the wave (wavelength and height), the drag loads dominate. A detailed analysis can be found in the book of Bernard Molin [16].

At the early stage of the design process, linear wave models based on the potential flow theory are usually used to assess the global hydrodynamic coefficients for diffraction and radiation of a FOWT. For these models to be accurate, the low wave steepness (linear waves) assumption must be valid. The fluid is supposed inviscid and the flow is supposed incompressible and irrotational. The dimensions of the structure should be large compared to its natural motion and the wave amplitudes (zone I and II on figure 1.8). The viscous effects are neglected in this approximation. The most popular tools based on this theory are WAMIT from the Massachusetts Institute of Technology [17], Diodore from Principia [18], NEMOH from LHEEA (Centrale Nantes) [19], or ANSYS-AQWA [20].

The hydrodynamic coefficients from the linear theory are often integrated into time-domain simulation tools that model viscous effects based on the so-called Morison equation [21]. This equation enables to assign drag coefficients to the members of the structure based on empirical values [22]. This equation is valid if the member dimensions are small compared to the wavelength (i.e. "hydrodynamic transparent") as described on figure 1.8. The software OrcaFlex developed by Orcina [23] is largely used for this task and is specialized in the analysis of moored floating structures. The shape of the structure is modeled by line members at which a length, diameter, mass, inertia, and drag coefficient can be assigned. This hydrodynamic software can be coupled to an aeroelastic simulation tool such as FAST [24] (Fatigue, Aerodynamics, Structures, and Turbulence) developed by NREL. This coupled model called OrcaFAST can simultaneously model all aspects of a FOWT, including platform motions, hydrodynamic loads on the floater, and aerodynamic loads on the turbine, structural and mooring responses... NREL also developed its own hydrodynamic subroutine as part of the FAST code, named Hydrodyn [25]. The method is similar to Orcaflex. It also requires providing the coefficients from the linear diffraction and radiation problems computed with WAMIT or similar codes. These tools have been compared in [26]. Just as OrcaFAST, Hydrodyn can be coupled with the other modules of FAST. A mooring package, called Moordyn, is also available in FAST [27]. Several other hydrodynamic modules have been coupling with FAST as described in [28].

Since 2005, a group of participants from universities, research institutions, or industries from all over the World has been working on a series of so-called "OC" projects to compare and validate aero-hydro-servo-elastic codes for modeling of FOWT. These projects operate under tasks from the International Energy Agency (IEA) and are led by NREL. The last project OC6 (Offshore Code Comparison Collaboration, Continued, with Correlation, with UnCertainty) is dedicated, in its first phase, to investigating the low-frequency wave response of semi-submersible platforms.

Some tools also improve the linear potential models with second-order corrections,

e.g. Orcaflex or Hydrodyn. In these tools, it is possible to add Quadratic Transfer Functions (QTF) to model the difference frequency or sum-frequency terms of pairs of linear wave components. The difference frequency term usually generates low-frequency contributions. The sum of these low-frequency contributions is called the wave drift force. They can have significant impacts on the FOWT as seen during the OC5 project. The sum frequency generates high-frequency contributions and is expected to have a limited impact on semi-submersible designs. Nevertheless, they can be critical for the TLP platform as they can excite natural frequencies of the system [23]. It can also have an effect on the tower frequency excitation.

Fully nonlinear potential flow models for wave-structure interactions analysis have also been developed to solve the Laplace equation. To solve this equation, three main groups of numerical methods exist. The first group is based on the Boundary Element Method (BEM) [29, 30, 31, 32, 33, 34]. The second group is based on field solvers in which the entire domain is discretized. The most popular methods of this group are the Finite Element Method (FEM) [35, 36, 37, 38], the Finite Difference Method (FDM) [39, 40], and the Finite Volume Method (FVM) [41]. The third group includes models based on the Harmonic Polynomial Cell methods (HPC) as introduced by Shao and Faltinsen [42], and used recently by Robaux and Benoit [43].

Depending on the required precision level, these models can be efficient for a limited computational cost. They are appropriated for predicting the behavior of FOWT in ‘operational’ conditions. They can also provide sufficient estimation of higher-order loads for weakly nonlinear conditions and simple geometries. However, all these methods cannot capture rotational or turbulent effects. These effects can have significant impacts on the structure, e.g. on the wave run-up, green water, breaking waves, water jets... In these conditions, Computational Fluid Dynamics (CFD) simulations may be necessary to better estimate the wave loads. Those conditions are the ones which drive certain aspects of the floater design. Some work has been done in developing coupled solver where the wave propagation is modeled using potential flow theory in the global domain, but a CFD model is used in the platform vicinity, as presented in the Ph.D. thesis of Robaux [44].

## 1.3 Modeling of Floating wind with CFD

The development of numerical wave tanks (NWT) using CFD is growing since the availability of computational power is continuously increasing. If well-validated, a CFD NWT can supplement –or even replace– expensive experimental testing campaigns to design offshore structures. The FOWT market is an emerging market with little available experimental or real-life data. However, the development of clean and renewable power production systems is becoming urgent. Therefore, the validation of high-fidelity NWT can be a key asset to design reliable and efficient FOWT in a fast and cost-effective way. In this method, the Navier-Stokes (NS) equations describe the motions of a viscous fluid. Unlike potential flow models, the viscous, turbulent, and rotational effects can be considered with the counterpart of higher computational cost.

### 1.3.1 Most popular CFD software tools for maritime purposes

A couple of CFD software are available on the market. The most common discretization approach for CFD simulations is the finite volume method (FVM). This method

is implemented in the two most popular commercial CFD software Ansys CFD (previously Fluent) developed by Ansys, and Star-CCM+ developed by Siemens. These tools have been widely used and validated in several fields, including multi-phase flows. They are robust, easy to take in hand, and licenses come with efficient supports from experts. It is possible to couple the CFD module with other software to solve multi-physics problems (structure, electronics...). They both include highly efficient Computer-Aided Design (CAD), meshing tools, and pre and post-processing modules. However, the source codes are not accessible, cannot be modified and are sometimes considered as a "black box". On top of that, licenses can be expensive.

The popular open-source code OpenFOAM® (Open Field Operation And Manipulation) is largely used in the research community. The code is fully transparent and easy to modify. It includes a large number of integration schemes and solvers for a large variety of problems. The solver InterFoam is developed for multi-phase flows, and is at the origin of additional extension solvers for wave modeling.

Other CFD software have been developed and optimized for maritime application. ReFRESKO (RELIable & Fast RANS Equations (solver for Ships (and) Constructions Offshore) is one example [45]. It has been developed and maintained by Marin (The Netherlands). The software also uses a FVM approach. It is possible to analyze the motions of solid structures with most of the available meshing methods for dynamic structures. The software is community-based and developed by several non-profit organizations. However, the libraries are not open-source software and require a license. Similarly, the CFD solver naoe-FOAM-SJTU (naoe stands for naval architecture and ocean engineering) has been developed by Shanghai Jiao Tong University (China) from OpenFOAM®, specifically for maritime applications including modules for wave generation and absorption, 6 DoF motions, mooring system, overset mesh or fluid-structure interactions [46]. Less common, the FEM method can also be used in CFD software as it is the case in the open-source tool Proteus developed at HR Wallingford [47]. This software has also been developed for fluid-structure interaction. In this thesis, OpenFOAM® was used in all simulations.

### 1.3.2 Wave Modeling in OpenFOAM®

To develop a NWT, it is crucial to have a reliable model of wave propagation. In CFD, the wave propagation modeling can be challenging, and the numerical model should ensure that there is no artificial (i.e. of numerical origin) dissipation or dispersion of the wave. Solutions for modeling multi-phase flow have been largely developed and validated for CFD. However, just as the experimental wave tank, the CFD NWT is bounded. Hence, the modeling of propagating waves requires some additional boundary conditions. The tool needs to integrate solutions to avoid undesirable reflection on boundaries, and to replicate more precisely what happens in the sea conditions.

The development of an efficient tool for wave generation and absorption takes a large place in the OpenFOAM® community, and two major packages have been developed and made freely available. The first one is the IHFoam tool developed at IH Cantabria (Spain) and presented by Higuera et al. in [48]. This modeling tool has been initially developed for coastal engineering applications. It can generate any type of wave in 3D, including regular waves (Stokes I, II, V...) and irregular waves from multiple directions. The great force of IHFoam lies in its wave absorption boundary that can be implemented at the extremities of the NWT. These boundaries have shown good results in canceling the wave reflection without extending the NWT length with relaxation zones, and in reducing the number of cells, and so the computation cost.

In spite of its good results in shallow water depths, the wave absorption boundary of IHFoam has not yet been adapted to deep water waves. This tool has been implemented in the core of the last OpenFOAM® versions and is very robust.

The second popular tool for wave generation and absorption in OpenFOAM® is the open-source package Waves2Foam. This toolbox was initially developed and validated by Niels Gjøøl Jacobsen [49]. Its maintenance and development are handled by the research institute Deltares (The Netherlands) [50]. It has been developed as a module compatible with most OpenFOAM® versions. It includes wave generation modules that can generate regular waves based on several theories, including Stokes I, II or V but also stream function waves or cnoidal waves. It is also possible to generate bi-chromatic waves that include all the interactions between the waves of different periods. Finally, irregular waves can also be generated based on the JONSWAP or Pierson-Moskowitz spectrum. The wave generation feature is associated with a wave damping functionality which is based on a relaxation technique to avoid reflection at the tank extremities. In this method, it is necessary to assign a fraction of the NWT size to the relaxation zone. The toolkit comes with a variety of post-processing tools. Wave2Foam has been used for this thesis, and a more in-depth description of the theory will be presented in the following chapter.

### 1.3.3 Modeling of Dynamic Structures in CFD

#### 1.3.3.1 Meshing methods for moving structures

The modeling of FOWT in CFD is recent. Although CFD is very popular in fluid flow modeling, the interaction with a moving structure is still a complex and computationally expensive task. As in CFD only the fluid domain is meshed, it necessarily needs to be transformed as the body moves. There are different techniques available for this task. The most popular is the mesh morphing method where the cells are contracted or stretched as the body moves. This method is efficient for small motions of the body. However, for large motions, the mesh quality can be extremely deteriorated and the computation may diverge. The remeshing method consists of building a new mesh at each time step. This method is more computationally expensive and requires a highly efficient meshing module that will guarantee the quality of the mesh at each time step. If the body has only one DoF, the sliding meshing method is the most efficient method. In this method, a zone of the mesh has to be defined around the body and interpolation is made at the interface with the global mesh. The last method, which has been used in this thesis, is the overset mesh method. In this method, two meshes are generated. One mesh represents the global domain and is generally fixed, while the other one surrounds the floating body and is body-fixed (so that it moves together with the body in case of a moving body). At each time step, interpolation is done between these two meshes to provide a single solution. The advantage of this method is that it maintains the mesh quality throughout the simulation and avoids mesh distortions. It is useful when dealing with large body displacements.

#### 1.3.3.2 Remeshing and Mesh Morphing methods for FOWT modeling

Almost all published CFD analysis of semi-submersible FOWT are using the Deep-CWind concept, mainly because experimental data are accessible and numerical results are available in the literature.

Benitz et al. [51] compare results from potential flow theory and Morison equation using the Hydrodyn module from FAST with results from a CFD model using OpenFOAM® for the DeepCwind semi-submersible concept. The forces on the structure are compared, and the platform is assumed to be fixed. Current-only and waves-only cases are considered. The components of the structure are divided into two groups, depending on which wave force type dominates (diffraction, drag, or inertial force), and the efficiency of FAST for modeling these different forces is analysed. CFD simulations have also been used in the Ph.D. thesis of Benitz [52] to assess the assumptions and limitations of engineering tools. In her thesis, she also used a model of the DeepCWind floater using a loosely-coupled Fluid-Structure Interactions (FSI) solver derived from OpenFOAM®, but the motion predictions were poor when comparing to experimental data. However, the use of a tightly-coupled solver provided better results.

Bruinsma et al. [53] also focused on free decay tests and wave-induced motions of the DeepCWind platform. They used waves2foam for wave generation and absorption and presented a quasi-static mooring method implemented in Waves2Foam. The results are compared with experimental results. The need for a stabilizing method for FSI simulation is emphasized. The simplified mooring model shows good efficiency. Both the stabilization method and the mooring model will be presented in chapter 2 of this thesis. A more detailed analysis can be found in the Master thesis of the first author [54]. This work has been continued in the master thesis of Rivera-Arreba [55]. In her work, she compared the CFD results of the platform with experimental results and a potential flow theory solver. In addition to the free decay tests, she performed an analysis in waves with increasing steepness. She compares the advantages of both models depending on the wave conditions and the geometry of the structure. She concludes that CFD models are useful to calibrate Potential flow based solvers especially for complex structures and to capture local non linear effects. These results are also presented in [56]. OpenFOAM® is also used to investigate the DeepCWind floater using OpenFOAM® in [57] and [58].

Burmester et al. [59] used the software ReFRESKO to analyze the surge motion of the DeepCWind platform with 3 DoF. A detailed sensitivity analysis is presented for the time step sizing. The mooring effects are emphasized. The velocity and vorticity contours around the platform are shown. They insist on the importance of a good estimation of the numerical error and the uncertainty to obtain credible results. A complete investigation of methods to improve the credibility of the results in CFD modeling of FOWT was presented in [60]. The ReFRESKO code was also used by Wang et al. [61] to compute the pitch decay motion of the same floater. They show that vorticity and pressure changes are mostly present around the heave damping plates. Huang et al. [62] and Cheng et al. [63] also investigated the DeepCwind floater using the naoe-FOAM-SJTU model. All the previously cited analyses consider only the wave or the current loads on the platform. In these studies, the wind turbine is not modeled, and the wind forces are not considered. Few studies have built CFD models of both the floating platform and the turbine including wind forces ([64], [65], [66] or [67]).

Spar type FOWT have also been investigated in the work of Quallen et al. [68] [69]. They performed a CFD analysis of the hydrodynamic flow around the floater and the aerodynamics of the turbine. Beyer et al. used a coupling method between CFD and the Multibody software SIMPACK, a commercial aero-servo-hydro-elastic simulation tool, to model a Spar in [70] and the Floatgen FOWT concepts.

CFD NWT are also used in other renewable energies fields such as the Wave Energy Converters (WEC) [71]. Islam et al. [72], and Courbois et al. [73] investigated the wave forces on 2D rectangular pontoons using OpenFOAM®. Courbois et al. analyzed the effect of heave plates located at the bottom of the pontoons in highly nonlinear waves. Palm et al. [74] investigated with OpenFOAM® the hydrodynamic response of a moored vertical cylinder with a high-order finite element model of mooring cables. De Lataillade et al. [47] modeled a similar body using the Proteus simulation toolkit. Paci et al. [75] also modeled a vertical cylinder with a larger draft using OpenFOAM® with the IHFOam wave generation tool.

### 1.3.3.3 Overset mesh method for floating structure in CFD

Whereas the overset mesh method is available in most of the CFD software, it is still at an early stage of development for floating bodies. However, a couple of analyses have already been presented in the literature and have shown good results. The main application of this technique is the modeling of ship motions. It is suitable to model large motions of the ship or rotating propeller. A research group from the Shanghai Jiao Tong University has published a large number of simulation results involving 3D ship motion and using an overset mesh method coupled with their OpenFOAM® solver naoe-FOAM-SJTU. Shen et al. analysis of a manoeuvring ship with and without rotating propeller, ship motions in waves, waves forces on the hull, and wave slamming are presented in [76, 77, 78, 79, 80, 81, 82, 46, 83]. A similar ship motion analysis can also be found in reference [84]. Water entry model of ships are presented in the works of Chen et al. [85] and Ma et al. [86] using OpenFOAM® solvers. This method is also available in commercial software. For instance, in the work of Khaware et al. [87], Ansys Fluent is used to model free surface flows using an overset mesh. Chen et al. [85] have developed a NWT using the overset mesh method from OpenFOAM® with the IHFOAM solver for wave modeling, and have validated it with several 2D and 3D floating cases. The overset method is also used by Di Paolo et al. [88], who obtained good results in modeling interaction between waves, current and a 3D moored body using the IHFOAM solver. A comparison between the overset mesh method of OpenFOAM® and the mesh morphing method with experimental measurements of a WEC is performed by Windt et al. in [89] and [90]. They concluded that the accuracy of the overset mesh is equivalent to the mesh morphing method but that run time is higher. They recommend using the overset method when the body motion exceeds the limit of stability of the mesh morphing strategy. Heilskov [91] presented a comparison between a flexible mesh approach with OpenFOAM®, an overset grid method with Star-CCM+, and experimental results of the nonlinear effects of a moored spar-type WEC subjected to waves. They showed that OpenFOAM® is subject to numerical instabilities due to mesh deformation even for small displacements. However, the Star-CCM+ results with overset mesh accurately captured the nonlinear response of the body.

Finally, the overset mesh technique has also been used to model FOWT. In [92], wave loads on a moored Spar type FOWT using Star-CCM+ are presented and compared to FAST results and experimental tests. Tran and Kim [93] also investigated a Spar FOWT with Star-CCM+. They showed that the CFD NWT was coherent with FAST and experimental results for low wave steepness, validating the model. The naoe-FOAM-SJTU solver with the overset mesh method has been used to model an entire semi-submersible FOWT including platform, turbine, and mooring system.

The DeepCWIND design was used and the aerodynamic loads on the turbine were discussed. Finally, the most complete work on the modeling of semi-submersible FOWT with overset mesh method was performed by Tran and Kim using Star-CCM+ ([94], [95], [96] and [97]). They first presented the hydrodynamic response of the DeepCWIND floater without modeling the turbine in [94] and compared the platform motion results in free decay tests or waves with experimental measurement and results from potential based codes. They emphasized that the CFD results are in good agreement with experiments without imposing additional damping. Laminar and turbulent solvers were compared, and they concluded that a laminar model gives accurate results in free decay tests. The mooring restoring forces were also investigated. Tran And Kim extended the hydrodynamic CFD model to a fully coupled aero-hydrodynamic analysis by integrating the wind turbine. Results of this full configuration, with an advanced dynamic fluid body interaction method, using an overset mesh method are presented in [96]. The platform motions and the aerodynamic loads on the turbine are described.

## 1.4 Experimental research on Semi-submersible FOWT

In this thesis, the DeepCWind concept will be investigated to validate the methods against experimental results. An experimental campaign for this design was carried out in the scope of the OC4 and OC5 projects at MARIN at 1/50<sup>th</sup> scale. Platform motions and mooring response in wave only or wave and wind conditions are presented in [98] and [99]. The experimental results are also presented in the OC4 and OC5 reports (e.g. [100]).

A new experimental campaign is ongoing in the scope of the OC6 project, and results should be shared in 2021. Bruinsma et al. [53] and Rivera et al. [56] also presented experimental results using the same floater, but with a different mooring system.

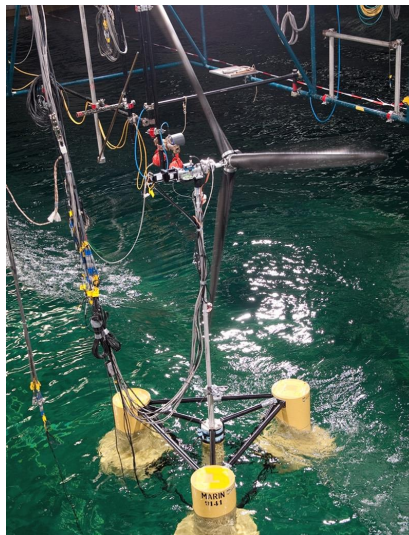


FIGURE 1.9: Experimental model of the DeepCWind floater tested in a wave basin at MARIN (The Netherlands) [100]

The dimensions of the DeepCwind platform are summarized on figure 1.10.

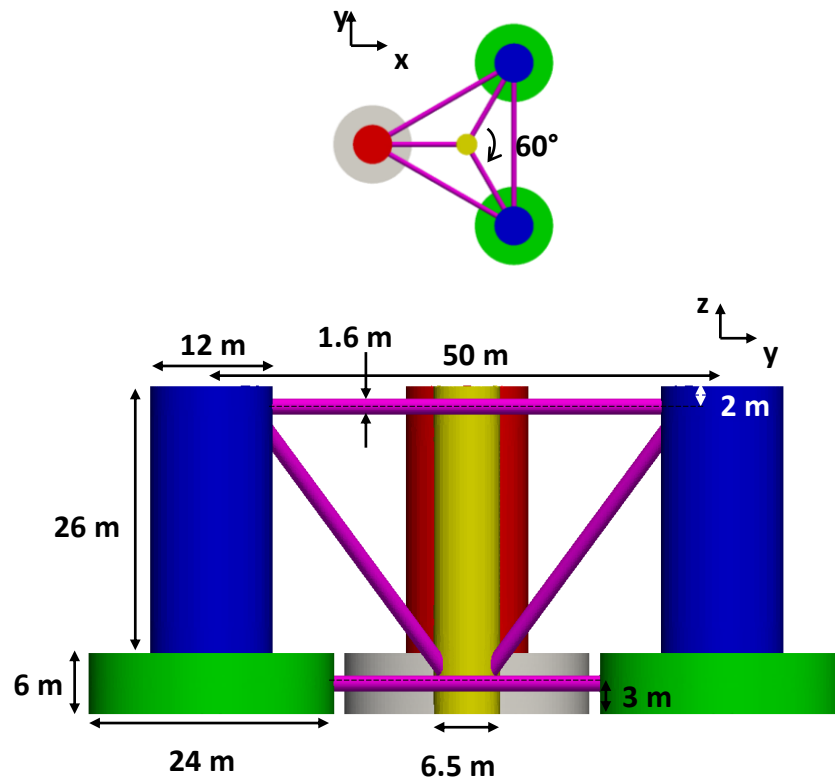


FIGURE 1.10: Main dimensions of the DeepCWind FOWT at full scale

In the scope of his Ph.D. thesis, Lacaze [101] carried out an experimental analysis of a semi-submersible composed of three floaters connected by braces at the middle of the triangle. The turbine is installed in the center. Thin damping plates are located at the bottom of each column. Wave and wind tests were performed in the Luminy facilities in Marseille (France).



FIGURE 1.11: Experimental model of the semi-submersible from Lacaze [101] tested in the wind-wave tank facility at Marseille-Luminy (France)

An experimental campaign of the WindFloat design was also performed at the early stage of development at UC Berkeley (CA, USA), and some results are presented in [11].

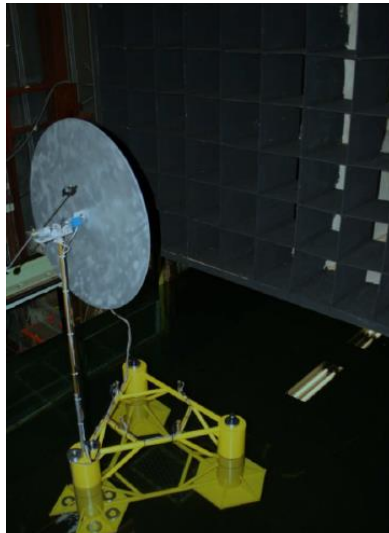


FIGURE 1.12: Experimental model of the WindFloat design at UC Berkeley (CA, USA) [11]

Other experimental campaigns can be found in the Ph.D. thesis of Maxime Philippe [102] and Vincent Arnal [103] carried out at Ecole Centrale de Nantes (France).

## 1.5 Objectives and outline of the Ph.D. thesis

This thesis aims to assess the ability of a CFD approach to model critical hydrodynamic aspects of semi-submersible FOWT. The overset meshing method built in the open-source software OpenFOAM® is used to handle the dynamic motions of the body. It allows larger motion amplitude and a better consistency in mesh quality

than other dynamic meshing methods. The wave generation and absorption toolbox `waves2Foam` is coupled with the overset solver to model the interaction between waves and structure. A description of the solver is presented in chapter 2.

A meshing process for NWT is presented in chapter 3 and convergence analysis on key meshing and numerical parameters are carried out to optimize the computational cost and the quality of regular wave propagating in the NWT.

2D models are considered to validate the main inputs of a NWT in chapter 4. Fixed and freely floating structures subjected to waves are considered. The results of the static structure are compared with linear and nonlinear potential flow theories for increasing wave steepness in section 4.1. Nonlinearities are observed and discussed. Convergence analysis and meshing methodologies are presented for the moving structure in section 4.2. Motions are compared to experimental results from the literature.

The overset mesh method is used in chapter 5 to investigate the vertical forced motion of heave damping plates largely used in FOWT designs. The cases of a single disk and a disk attached to a vertical column at different water depths are considered. Added mass and damping coefficients are compared with experimental results from the literature. The CFD results of the models of both structures match well the experimental measurements, including large oscillation periods and various amplitudes of heaving motion.

A 3D model of the fixed `DeepCWind` semi-submersible FOWT in waves is presented based on the research project OC6 led by NREL in chapter 6. Forces, pressure, and run-up on the structure are investigated for monochromatic and bichromatic wave cases. The results are compared with both the ones from other participants of the project and experimental measurements. The difference frequency responses of the floater for the bichromatic wave cases is emphasized.

Finally, in chapter 7, the 2D NWT is extended to model 3D moving structures. The free decay tests in heave, pitch and surge motion of a simple cylinder are carried out and validated against experimental measurements from the literature in section 7.1.1. A quasi-static mooring module from `Waves2Foam` is used. Free decay tests are also conducted with the `DeepCWind` semi-submersible platform in section 7.1.2. Damping coefficients and natural periods are compared with experimental data. Eventually, the wave induced response of this FOWT is presented for several regular wave conditions in section 7.2. Structure motions, forces, and run-up are analyzed.

## 1.6 Publications

Parts of the work of this thesis were presented in international conferences and published in Journals. The author of this thesis was first author of two conference papers:

- Romain Pinguet, Sam Kanner, Michel Benoit, Bernard Molin. “Validation of Open-Source Overset Mesh Method using Free-Decay Tests of Floating Offshore Wind Turbine”. In: the Thirtieth (2020) International Ocean and Polar Engineering Conference. Virtual, November 22-25, 2020.
- Romain Pinguet, Sam Kanner, Michel Benoit, Bernard Molin. “Modeling the dynamics of freely floating offshore wind turbine subjected to waves with an

open source overset mesh method". In: ASME 2021 3rd International Offshore Wind Technical Conference (IOWTC). Virtual, February 16-17, 2021

The chapter 5 of this thesis was accepted for publication in its entirety to the Journal of Fluids and Structures:

- Romain Pinguet, Michel Benoit, Bernard Molin, Flavia Rezende. "CFD analysis of added mass, damping and induced flow of isolated and cylinder-mounted heave plates at various submergence depths using an overset mesh method". In: Journal of Fluids and Structures DOI: 10.1016/j.jfluidstructs.2021.103442

In the scope of the OC6 project, results obtained during this thesis were presented to a conference as co-author:

- Lu Wang, Amy Robertson, Jason Jonkman, Yi-Hsiang Yu, Arjen Koop, Adrià Borràs Nadal, Haoran Li, Wei Shi, Romain Pinguet, Yang Zhou, Qing Xiao, Rupesh Kumar, and Hamid Sarlak. "Investigation of nonlinear difference-frequency wave excitation on a semi-submersible offshore-wind platform with bichromatic-wave CFD simulations". In: ASME 2021 3rd International Offshore Wind Technical Conference (IOWTC). Virtual, February 16-17, 2021

and published in the Journal of Ocean Engineering:

- Lu Wang, Amy Robertson, Jason Jonkman, Yi-Hsiang Yu, Arjen Koop, Adrià Borràs Nadal, Haoran Li, Erin Bachynski-Polić, Romain Pinguet, Wei Shi, Xinneng Zeng, Yang Zhou, Qing Xiao, Rupesh Kumar, Hamid Sarlak, Edward Ransley, Scott Brown, Martyn Hann, Stefan Netzband, Malwin Wermbter, Beatriz Méndez López. "OC6 Phase Ib: Validation of the CFD predictions of difference-frequency wave excitation on a FOWT semisubmersible". In: Ocean Eng., vol 241, December 2021. DOI: 10.1016/j.oceaneng.2021.110026

The work presented in section 4.1 was done in collaboration with Dr. Fabien Robaux (former Ph.D. student at Irphé lab and Aix-Marseille University) and Pr. Michel Benoit, and reported at the CITEPH project 35-2018.

- Fabien Robaux, Romain Pinguet, Michel Benoit. Comparison of wave loads and run-up on a 2D section of a OC5-DeepCWind semi-submersible column computed with three different numerical models. Livrable de la tâche 2 (Improvement of existing approaches) du projet CITEPH 35-2018. "Hydrodynamic issues for Floating Offshore Platforms"

Additional research work, not presented in this thesis, was also carried out during the PhD research and published in the proceedings of a conference:

- Daewoong Son, Romain Pinguet, and Dominique Roddier. "Global Sizing of the WindFloat for a 10 MW Generic Wind Turbine". In: ASME 2018 1st International Offshore Wind Technical Conference (IOWTC). San Francisco, California, USA: American Society of Mechanical Engineers, November 2018, doi: 10.1115/IOWTC2018-1104.
- This work was also presented with a poster by the author of this thesis in the conference: 16e Journées de l'hydrodynamique, Marseille, 27-29 November 2018.



## 2 Theory

An overview of the theory implemented in the open-source solver OpenFOAM® and external modules used in this study is presented in this section.

### 2.1 Introduction of parameters of interest

The Keulegan-Carpenter ( $KC$ ) is a dimensionless quantity that characterizes the relative importance of the drag force over inertia force:

$$KC = \frac{2\pi A}{L} \quad (2.1)$$

where  $A$  is the amplitude of oscillation and  $L$  the characteristic length of the structure in the orthogonal direction of the motion.

Viscosity effects are quantified with the Reynolds number ( $Re$ ). It is used to quantify the ratio of viscous forces and inertia forces for a flow in interaction with a body, and to determine whether the fluid flow is laminar or turbulent. It is defined as:

$$Re = \frac{\omega AL}{\nu} \quad (2.2)$$

The Courant-Friedrichs-Lewy (CFL) number, also called Courant number in short, is a key parameter to ensure numerical stability of computational codes. It is defined as:

$$C_o = \frac{u\delta_t}{\delta_x} \quad (2.3)$$

where  $u$  is the fluid velocity,  $\delta_t$  is the time step and  $\delta_x$  is the cell dimension. This number will be largely discussed in this thesis.

### 2.2 Governing Equations

#### 2.2.1 Navier-Stokes equations

All fluid flows are governed by the mass, momentum, and energy conservation principles. In the case of ocean hydrodynamics, incompressible fluid with constant viscosity can be considered. The mass continuity equation for an incompressible fluid is:

$$\nabla \cdot \underline{u} = 0 \quad (2.4)$$

where  $\underline{u}$  is the velocity vector of the fluid flow. Considering a Newtonian fluid, the momentum conservation principle is given by the Navier-Stokes equations as follow:

$$\rho \left( \frac{\partial \underline{u}}{\partial t} + \underline{u} \cdot \nabla \underline{u} \right) = \mu \nabla^2 \underline{u} - \nabla p^* \quad (2.5)$$

Here,  $\rho$  is the fluid density,  $\mu$  is the dynamic viscosity, and  $p^*$  is the hydrodynamic pressure equal to  $p^* = p - \rho gh$  where  $p$  is the absolute pressure,  $h$  is the vertical coordinate, and  $g$  is the acceleration of gravity. These equations combined with suitable boundary conditions describe the motion of the fluid flow.

### 2.2.2 Multiphase Modeling: Volume of Fluid (VOF) Model

In order to track the interface between the two phases (water and air), the Volume of Fluid (VOF) model developed by Hirt and Nichols ([104]) is used. This model is an interface capturing method. The free surface is followed through the computation of volume fractions, which represent the quantity of a given fluid in each cell. In the case of air/water interface, each cell has a volume fraction  $\alpha \in [0, 1]$  where 0 is the air and 1 is the water. The cells where  $\alpha \in ]0, 1[$  contain the interface between the two fluids.

In order to follow the phases of the fluid, the volume fraction function  $\alpha$  is calculated and updated using the transport equation:

$$\frac{\partial \alpha}{\partial t} + \nabla \cdot (\underline{u}\alpha) + \nabla \cdot (\underline{u}_r\alpha(1 - \alpha)) = 0 \quad (2.6)$$

where  $u_r$  is an artificial velocity, usually called compression velocity. The last term of equation (2.6) is an artificial compression term ([105], [106]) only active in the interface zone, aiming at counteracting numerical diffusion with negligible effects on the solution. The boundedness of the phase-field is guaranteed using the Multi-dimensional Limiter for Explicit Solution (MULES). This limiter ensures a value of  $\alpha$  between 0 and 1.

The density  $\rho$  and the dynamic viscosity  $\mu$  in each element are then defined by:

$$\rho = \alpha\rho_a + (1 - \alpha)\rho_w \quad (2.7)$$

$$\mu = \alpha\mu_a + (1 - \alpha)\mu_w \quad (2.8)$$

where  $(\rho_a, \mu_a)$  and  $(\rho_w, \mu_w)$  are the density and the dynamic viscosity of the air and the water respectively.

### 2.2.3 Turbulence Closure Model

The Reynolds Averaged Navier-Stokes (RANS) turbulence modeling approach is used in a few cases of this thesis. In the RANS method, Navier-Stokes equations are statistically averaged (over a large number of realizations), and a mean flow is calculated, whereas the small structures of the flow (down to the Kolmogorov scale) are modeled. The basic of the method consists of decomposing the variables of the equations into a mean part and a fluctuating part:

$$\varphi = \bar{\varphi} + \varphi' \quad (2.9)$$

Here,  $\bar{\varphi}$  is the mean part of the variable (in the Reynolds averaging sense), and  $\varphi'$  is the fluctuating part. This decomposition is injected into the Navier-Stokes system of equations (2.4-2.5) to obtain a problem on these new variables. A closure model needs to be added to approximate the Reynolds Stress Tensor and model the small-scale interactions. The new system of equations is called the RANS system.

The closure model used in this work is the stabilized k- $\omega$  turbulence model, presented recently by [107]. This model proposes a solution to avoid a well-known instability in the current two-equation turbulence models. The waves used to decay

because of the exponential growth of the eddy viscosity in the region of nearly potential flow. Based on [107], we initially set the dissipation rate  $\omega = \omega_\infty = 2.71\sqrt{p_0}$  where  $p_0$  is the turbulent kinetic energy production. After period averaging and depth averaging, it is given by:

$$\langle\langle p_0 \rangle\rangle = \frac{k_\omega^2 H^2 \sigma^2}{2k_\omega d \tanh(k_\omega d)} \quad (2.10)$$

where  $k_\omega$  the wave-number,  $\sigma$  is the angular frequency,  $d$  is the water depth, and  $H$  is the wave height. The kinetic turbulence energy is set to  $k = k_0 = \omega_\infty$  to initially yield  $\frac{\nu_T}{\nu} = 1$  where  $\nu$  is the kinematic viscosity of the water, and  $\nu_T$  is the eddy viscosity.

Turbulence effects are expected to have a limited impact on the cases presented in this thesis. A laminar flow hypothesis is therefore considered in most of the simulations.

## 2.3 Wave generation and absorption with Waves2Foam

### 2.3.1 Wave theories

The waves2Foam toolbox with its solver *waveFoam* developed by Niels Gjøøl Jacobsen [49] was used in this thesis to generate and absorb free surface waves. It has been developed for OpenFOAM® and is maintained compatible for most versions. It is based on the VoF method described above. Several wave theories are available in waves2Foam and can be chosen depending on the simulation case. Regular, bichromatic, or irregular waves can be generated. The regular wave theories available are Stokes first, second, and fifth-order theories. First-order cnoidal theory and stream function waves are also available. In this thesis, the fifth-order wave theory was used in all simulations. The user can specify the period  $T$ , the height  $H$ , the direction, and the phase of the wave. A ramp time for wave generation should also be chosen. For the fifth wave theory, a Stokes drift can also be defined. However, it was not taken into account in this thesis, and the Stokes drift was set to 0.

Waves2foam also allows the generation of bichromatic waves. Two models are available: the first-order bichromatic wave which is a linear superposition of two Stokes first-order waves, with two different characteristics and the second-order bichromatic wave which is similar to the first order but also includes second-order wave-wave interactions. The second-order wave model showed significant improvements in the results and will be discussed in chapter 6.

Finally, first-order irregular waves can also be implemented. The JJONSWAP and the Pierson-Moskowitz spectrum are available. No irregular wave case has been presented in this work because of computation time constraints.

### 2.3.2 Wave relaxation

A wave relaxation technique is implemented in waves2Foam to remove unwanted reflections on the boundaries of the numerical domain. The method uses an explicit approach where the field is modified in the defined relaxation zone through the equation:

$$\Phi = (1 - \omega_R)\Phi_{target} + \omega_R\Phi_{computed} \quad (2.11)$$

The corrected  $\Phi$  is the volume fraction  $\alpha$  or the flow velocity  $u$ .  $\omega_R \in [0, 1]$  is a weighting function described below. The fields  $\alpha$  and  $u$  are corrected within each time step of the simulation. The method is described in [49].

In this method, one should define the shape of the relaxation zone. Relaxation zones can be implemented at both inlet and outlet side of the NWT. At the inlet, the relaxation zone coincides with the generation zone. Depending on the case, these zones can be rectangular, cylindrical, or semi-cylindrical. In this thesis, rectangular zones were used because it is more appropriate for the parallelepipedic NWT.

Different relaxation weights are available in the toolbox. One can use exponential weight, taken from Fuhrman et al. [108], free polynomial weight or third order polynomial weight [109].

In this thesis, the exponential weight model was used and is defined as follow:

$$\omega_R = \frac{\exp \sigma^{p_{exp}} - 1}{\exp 1 - 1} \quad (2.12)$$

where  $\sigma \in [0, 1]$  is the local coordinate within the relaxation zone.  $\sigma = 0$  corresponds to the beginning of the zone and  $\sigma = 1$  to the end. The factor  $p_{exp}$  characterizes the relaxation rate and can be specified by the user.

A correction on  $\omega_R$  can be made based on the local CFL number [110]:

$$\tilde{\omega}_R = 1 - (1 - \omega_R^*)^{Co/Co_{max}} \quad (2.13)$$

where  $Co$  is the local CFL or Courant number and  $Co_{max}$  is the maximum Courant number. This correction has shown to significantly improve the quality of the generated waves in this thesis, especially for bichromatic wave cases.

### 2.3.3 Dynamic Solver and Restraint Forces

The *waveFoam* solver was coupled with the OpenFOAM® solver for multiphase flow and dynamic mesh *interDyMFoam* following the guidelines described in [50]. The resulting solver is called *waveDyMFoam*.

At the beginning of each time step, *waveDyMFoam* calls the native dynamic solver of OpenFOAM® *sixDoFRigidBodyMotion* to solve the interactions between the fluid and the structure. At each time step, the resulting force  $\underline{F}_{body}$  and moment  $\underline{M}_{body}$  on the body are computed from the integration of the pressure and the shear forces over the boundary surface representing the body  $S$  as [85]:

$$\underline{F}_{body} = \iint_S (p\hat{n} + \underline{\tau}) dS + \underline{F}_m + m_{body}\underline{g} \quad (2.14)$$

$$\underline{M}_{body} = \iint_S (\underline{r}_{CS} \times (p\hat{n} + \underline{\tau})) dS + \underline{r}_{CM} \times \underline{F}_m + \underline{r}_{CG} \times m_{body}\underline{g} \quad (2.15)$$

Here,  $\underline{\tau}$  is the viscous stress,  $\underline{F}_m$  the constrained force of the mooring,  $m_{body}$  the mass of the body,  $\underline{r}_{CS}$ ,  $\underline{r}_{CM}$  and  $\underline{r}_{CG}$  are vectors between the CoG of the body and the application point of the hydrodynamic force, the mooring force, and the gravity force respectively. A new velocity boundary condition at the wall of the structure is sent by the dynamic motion solver to the fluid solver. The 6 DoF of the floating body are solved using a second-order implicit solver based on the Newmark method ([111]).

To improve the stability of the solver, a relaxation of the acceleration of the rigid body is applied, using a relaxation coefficient  $f_a$  defined as:

$$a_t^* = f_a a_t + (1 - f_a) a_{t-1}^* \quad (2.16)$$

where  $a_{t-1}^*$  is the acceleration computed at the previous time step,  $a_t$  is the acceleration initially computed with the Newmark scheme and  $a_t^*$  is the relaxed acceleration eventually used in the model. As described in [53], this relaxation technique reduces the non-physical high-frequency oscillations of the acceleration. The impact of the value of the coefficient  $f_a$  is discussed in chapter 3.

The solver also enables the user to control the number of active DoF by restraining the body. It is also possible to constrain the body by applying external forces, such as a mooring forces.

The built-in version of OpenFOAM® allows only spring-type representation of the mooring force. However, a more advanced tool has been developed within the waves2Foam package ([49]) where catenary mooring lines can be defined. A description of the catenary model is given by Bruinsma et al. [54]. In the present study, the catenary lines are modeled using the resting state method. In this state, a part of the mooring line is resting on the seabed while the rest of the line behaves as a catenary line (see figure 2.1).

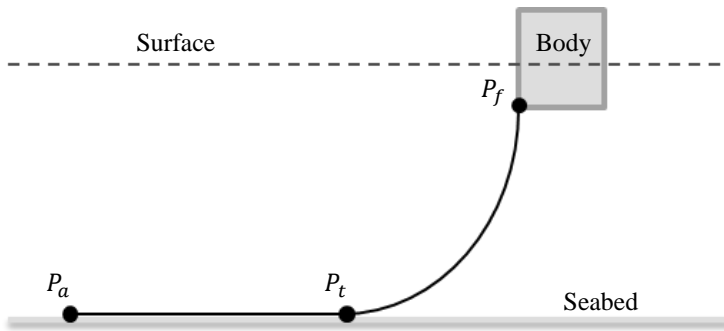


FIGURE 2.1: Sketch of the mooring model including a resting state

The user can provide the position of the fairlead point  $P_f$ , the anchor point  $P_a$ , the total length of the line, and the mass per unit length of the mooring line. Based on these inputs, the model computes the position of the touchdown point  $P_t$  and the forces on the body at each time step. In this quasi-static approach, no interaction between the fluid and the mooring line is considered.

## 2.4 Overset Grid Method

To capture the motion of the floating body, an overset mesh method is used. The *waveDyMFoam* solver described above was coupled with the overset solver from OpenFOAM®. The resulting solver is named *overWaveDyMFoam*. In this method, a background (fixed) mesh is first generated as shown in orange in figures 2.2 and 2.3. Then, a separate mesh is generated around the body. This fitted mesh is represented in green in figures 2.2 and 2.3. It can be of any shape but should include the entire body. These two grids are not deformable, which maintains their initial quality over time. In the present work, the fitted mesh is always rectangular because it is easier to generate. Based on experience, one should keep a certain number of cells between the boundary of the floating body and the outer boundary of the fitted mesh to ensure the quality of interpolation between the two meshes.

Once these two meshes are generated, they are overlaid on top of each other as shown in figures 2.2 and 2.3.

At each time step of the simulation, the solver operates three main steps. The first one (1) is called hole cutting. The cells of the background mesh that are located inside the body are deactivated (blue cells in figure 2.2). In the case of a single floating body, these cells are always located in the background mesh. If there are several bodies, these cells could be in the fitted mesh of another body.

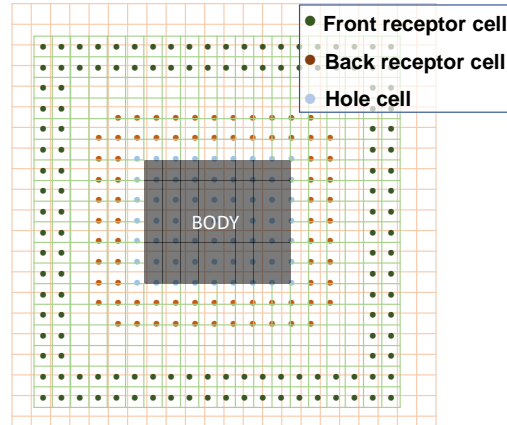


FIGURE 2.2: Background mesh (green) and body-fitted mesh (orange) in the overset mesh method. Description of the location of the receptor and hole cells. The grey box is the body of the fitted mesh

In the second step (2), the receptor cells (green and orange filled circles in figures 2.2 and 2.3) and the donor cells (green and orange circles in figure 2.3) are identified. Near the internal boundary, around the body (blue line in figure 2.2), the donor cells are in the body-fitted mesh, and the receptor cells are in the background mesh as described in figure 2.3. Conversely, near the external boundary (red line in figure 2.3), the donor cells are in the background mesh, whereas the receptor cells are in the body-fitted mesh.

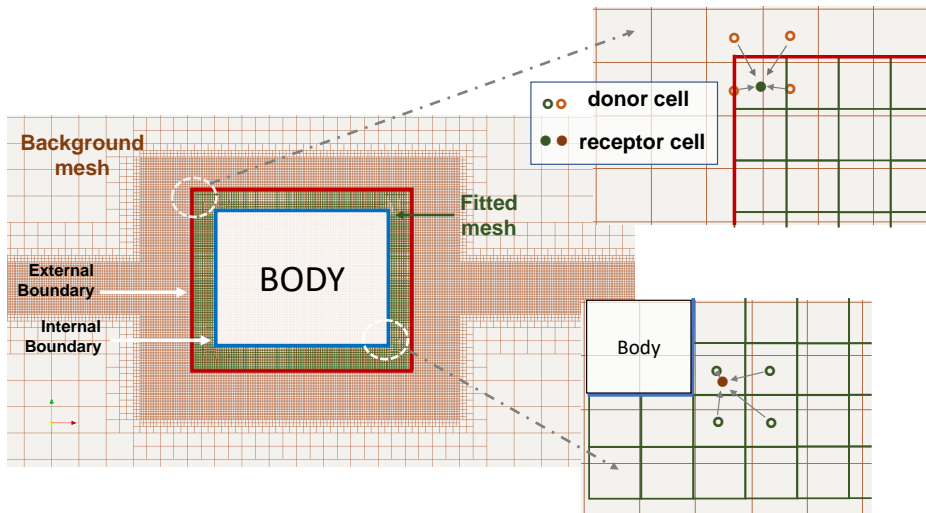


FIGURE 2.3: Description of the interpolation between donor and receptor cells at the internal and external boundaries. Adapted from [85].

The information (the computed fields) travels from the background mesh to the

body-fitted mesh through the external boundary, and travels back from the body-fitted mesh to the background mesh through the internal boundary as described in figure 2.4.

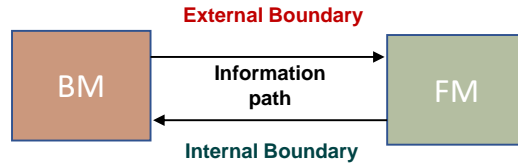


FIGURE 2.4: Information flow in the overset mesh method

The last step (3) is the interpolation between the donor and the receptor cells. Receptor cells (disks) receive information from donor cells (circles) by an interpolation method. Figure 2.3 describes the interpolation near the internal (bottom right) and external (top right) boundaries of the fitted mesh. Different interpolation methods are available in OpenFOAM®. In this thesis, and as mostly done in literature (see [85] or [89]), the inverse distance method has been used. This interpolation method is characterized by:

$$\phi_r = \frac{\sum_{i=1}^N \phi_i / d_i}{\sum_{i=1}^N 1/d_i} \quad (2.17)$$

where  $\phi_r$  is the flow variable at the receptor cell,  $\phi_i$  is the flow variable at the donor cell, and  $d_i$  is the distance between the centers of the donor cell and the receptor cell.

This technique can also be applied with a static body. In that case, the first two steps are done only once at the beginning of the simulation. More information can be found in the work of Chen et al. [85].

## 2.5 Boundary conditions

Boundary conditions need to be defined for each flow variable being solved in the simulation. These conditions impose a value of the variable or the gradient of the variable on the whole boundary. The boundary conditions used will be specified for each simulation.

## 2.6 Finite Volume Method (FVM)

The numerical technique of the finite volume method (FVM) is used to discretize and solve the transport momentum equations of the Navier-Stokes or RANS equations described above. The FVM is largely used in CFD. It is an efficient tool to solve any transport equation of a quantity  $\phi$ . In the case of the momentum equations (2.5), the quantity  $\phi$  corresponds to the fluid velocity  $\underline{u}$ . The steps of this method are briefly reminded:

- The fluid domain is discretized into small arbitrary elements called control volumes, which form a mesh. These cells can be of any shape as long as they are convex, and their faces are planar. In this work, the cells will be mostly hexahedral cells which are expected to give better convergence in the case of the free surface interface. Some control volumes are internal, while others are on the boundaries.

- The transport equation for  $\phi$  is integrated in space over all control volumes. The cells are small enough to consider that  $\phi$  varies linearly inside the cell. The quantity  $\phi$  is stored at the center of each cell.
- The volume integral are projected on the face centers using the Gauss theorem. So the volume integrals are converted into surface integrals.
- The system of integral equations generated is discretized in both space and time (for unsteady calculation) into a system of algebraic equations. A large variety of discretization schemes for space and time can be used in OpenFOAM®. For each case presented in the thesis, the schemes used will be specified.
- Conditions are specified at the boundaries of the domain to impose the value of  $\phi$  and close the system of equations.
- The system of equations can be solved using an iterative method.

In the case of the NS momentum equations, the system of linear algebraic equations for the entire domain can be written for each velocity components with a matrix form:

$$M.U = -\underline{\nabla}p^* \quad (2.18)$$

where  $M$  is a matrix of coefficients that are calculated by discretizing equation (2.5) using the FVM. All these coefficients are known.  $U$  is the velocity field (the velocity components at each cell of the mesh).

The FVM is also used to solve other transport equation such as equation (2.6) for the volume fraction.

## 2.7 Solution and Algorithm Control

The velocity field of equations (2.18) has to verify the continuity equation (2.4). There are 4 equations and 4 unknowns ( $u_x$ ,  $u_y$ ,  $u_xz$ , and  $p$ ). However, in the case of incompressible flow, there is no equation for the pressure.

The first solution is to use the pressure from the previous iteration to solve the equation (2.18). It is called the momentum predictor stage. This stage has been used in all simulations of this thesis. However, by doing this, the computed field  $U$  does not satisfy the continuity equation. It is only an initial guess that helps in stabilizing the solution for velocity. An equation for pressure must be derived from the momentum and continuity equations.

The first step of the algorithm is to separate the matrix  $M$  into a diagonal matrix and an off-diagonal matrix:

$$MU = AU - H = -\underline{\nabla}p^* \quad (2.19)$$

where  $A$  is the diagonal matrix. The matrix  $H$  is defined as:

$$H = AU - MU \quad (2.20)$$

$H$  is computed explicitly from the known coefficients of  $A$  and  $M$  and the velocity field of the previous iteration.

Equation (2.19) can be rewritten:

$$U = A^{-1}H - A^{-1}\underline{\nabla}p^* \quad (2.21)$$

Equation (2.21) can be substituted into the continuity equation (2.4), yielding:

$$\nabla \cdot [A^{-1}H - A^{-1}\underline{\nabla}p^*] = 0 \quad (2.22)$$

which gives a Poisson equation for the pressure:

$$\nabla \cdot (A^{-1}\underline{\nabla}p^*) = \nabla \cdot (A^{-1}H) \quad (2.23)$$

A pressure-velocity coupling algorithm must be used to solve the coupling equations (2.18) and (2.23). There are two algorithms available in OpenFOAM® based on the so-called pressure correction method: the Pressure Implicit With Splitting Operators (PISO) and the Semi-Implicit Method for Pressure-Linked Equations (SIMPLE). Additionally, a hybrid version of these two algorithms, called PIMPLE, is also available.

In the PISO algorithm, the momentum predictor (equation (2.18)) is solved once using the pressure of the previous time step to get a first estimation of the velocity field. Based on this velocity field, the  $H$  matrix ((2.20) is computed. Then, the pressure equation (2.23) can be solved. From  $H$  and  $\underline{\nabla}p^*$ , the velocity can be corrected using equation (2.21). This new velocity field is used to restart the loop on equations (2.20), (2.23) and (2.21) until the pressure field converges. These loops are called "inner loops". The number of inner loops can be defined by the user, or depend on convergence criteria.

In the SIMPLE algorithm, the method is very similar. The difference is that the loop includes the momentum predictor step which is computed at each "outer iteration" of the algorithm based on the updated velocity field  $U$ . In each outer iteration, the volume fraction  $\alpha$  is recalculated. It is also possible to update the body position within each iteration. The PIMPLE algorithm uses both inner and outer iterations. The PISO algorithm was mainly used in this thesis.

For each variable being solved in the discretized equations, a linear solver is defined. In the present cases, equations are solved for the pressure  $p$ , the velocity  $u$ , the volume fraction  $\alpha$ , and the cell displacement.

In this model, the preconditioned conjugate gradient (PCG) solver is used for the cell displacement and the pressure  $p$ . From the OpenFOAM® user guide, PCG solver is valid for both symmetric and asymmetric matrices. This solver requires the use of a preconditioner. In the case of an overset mesh method, the matrix from interpolation is asymmetric; therefore, the diagonal incomplete-Cholesky (DIC) preconditioner for symmetric matrices is used for the pressure  $p$  and the cell displacement ([85]). For the volume fraction  $\alpha$  and the velocity  $u$ , the smooth solver is used with the Gauss-Seidel (symGaussSeidel) smoother.

## 2.8 Summary

In this chapter, the main solvers used in the different simulations of this thesis were described. A summary of the global algorithm is presented in figure 2.5.

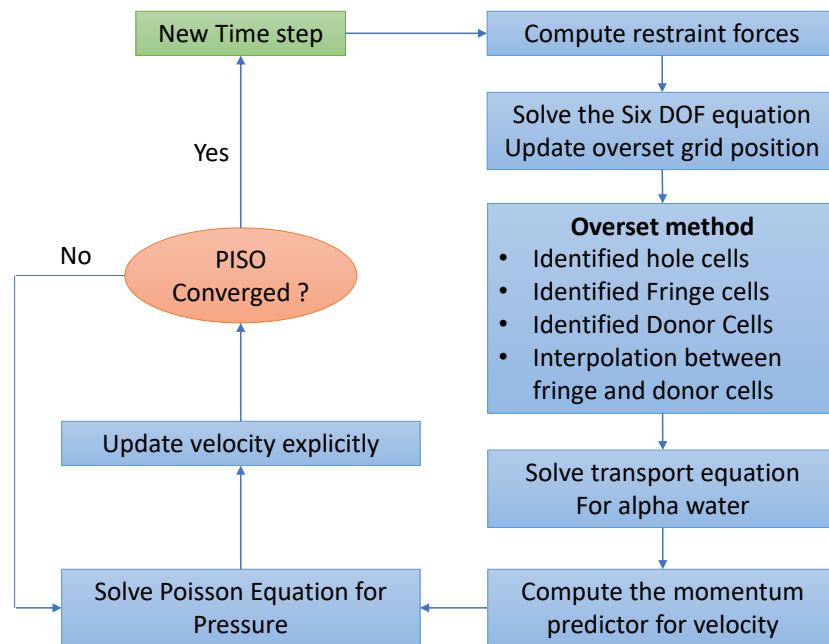


FIGURE 2.5: Flow chart of the solver coupling free surface flow solver, overset mesh method and the PISO algorithm for velocity-pressure coupling

# 3 Meshing method and convergence analysis of wave modeling in the NWT

In this chapter, the NWT model is introduced, and a meshing methodology is presented to model the wave propagation in this NWT. Key meshing criteria are emphasized. A convergence analysis is presented on these criteria along with key numerical inputs. The accuracy of the amplitude of the generated wave along the tank and over time is used as convergence criterion. The equivalent computational cost is also compared for each simulation. Only uni-directional (long-crested) incident wave cases are presented in this thesis. So this convergence analysis is presented in 2D, but the results can be extrapolated in 3D. A similar convergence analysis for NWT can also be found in [112].

## 3.1 Description of the NWT

### 3.1.1 Geometry of the NWT

In this thesis, the NWT is a rectangular domain. Incident waves propagate along the  $x$ -axis, and the  $z$ -axis is the vertical direction. The geometry of the NWT is presented in figure 3.1. The  $x = 0$  m is the position where the center of the structure will be placed afterwards. A wave generation and absorption zone is located at the left end of the tank, and an absorption zone is located at the right end. The red curve represents the exponential weight  $\omega_R$  distribution in the damping zone for a random relaxation rate  $p_{exp}$  (see section 2.3.2).

The zone in the middle is named the propagation zone. The Still Water Level (SWL) is located at  $z = 0$  m. The water depth  $d$  is the distance between the SWL and the bottom of the NWT. The distance  $atm$  is the distance between the SWL and the top of the NWT. This distance should be large enough to ensure that the structure does not exit the domain when it starts moving during the simulation.

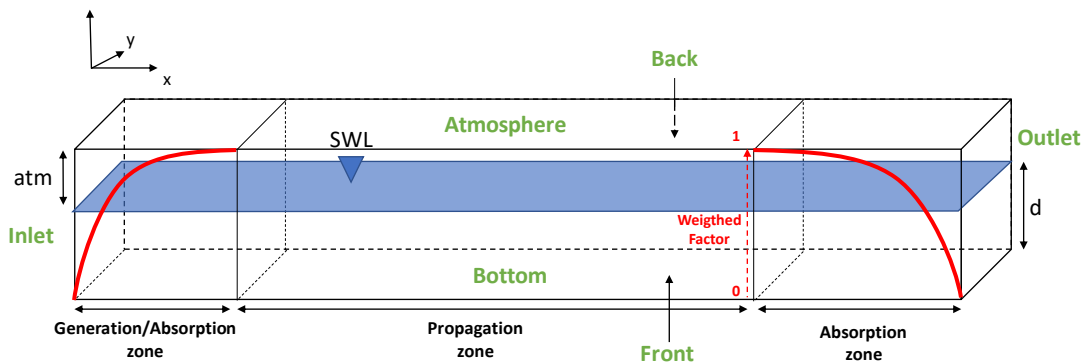


FIGURE 3.1: General description of the NWT and its boundaries

### 3.1.2 Boundaries of the NWT

In the case of the NWT without structure, 6 boundaries conditions need to be defined (Inlet, Outlet, Atmosphere, Bottom, Front, and Back) as described in green in figure 3.1. The same types of boundary conditions have been defined for most of the cases presented in this thesis. These conditions are summarized in table 3.1.

	Alpha ( $\alpha$ )	Pressure (p)	Velocity (U)
<b>Atmosphere</b>	inletOutlet	totalPressure	Pressure Inlet Outlet Velocity
<b>Bottom</b>	zeroGradient	fixedFluxPressure	Fixed Value 0
<b>Front/back</b>	empty (2D)	empty (2D)	empty (2D)
<b>Inlet</b>	waveAlpha	fixedFluxPressure	waveVelocity
<b>Outlet</b>	zeroGradient	fixedFluxPressure	Fixed Value 0

TABLE 3.1: Description of the boundary conditions used by default for the simulations of this thesis (unless otherwise stated) for volume fraction, pressure and velocity

The waveAlpha and waveVelocity boundary conditions are OpenFOAM® specific conditions for wave modeling. These conditions work well with the waveFoam solver. However, they are currently not working when using the overWaveDyMFoam solver.

## 3.2 Global Meshing Process

The general mesh of the domain is described in figure 3.2. It is composed of several zones with different mesh refinements. The goal is to optimize the number of cells and so the computational time. The mesh is generated using the OpenFOAM® modules BlockMesh© and SnappyHexMesh©. All the meshes presented in this thesis were created using these software. At the first step of the meshing, the green cells in figure 3.2 are generated using BlockMesh©.

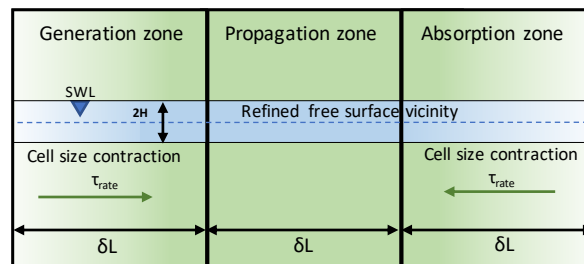


FIGURE 3.2: Description of the refinement zones of the mesh

In the generation and absorption zones, a cell contraction rate  $\tau_{rate}$  is used along the  $x$ -axis. It means that the horizontal length  $\delta_x$  of a cell at the zone extremities (inlet and outlet) is  $\tau_{rate}$  times bigger than the length of a cell in the propagation zone. The influence of the value of  $\tau_{rate}$  is analyzed in the following section. In the propagation zone, the size  $\delta_x$  of the cells is constant.

In figure 3.2, the light green colored area represents the longest cells, and the dark green colored area represents the smallest cells along the  $x$ -axis. In this first step of the meshing process, the cell height  $\delta_z$  is constant. The length and height of the cells are chosen to guarantee an aspect ratio  $\delta_z/\delta_x = 1$  for the cells in the propagation zone.

In the second phase of the meshing process, the vicinity of the free surface is refined using the level tool of SnappyHexMesh<sup>©</sup>. Each level consists of dividing the cells generated with BlockMesh<sup>©</sup> by 2 in all directions. In this model, a level 4 is used near the free surface (blue cells in figure 3.2), which means that the cells are 16 times smaller than the cells far from the free surface. This level refinement is progressive with at least 2 cells per level. It aims to better capture the free surface. The height of this refined band is  $2H$ , centered on the SWL (where  $H$  is the crest-to-trough incident wave height). In the rest of the study, the number of cells per wave amplitude along  $z$ -axis is defined in this free surface refinement zone. This number will be used as a convergence parameter. The amount of cells along  $x$ -axis can automatically be deduced with the aspect ratio of 1.

### 3.3 Incident Wave Calibration

In this section, convergence analysis of key parameters for the modeling of the wave propagation in the NWT without structure is presented. The wave conditions are  $T = 1.71$  s,  $H = 0.14$  m (model scale). A laminar flow is considered. The PISO algorithm with 3 iterations is used. The simulations were run in parallel on 32 cores. The wave propagation is captured with a regular distribution of 50 wave probes along the tank.

For each parameter, two figures are presented. The left figures present the amplitude of the RAO for the steady-state wave amplitude along the tank normalized by the target wave amplitude. The second figure corresponds to the amplitude of the RAO of the wave at  $x = 0$  m, obtained using a Fourier averaging analysis on the steady-state of the wave, with a sliding window of 3 oscillation periods, and normalized by the wave amplitude. In parallel, the execution time per wave period  $T$  is presented. The base case for the convergence analysis is Case 1.3 from table 3.2.

#### 3.3.1 Mesh convergence

First, 3 key parameters of the mesh described above are analysed. The global mesh refinement, the contraction rate  $\tau_{rate}$  and the length of the relaxation zone.

##### 3.3.1.1 Global mesh refinement

The global mesh refinement is first analyzed. Based on the method described above, the number of cells per wave amplitude in the refined zone is sufficient to characterize the mesh. Table 3.2 describes the key input parameters used for the 5 cases presented. Only the number of cells per amplitude varies (tested values: 3, 5, 8, 10 and 15 cells per amplitude).

Case	$\delta_t$	tolPi	tolPf	$N_{l_{gene}}$	$N_{l_{relax}}$	cells/A	$\tau_{rate}$	relax coeff
1.0	T/1700	1.00E-05	1.00E-06	2	2	<b>3</b>	4	3.5
1.1	T/1700	1.00E-05	1.00E-06	2	2	<b>5</b>	4	3.5
1.2	T/1700	1.00E-05	1.00E-06	2	2	<b>8</b>	4	3.5
1.3	T/1700	1.00E-05	1.00E-06	2	2	<b>10</b>	4	3.5
1.4	T/1700	1.00E-05	1.00E-06	2	2	<b>15</b>	4	3.5

TABLE 3.2: Cases for the convergence analysis of the global refinement

In figure 3.3a, it can be observed that for a low number of cells per amplitude, the wave dissipates along the NWT, especially for 3 cells/A. As the mesh is refined, the

wave dissipation reduces, and the targeted wave amplitude is reached all along the tank. The most accurate wave is reached for 15 cells/A. In figure 3.3b, the amplitude of the RAO of the wave at  $x = 0$  m also reveals a wave dissipation for the coarser mesh. As the mesh is refined, the wave amplitude gets closer to the targeted wave amplitude. Nevertheless, it should be noted that even for the coarser mesh, the error is less than 3%. However, the computational cost drastically increases with the mesh refinement. The execution time is multiplied by 17 between the 3 cells/A and the 15 cells/A cases. One should use a refinement depending on the level of accuracy needed, and the computational resource available. In this thesis, 5 cells/A or 10 cells/A will be used depending on the cases.

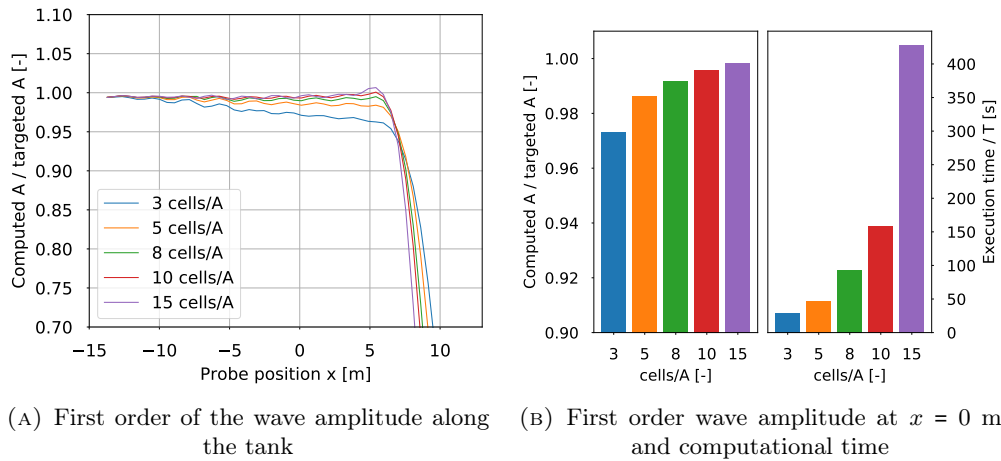


FIGURE 3.3: Convergence analysis as a function of the global refinement

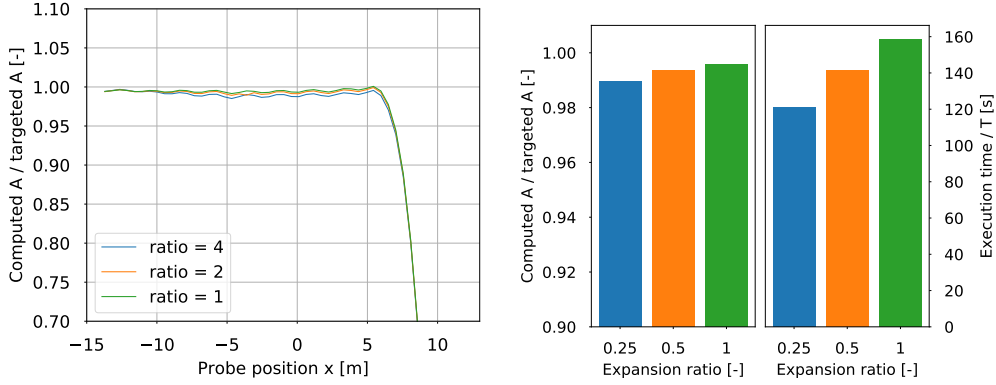
### 3.3.1.2 Impact of the cell size expansion ratio

As described previously, the cells are expanded far from the location of the structure, toward the generation and relaxation zones. This technique enables the reduction of the number of cells while guarantying an aspect ratio of 1 around the structure. This convergence analysis aims to verify that it does not affect the quality of the results. Table 3.3 describes the input parameters of the case. Three values of  $\tau_{rate}$  are considered.

Case	$\delta_t$	tolPi	tolPf	$Nl_{gene}$	$Nl_{relax}$	cells/A	$\tau_{rate}$	relax coeff
2.0	T/1700	1.00E-05	1.00E-06	2	2	10	4	3.5
2.1	T/1700	1.00E-05	1.00E-06	2	2	10	2	3.5
2.2	T/1700	1.00E-05	1.00E-06	2	2	10	1	3.5

TABLE 3.3: Cases for the convergence analysis of the expansion ratio

It can be seen on figure 3.4 that different values of  $\tau_{rate}$  have almost no influence on the quality of the results. The difference between  $\tau_{rate}=0.25$  and  $\tau_{rate}=1$  is less than 0.5%. However, the gain on execution time is important. So the use of a large contraction rate can be safely used for this mesh. In this thesis,  $\tau_{rate} = 0.25$  is used.



(A) First order of the wave amplitude along the tank (B) First order wave amplitude at  $x = 0$  m and computational time

FIGURE 3.4: Convergence analysis as a function of the expansion ratio

### 3.3.1.3 Impact of the relaxation zone length

The relaxation zone length is a key parameter of the relaxation method from waves2Foam. As described in figure 3.2. Two relaxation zones need to be defined. The length of the zones are defined in term of the number of wavelengths  $NL_{gene}$  (on the incident wave) for the generation/relaxation zone at the inlet and  $NL_{relax}$  for the relaxation at the outlet. Table 3.4 describes the input parameters of the 5 cases, where only the lengths of the generation and relaxation zones are modified.

Case	$\delta_t$	tolPi	tolPf	$Nl_{gene}$	$Nl_{relax}$	cells/A	$\tau_{rate}$	relax coeff
3.0	T/1700	1.00E-05	1.00E-06	<b>2</b>	<b>0.5</b>	10	4	3.5
3.1	T/1700	1.00E-05	1.00E-06	<b>2</b>	<b>1</b>	10	4	3.5
3.2	T/1700	1.00E-05	1.00E-06	<b>2</b>	<b>2</b>	10	4	3.5
3.3	T/1700	1.00E-05	1.00E-06	<b>2</b>	<b>3</b>	10	4	3.5
3.4	T/1700	1.00E-05	1.00E-06	<b>1</b>	<b>2</b>	10	4	3.5

TABLE 3.4: Cases for the convergence analysis of the relaxation zones lengths

From figure 3.5a, it can be seen that a large reflection occurs when using a length  $NL_{relax} = 0.5$  or 1 wavelength for the absorption zone. The zone is too short, and the waves do not have enough distance to dissipate. However, when using  $NL_{relax} = 2$  or 3, the wave is correctly absorbed, there is almost no reflection on the outlet boundary. When looking at the execution time, it is better to use  $NL_{relax} = 2$  to reduce the computational cost.

The last case uses  $NL_{gene} = 1$  instead of 2 for the generation zone. It can be observed that reducing the generation zone length has a low impact on the wave quality, but it reduces significantly the computational cost. It should be noted that without any structure there is no wave propagating toward the inlet boundary. However, if a structure is placed in the NWT that imposes moderate or large reflections, the same consideration as for absorption zone should be used (i.e.  $NL_{gene} = 2$ ).

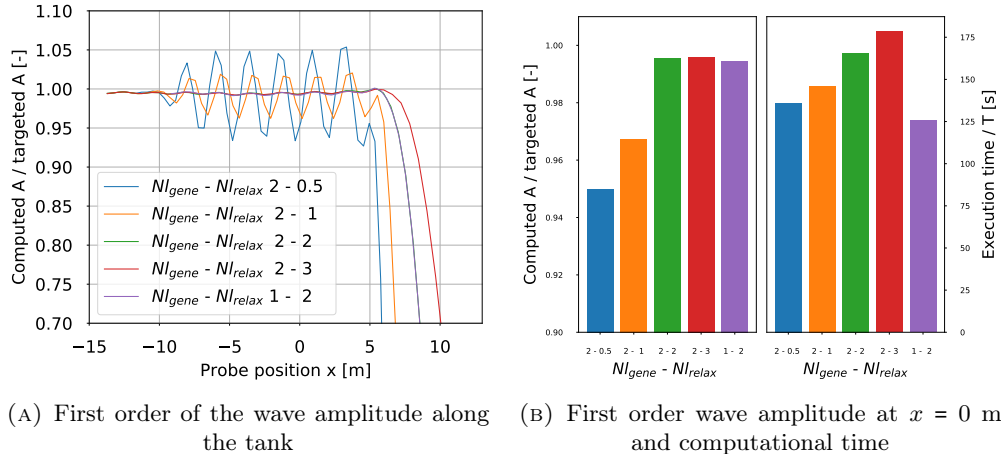


FIGURE 3.5: Convergence analysis as a function of the relaxation zones lengths

### 3.3.2 Convergence of key numerical parameters

Similarly, 3 key numerical parameters are investigated. First, the relaxation exponent  $p_{exp}$  described in section 2.3.2 of chapter 2, then the time step of the simulation, and finally the maximum residual for pressure solution of the Poisson equation.

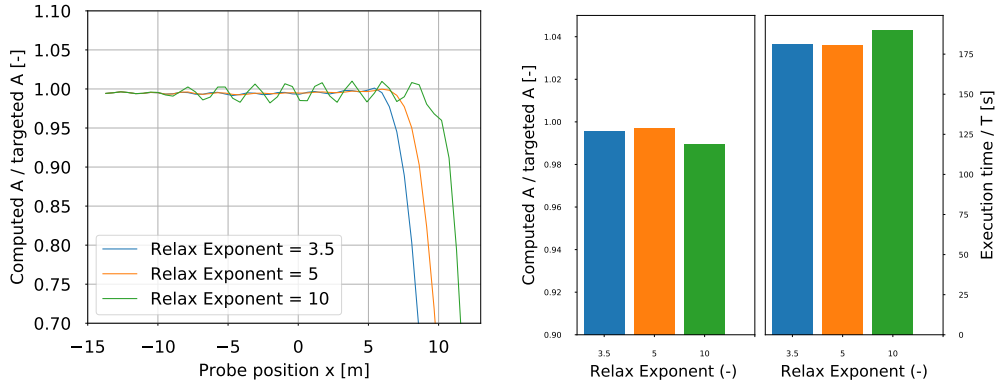
#### 3.3.2.1 Relaxation coefficient in the damping zone

The relaxation method used by waves2Foam was presented in chapter 2. The rate of wave absorption depends on the relaxation exponent  $p_{exp}$  of the weight formula 2.12. In this analysis 3 values of  $p_{exp}$  are considered, as described in table 3.5.

Case	$\delta_t$	tolPi	tolPf	$NI_{gene}$	$NI_{relax}$	cells/A	$\tau_{rate}$	relax coeff
4.0	T/1700	1.00E-05	1.00E-06	2	2	10	4	<b>3.5</b>
4.1	T/1700	1.00E-05	1.00E-06	2	2	10	4	<b>5</b>
4.2	T/1700	1.00E-05	1.00E-06	2	2	10	4	<b>10</b>

TABLE 3.5: Cases for the convergence analysis of the relaxation exponent

It is interesting to observe that there is no visible difference in the results for  $p_{exp} = 3.5$  and  $p_{exp} = 5$ . However, reflected wave can be observed in figure 3.6a for the largest value  $p_{exp} = 10$ . When  $p_{exp}$  is too large, the absorption is too fast in space, and the relaxation zone acts like a wall on which the wave is partially reflected. As expected, there is almost no impact on the execution time. So a value of  $p_{exp} = 3.5$  is used in most of the simulations of this thesis. It corresponds to the default value proposed in waves2Foam user guide [50].



(A) First order of the wave amplitude along the tank (B) First order wave amplitude at  $x = 0$  m and computational time

FIGURE 3.6: Convergence analysis as a function of the relaxation exponent

### 3.3.2.2 Time step

The time step size of the simulation is probably the most critical numerical parameter. There are two main methods to define the time step size in OpenFOAM<sup>®</sup>, either by setting a fixed value of time step during the whole simulation or by setting the maximum CFL number  $Co$ . In the latter case, the software determines the time step dynamically accordingly. Both methods were used in this thesis. At the earliest stage of this research, the maximum  $Co$  method was used. However, when looking more closely at the wave amplitude, it appeared that this method could lead to some errors in the wave quality. Convergence analysis of a fixed time step has revealed that a maximum  $Co = 1$  induced a time step too large for the wave propagation. Table 3.6 lists the input parameters used for the time step convergence analysis. The time step is defined relative to the wave period. 4 time steps are compared.

Case	$\delta_t$	tolPi	tolPf	$Nl_{\text{gene}}$	$Nl_{\text{relax}}$	cells/A	$\tau_{\text{rate}}$	relax coeff	
5.0	<b>T/500</b>	1.00E-05	1.00E-06	2	2	10	4	3.5	
5.1	<b>T/1000</b>	1.00E-05	1.00E-06	2	2	10	4	3.5	
5.2	<b>T/1700</b>	1.00E-05	1.00E-06	2	2	10	4	3.5	
5.3	<b>T/2000</b>	1.00E-05	1.00E-06	2	2	10	4	3.5	

TABLE 3.6: Cases for the convergence analysis of the time step

It can be observed in figure 3.7 that for the largest time steps ( $T/500$  and  $T/1000$ ), the wave amplitude tends to increase while progressing along with the tank. It leads to amplitudes largest than the targeted one. However, when the time step is equal to  $T/1700$  or  $T/2000$ , the resulting amplitude is converged with a difference of less than 0.5%. As observed in figure 3.7, the computational cost increases linearly with the time step size. A time step equal to  $T/1700$  offers the best quality/cost ratio.

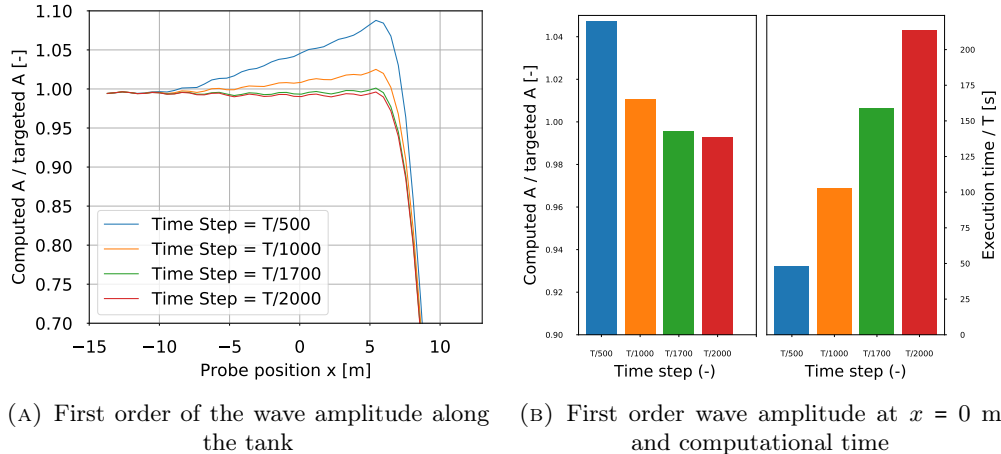


FIGURE 3.7: Convergence analysis as a function of the time step

It should be noted that the choice of the time step also depends on the pressure velocity coupling method chosen.

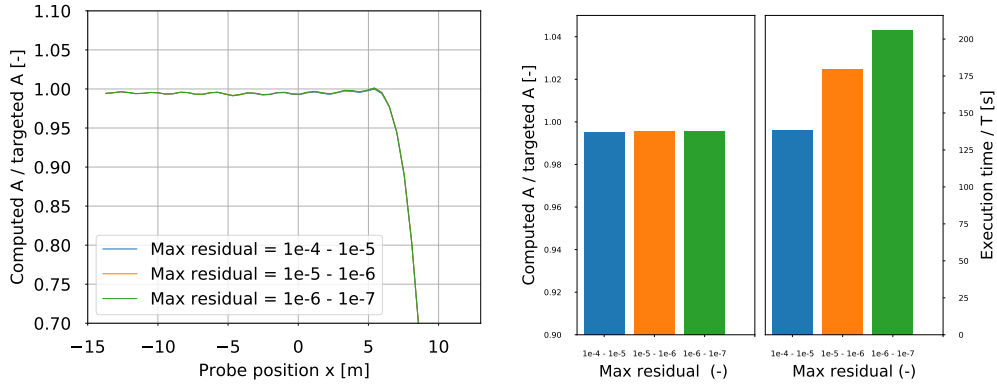
### 3.3.2.3 Maximum residual in the Poisson iterative solution for pressure

Finally, the maximum residual of the pressure  $p$  calculation is investigated. In OpenFOAM<sup>®</sup>, it is possible to increase the accuracy in the last iteration of the PISO algorithm. So, two residual values are specified. The first one is for all iterations but the last, and the second one is for the last iteration. In OpenFOAM<sup>®</sup>, the maximum residual for other flow variables must also be defined. However, the other variables are cheaper to solve compared to the pressure. So a high accuracy can be set without impacting much the execution time. Three different sets of values for the maximum pressure residual are compared, as shown in table 3.7.

Case	$\delta_t$	tolPi	tolPf	$Nl_{gene}$	$Nl_{relax}$	cells/A	$\tau_{rate}$	relax coeff
6.0	T/1700	<b>1.00E-04</b>	<b>1.00E-05</b>	2	2	10	4	3.5
6.1	T/1700	<b>1.00E-05</b>	<b>1.00E-06</b>	2	2	10	4	3.5
6.2	T/1700	<b>1.00E-06</b>	<b>1.00E-07</b>	2	2	10	4	3.5

TABLE 3.7: Cases for the convergence analysis of the maximum residual of pressure.

From figure 3.8, it can be seen that the results are visually the same for the 3 cases. In the range chosen in this analysis, there is no impact of the maximum residual on the wave quality. However, the execution time increases significantly when the maximum residual decreases: the solver does more iterations in the pressure calculation to meet the prescribed threshold. In this thesis, the maximum residual used for pressure is 1.00E-06 to ensure pressure convergence even after adding the structure in the NWT.



(A) First order of the wave amplitude along the tank (B) First order wave amplitude and computational time

FIGURE 3.8: Convergence analysis as a function of the maximum residual of pressure. The second value is considered for the last iteration

### 3.4 Conclusion

In this Chapter, a NWT model was proposed with a meshing methodology. A convergence analysis was presented for some key parameters of the model. The objective of this work is to optimize a NWT model that will provide sufficiently accurate results at an acceptable computational cost. One can adapt the parameters to the accuracy desired and the computation resource available. For a better validation, this analysis could be done on a larger number of wave conditions.

The parameter that has the biggest impact on the computation time is the global refinement, especially when moving to 3D cases. The base case (e.g. case 1.3 in table 3.2) offers the best ratio accuracy vs computational cost. However, a global refinement of 10 cells/ $A$  can lead to a large mesh in 3D. So 5 cells/ $A$  can be considered in 3D, at least for preliminary computations.



## 4 2D simulations of inverted T-sections in nonlinear waves

In this chapter, 2D simulations are first presented in order to set up the numerical model, carry out convergence analyses, and validate some input parameters. In comparison with 3D cases, the lower computational cost of 2D simulations enables to run more validation cases and to improve the choice of numerical parameters and settings, that can be then extended to 3D. 2D analyses of bodies having inverted T-sections are presented under nonlinear waves. First, the case of a static structure is presented, and CFD results are compared to those obtained by other numerical models. Then, the motions of a freely floating body under highly nonlinear waves are compared with experimental results.

### 4.1 Wave induced forces on a fixed structure

The work presented in this section was done in collaboration with Dr. Fabien Robaux (former Ph.D. student at Irphé lab and Aix-Marseille University) and Pr. Michel Benoit, and reported during the CITEPH project 35-2018.

The objectives of this work are to compare three numerical models (presented in section 4.1.2). A linear code based on the linear potential theory, a nonlinear potential code using the Harmonic Polynomial Cell (HPC) method, and a nonlinear, viscous and turbulent model using the Computational Fluid Dynamics (CFD) code OpenFOAM®. A 2D analysis is carried out on a section of the semi-submersible column (test-case presented in Section 4.1.1). Numerical simulations are carried out considering regular waves (section 4.1.3). Forces and run-up are evaluated on the structure, and the impact of nonlinearities and fluid viscosity are analyzed.

#### 4.1.1 Description of the selected test-case

The geometry of the structure chosen for testing the numerical models in this study is a 2D vertical section of the column of the semi-submersible platform for floating wind turbine DeepCWind, developed by NREL (National Renewable Energy Laboratory, USA) [113]. The geometry of the column is shown in figure 4.1. It is composed of a main column that has a diameter of 12 m (here, in 2D, this is a width) and a damping plate with a diameter of 24 m and a height of 6 m. The structure is fixed; only diffraction and reflection effects are considered. The total draft of the platform is 20 m and the water depth is set to 150 m when the wavelength is lower than 300 m to meet the deep water condition. Otherwise, a depth of 200 m (corresponding to the one used during the experiments) is considered.

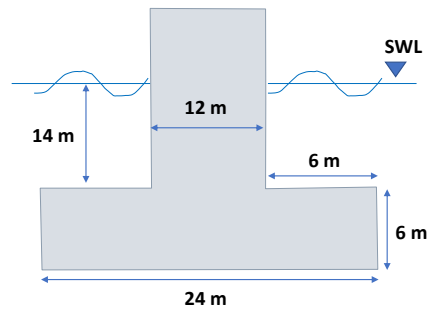


FIGURE 4.1: Geometry of the inverted T-section, corresponding to a vertical slice of a DeepCWind floater column [113]

## 4.1.2 Numerical Models

Three numerical methods were considered and the results were compared between each other. A short description of these models is presented hereafter.

### 4.1.2.1 Potential models

Two potential flow approaches were considered: a first-order linear model and a non-linear potential flow model.

#### 4.1.2.1.1 Linear Model

The first model used is based on the linear potential flow theory. The flow is assumed to be irrotational  $\nabla \times \underline{v} = \underline{0}$  and the viscosity of the fluid is neglected ( $\nu \rightarrow 0$ ). Under those assumptions, the velocity potential completely describes the flow:  $\nabla\phi = \underline{v}$ . This potential function should be solution of the Laplace equation in the whole fluid domain:

$$\nabla^2\phi = 0 \quad (4.1)$$

This equation is supplemented with a linearized free surface boundary condition and impermeability conditions on the boundaries of the body (the normal component of the velocity vanishes on these boundaries).

The domain is divided into 5 sub-domains as shown in figure 4.2. In each sub-domain, the potential is calculated using an adapted analytical expansion of the potential, truncated at a given order. Boundary conditions are formulated at each boundary of the sub-domains (continuity of pressure and normal velocity). By matching the expansions of the potential at these boundaries, a set of equations are established whose solution gives the coefficients appearing in the analytical expressions of the potential. Once the potential is known, forces and moments on the body can be calculated, as well as reflection and transmission coefficients.

The code used for this model has been developed by Pr. Bernard Molin prior to this work.

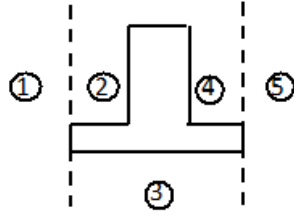


FIGURE 4.2: Sub-domain decomposition used with the linear potential flow model developed by Pr. Molin

#### 4.1.2.1.2 Nonlinear potential model with HPC method

In a second approach, we still use the potential flow assumption but keep the non-linearity of the waves. The Laplace equation (4.1) and the impermeability conditions remain the same as in the linear case, but now two nonlinear free surface boundary conditions are considered.

The potential problem is solved by using the Harmonic Polynomial Cell (HPC) method, introduced by [42]. This method aims at solving this problem by discretizing the volume into overlapping cells. In those cells, the potential is approximated as a weighted sum of the first harmonic polynomials (these polynomials are fundamental solutions of the Laplace equation). Currently, this method is applied in 2D: the cell is composed of 9 nodes, as shown in figure 4.3. The potential is then approximated by the first 8 harmonic polynomials ( $f_1(x, z)$ ,  $f_2(x, z)$ ,  $f_3(x, z)$ , ...) =  $(x, z, xz, x^2 - z^2, x^3 - 3xz^2, \dots)$ , as:

$$\phi(\underline{x}) = \sum_j b_j f_j(\underline{x}) \quad (4.2)$$

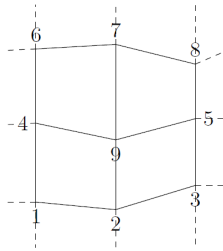


FIGURE 4.3: Typical shape of a 2D cell used with the HPC method

This equation should be enforced at each node on the outer boundary of the cell:  $\phi_i = \phi(\underline{x}_i) = b_j f_j(\underline{x}_i)$ . Thus, the  $b_j$  coefficients can be obtained geometrically by inverting the matrix defined by  $C_{ij} = f_j(\underline{x}_i)$ . Then, the interpolation formula for the potential in the cell becomes:

$$\phi(\underline{x}) = \sum_{i=1}^8 \left( \sum_{j=1}^8 C_{ji}^{-1} f_j(\underline{x}) \right) \phi_i \quad (4.3)$$

Still, the 9th potential at the center of the cell (node 9 in figure 4.3) has not been used. Thus, applying the previous equation at this point results in an equation that will be incorporated as the corresponding line in the general matrix. A Dirichlet

boundary condition can be set directly in the matrix by imposing the value of the potential at the considered node. For a Neumann condition, the equation (4.3) needs to be derived before the implementation in the general matrix.

The free surface is treated with an Immersed Boundary Method (IBM) [114], and the body is included through a new mesh, fitting the body contour. Those methods allow the cells to be rigid during the movement of the free surface and body. That way,  $C_{ij}$  matrices need to be inverted only once (at the beginning of the simulation). The inversion of the matrix is performed with a GMRES LU-preconditioned solver. The free surface boundary conditions, formulated as Zakharov equations [115], are used to march the free surface elevation and the free surface potential in time, with a Runge-Kutta time scheme of order 4 with a constant time-step.

Full details on this HPC model can be found in the Ph.D. thesis of Fabien Robaux [44] and in Robaux and Benoit [43].

#### 4.1.2.2 CFD Numerical model

##### 4.1.2.2.1 Wave Model

The tool wave2foam presented in chapter 2 is used to generate and absorb the waves [50]. Relaxation zones are used at both ends of the NWT to absorb reflected and transmitted waves. The 5<sup>th</sup> order Stokes wave theory is used to generate incident waves in all the simulations of this chapter.

##### 4.1.2.2.2 Turbulence Model

The stabilized  $k-\omega$  SST turbulence model presented in chapter 2 was used in this model.

##### 4.1.2.2.3 Meshing method

A structured mesh is generated using the OpenFOAM® tools blockMesh and SnappyHexMesh. This analysis was done before the elaboration of the meshing process of chapter 3. However, the idea is similar. The mesh is divided into blocks. In each block, the cell size respects the criteria described in figure 4.4.

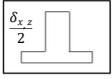
$\delta_z = \frac{2A}{10}$ $\delta_x = \frac{\lambda}{100}$	$\delta_z = \frac{2A}{10}$ $\delta_x = \frac{\lambda}{2 * 100}$	$\delta_z = \frac{2A}{10}$ $\delta_x = \frac{\lambda}{100}$
$\delta_z = \frac{A}{10}$ $\delta_x = \frac{\lambda}{2 * 100}$	$\delta_z = \frac{A}{10}$ $\delta_x = \frac{\lambda}{4 * 100}$ 	$\delta_z = \frac{A}{10}$ $\delta_x = \frac{\lambda}{2 * 100}$
$\delta_z = \frac{2A}{10}$ $\delta_x = \frac{\lambda}{100}$	$\delta_z = \frac{2A}{10}$ $\delta_x = \frac{\lambda}{2 * 100}$ 	$\delta_z = \frac{2A}{10}$ $\delta_x = \frac{\lambda}{100}$

FIGURE 4.4: Decomposition of the OpenFOAM® mesh and cell size criteria

Here,  $A$  is the wave amplitude,  $\lambda$  the wavelength,  $\delta_x$  the width of the cell, and  $\delta_z$  the height of the cell. These criteria give a good representation of the wave. In OpenFOAM®, it is recommended to have an aspect ratio ( $\delta_z/\delta_x$ ) close to 1 for each cell. For this study, a maximum aspect ratio of 2 is used. So if  $\delta_x > 2\delta_z$  then the cell width is divided by 2. The number of cells of each case depends on the wave conditions. In this study, the number of cells varies between 500,000 and 1,500,000.

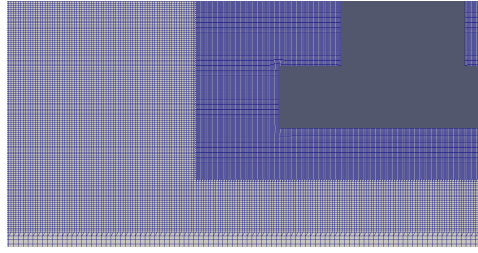


FIGURE 4.5: Partial view of the NWT and column meshing in OpenFOAM®

The maximum CFL number is set to  $C_o < 1$  in all cases. The time step is automatically set accordingly.

#### 4.1.2.2.4 Computational domain

The absorption zone lengths at the inlet and outlet are equal to 1 wavelength on each side. The propagation zone is set to 2 wavelengths at both sides of the structure as described in figure 4.6. The depth is adapted to the wavelength to be in deep water conditions as described section 4.1.1.

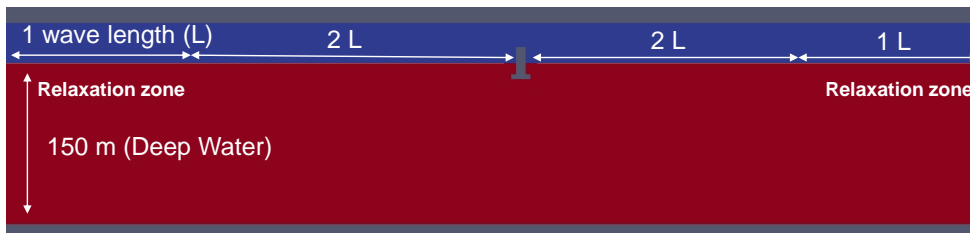


FIGURE 4.6: Overview of OpenFOAM® global computational domain

### 4.1.3 Numerical simulations with regular waves

In this section, we present and discuss the simulations performed with the three models considering regular (monochromatic) incident wave conditions. The types of results we are mainly interested in are : (i) the horizontal and vertical components of the forces exerted by the waves on the structure, and (ii) the run-up of the wave on the vertical wall representing the column of the floater in 3D. In the first sub-section, the influence of the wave period is examined.

#### 4.1.3.1 Influence of wave period (at constant wave steepness)

To observe the influence of wave period on the loads and run-up on the platform, models have been verified against each other for different wave periods  $T$  with fixed wave steepness  $\frac{H}{\lambda}$  to control the nonlinearity of the incident waves. We consider two different values of the wave steepness: 0.5% and 2%. The low value is chosen to get results in the linear regime. The harmonic 1 (fundamental component) of both the results from the HPC method and the CFD computations for different values of wave steepness are shown in figure 4.7. Sub-figures represent the first harmonics of respectively the horizontal load, the vertical load, and the run-up on the front face of the body. The value given by the linear potential model is added for information, to compare the results at this relatively small wave steepness.

Note that the order of magnitude of the maximum vertical and horizontal loads are different (respectively  $4.10^4$  and  $4.10^5$  N/m<sup>2</sup>). Thus, similar absolute errors have different effects on both values. Also, note that the vertical load is predicted by the linear potential model to vanish at a given period ( $T = 11.7$  s). This particular period will be termed the “cancellation period” hereafter. This effect will largely amplify relative differences between models in the vicinity of this particular period.

Furthermore, the limit of the run-up when  $T$  goes to 0 was –as obtained and shown– expected to be 2 as the problem tends to a simple vertical wall in infinite depth conditions. First, a good agreement between potential models (linear and HPC nonlinear) can be observed for both wave steepness values 0.5% and 2%. The HPC first harmonic represents well linear computed amplitudes (error < 3% almost everywhere) for a wide range of wave periods  $T \in [4 \text{ s}, 16 \text{ s}]$ , i.e.  $\lambda \in [25 \text{ m}, 398 \text{ m}]$ .

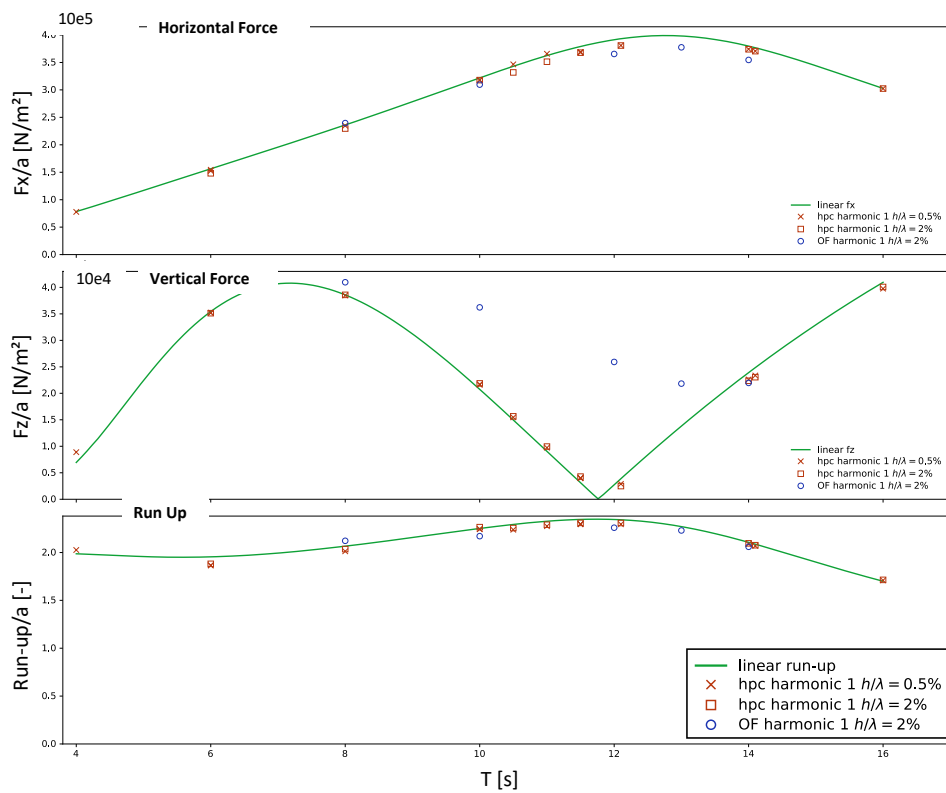


FIGURE 4.7: First harmonic amplitude of normalized  $F_x$ ,  $F_z$  and run-up compared to the linear results

The behavior of the vertical load close to the “cancellation period” is well captured by the HPC model, as shown in the second sub-figure. In general, the horizontal load and run-up are well captured via the CFD computation. However, a different behavior is denoted in the vicinity of the vertical force cancellation period. Physically, it is possible to anticipate that viscous effects will probably play an important role when potential loads cancel, which will prevent the first harmonic of the vertical load to be zero. For periods larger than  $T = 12.1$  s, the CFD computation globally agrees with potential models even if too few points are available to conclude definitively.

The three models exhibit similar results as long as the first harmonic is concerned. But it can be noted that the nonlinear parts of HPC and CFD play an important role,

even for waves of small steepness. This is particularly true when the vertical load is considered, as the first harmonic component tends to be of smaller amplitude.

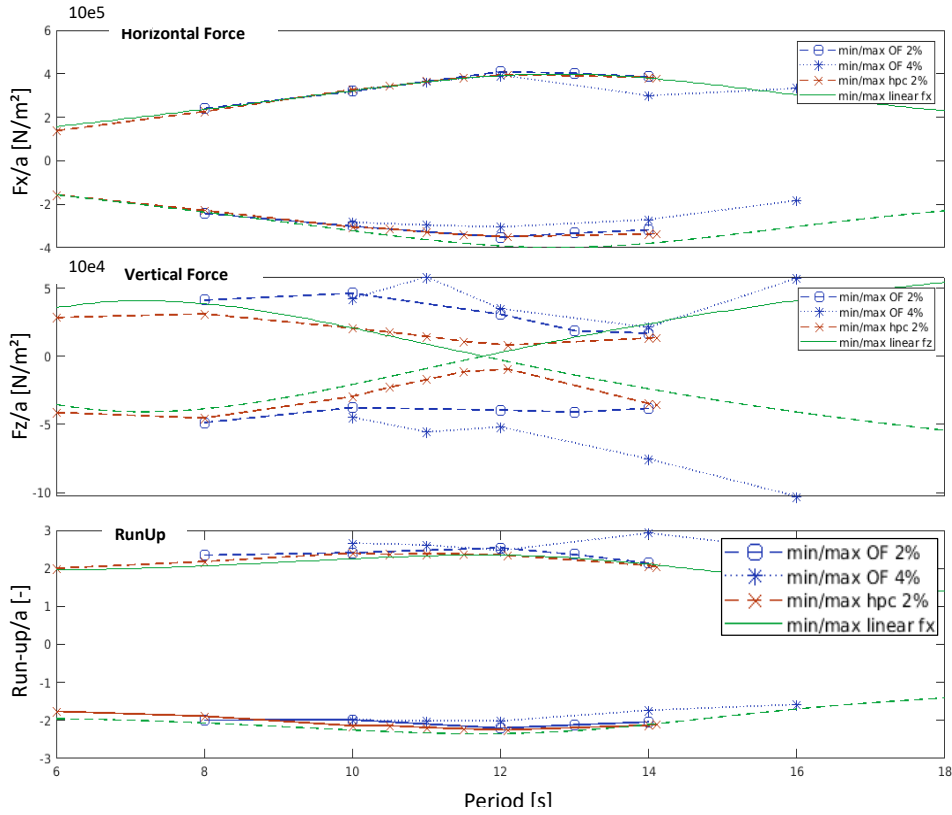


FIGURE 4.8: Maximum and minimum values of the RAO of  $F_x$  and  $F_z$  and run-up compared to the linear case

The impact of higher harmonics can be seen in figure 4.8. The maximum and minimum values of the vertical and horizontal forces and the run-up are plotted for several wave periods, and compared to the linear model. Different values of wave steepness are considered: 2% for the HPC method, 2% and 4% for the CFD code. As seen before, the horizontal force and the run-up are in good agreement between the three models. It means that the nonlinear effects do not affect much these quantities because the first order component remains high compared to the others. However, the vertical force is clearly affected by the nonlinearities. The contribution of second and third orders prevents the force to go to zero as it happens for the linear model and the first harmonic of the nonlinear potential model (as seen in figure 4.7).

The CFD results for the vertical force show a significant discrepancy with results from the potential codes. These differences can be explained by the influence of the viscous effects coupled with the nonlinear effects, but it would require additional investigations. As expected, discrepancies increase with wave steepness, as the nonlinear and viscous effects both increase.

#### 4.1.3.2 Analysis of the test case $T = 12.1$ s

##### 4.1.3.2.1 Time series

In order to understand the impact of the wave steepness at  $T = 12.1$  s (the period of the load case 3.1 in the OC5 test series), different computations were run for increasing

wave heights such that the wave steepness varies in  $H/\lambda \in [0.5\%, 1.3\%, 2.2\%, 2.8\%, 3.1\%]$ . First, note from figure 4.7 that this period is really close to the “cancellation period”. It can then be expected small values of the vertical loads and large relative errors between the three models.

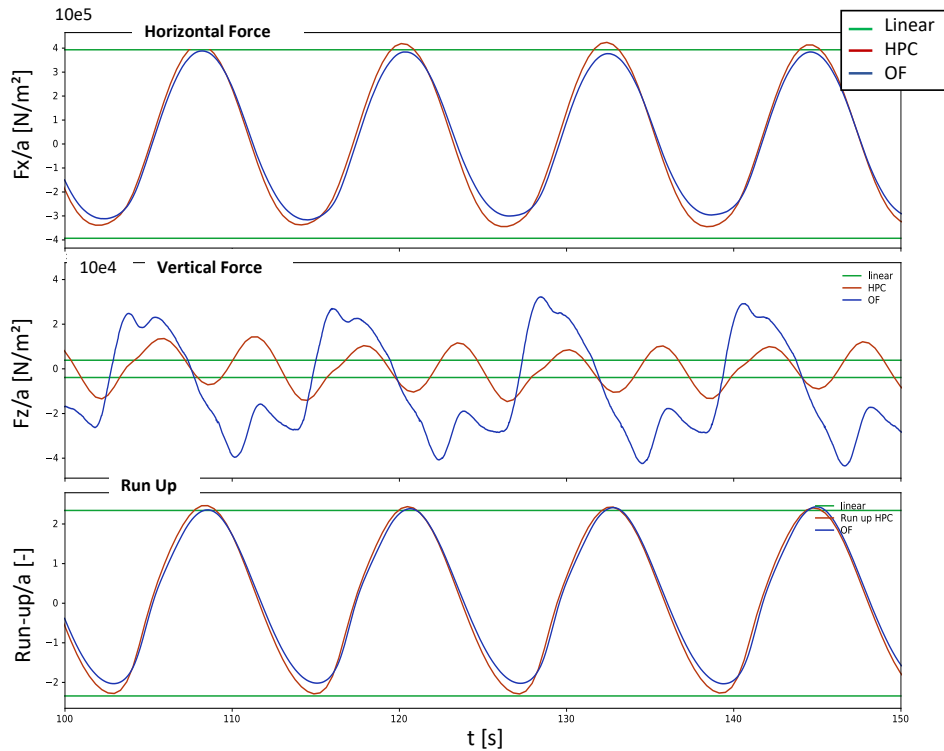


FIGURE 4.9: HPC and OpenFOAM® forces ( $F_x$ ,  $F_z$ ) and run-up compared to the linear model - case  $T = 12.1$  s, steepness  $H/\lambda = 3.1$

OpenFOAM® was able to compute accurate results for the five values of incident steepness for a relatively contained CPU time. As long as the steepness increases, the horizontal loads and run up develop nonlinear shapes. Mean values (drift force and mean run-up) diverge from 0, and higher-order harmonics can be seen as having a growing effect. The CFD computations emphasize similar results similar to the HPC computation for those variables, with also a growing impact of higher-order harmonics and mean values.

The behavior of the vertical load is more complex, as the first harmonic is of very small amplitude. Thus, the second harmonic is seen on HPC as soon as  $H/\lambda = 0.5\%$  with a growing effect as the steepness increases. For instance, at wave steepness 3.1% (figure 4.9), the vertical load seems to be of period twice the incident period which denotes an important contribution from the second-order harmonic.

OpenFOAM® exhibits different results, with a vertical load having a much different shape and composition in terms of harmonic components. It is speculated that non-potential effects are driven by the vertical load, even if a second-order peak can be seen for all values of wave steepness. Those non-potential effects originate from the viscous term which manifests as the potential part is small.

#### 4.1.3.2.2 Comparison of the nonlinearities

Important differences for  $T = 12.1$  s were observed between the linear amplitudes and the other models on the time series of both loads and run-up. A Fourier decomposition of time series into harmonics has been conducted to compare, first the fundamental harmonic at a fixed period with the linear model, and the second and third harmonics between the HPC and CFD models. The varying parameter is the wave height, so the linear values are represented with a straight line. Thus, the wave steepness, controlling the nonlinearity varies  $H/\lambda \in [0.5\%, 3.1\%]$ . It is then expected that the second and third harmonics increase faster than the first one as the wave steepness increases. This is effectively what can be observed in figure 4.10 on the three variables and whatever the nonlinear model.

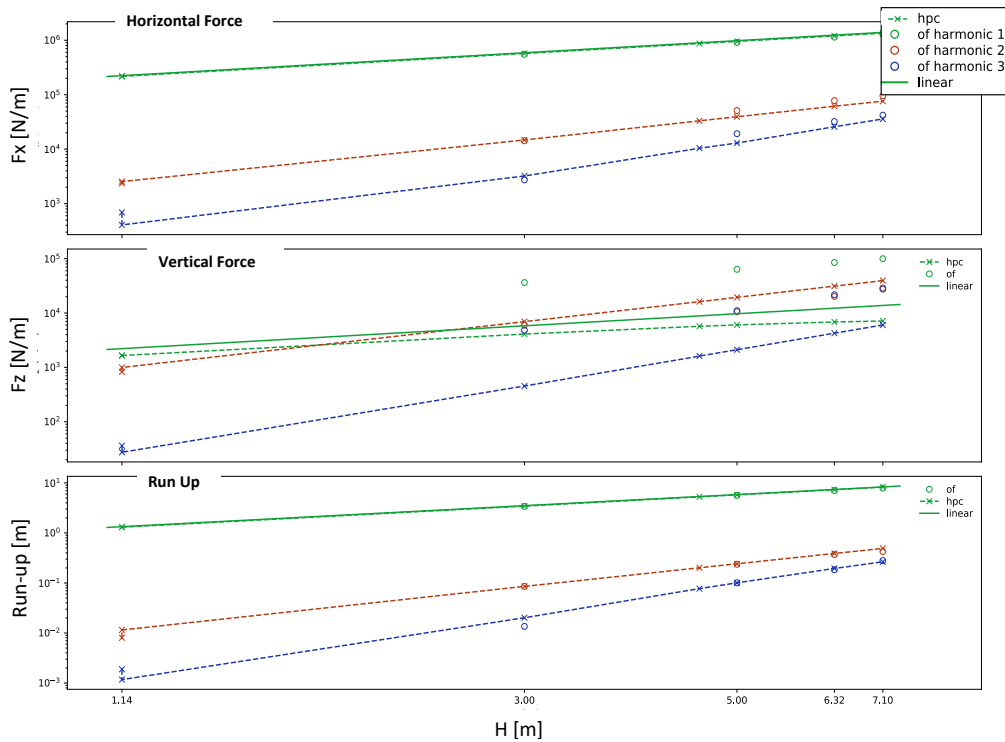


FIGURE 4.10: Harmonics 1, 2 and 3 of  $F_x$ ,  $F_z$  and run-up from the HPC model and CFD computation.  $T = 12.1$  s. Linear amplitude is also superimposed to compare the first harmonics.

A good agreement between the linear model, the HPC method, and OpenFOAM® first harmonic is shown on the horizontal load and run-up. Moreover, the second and third harmonics coincide between the HPC and OpenFOAM on those variables.

The amplitudes of the nonlinear harmonic are not negligible there, as the second and third harmonics of  $F_x$  represent respectively almost 6% and 3% of the first one for  $H/\lambda = 3.1\%$ . The same ratio of nonlinearity is observed on the run-up.

The behavior on the vertical load is, once again, really different. An error is shown between the HPC first harmonic and the linear value.  $T = 12.1$  s is close to the linear gap (cf. figure 4.7) of  $F_z$  leading to an important relative error, while the absolute error remains moderate. The linear gap is also visible when focusing on the amplitude of second and third potential harmonics, which out-passe the first one as soon as  $H = 2.5$  m ( $H/\lambda = 1\%$ ) and  $H = 7.1$  m ( $H/\lambda = 3.1\%$ ) respectively. The CFD computations also show different results. The first order shows that potential methods

way underestimate the vertical load (by a factor 6 -already observed in figure 4.8). The second harmonic is of the same order of magnitude as the HPC one, but the third harmonic is way more important (by a factor of 6) than the potential one. The results from the models are completely different, and it is no surprise that the viscous terms, neglected in both potential models, are of huge relative importance where the potential models predict an almost null vertical load.

## 4.2 Wave Induced Motion of a T-shape structure

The numerical model with the overset mesh method described in chapter 2 is first validated on the wave-induced motion of a 2D structure. The shape of the body is very similar to the previous fixed structure. However, the dimensions at the model scale are different and are described in section 4.2.2.1. The CFD results are compared to experimental data from [116]. Chen et al. [85] also presented results of a CFD model using the overset mesh method. However, they used the integrated OpenFOAM® wave generation and absorption tool previously named IHFOAM© [48]. In this section, a mesh convergence analysis is presented. One wave condition is considered. The wave height is  $H = 0.062$  m and the wave period is  $T = 1$  s. The discrepancies between the numerical model and the experimental results are discussed.

### 4.2.1 Description of the experimental set-up

In [116], the results of an experimental campaign that analyzed the motion of the 2D structure in extreme waves are presented. The experimental set-up of [116] is described on figure 4.11.

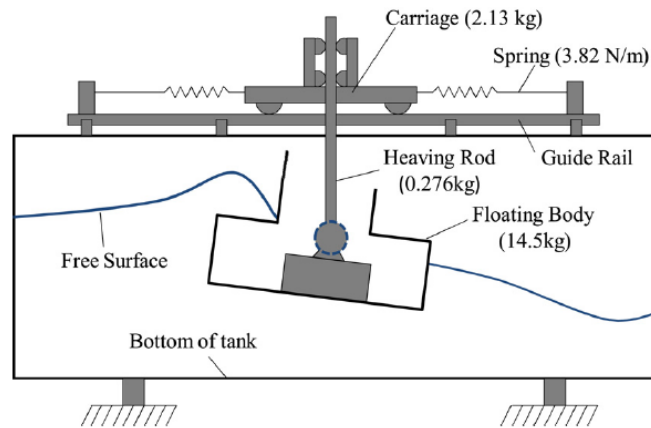


Fig. 3. Schematic of experimental setup.

FIGURE 4.11: Description of the experimental set up (adapted from [116])

The water depth is  $d = 0.4$  m. Due to experimental constraints, the center of rotation of the experimental model is a rotational joint. However, because of the limitation in the type of constraints available in the dynamic motion solver, this joint could not be modeled in the CFD model. We consider that the center of rotation is the same as the Center of Gravity (CoG) in the numerical model. The comparison of the results must take this difference into account.

## 4.2.2 Description of the numerical case

### 4.2.2.1 Geometry

The geometry of the structure is presented on figure 4.12. The structure is very similar to the structure presented in section 4.1. It consists of a section of a vertical column with a horizontal rectangle at its bottom. The still water level (SWL) is located 0.023 m below the top of the bottom section of the structure and the draft is 0.1 m. Considering the wave parameters used, the hypothesis of intermediate water depth is verified and the wavelength is  $\lambda = 1.47$  m.

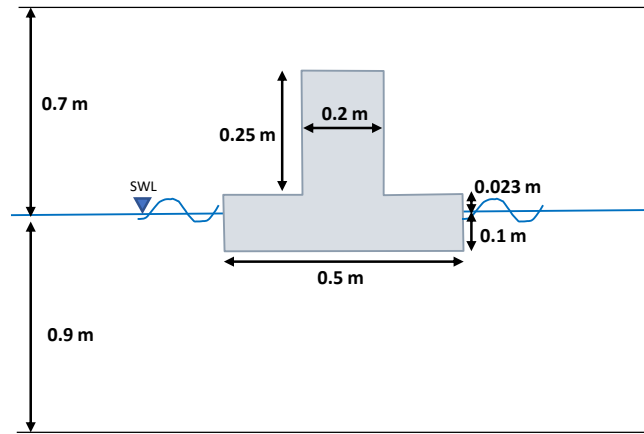


FIGURE 4.12: Sketch of the numerical 2D model with main dimensions

The total mass of the structure is 15 kg and no mooring system is considered. The structure is free to move vertically along  $z$ -axis (heave motion) and rotate around the  $y$ -axis (pitch motion). The horizontal motion along the  $x$ -axis is constrained. As shown in figure 4.13, the domain is divided into three zones along the  $x$ -axis: the generation zone, the propagation zone, and the absorption zone. In this model, the length of these zones is defined with respect to the wavelength of the incident waves. Based on the convergence analysis on the length of the absorption zone presented in chapter 3, each of the 3 zones is 2 wavelengths long.

### 4.2.2.2 Numerical Schemes

The integration and numerical schemes used in OpenFOAM® are summarized in table 4.1.

Time scheme	Backward Euler: first order
Gradient scheme	Gauss linear
Divergence scheme	$\rho \underline{u} \cdot \nabla \underline{u}$ : Gauss linear $\nabla(u\alpha)$ : Gauss van Leer $\nabla(u_r \alpha(1 - \alpha))$ : Gauss linear
Laplacian scheme	Gauss linear corrected
Overset Interpolation	Inverse Distance

TABLE 4.1: Numerical schemes used in the CFD model

Only laminar flow conditions are considered in this section. No turbulence model was used

In this section, the PIMPLE algorithm described in chapter 2 is used. The number of outer corrector (SIMPLE) steps is set to 2, which means that the entire system of equations is solved twice per time step. 2 inner iterations are used for the PISO loop. For each variable, the convergence tolerance is set below  $10^{-6}$ .

An adaptive time step is used for all the simulations. This time step is chosen automatically based on a given maximum CFL number. A convergence analysis on this maximum CFL number is presented in section 4.2.4.1.

### 4.2.2.3 Boundary Conditions

The set of boundary conditions is defined in table 4.2.

	<b>Alpha (<math>\alpha</math>)</b>	<b>Pressure (p)</b>	<b>Velocity (U)</b>
<b>Atmosphere</b>	inletOutlet	totalPressure	Pressure Inlet Outlet Velocity
<b>Bottom</b>	zeroGradient	fixedFluxPressure	Fixed Value 0
<b>Front/back</b>	zeroGradient	fixedFluxPressure	Fixed Value 0
<b>Inlet</b>	zeroGradient	fixedFluxPressure	Fixed Value 0
<b>Outlet</b>	zeroGradient	fixedFluxPressure	Fixed Value 0
<b>Cylinder</b>	zeroGradient	fixedFluxPressure	Moving wall velocity
<b>Sides</b>	overset	overset	overset

TABLE 4.2: Description of the boundary condition for volume fraction, pressure and velocity

More information on the boundary conditions can be found in the OpenFOAM® user guide. The main difference with a non-overset case is the use of the overset boundary condition for the sides of the fitted mesh. A moving wall velocity boundary condition is used for the wall of the floating cylinder. A point displacement variable is also initialized: it is the difference between the initial point location and the current location. The zone ID is a variable that defines whether a cell is in the fitted mesh or in the background mesh, which is specific to overset models.

### 4.2.3 Mesh convergence analysis

The mesh quality has a major impact on a CFD simulation and even more so when using an overset mesh method. In this section, mesh convergence analyses are presented. Time series of the surface elevation at a distance of 1.9 m upstream of the body, as well as rigid body motion (heave and pitch), are shown. The computational cost is also discussed.

All the simulations of the 2D case were run in parallel on an aRyzen Threadripper 2990WX - AMD 32-core processor, which operates at a base frequency of 3 GHz.

#### 4.2.3.1 Global Meshing method

The general mesh of the domain is described in figure 4.13. It is composed of several zones with different mesh refinements. The goal is to optimize the number of cells and so the computational time. The background mesh is first generated, on top of which the background mesh is then created.

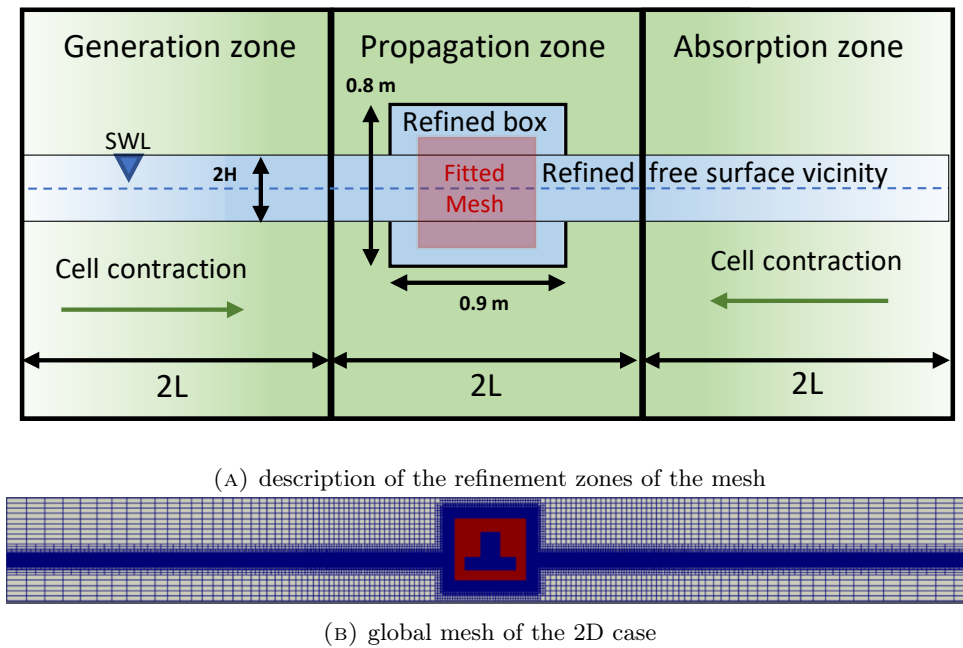


FIGURE 4.13: Global meshing process of the 2D case with the overset mesh method

At the first step, the background mesh is generated following the process presented in chapter 3. In the generation zone and the absorption zone, a cell contraction rate of 4 is used. In the propagation zone, the length of the cells is constant. The length and the height of cells are defined to obtain an aspect ratio of 1 for the cells in the propagation zone including in the refined box and the free surface vicinity.

In the second phase of the meshing process, the vicinity of the free surface is refined using the level tool of SnappyHexMesh© as described in chapter 3. The height of this refined band is  $2H$ , centered on the SWL. Convergence analysis of the number of cells per wave amplitude is presented in section 4.2.3.2.

A refined box is also generated in the background mesh to improve the accuracy of the interpolation of the variables between the two meshes. The size of this box is chosen to guarantee that the overset mesh will remain in that area in the course of the simulation. A convergence study of the refinement rate in this zone is presented below.

In the last phase, the overset mesh is generated around the structure (in red on figure 4.13 and figure 4.14). The geometry used in this model is easy to mesh with structured meshes. All the cells of the overset mesh have the same size, which is the size of the cells in the free surface vicinity of the propagation zone. So, these cells also have an aspect ratio of 1.

Chen et al. [85] have shown that the width of the overset mesh has a low influence on the results. They suggested that the size of the overset mesh should be reasonably small to reduce the number of cells. However, the external boundary of the overset mesh should be far enough from zones where sharp gradients occur, in our case in the vicinity of the structure. In the present study, the overset mesh is 0.6 m high and 0.7 m wide.

### 4.2.3.2 Influence of the global mesh refinement

In this section, the influence of the global refinement of the mesh is analyzed. In all cases, the meshing method described above is used. A level 4 is always imposed in the free surface vicinity, the total number of cells vertically and horizontally is defined to reach the targeted number of cells per wave amplitude in the free surface vicinity. Three simulations are presented: one with 15 cells per wave amplitude in the free surface vicinity ( $\delta_z = 0.002$  m), one with 10 cells per wave amplitude ( $\delta_z = 0.003$  m) which is the case of reference, and one with 5 cells per wave amplitude ( $\delta_z = 0.006$  m). In all cases the refined box 1 described on figure 4.14 is used. It means that the cells in the refined box have the same size as the cells in the free surface vicinity in the propagation zone. The cells of the overset mesh have also the same size.

The maximum Courant number is set to 0.5. The wave condition and numerical parameters described above are used. The results of the free surface elevation at 1.9 m before the center of the structure, the heave and pitch motion of the structure are compared in figure 4.14. The size of the cells along  $x$ -axis is adapted to maintain an aspect ratio of 1 in the propagation zone as described in the global meshing method section.

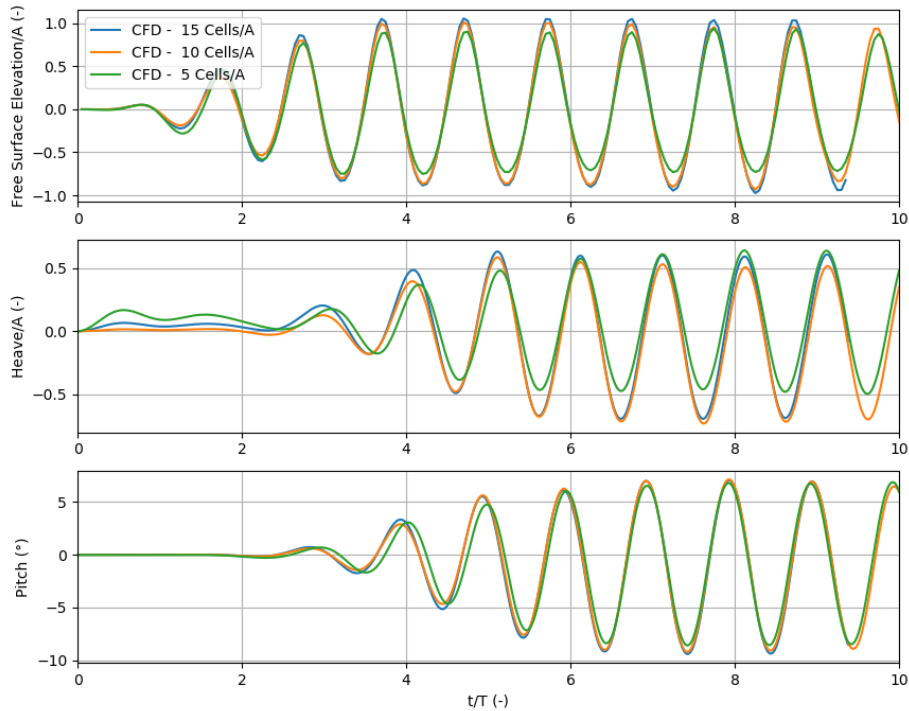


FIGURE 4.14: Time series of free surface elevation, heave and pitch motions. Influence of the global refinement of the meshes

We observe that the free surface elevation amplitude is reduced when using 5 cells per wave amplitude compared to the cases with 10 or 15 cells. Some discrepancies can also be seen on the heave motion: the negative amplitude is lower for the case with 5 cells. It can also be noticed that the platform does not stay at its initial rest position (heave = 0) at the beginning of the simulation using 5 cells per wave amplitude, while it mostly does in the case with 10 or 15 cells. It is not clear why the case with 15 cells

is slightly less stable than the case with 10 cells before the waves reach the structure. There is a small difference in the period of the pitch motion. The positive amplitude of the 10 cells per amplitude case is slightly lower than the amplitude of the 15 cells per amplitude case. Overall, the results of the cases with 10 and 15 cells per amplitude are in good agreement.

Table 4.3 summarizes the input parameters of the cases comparing the different refinements in the free surface vicinity and the computational information.

Case	Refined box	Free surface Refinement (cells/amp)	Max Co	Accel. Relax. Coeff.	Run time per period (min)	Mean time step (sec)	Number of time steps per period	Number of cells
4	Box 1	15	0.5	0.4	194	6.17E-04	1,621	376 629
1	Box 1	10	0.5	0.4	29	9.56E-04	1,046	165 335
5	Box 1	5	0.5	0.4	3	1.78E-03	562	43 744

TABLE 4.3: Comparison of the input parameters and the computational outputs for the convergence analysis of the global refinement of the mesh

As expected, case 4 has a much longer run-time than the other cases. The run-time per period is almost 7 times higher in case 4 compared to case 1. Figure 4.14 shows that the results are close between these two cases. Thus, it can be concluded that the discretization with 10 cells per amplitude offers the best trade-off between computational time and accuracy of results.

#### 4.2.3.3 Influence of the Refined Box in the background mesh

To avoid losing information during the interpolation step of the variables between the two meshes of the overset process, the cells where the interpolation occurs should be of similar size. The use of a refined box in the background mesh guarantees this criterion (blue cells inside the black outline in figure 4.15). However, it requires a lot of cells. In this section, the influence of the refinement rate of the box in the background mesh is investigated. Three cases are compared: one case with a box with a level 4 of refinement (Box 1 of figure 4.15, so with the same refinement as the overset mesh and the free surface vicinity), one case with a box with a level 2 of refinement (Box 2) and one case without box (No Box). These three meshes are shown in figure 4.15.

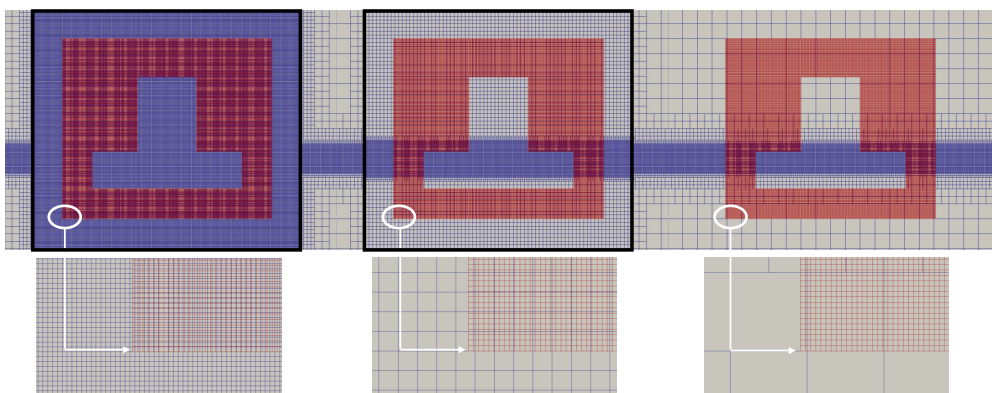


FIGURE 4.15: Refined box in the background mesh and zoom at the bottom left corner of the overset mesh – Box 1: level 4 of refinement  
– Box 2: level 2 of refinement – Box 3: no refinement box

The wave and numerical parameters described above are used to run simulations with each of these meshes. 10 cells per wave amplitude are used in the free surface zone.

The results of the free surface elevation at 1.9 m before the center of the structure, the heave and pitch motions of the structure are compared in figure 4.16. The free surface elevation and the heave position are normalized by the wave amplitude, the time is normalized by the wave period. Overall, the impact of the refined box on the results is small. The cases with Box 2 and with no box show a slightly lower amplitude in heave and pitch motions compared to the case with Box 1. The free surface elevation curves of the cases with Box 2 and with no box are superposed, but the amplitude is slightly smaller than the case with Box 1.

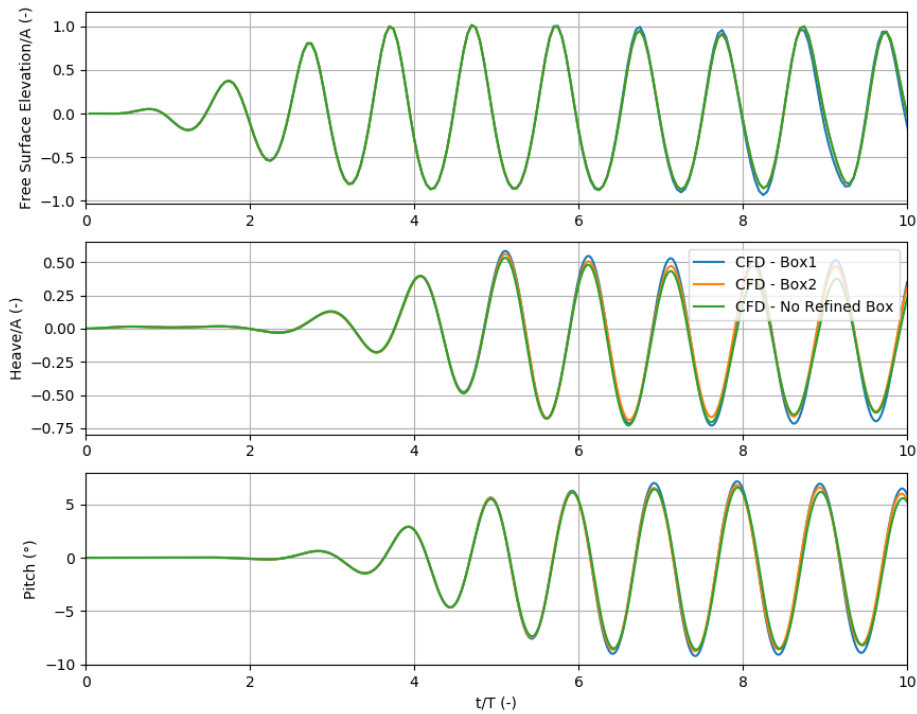


FIGURE 4.16: Time series of free surface elevation, heave and pitch motions. Influence of the refinement of the background box

Table 4.4 summarizes the input parameters of the cases comparing the different refined boxes and the computational information. Case 1 is the case of reference in all this study.

Case	Refined box	Free surface Refinement (cells/amp)	Max Co	Accel. Relax. Coeff.	Run time per period (min)	Mean time step (sec)	Number of time steps per period	Number of cells
1	Box 1	10	0.5	0.4	29	9.56E-04	1,046	165 335
2	Box 2	10	0.5	0.4	19	7.86E-04	1,273	105 740
3	No Box	10	0.5	0.4	23	9.64E-04	1,037	100 256

TABLE 4.4: Comparison of the input parameters and the computational outputs for the refined box convergence analysis

As expected, the computational time for case 1 is the largest (29 min). However, it is interesting to note that the run time of case 2 (19 min) is smaller than the run time of case 3 (23 min) even if the number of cells is larger in case 2 than in case 3 and the mean time step of case 2 is smaller than the time step of case 3. It might be explained by a slower convergence when no box is used. This confirms the importance of having cells of similar size between the background mesh and the overset mesh.

#### 4.2.4 Solver stability

In this section a convergence analysis of two important parameters is presented: the Courant number  $Co$  and the acceleration relaxation coefficient  $f_a$ .

##### 4.2.4.1 Influence of the Courant number

The influence of the maximum allowable Courant number has been investigated, and the results are presented on figure 4.17 for  $Co = 0.5, 1,$  and  $2$ . In these simulations, the same wave as previously is used, 10 cells per amplitudes are generated in the free surface vicinity zone, and the Box 1 of figure 4.14 is used. Again, the free surface elevation in front of the structure, the heave, and the pitch motion are presented on figure 4.17.

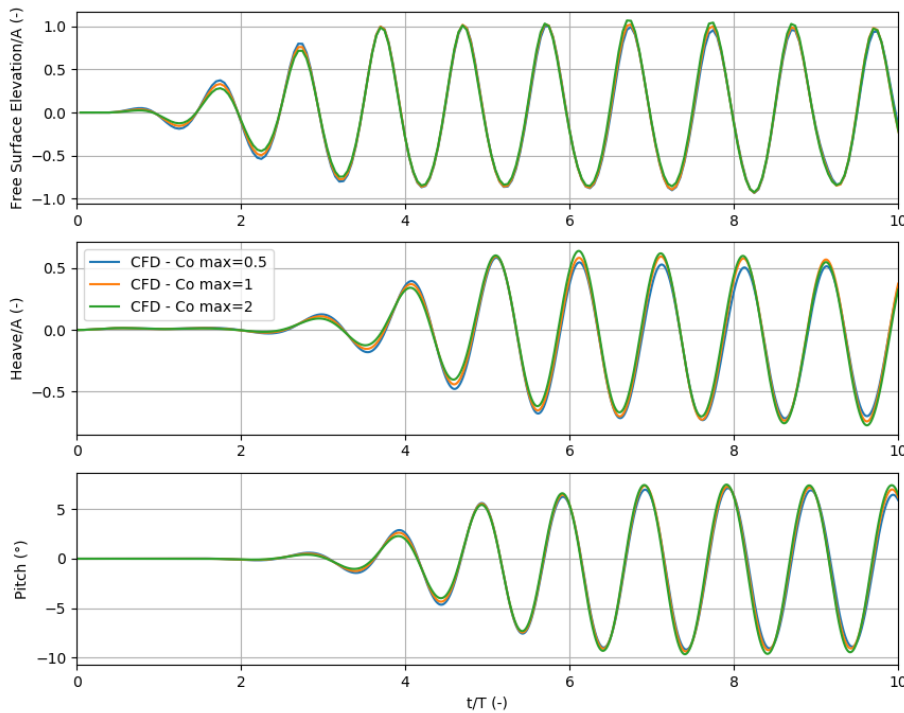


FIGURE 4.17: Time series of free surface elevation, heave and pitch motions. Influence of the maximum Courant number  $Co$

Increasing the maximum Courant number tends to reduce the amplitude of the free surface elevation in the transient state of the simulation. It also reduces the heave motion and pitch motion amplitude at the beginning. However, the impact remains very small once the simulation has reached a steady state. Table 4.5 summarizes

the input parameters and the computational information of three cases with three different  $Co$ .

Case	Refined box	Free surface Refinement (cells/amp)	Max $Co$	Accel. Relax. Coeff.	Run time per period (min)	Mean time step (sec)	Number of time steps per period	Number of cells
1	Box 1	10	0.5	0.4	29	9.56E-04	1,046	165 335
6	Box 1	10	1	0.4	16	1.87E-03	535	165 335
7	Box 1	10	2	0.4	9	3.20E-03	313	165 335

TABLE 4.5: Comparison of the computational times for three values of the maximum Courant number  $Co$

As expected, the run-time of the simulation becomes smaller and the time step becomes larger as the Courant number increases.

Using a  $Co$  greater than 1 is acceptable for the stability of the OpenFOAM® simulations, but may lead to a loss of accuracy. However, this analysis suggests that a  $Co$  of 2 can provide an accurate enough solution when looking at global motion and wave elevation, at least for this specific mesh.

#### 4.2.4.2 Influence of the acceleration relaxation coefficient

The influence of acceleration relaxation coefficient  $f_a$  has also been investigated, the results are presented on figure 4.18 for four values:  $f_a = 0.2, 0.4, 0.6,$  and  $0.8$ . Again, the incident wave described above is used. 10 cells per amplitudes are generated in the free surface vicinity zone, and the Box 1 of figure 4.14 is used. Again, the free surface elevation in front of the structure, the heave, and the pitch motion are presented.

Results of figure 4.18 show that the difference is very small between the case with  $f_a = 0.2$  and  $f_a = 0.4$ . There is no visible impact on the free surface elevation, nor the heave motion. The pitch amplitude is slightly higher with  $f_a = 0.2$ . However, the heave position diverged at the beginning of the simulation when using  $f_a = 0.6$  or  $0.8$ . It is caused by a divergence in the computation of the acceleration of the body.

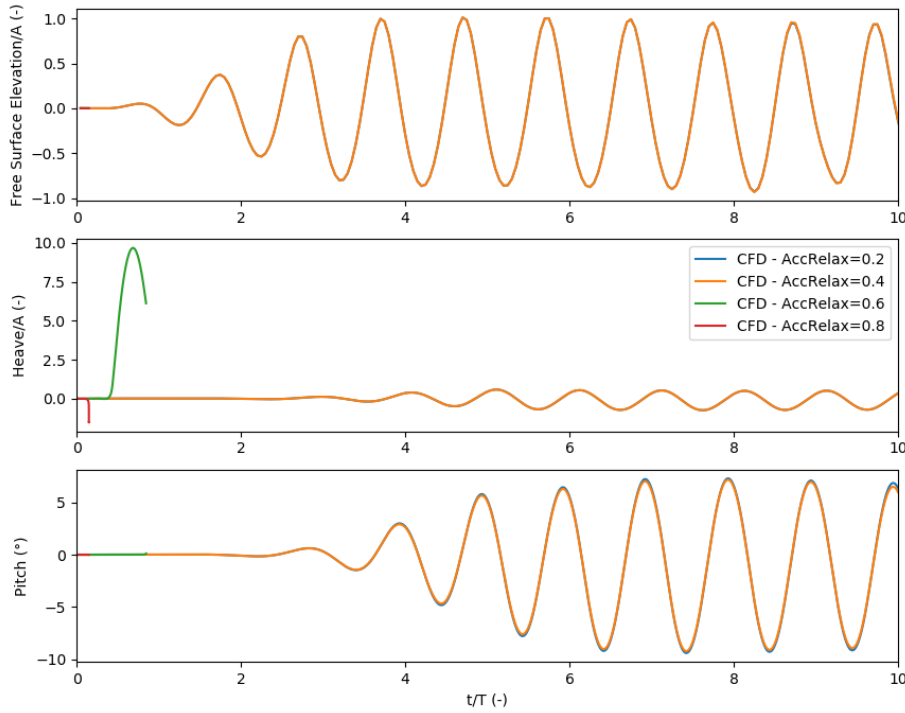


FIGURE 4.18: Time series of free surface elevation, heave and pitch motions. Influence of the acceleration relaxation coefficient  $f_a$

Table 4.6 summarizes the input parameters and the computational information of four cases with different acceleration relaxation coefficients.

Case	Refined box	Free surface Refinement (cells/amp)	Max $C_o$	Accel. Relax. Coeff.	Run time per period (min)	Mean time step (sec)	Number of time steps per period	Number of cells
8	Level 4	10	0.5	0.2	29	9.61E-04	1,041	165 335
1	Level 4	10	0.5	0.4	29	9.56E-04	1,046	165 335
9	Level 4	10	0.5	0.6	diverged	diverged	diverged	165 335
10	Level 4	10	0.5	0.8	diverged	diverged	diverged	165 335

TABLE 4.6: Comparison of the computational times for four values of the acceleration relaxation coefficient

When the simulation does not blow up, the relaxation coefficient does not influence the time step nor the run-time of the simulation.

This analysis shows the importance of this relaxation method to ensure a convergence of the acceleration of the moving body.

#### 4.2.5 Comparison with experimental results

Based on the convergence analysis, the numerical model is compared with the experimental case of [116]. The wave generated is the same as in the convergence analysis ( $T = 1$  s,  $H = 0.062$  m). A wave probe is located 1.9 m before the structure.

#### 4.2.5.1 Results and discussion

Reference case 1 is used. 10 cells per wave amplitude are generated in the vicinity of the free surface, the refined Box 1 is used in the background mesh. It means that the interpolated cells between the background mesh and the overset mesh have the same size, and this size is the same as the size of the cells near the free surface. The maximum Courant number is set to  $Co = 0.5$ , and the acceleration relaxation factor is  $f_a = 0.4$ . The numerical results are compared with the experimental results in figure 4.19.

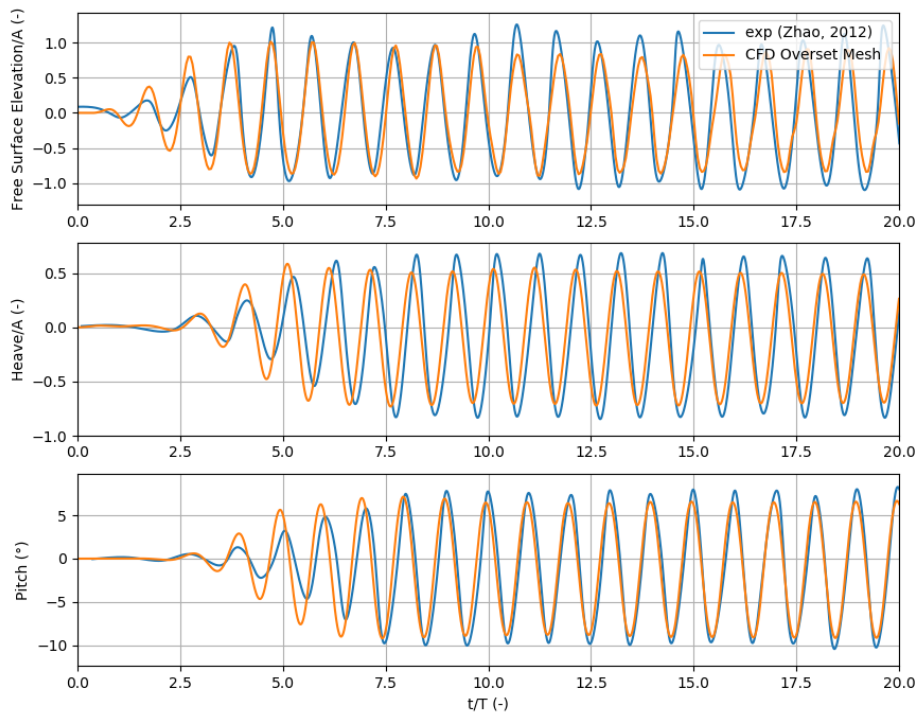


FIGURE 4.19: Comparison of the numerical results (case 1) with the experimental measurements from [116]

The distance between the wavemaker and the structure is different between the experimental set-up and the numerical model. To be able to compare the relative phase difference of the structure motion, the experimental results of the free surface elevation, the heave position, and the pitch angle were shifted so that the numerical wave and the experimental wave are in phase at the beginning of the time series (before the wave is reflected from the structure).

The results show that the amplitude of the heave and pitch motion is slightly smaller in the numerical model than in the experiments. There is also a small difference in the period of oscillation for heave and pitch. However, the numerical results are globally in good agreement with the experimental measurements. The small differences can be justified by the difference in the point of rotation between the two models. The free surface elevation amplitude and period are in good agreement between numerical and experimental models before the 10<sup>th</sup> period, then the numerical amplitude is smaller than the experimental one. It could be explained by reflected waves in the experimental wave tank.

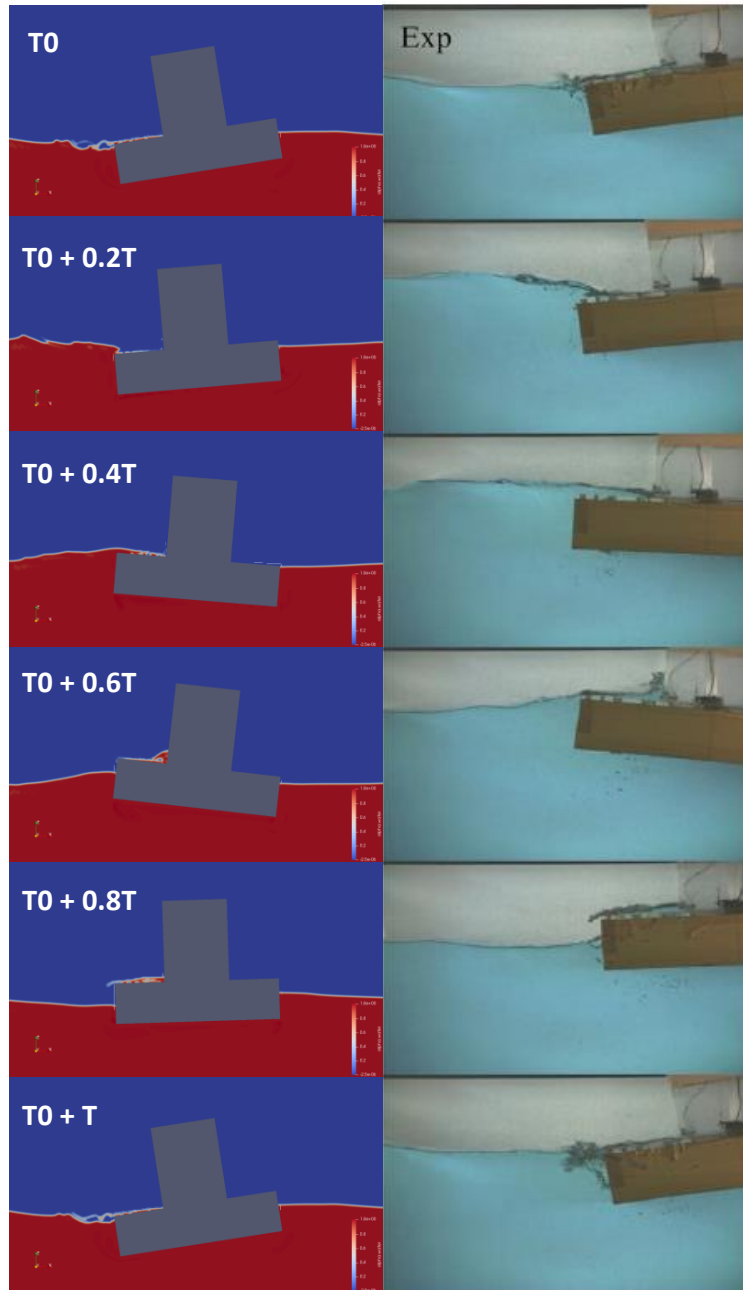


FIGURE 4.20: Comparison of the green water event on the platform and the position of the floater. Left: present numerical CFD simulations, right: experimental pictures from [116]

Water on deck phenomenon is observed on the structure as shown on figure 4.20. Screenshots of the free surface elevation of the CFD simulation and position of the structure are presented on the left side where the red color represents the water phase and the blue one the air phase. The overset grid external boundary is also represented in white. It can be observed that there is no deformation of the free surface at the interfaces between the two meshes. It is compared to the pictures of the experiments from [116] on the right side.

The green water dynamics on top of the bottom part of the structure is well captured, especially at  $T_0 + 0.8T$ . However, the quantity of water seems slightly underestimated, as it is also shown in the simulation of [85].

These green water events can be the cause of the non-zero mean value of the heave and pitch positions (figure 4.19) as described in [116]. The analysis on the 2D case has shown overall good agreement with experimental measurements.

### 4.3 Conclusions

This section first focused on the numerical simulations of wave-body interactions for a 2DV section inspired from the DeepCwind semi-submersible platform, under different wave conditions. First, a complete study was performed with regular waves of small steepness for a wide range of period  $T \in [4 \text{ s}, 16 \text{ s}]$ . The objective was to compare, under linear incident waves conditions, the CFD results (obtained with OpenFOAM®), the nonlinear potential method (obtained with an HPC method introduced by [42] and developed by [43]) with a linear potential model. Even if the domain of study is inside the linear approximation domain, important differences were highlighted, particularly on the vertical load predicted as being small by the linear potential theory (and even vanishing for a particular wave period). Higher-order harmonics come into play, even for very small values of wave steepness.

After that, this work focused on the period  $T = 12.1 \text{ s}$ , for which a large number of computations has been conducted for different wave conditions. Time series were compared in detail, and harmonics were extracted to emphasize a relatively important contribution of both higher-order effects (from HPC simulations) and viscous and turbulence effects (from OpenFOAM® simulations). As expected, those effects increase when the linearity assumptions ( $H/\lambda$  small) are relaxed. However, even for very small wave steepness, the vertical load is strongly subjected to high-order contributions and viscous effects. This is due to a very low value of the fundamental harmonic of the vertical load for this wave period.

Then, the capability of the coupling solver between waves2Foam and the overset mesh module of OpenFOAM® was presented on a 2D inverted T-section structure. A meshing methodology for a NWT was presented and optimized with this mesh convergence analyses. The constraints of the cell size between the background and the overset mesh were discussed. An optimized mesh was used to analyze the CFD model of the 2D structure with experimental measurements. Results showed good agreement for free surface elevation and body motions. The discrepancies due to some differences in the numerical model were discussed. The influence of the Courant number was also investigated. It showed that it has a small impact on the accuracy of the results for wave elevation and body motion in the range of values considered here. However, it is expected to influence more local phenomena, such as vorticity near sharp angles. The importance of a relaxation scheme of the body acceleration was also analyzed. Overall, the numerical results showed good agreement with the experimental data.

# 5 CFD analysis of added mass, damping and induced flow of isolated and cylinder-mounted heave plates at various submergence depths using an overset mesh method

This chapter corresponds to a paper that has been submitted to the Journal of Fluids and Structures on December 8, 2020.

**Abstract:** Fluid-structure interaction processes of heave damping plates in forced vertical motion are investigated using a CFD numerical model. First, a single isolated disk is considered with two submergence depths, including a case where the disk is very close to the mean water level with  $d/D = 1/12$  ( $d$  is the submergence depth and  $D$  the diameter of the disk). Then, the case of a disk attached to a vertical cylinder is analysed, corresponding to one leg of a semi-submersible floater. The open source software OpenFOAM® is used to model the flow around the disk and to extract the relevant hydrodynamic coefficients of the structures. The dynamics of the structure and induced flow and free surface waves are tackled with the overset mesh tool implemented in OpenFOAM®. Considering the rotational symmetry of the problem, an axisymmetry model is used with wedge symmetry boundary conditions. The results are compared with experimental measurements and linearized potential flow modeling approaches with empirical correction. The CFD results of the models of both structures predict well the experimental measurements, including large oscillation periods and various amplitudes of heaving motion, where the potential model results are deteriorated.

## 5.0.1 Overview of heave plates for offshore structures

In offshore design, heave plates are frequently used to improve the stability of the floating structures by increasing the viscous damping and added mass. These plates, having usually a circular (disk) or polygonal shape in the horizontal plane, are key components in the design of some concepts of Floating Offshore Wind Turbines (FOWT). They can be relatively close to the free surface in the case of a semi-submersible platform [117], or deeper in the case of spar concepts.

The assessment of the hydrodynamic forces acting on such heave plates is crucial to design reliable structures for FOWT. The analysis of these plates has been largely shared in the literature, and is discussed hereafter. To analyse the hydrodynamic forces, a forced harmonic motion is usually imposed to the structure, as shown

schematically in figure 5.1a for the case of an isolated disk and in figure 5.1b for the case of a disk at the bottom of a vertical cylinder. The forces acting from the fluid on the disk are the hydrostatic restoring force, the inertia force characterized by the added mass coefficient  $C_a$  (i.e. non-dimensional added mass), and the damping force characterized by the damping coefficient  $C_b$  (i.e. non-dimensional damping term). The damping force usually encompasses several contributions: a linear damping force due to wave radiation, and a drag force due to vortex shedding, that can be linearized [118]. The drag force is characterized by the drag coefficient  $C_d$ .

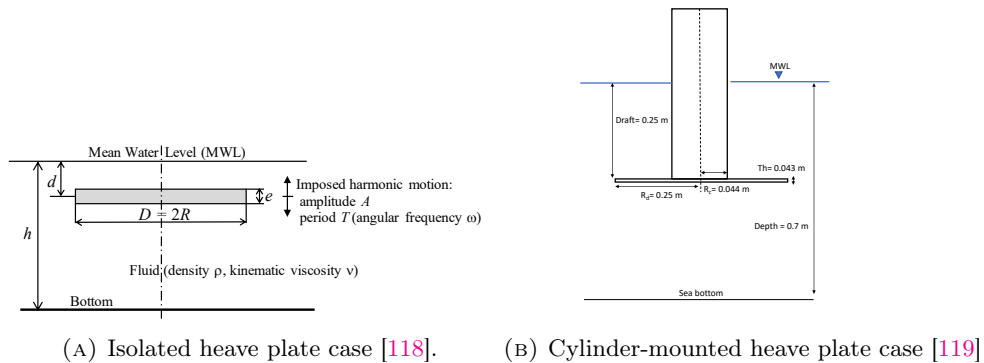


FIGURE 5.1: Definition sketches of the two considered cases (not on scale)

The most common design presented in the literature is the case of a circular plate located at the bottom of a vertical cylinder (cf. Figure 5.1b). A forced heave motion of the structure is classically imposed to assess the hydrodynamic coefficients. Numerical analyses were presented in the literature, e.g., Tao and Thiagarajan [120] used a direct numerical simulation with a finite difference method, Garrido-Mendoza et al. [121] used CFD (Computational Fluid Dynamics) based on a finite volume method. Experimental analyses are also presented in [119] and [122]. Scale effects were recently investigated by Anglada-Revenga et al. [123]. The impact of waves or current was investigated in [124] and [125].

A couple of studies focused on the heave plate alone ([121], [126], [118], [127], [128]). Other designs were also considered to improve the performances of the heave plates. In [129], [130], [131] and [132], the authors used for example several heave plates stack on top of each other. It was shown that using an appropriate spacing and diameter ratio can improve the hydrodynamic performances of the structure. Lake et al. [133] showed experimentally that separating the disk from the column could increase the global damping and the added mass. Zhu and Lim [134] also described the effect of separating the plate from the column. They showed that varying the disk diameter had the most significant impact on the hydrodynamic results compared with the distance between the disk and the column. They compared a case with plate and a case without and found that the linearized damping coefficient of the structure increases by 200% when a disk is added compared with a cylinder alone.

Perforated plates are also commonly analyzed and have shown good results in improving the damping performance of the structure (see e.g. [118], [126], [135]). The heave plates can have polygonal shapes that make the fabrication easier [117]. Moreno et al. [136] investigated the comparison between a polygonal plate and a circular plate. They showed that hexagonal shapes could be safely approximated by circular geometries, but the difference becomes significant with square plates. Rectangular plates were also considered in [137] [128] and [135].

The thickness of the plate is an important parameter in its hydrodynamic response. He et al. [138] analyzed the influence of thickness to diameter ratio and showed that when this ratio increases, the damping decreases. Li et al. [135] also showed that this ratio has a significant impact on the drag coefficient and so the damping, but has little influence on the added mass. The proximity of the free surface and the sea bottom has major impacts on the dynamics response of these heave plates [121]. When the plate is deep enough, the influence of the free surface and so the radiated waves are negligible on the dynamics of the disk. The linear potential flow model (LPFM), coupled with a viscous term based on empirical coefficients, showed good agreement with experimental results as described in [118]. However, Molin et al. [118] also emphasized that the models exhibit some limitations as the plate comes closer to the free surface. At small periods, the hydrodynamic coefficients are weakly dependent on the amplitude and the linear theory, with an empirical correction for the drag term, remained satisfactory. However, as the period increases, the numerical results deteriorated compared with experimental measurements. Similarly, Garrido-Mendoza et al. [121] have shown that the hydrodynamic coefficients are more impacted when the plate gets closer to the sea bed.

The drag component is caused by flow separation and vortex shedding at the edge of the disk. These vortices interact with the free surface or the sea bottom and can influence the flow around the structure and so, the hydrodynamic coefficients. The shedding of the vortices and their influence on the hydrodynamic coefficients have been studied in [121], [138] or [120]. In these references, the authors have shown that the vortex shedding is dependent on the ratio thickness of the disk vs diameter of the disk. Tao et al. [120] describe three vortex shedding modes depending on this ratio and the the Keulegan-Carpenter number  $KC$ , defined by eq. (5.1). When oscillating, the plate generates vortices at the top of the edge and the bottom of the edge. When  $KC$  is small and the disk is thick enough, there is no interaction between the two vortices. This is the independent mode. However, when  $KC$  becomes larger and the ratio smaller, the so-called vortices interact and mix. This is the interactive mode. Finally, when  $KC$  is large and the ratio is small, only one large vortex is generated at the disk edge. This is the uni-directional mode. [138] also described different modes of vortex shedding depending on  $KC$  and thickness to diameter ratio, and showed how these vortices impact the damping effectiveness of the plate.

The drag coefficient is commonly assessed based on experimental campaign measurements or empirical values [22]. However, experimental campaigns are expensive and not flexible in the design process of such plates. Empirical values do not exist for all geometries. The use of CFD is a good alternative solution to assess these loads. Several studies used CFD models and showed satisfactory results (see, e.g., [121], [129], [139], [140], [141]). They provide good representations of the vortex shedding around the plates.

### 5.0.2 Physical analysis of the problem of interest

The two configurations considered in this work are depicted in Figure 5.1. In both cases the heave plate is an horizontal circular disk of diameter  $D = 2R$  and width  $e$ , placed at a submergence  $d$  below the Mean Water level (MWL) in a supposedly unbounded fluid domain of uniform depth  $h$ . The disk can be considered as an isolated body (Figure 5.1a, case studied in section 5.2) or mounted at the bottom of a vertical cylinder having a diameter  $D_c = 2R_c$  and sharing the same vertical axis as the disk (Figure 5.1b, case studied in Section 5.3). The fluid is characterized by its density  $\rho$  and kinematic viscosity coefficient  $\nu$  (surface tension effects are neglected here).

A periodic heave motion is imposed to the body, characterized by its period  $T$  (or angular frequency  $\omega = 2\pi/T$ ) and amplitude  $A$ .

Considering the action of gravity (denoted  $g$ ), a dimensional analysis shows the number of independent variables in the case of the isolated disk is equal to 9, namely:  $D$  (or  $R$ ),  $e$ ,  $d$ ,  $h$ ,  $\rho$ ,  $\nu$ ,  $A$ ,  $T$  (or  $\omega$ ) and  $g$ . We may also use the wave-number  $k$  of the surface waves induced by the structure motion to characterize the periodic nature of the waves, this dependent variable being a function of mainly  $T$  and  $h$  through the dispersion relation of surface waves (with additional influence of  $A$  if nonlinearity is significant).

Let us consider a dependent variable as, for instance, the added mass  $M_a$  of the disk. In this situation, the total number of physical variables is  $n = 10$ , which are function of  $p = 3$  fundamental units. From the Vaschy-Buckingham theorem, a relation between  $n - p = 7$  non-dimensional numbers is expected to apply, i.e. the (non-dimensional) added-mass coefficient  $C_a = M_a / (\frac{8}{3}\rho R^3)$  is a function of 6 non-dimensional numbers in the general case. This relation can be expressed in different ways, for instance as  $C_a = C_a(KC, Re, Fr, e/D, d/D, T\sqrt{g/h})$  or  $C_a = C_a(KC, Re, Fr, e/D, d/D, kR)$ . The Keulegan-Carpenter ( $KC$ ) number, expressed in the case of an oscillating body by:

$$KC = 2\pi \frac{A}{D}, \quad (5.1)$$

describes the relative importance of drag forces over inertia forces (it can also be seen as the non-dimensional amplitude of motion). Viscosity effects are quantified with the Reynolds number ( $Re$ ), defined as:

$$Re = \frac{\omega AD}{\nu}, \quad (5.2)$$

using  $\omega A$  as a characteristic fluid velocity. Finally, the Froude number ( $Fr$ ) describes the relative importance of inertia forces over gravity forces:

$$Fr = \frac{A\omega}{\sqrt{gh}}. \quad (5.3)$$

Note that alternative non-dimensional numbers could be considered, in particular the so-called frequency parameter [142, 138]:

$$\beta = \frac{Re}{KC} = \frac{D^2}{\nu T}, \quad (5.4)$$

leading to a relation of the form  $C_a = C_a(KC, \beta, Fr, e/D, d/D, kR)$  for instance.

A detailed study of the effects of all these non-dimensional numbers is hardly possible, and beyond the scope of this paper. Some of these numbers will be considered fixed (e.g. the non-dimensional plate width  $e/D$ ) or taking a limited number of values, as the relative submergence  $d/D$ . Furthermore, for the type of situation considered here, it is anticipated the Reynolds number has little influence. The horizontal plate has sharp angles which impose separation of the flow. The oscillating boundary layer on and under the disk has a thickness of order  $O(\sqrt{\nu/\omega})$  and is thus very thin, so that the friction on the disk does not affect the vertical force. Viscosity plays a more pronounced role on the evolution and disintegration of the vortices. So, as observed by many other authors ([131], [134], [119], [136]), the hydrodynamic coefficients are expected to depend more on  $KC$  number than on  $Re$  number. We will therefore base our analyses essentially on the  $KC$  number.

### 5.0.3 Objectives of this study and lay-out of the article

To the best of the authors' knowledge, all the CFD simulations of heaving plates use remeshing, sliding meshes, or adaptive meshing techniques to deal with the motion of the structure. These techniques can have limitations in the amplitude of motion or for the representation of complex geometries, especially when multiple degrees of freedom are considered. This paper aims to validate a CFD method using an overset mesh technique. The overset mesh method has the great advantage to guarantee the same mesh quality throughout the simulation. This work is part of a more general work aiming to validate the overset mesh technique in CFD for modeling realistic FOWT in oceanic wave conditions.

The remainder of this paper is organized as follows. The numerical model and overset mesh technique are presented in Section 5.1, together with the methodology used to extract the hydrodynamic coefficients. An already implemented tool from OpenFOAM® is used. A forced heave motion of the structure is considered in this study. Two cases are presented in Sections 5.2 and 5.3 respectively: an isolated circular plate and a cylinder with a disk corresponding to one leg of a typical semi-submersible tri-floater for FOWT [143]. Both geometries have axial symmetry, which brings several benefits regarding the computational requirements in terms of memory and computing time. The numerical results are compared with experimental measurements from [118] for the isolated disk and from [119] for the disk+column case. Conclusions are summarized in Section 5.4.

## 5.1 Numerical Methods

The CFD model is based on the open-source solver OpenFOAM® version 1712 and uses the finite volume method. It includes built-in modules and external tools, which are described in this section.

### 5.1.1 Prescribed dynamics of the structure

Throughout this work, a vertical harmonic motion (heave) is imposed to the structure. The position of the center of gravity of the structure is imposed by:

$$z(t) = A \cos(\omega t) \quad (5.5)$$

where  $A$  is the amplitude of motion,  $\omega = \frac{2\pi}{T}$  the angular frequency and  $T$  the period of oscillation. Using complex notation, the heave position, velocity and acceleration can be written respectively as:

$$z(t) = Ae^{i\omega t}, \quad (5.6)$$

$$\dot{z}(t) = i\omega Ae^{i\omega t}, \quad (5.7)$$

$$\ddot{z}(t) = -\omega^2 Ae^{i\omega t}. \quad (5.8)$$

### 5.1.2 CFD Numerical model

#### 5.1.2.1 Governing equations and boundary conditions

Fluid flows are governed by the mass, momentum, and energy conservation principles. In the case of ocean hydrodynamics, incompressible fluid with constant viscosity can be considered. The mass continuity equation for an incompressible fluid is:

$$\nabla \cdot \underline{u} = 0 \quad (5.9)$$

where  $\underline{u}$  is the velocity vector of the fluid flow. Considering a Newtonian fluid, the momentum conservation principle is given by the Navier-Stokes equations as follows:

$$\rho \left( \frac{\partial \underline{u}}{\partial t} + \underline{u} \cdot \nabla \underline{u} \right) = \mu \nabla^2 \underline{u} - \nabla p^*. \quad (5.10)$$

Here,  $\rho$  is the fluid density,  $\mu$  is the dynamic viscosity, and  $p^*$  is the hydrodynamic pressure equal to  $p^* = p + \rho g z$  where  $p$  is the absolute pressure,  $z$  is the vertical coordinate, and  $g$  is the acceleration of gravity. These equations combined with suitable boundary conditions describe the motion of the fluid flow. The interface between air and water is track using the Volume Of Fluid (VOF) method. The numerical domain is presented in figure 5.2 and the boundary conditions are summarized in table 5.1.

	Alpha ( $\alpha$ )	Pressure ( $p$ )	Velocity ( $U$ )
<b>Atmosphere</b>	inletOutlet	totalPressure 0	Pressure Inlet Outlet Velocity
<b>Bottom</b>	zeroGradient	fixedFluxPressure	Fixed Value 0
<b>Front/back</b>	wedge	wedge	wedge
<b>Inlet</b>	empty	empty	empty
<b>Outlet</b>	zeroGradient	fixedFluxPressure	Fixed Value 0
<b>Structure</b>	zeroGradient	fixedFluxPressure	Moving wall velocity
<b>Overset boudaries</b>	overset	overset	overset

TABLE 5.1: Description of the boundary conditions for volume fraction, pressure and velocity

The inletOutlet condition ensures that  $\alpha = 0$  in case of return flow. The fixedFluxPressure boundary condition sets the pressure to ensure that the flux on the boundary is as defined in the velocity boundary condition. The totalPressure boundary condition sets the pressure to 0 at the atmospheric boundary.

### 5.1.2.2 Numerical inputs

Table 5.2 summarizes the numerical schemes used in all the simulations. The same schemes have been used in [144]. The time-step is adaptive in all the simulations and determined based on the condition that the maximum Courant number is equal to 1.

Time scheme	Backward Euler: first order
Gradient scheme	Gauss linear
Divergence scheme	$\rho \underline{u} \cdot \nabla \underline{u}$ : Gauss linear $\nabla(u\alpha)$ : Gauss van Leer $\nabla(u_r \alpha(1 - \alpha))$ : Gauss linear
Laplacian scheme	Gauss linear corrected
Overset Interpolation	Inverse Distance

TABLE 5.2: Numerical schemes used in the CFD model

Although [121] and [139] suggested that turbulence effects might be observed, only laminar flow is considered in this analysis (no turbulence models have been used). In the case of the isolated disk, the boundary layer at either side of the disk is oscillatory. From figure 10 in [118], the maximum oscillatory velocity of the outer flow, by the

edge of the disk, occurs at a period of 1.4 s and can be evaluated as  $U_{0m} \approx 9A\omega$ . Following Jensen et al. [145], an oscillatory Reynolds number can be defined for such situations:

$$Re_o = \frac{U_{0m}^2}{\omega\nu} = \frac{81A^2\omega}{\nu}. \quad (5.11)$$

Here, it reaches  $Re_o \sim 8.2 \cdot 10^4$ , for  $A = 0.015$  m and at  $T = 1.4$  s, indicating the boundary layer remains laminar (see e.g. [145]). It is thus considered that turbulence only comes into play for the disintegration of the vortices shed from the disk edge, and has a minor effect on the loads. In the case of the disk and column, the oscillatory Reynolds number is even lower, so the boundary layer is also expected to remain laminar.

### 5.1.3 Overset mesh method

The main objective of this work is to validate the use of the overset mesh tool available in OpenFOAM® to model the dynamics of the structure and induced flow. This technique has great advantages. First, there is no need of mesh deformation or remeshing in comparison to other methods for moving bodies. It maintains the same mesh quality all over the simulation. This is very appealing for large body motions or complex geometries as it is usually the case for FOWT. In this method two meshes are generated: one fixed mesh of the background domain and one fitted moving mesh attached to the moving body. These two meshes are overlapping as shown in Figure 5.2.

Two boundaries are defined by the tool: one boundary close to the body wall and a second boundary at the external limit of the fitted mesh. The interpolation of the variables of interest (pressure, velocity, water/air fraction) occurs at these two boundaries. The position of the body is updated based on the prescribed motion. The process is repeated at each time step. More information on the overset method can be found in [85] or [144].

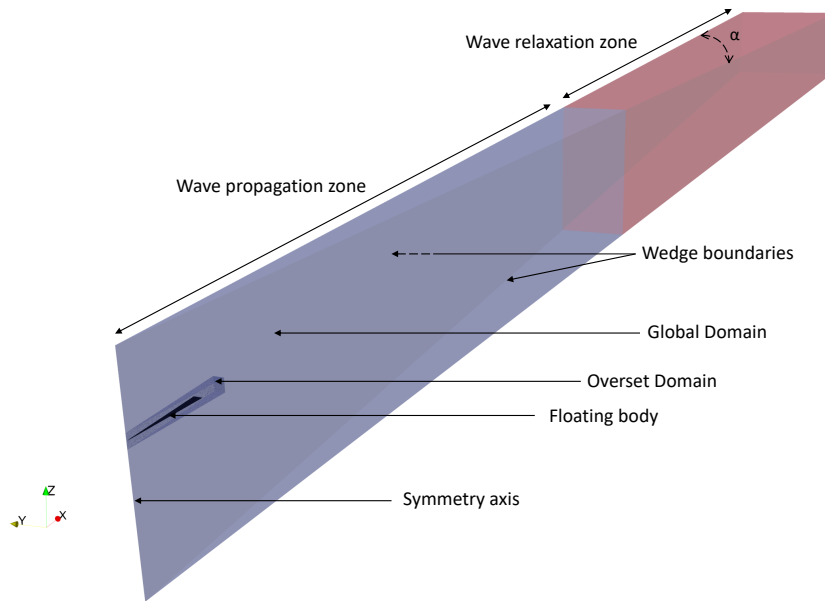


FIGURE 5.2: View of the wedge domain used in the CFD simulation using the axisymmetry of the problem. The propagation zone is in blue and the relaxation zone in red. The portion of the disk appears in black in the left part of the figure

### 5.1.4 Representation of a cylinder with a wedge section

To reduce the number of cells used in the CFD model, the axisymmetry of the structure and induced flow is considered. The simulations are run using the wedge boundary condition from OpenFOAM® with one cell in the orthoradial direction ( $\theta$ -axis). The mesh is extruded around a small angle. This angle should not be too small to avoid too thin cells near the symmetry edge that might affect the convergence of the computation. On the contrary, a too large angle might affect the accuracy of the results when extrapolated to full structure. Figure 5.3 shows that an angle of  $0.1^\circ$ ,  $1^\circ$ , or  $5^\circ$  does not affect much the results. However, it is advised not to exceed  $5^\circ$ <sup>1</sup>, and so this value of  $5^\circ$  is chosen throughout this work. The vertical force is calculated on this small portion of the disk and extrapolated to get the total force on the entire disk.

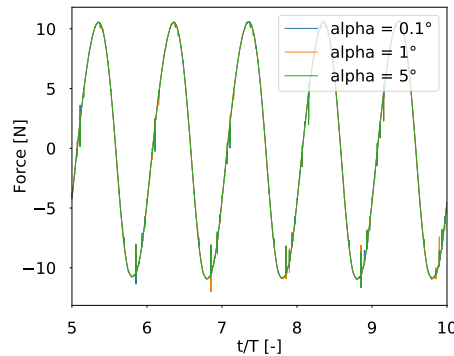


FIGURE 5.3: Time series of the vertical force on the full disk for 3 wedge angles,  $A = 0.005$  m,  $T = 2$  s,  $d = 0.05$  m ( $d/D = 1/12$ ,  $kR = 0.47$ ,  $KC = 0.052$ )

The dimension of the cells in the  $\theta$ -direction increases with the distance from the center of the disk. The wedge boundary conditions reflect this variation of cell size when computing the flow variables in each cell.

### 5.1.5 Wave relaxation with waves2Foam

When the disk oscillates close to the free surface, it generates radiated waves of significant amplitude. These waves are analyzed in this study. The tool waves2foam [49] is used to guarantee that reflected waves from the external boundary of the finite domain do not impact the results on the structure. Wave relaxation zones are defined in the domain as shown in Figure 5.2. The choice of the length of these zones depends on the length of the waves. To compute the wavelength we consider that the radiated wave has the same period as the oscillation period of the body  $T$ . In this study, a distance of two wavelengths is used for this relaxation zone. It has been shown to provide sufficient absorption of radiated waves [144].

### 5.1.6 Computation of hydrodynamic coefficients

This section describes the method used to compute the hydrodynamic coefficients. In the case of a cylindrical structure having a vertical axis of symmetry forced to oscillate harmonically in heave, the vertical force acting on the structure can be written as the sum of two terms, namely the external mechanical excitation force, denoted  $F_e(t)$ ,

<sup>1</sup><https://www.openfoam.com/documentation/user-guide/4-mesh-generation-and-conversion/4.2-boundaries>

necessary to move the structure with the prescribed dynamics, and the force exerted by the fluid on the structure, denoted  $F_f(t)$ . The second Newton's law applied to the structure then gives, denoting  $M$  the mass of the structure:

$$M\ddot{z}(t) = F_e(t) + F_f(t). \quad (5.12)$$

In the experiments of [118] the fluid force was obtained as  $F_f(t) = M\ddot{z}(t) - F_e(t)$  using the imposed body acceleration and the measured excitation force. In the present simulations,  $F_f(t)$  is obtained by a numerical integration of the stress exerted by the fluid on the whole structure boundary.

This fluid force is then decomposed as the sum of three contributions:

$$F_f(t) = F_k(t) + F_a(t) + F_b(t), \quad (5.13)$$

where:

- $F_k(t)$  is the hydrostatic restoring force, present when the immersed volume of the structure varies in time (here, this force is present only in the disk+column case). It is in phase with the vertical position of the structure and expressed as  $F_k(t) = -K_{33}z(t)$ , where the hydrostatic stiffness is given by  $K_{33} = \rho S_0 g$  where  $S_0$  the waterplane area of the structure,
- $F_a(t)$  is the added mass force, in phase opposition with the acceleration, written as  $F_a(t) = -A_{33}\ddot{z}(t)$ , where  $A_{33}(\omega)$  is the added mass of the system in heave motion,
- $F_b(t)$  is a damping force, assumed in phase opposition with the velocity, written as  $F_b(t) = -B_{33}\dot{z}(t)$ . Here,  $B_{33}(\omega)$  is the linear damping term, including both the radiation damping (due to radiation of surface waves propagating away from the structure) and a linearized drag component. This drag component is based on a linearization of the drag component of the Morison-like force:

$$F_d(t) = -\frac{1}{2}\rho C_d S w(t)|w(t)| \approx -\frac{4}{3\pi}\rho C_d S A \omega \dot{z}(t) = -B_d \dot{z}(t), \quad (5.14)$$

where  $w(t)$  is the velocity,  $S$  is the projected area of the structure onto the plane normal to the direction of motion (thus corresponding here to the area of the disk), and  $C_d$  is the drag coefficient. In equation 5.14 we have used the approximation  $\sin \theta |\sin \theta| \approx \frac{8}{3\pi} \sin \theta$ , noting this coefficient  $\frac{8}{3\pi}$  allows to get the same power for the original and linearized expressions of the drag force, when averaged over an integer number of oscillation periods.

In the following, we focus of attention to the so-called hydrodynamic vertical force, simply denoted  $F(t)$ , defined as the sum of the added mass and damping components of the fluid force:

$$F(t) = F_a(t) + F_b(t) = F_f(t) - F_k(t) = M\ddot{z}(t) - F_e(t) - F_k(t). \quad (5.15)$$

From the time series of the computed hydrodynamic force, the amplitude and the phase of the first harmonic are extracted using a Fourier analysis. To improve the accuracy of the results, the Fourier averaging analysis was run on a sliding window of  $3T$  over steady state periods of simulation to remove the transient state. The first harmonic  $F_1(t)$  of the hydrodynamic force can then be expressed as:

$$F_1(t) = A_F e^{i(\omega t + \phi_F)}, \quad (5.16)$$

where  $A_F$  is the amplitude of the force and  $\phi_F$  is the phase difference between the first harmonic of the force and the heave position. If considering only the first order, equation 5.15 can be written as:

$$F_1(t) = -A_{33}\ddot{z}(t) - B_{33}\dot{z}(t). \quad (5.17)$$

By inserting equations 5.7, 5.8 and 5.16 in equation 5.17, and separating the real and imaginary parts, the added mass and the damping term can be calculated as:

$$A_{33} = \frac{A_F \cos \phi_F}{\omega^2}, \quad (5.18)$$

and

$$B_{33} = -\frac{A_F \sin \phi_F}{\omega}. \quad (5.19)$$

Non-dimensional added mass ( $C_a$ ) and damping ( $C_b$ ) coefficients can be introduced. In the case of the simple disk of radius  $R$ , one can use:

$$C_a = \frac{A_{33}}{\frac{8}{3}\rho R^3}, \quad (5.20)$$

and

$$C_b = \frac{B_{33}}{\frac{8}{3}\omega\rho R^3}, \quad (5.21)$$

noting that  $8/3\rho R^3$  is the theoretical added mass in an unbounded fluid domain [118].

In the case of the disk at the bottom of a vertical cylinder, Thiagarajan et al. [119] used an approximation of the theoretical added mass for this specific structure. In their work, the hydrodynamic coefficients are expressed as:

$$C_a = \frac{A_{33}}{\frac{1}{12}\rho(D^3 + 3D^2D_e - D_e^3 - 3D_c^2D_e)}, \quad (5.22)$$

and

$$C_b = \frac{B_{33}}{\omega\frac{1}{12}\rho(D^3 + 3D^2D_e - D_e^3 - 3D_c^2D_e)}, \quad (5.23)$$

where  $D_e = \sqrt{D^2 - D_c^2}$ .

In this study, the definitions (5.20-5.21) are used for the case of the disk only while the definitions (5.22-5.23) are used for the case of disk+column.

## 5.2 Case of an isolated disk

In this study, the forced heave motion of a solid disk is analyzed at two submergence depths. This section describes first the experimental setup of [118] and the CFD model used in this work, and then presents the results for the two considered cases.

### 5.2.1 Experimental model

The experimental campaign used as a reference in this study was carried out in the BGO-FIRST offshore wave tank in La Seyne sur Mer (France). The results are presented in [118]. The tank has a width of 16 m and a length of 40 m. The water depth was  $h = 0.5$  m. The disk used had a radius  $R = 0.3$  m and a thickness  $e = 0.001$  m. Radial stiffeners were added on top of the disk to guarantee its rigidity. Rigidity tests

were carried out by Molin et al. in [118] and showed satisfactory results. A picture of the disk can be seen in Figure 5.4. Two submergence depths were tested, namely  $d = 0.05$  m and 0.25 m beneath the free surface level at rest. Periods from 0.6 s to 2 s with 0.1 s increment were tested. The amplitudes of oscillation tested were  $A = 0.003$ , 0.005, 0.01 and 0.015 m. In this work, only the amplitudes of 0.005 and 0.015 m are considered.

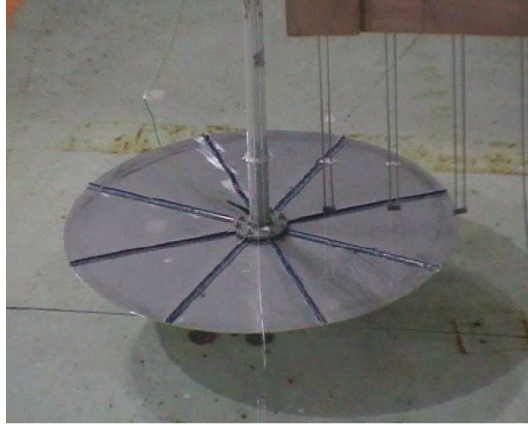


FIGURE 5.4: Solid disk used in the experiments of [118]

The excitation force on the disk was measured with a force sensor located between the jack and the axial rod. Wave probes were also used to capture the free surface elevation at radial distances of 0.1, 0.2, 0.3, 0.4, and 0.5 m from the center of the disk.

### 5.2.2 Mesh generation of the CFD model

Figure 5.5 gives a global description of the mesh in the vertical plane. The meshing method is similar to the one used in [144]. As described previously, two meshes need to be generated for the overset mesh technique. In the background mesh, two refinement zones are used: one zone close to the free surface and one zone where the overset grid is expected to move. Water jets have been observed experimentally and numerically at large oscillation periods (figures A.1 and A.2), therefore the refined box has been extended above the moving zone of the disk to capture these jets. All the cells have a squared shape in the vertical plane. The size of the cells in these refinement zones is the same, and is discussed below. In the overset grid (in red in Figure 5.5), the size of cells far from the structure and near the external boundary is the same as the size of the cell of the refined zones. The mesh in the vicinity of the disk is refined to better capture its geometry.

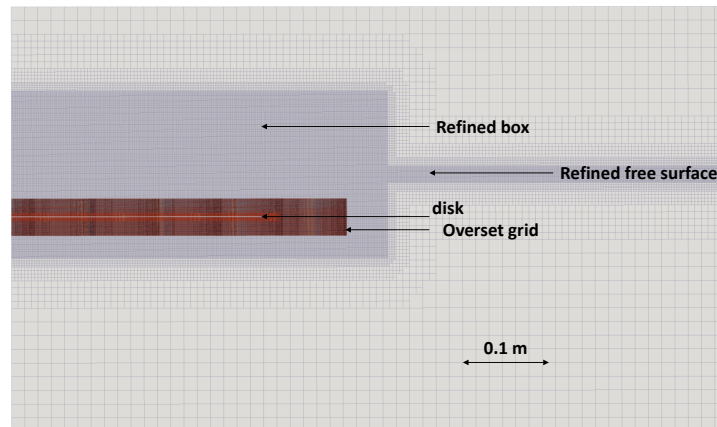


FIGURE 5.5: Global mesh of the model of the disk only. The background mesh is in blue and the overset mesh is in red,  $d = 0.05$  m ( $d/D = 1/12$ )

The dimension of the cells in the refinement zones is calibrated in terms of the number of cells per amplitude of disk oscillation. The same mesh is used in all the cases of this study and the smallest amplitude analyzed ( $A_{min} = 0.005$  m) is considered. Two grid sizes have been tested: one case with 5 cells per  $A_{min}$  (figure 5.6a) and one case with 10 cells per  $A_{min}$  (figure 5.6b). Figure 5.7 shows the time series of the forces for these two meshes for the case controlling the mesh size where  $A = A_{min} = 0.005$  m,  $T = 2$  s,  $KC = 0.052$  and  $d = 0.05$  m. All the other parameters are the same. It can be seen that the results are very close.

The number of cells in the case of 10 cells per  $A_{min}$  is considerably higher (1 436 588 cells) than in the case of 5 cells per  $A_{min}$  (342 875 cells) and so is the computational time. In Figure 5.7 the computation with 10 cells per  $A_{min}$  was intentionally stopped after 3  $T$  because of excessive computing resources. Therefore, 5 cells per  $A_{min}$  are used in all the cases of this study. The dimension of the cell side is thus fixed:  $\delta_x = \delta_z = 0.001$  m.

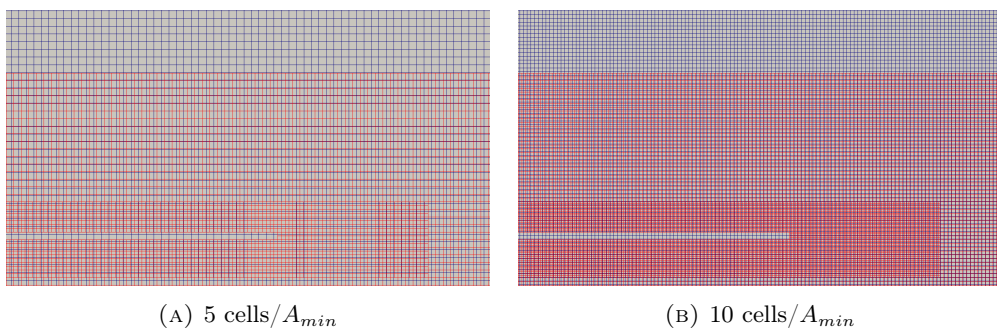


FIGURE 5.6: Global mesh refinement. The cell size is defined by a number of cells per amplitude of vertical motion, considering the minimum value of this amplitude namely  $A_{min} = 0.005$  m.

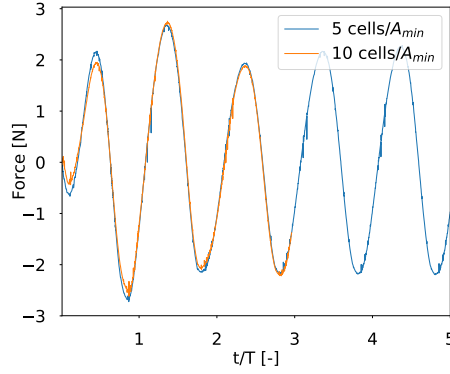


FIGURE 5.7: Time series of the vertical force for two refinements of the global mesh,  $A = 0.005$  m,  $T = 2$  s,  $d = 0.05$  m ( $d/D = 1/12$ ,  $kR = 0.47$ ,  $KC = 0.052$ )

The mesh is also refined close to the disk to better capture the flow in its vicinity. The level refinement method from the built-in meshing module SnappyHexMesh is used. In this method, a first global mesh is generated. When the level increases by 1, the cell size is divided by 2 in all directions. Two different refinement levels near the wall of the disk have been compared. One case with a level 1 (figure 5.8a) and one case with a level 4 (figure 5.8b). The time series of the force of these two cases are compared in figure 5.9 for the size limiting case where  $A = 0.005$  m,  $T = 2$  s,  $KC = 0.052$  and  $d = 0.05$  m. Both results are very similar, showing that the refinement level has a low impact on the global results. The small spikes that appear in the force time-series are not physical and seem to be caused by the overset mesh interpolation (as also observed in [90]). The spikes can be mitigated by refining the mesh near the disk. In figure 5.8, it can be seen that the spikes are reduced when the refinement level is increased. Nevertheless, the spikes do not influence the hydrodynamic coefficients that are integrated values. So, to reduce the computational time, level 1 of refinement has been used for this work.

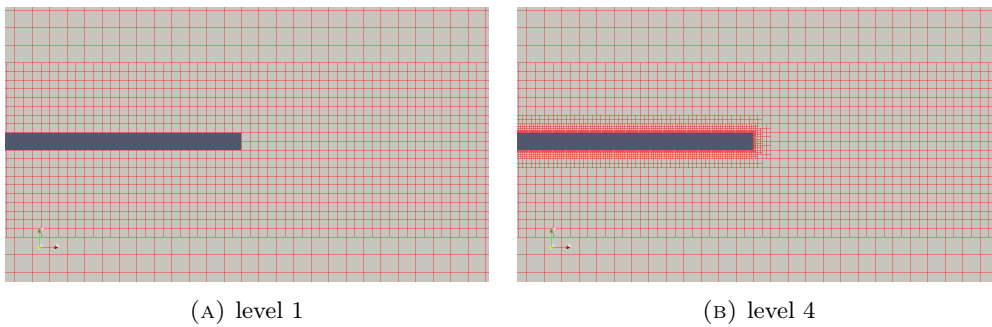


FIGURE 5.8: Level refinement at the disk vicinity

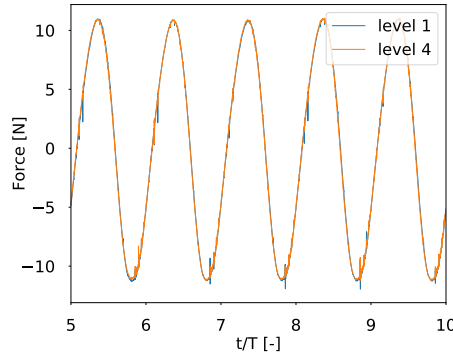


FIGURE 5.9: Time series of the force for two different refinement levels in the disk vicinity,  $A = 0.005$  m,  $T = 2$  s,  $d = 0.05$  m ( $d/D = 1/12$ ,  $kR = 0.47$ ,  $KC = 0.052$ )

Far from the disk, in the background mesh, where the variation of pressure and velocity are small, an expansion ratio has been used to reduce the number of cells.

Finally, the mesh used for all the cases of this study has a wedge shape with square cells in the vertical plane. Minimum 5 cells per amplitude are used in the vertical plane. A level 1 of refinement is used close to the disk, so the cells are 2 times smaller than in the refinement zones (box and free surface). In total, the mesh is composed of 342 875 cells.

### 5.2.3 Immersion $d = 0.05$ m ( $d/D = 1/12$ )

The disk at the smallest submergence depth  $d = 0.05$  m is first considered.

#### 5.2.3.1 Comparison of time series of vertical load on the disk and radiated waves

In this section, the time series of the CFD results are compared with the experimental time series measured in [118]. Three amplitudes of motion and two periods of oscillation are presented in Figures 5.10, 5.11 and 5.12. The vertical position of the disk, the total force on the disk normalized as :

$$C_F = \frac{F_f}{\rho g \pi R^2 A}, \quad (5.24)$$

and the free surface elevation  $\eta$  normalized by  $A$  at 0.2 m from the edge of the disk (i.e. 0.50 m from the axis of the disk) are compared. The transient state has been removed from the CFD results and the experimental results. However, the transient state was not the same between CFD and experiment. In the case of the CFD model, the first 5 periods have been removed. In the experimental model, the periods have been selected after the steady-state was reached and before the reflected wave from the side-walls of the tank could reach the disk. In both cases, a zero up-crossing of the disk position is considered as the beginning so that the phase difference of the force and the free surface elevation can be compared. The time is normalized by the period of oscillation and the vertical position is normalized by the amplitude of oscillation.

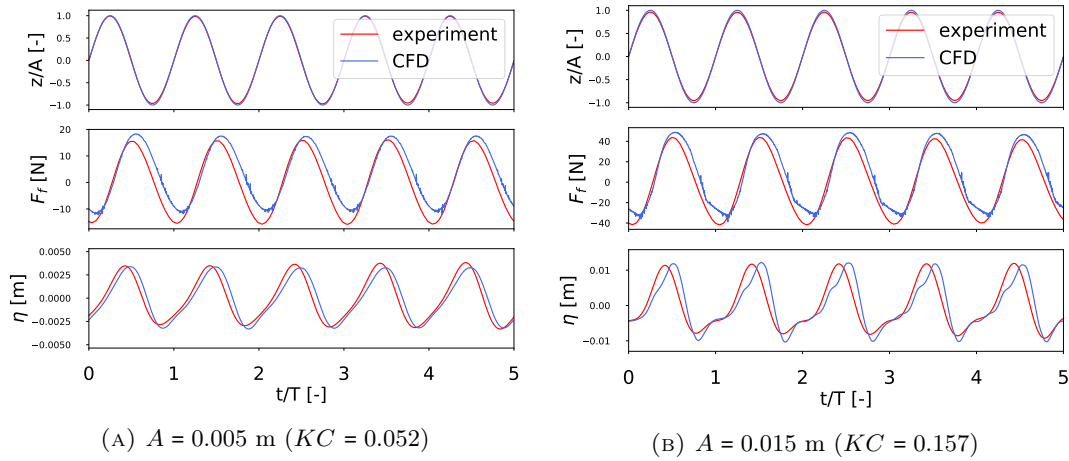


FIGURE 5.10: Time series of the position normalized by the amplitude of motion (top),  $C_F$ , and the free surface elevation  $\eta$  normalized by  $A$  at 0.20 m from the edge of the disk (bottom) for two amplitudes of oscillation. The red line is the experimental result [118] and the blue line is the CFD result.  $T = 1.1$  s,  $d = 0.05$  m ( $d/D = 1/12$ ,  $kR = 1.06$ )

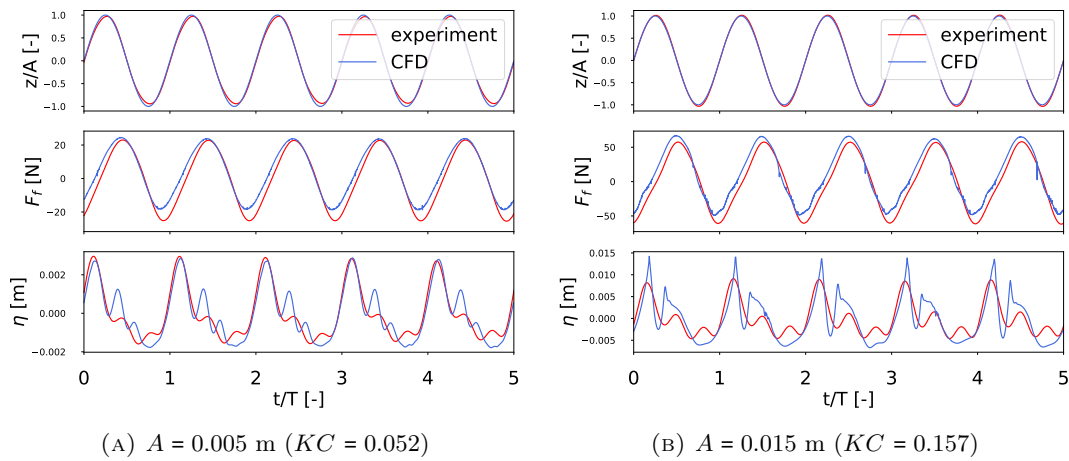


FIGURE 5.11: Time series of the position normalized by the amplitude of motion (top),  $C_F$ , and the free surface elevation  $\eta$  normalized by  $A$  at 0.20 m from the edge of the disk (bottom) for two amplitudes of oscillation. The red line is the experimental result [118] and the blue line is the CFD result.  $T = 1.6$  s,  $d = 0.05$  m ( $d/D = 1/12$ ,  $kR = 0.61$ )

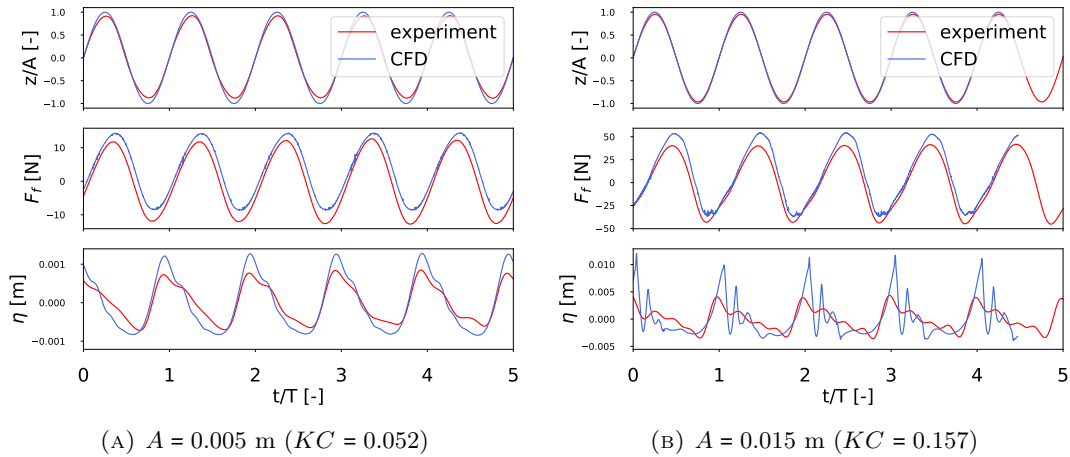


FIGURE 5.12: Time series of the position normalized by the amplitude of motion (top),  $C_F$ , and the free surface elevation  $\eta$  normalized by  $A$  at 0.20 m from the edge of the disk (bottom) for two amplitudes of oscillation. The red line is the experimental result [118] and the blue line is the CFD result  $T = 2$  s,  $d = 0.05$  m ( $d/D = 1/12$ ,  $kR = 0.47$ )

Globally, the CFD model results agree with the experimental measurements. The force amplitude and phase are well calculated by the CFD model, no matter the amplitude or the period of oscillation. The free surface elevation is well captured for the lowest period  $T = 1.1$  s (figures 5.10a and 5.10b). As the period increases, the free surface becomes highly nonlinear (figures 5.11 and 5.12). Note that for the larger amplitude of motion ( $A = 0.015$  m), the total vertical excursion of the disk is 0.03 m which is large in comparison with the submergence depth ( $d = 0.05$  m). As a consequence, free surface effects are highly nonlinear and water jets occur experimentally and numerically. It makes the comparison more difficult. However, the phase difference remains similar. It also seems that the first orders of the response are well captured by the CFD model. Response Amplitude Operators (RAO) of the free surface are discussed in 5.2.3.3. It should be noted that both the force and the free surface elevation increase with the amplitude of oscillation (comparing panels (a) and (b) in figures 5.10, 5.11 and 5.12). Also, the force and the free surface elevation are maximum for  $T = 1.6$  s.

### 5.2.3.2 Comparison of the hydrodynamic coefficients

Based on the theory described in 5.1.6, the hydrodynamic coefficients  $C_a$  and  $C_b$  are calculated and compared with the experimental results. On the numerical results, the sliding window for the Fourier averaging analysis has been done on 5 periods. The first 5 periods of the simulations are removed to avoid the transient state. Figure 5.13 compares the added mass coefficient of the CFD model with the experimental results. In addition, numerical results of the radiation problem from [118], using the potential flow theory only are plotted. The coefficients are compared for different values of  $kR$  by modifying  $T$ , and 2 amplitudes 0.005 m and 0.015 m. These amplitudes correspond to  $KC = 0.052$  and  $KC = 0.157$  respectively.

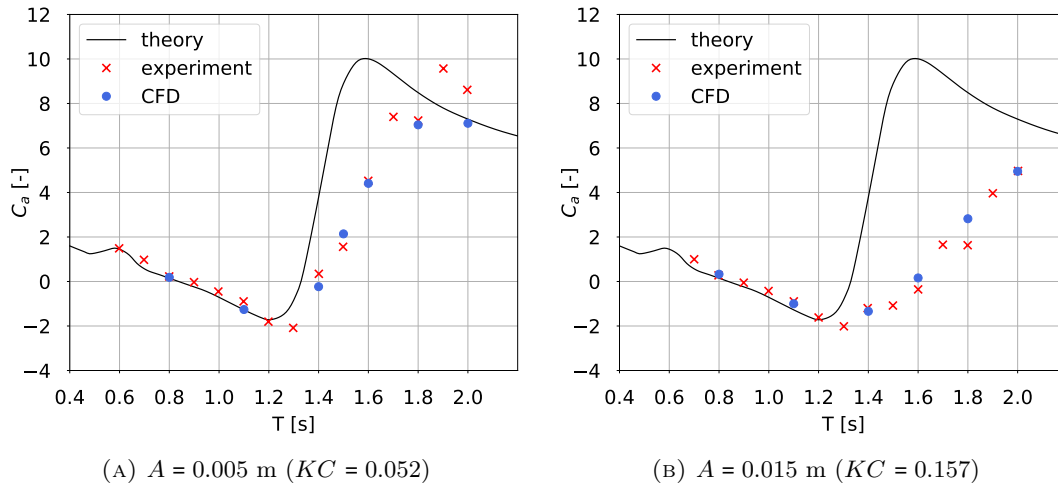


FIGURE 5.13: Added mass coefficients for two amplitudes of oscillation at different value of  $kR$  (modifying  $T$ ). The black line is the theoretical result of the LPFM [118], the red crosses are the experimental results [118] and the blue dots are the CFD results.  $d = 0.05$  m ( $d/D = 1/12$ )

It can be noted that the added mass coefficients computed with the CFD model can reproduce the results measured experimentally for both amplitudes. At lower periods (larger  $kR$ ), the CFD and experimental results are in good agreement with the theoretical values from [118], and the coefficients do not depend markedly on the amplitude. However, as the period increases, the theoretical model from [118] deviates from the experimental results whereas the CFD results match well. Moreover, the added mass coefficient depends largely on the amplitude of oscillation. It is interesting to note that CFD also shows negative values of the added mass for  $kR$  between 0.8 and 1.5 as predicted by the theoretical approach [118]. Martin and Farina [146] proposed an alternative numerical model to analyse this problem and also found a negative added mass coefficient for a certain range of period. The negative added mass, when considering a body close to the free surface, is also observed in [147] and [148]. Figure 5.14 compares the damping coefficient of the CFD model, the experimental results, and the theoretical model.

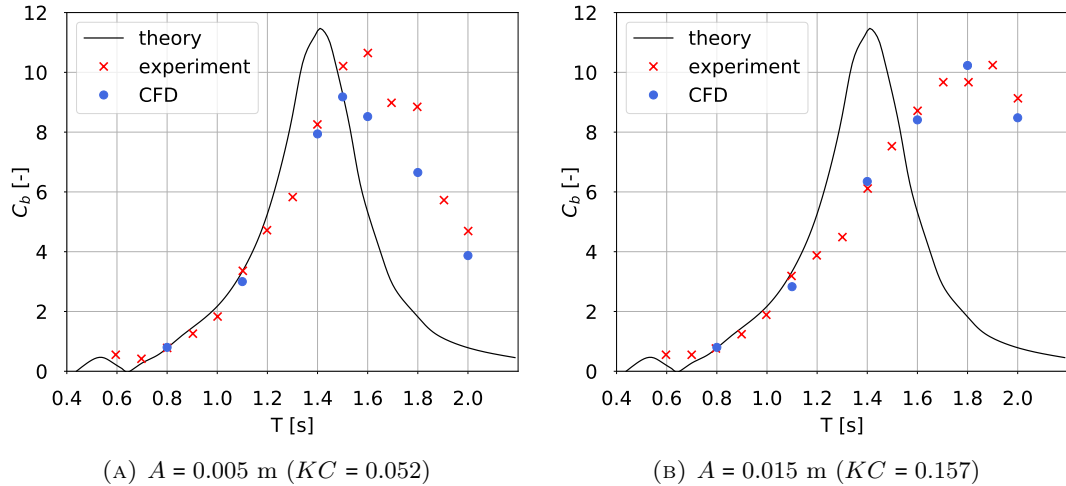


FIGURE 5.14: Damping coefficients for two amplitudes of oscillation at different value of  $kR$  (modifying  $T$ ). The black line is the theoretical result of the LPFM [118], the red crosses are the experimental results [118] and the blue dots are the CFD results.  $d = 0.05$  m ( $d/D = 1/12$ )

The damping coefficients computed with the CFD model are very close to the experimental results. In the same way as for  $C_a$ , the damping coefficients from CFD and experiments follow the theoretical results at small periods (large  $kR$ ) and do not depend on the amplitude of oscillation. For smaller  $kR$  or higher periods ( $T \geq 1.2$  s), the theoretical model fails to predict the damping coefficient compared with both experimental and CFD results for both amplitudes. It should be noted that a peak occurs in the damping coefficient for  $kR = 0.61$  to  $0.67$  ( $T = 1.6$  to  $1.5$  s) when  $A = 0.005$  m, and for  $kR = 0.5$  ( $T = 1.8$  s) when  $A = 0.015$  m. This confirms what was observed on the time series of the vertical force in Figures 5.10, 5.11 and 5.12.

### 5.2.3.3 Comparisons of the RAOs of the free surface elevation

The radiated wave generated from the oscillation of the disk is investigated. The modulus and phase of the RAO of the free surface elevation at 0.20 m from the edge of the disk are analyzed. The CFD results are compared with the experimental data and the theoretical results from [118]. Similarly to the hydrodynamic coefficients, a Fourier averaging analysis has been carried out on the time series of surface elevation. A sliding window of 3 periods has been considered in both the CFD and experimental results after discarding the transient state in the same way as described for the hydrodynamic coefficients. Again, 2 amplitudes of oscillation of the disk are considered.

Figure 5.15 compares the modulus of the RAO of the first order of the surface elevation for different periods

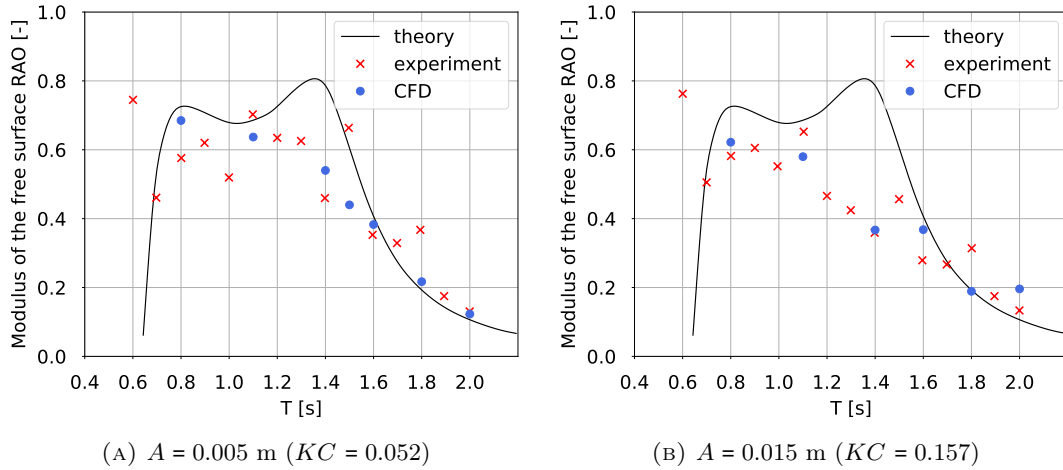


FIGURE 5.15: Modulus of the RAO of the free surface, 0.20 m from the edge of the disk, for two amplitudes of oscillation, at different value of  $kR$  (modifying  $T$ ). The black line is the theoretical result of the LPFM [118], the red crosses are the experimental results [118] and the blue dots are the CFD results.  $d = 0.05 \text{ m}$  ( $d/D = 1/12$ )

The agreement of the CFD results and the experimental values is good for both amplitudes of oscillation. The theoretical model predicts rather well the results for higher periods, but reveals some discrepancies at periods lower than 1.6 s.

Figure 5.16 compares the phase of the RAO of the first order of the surface elevation for different periods. The trend of the CFD results follows the experimental data for both amplitudes of oscillation.

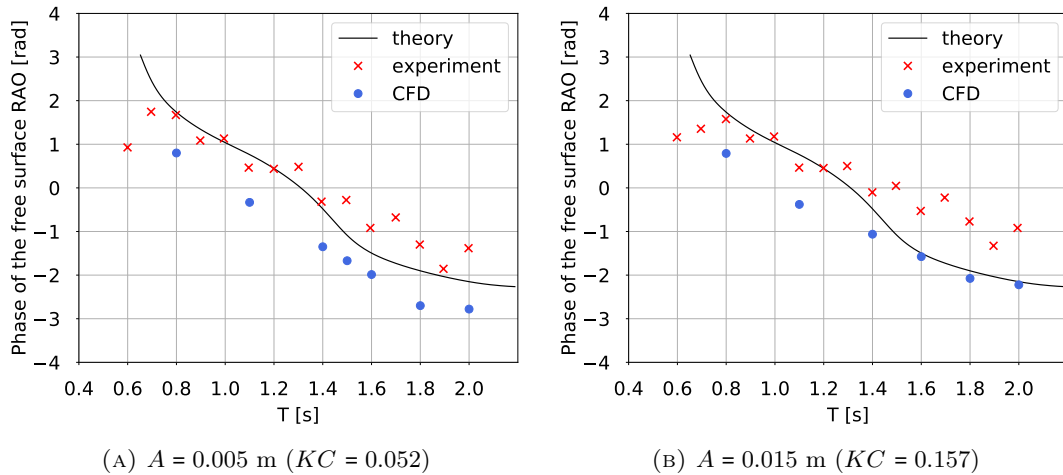


FIGURE 5.16: Phase of the RAO of the free surface, 0.20 m from the edge of the disk, for two amplitudes of oscillation, at different values of  $kR$  (modifying  $T$ ). The black line is the theoretical result of the LPFM [118], the red crosses are the experimental results [118] and the blue dots are the CFD results.  $d = 0.05 \text{ m}$  ( $d/D = 1/12$ )

### 5.2.3.4 Interactions between vortices and free surface

As described in [121], vortices are generated at the edge of the disk, and are dissipated away from the disk and at the free surface. When the amplitude is large and the disk is excited near the frequency at which the force is maximum (as shown on the time

series in figure 5.11), water jets appear above the disk. Figure 5.17 shows the free surface and the contour of the transverse vorticity (around  $y$ -axis) during one period, for a disk oscillating at a period  $T = 1.6$  s and an amplitude  $A = 0.015$  m. This case corresponds to the case with the largest force acting on the disk. The disk and the vorticity field are mirrored to ease the visualization.

$t_0$  corresponds to the highest position of the disk, and  $t_0 + 0.25T$  corresponds to its lowest position. When the disk is moving upwards, a positive vortex is generated at the bottom edge of the disk, starting at  $t_0 + 0.75T$  (in red). The vortex increases and stays attached to the edge until the disk reaches its highest position ( $t_0$ ). Then, the vortex detaches from the disk when the disk starts to go down. Another vortex is generated above the disk, circulating in the opposite sense (in blue). Both these vortices lose magnitude and travel toward the free surface ( $t_0 + 0.4T$ ). The vortices are dissipated at the surface and impact the radiated waves that travel toward the center of the disk. Because of the symmetry of the problem, a jet is generated at the center of the disk ( $t_0 + 0.45T$ ). In this specific case, the wave breaks ( $t_0 + 0.5T$ ) as it travels away from the disk. A 3D extrapolation of the free surface for this same case is presented in the figures A.1 and A.2 in the Appendix, and compared to pictures taken during the experiments. The water jet can be identified on both experimental (panel A.2i) and CFD results (panel A.2j).

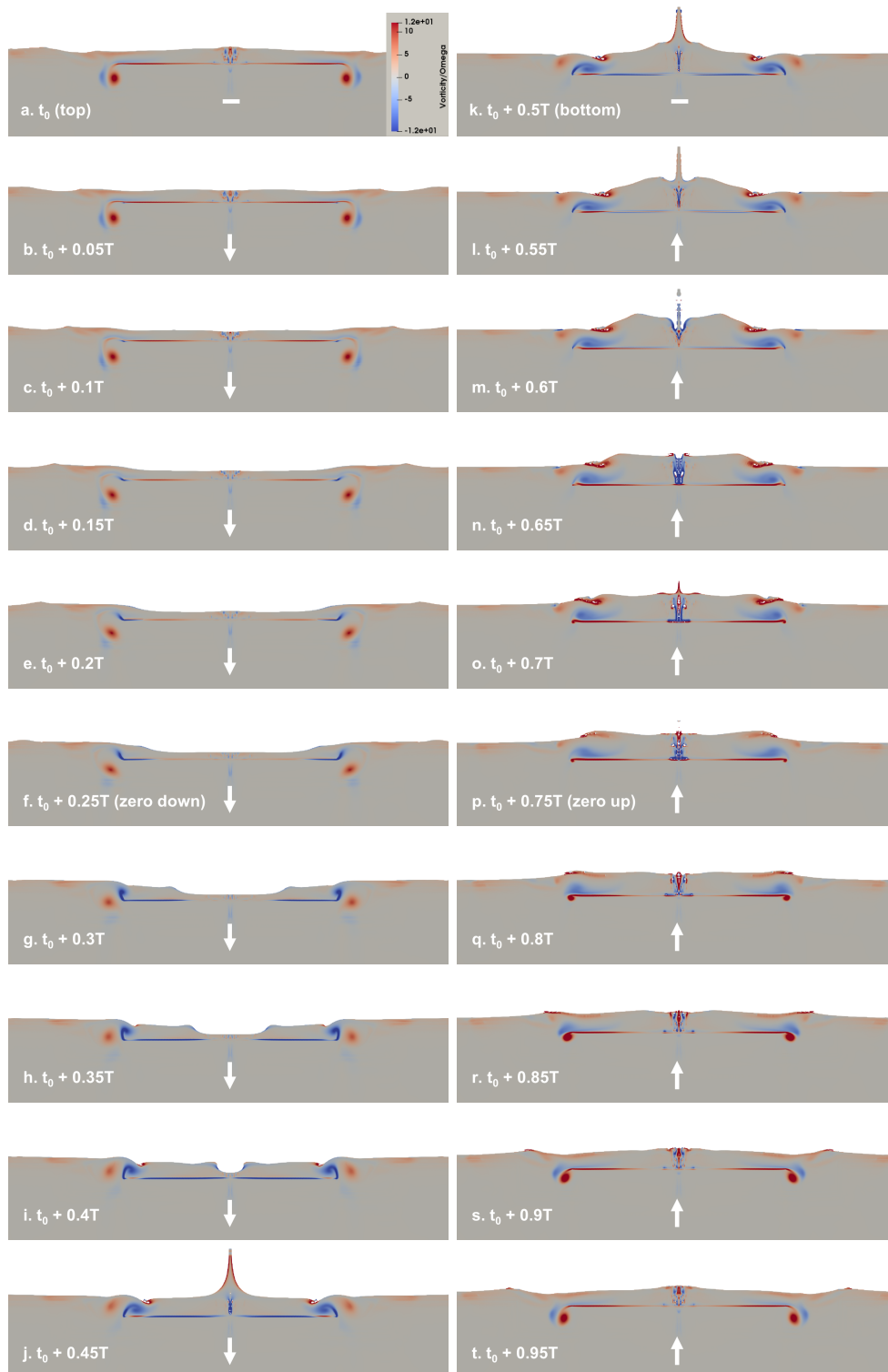


FIGURE 5.17: vorticity/ $\omega$  induced by the vertical motion of the disk only (left : downward, right upward).  $A = 0.015$  m,  $T = 1.6$  s,  $d = 0.05$  m ( $d/D = 1/12$ ,  $kR = 0.61$ ,  $KC = 0.157$ )

#### 5.2.4 Immersion $d = 0.25$ m ( $d/D = 5/12$ )

The same disk at a submergence depth of 0.25 m is now considered. It corresponds to the midway position between the free surface and the bottom of the tank. Computations were performed for various amplitudes of oscillation at three different periods. The same method as the previous case has been used, but the refinement zone of the mesh has been adapted at the new position of the disk. The added mass and damping coefficients are compared with the experimental values from [118]. Figures 5.18 and 5.19 show a comparison between the CFD results, the experimental values and the theoretical values of the added mass and damping coefficients. In Figure 5.18, the theoretical added mass is the result of the potential theory. In Figure 5.19, the theoretical results for the damping are based on an approach proposed in [118]. In this approach, a viscous force based on an empirical assessment of the drag coefficient is added to the potential model. The supplementary damping coefficient is given by  $\Delta C_b = \frac{4}{3}C_d \frac{A}{R}$ . The drag coefficient is taken by Molin et al. [118] as  $C_d = \alpha KC^{-1/3}$  where  $\alpha$  is a coefficient determined by the authors to fit the experimental results. The value of  $\alpha$  depends on the period of oscillation.

Figure 5.18 shows that the CFD results overpredict the added mass coefficient. The gap between experimental results and numerical results increases with the period. The large amplitude of the oscillation and so of  $KC$  can explain the difference. The CFD model seems to be taking longer time to reach a steady state compared to the previous case. The same problem might have occurred during the experiments. However, the error is of the same order of magnitude as the error in the case close to the free surface. The potential theory results predict well the added mass for low amplitudes. An increase of  $C_a$  in the experimental and CFD models can be observed as the amplitude increases for the three periods. This increase is more marked for the larger period  $T = 1.6$  s. It means that nonlinear phenomena, not captured by the potential model, impact the added mass and that this impact increases with either amplitude or period. Some frequency dependence can also be observed that can be caused by interaction with the free surface or the sea bottom.

The CFD model evaluates well the damping coefficient for  $T = 0.8$  s (figure 5.19). The results are also good for larger periods as long as the amplitude remains below 0.04 m. For larger amplitude, the CFD model underpredicts the damping coefficient compared with the experimental values. However, the difference is limited and within the error range of the previous case. It should be noted that the theoretical model predicts well the damping coefficient for all periods and amplitudes. [118] underlines that the damping coefficient is mostly dominated by the drag force, the potential contribution (i.e. radiation damping) is small at this immersion of the disk.

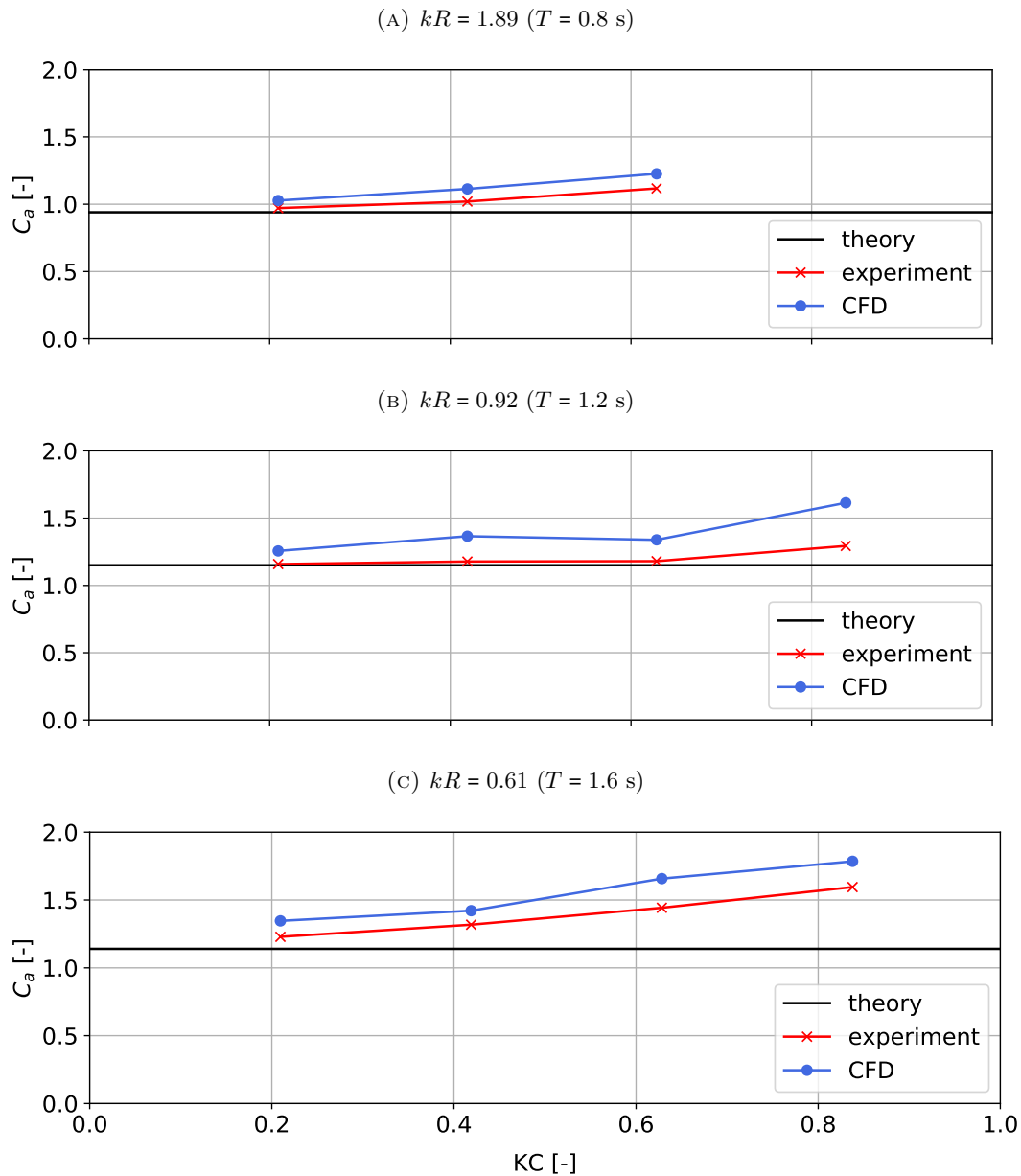


FIGURE 5.18: Added mass coefficients for different amplitudes and for three periods of oscillation. The black line is the theoretical result of the LPFM [118], The red crosses are the experimental results of the LPFM [118], and the blue dots are the CFD results.  $d = 0.25$  m ( $d/D = 5/12$ )

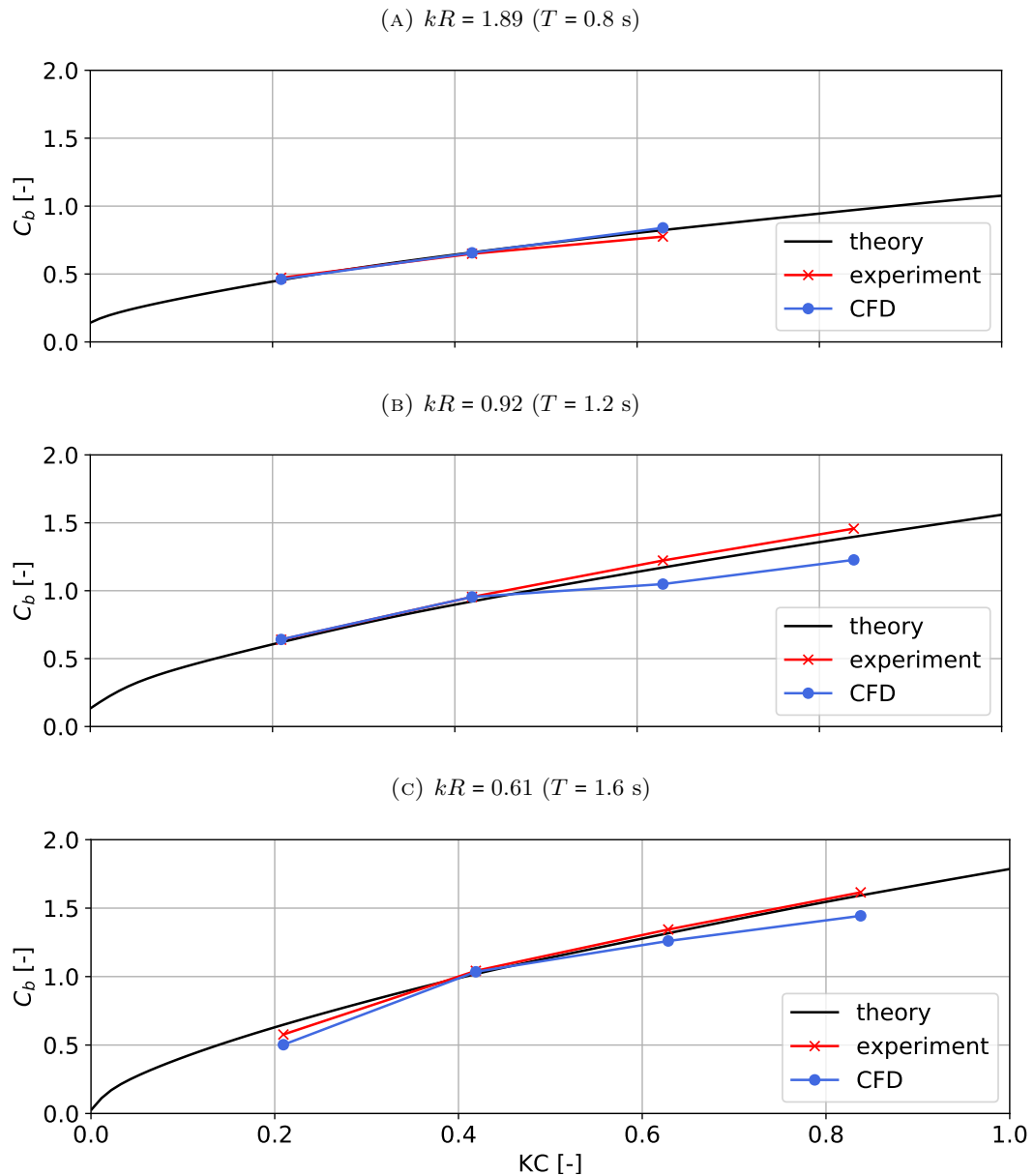


FIGURE 5.19: Damping coefficients for different amplitudes and for three periods. The black line is the theoretical result of the LPFM + empirical correction [118], The red crosses are the experimental results [118], and the blue dots are the CFD results.  $d = 0.25$  m ( $d/D = 5/12$ )

### 5.3 Case of disk at the bottom of a vertical cylindrical column

The case of the heave motion of a cylinder plus disk is now considered. A similar method to the disk only is used. The results computed with the CFD model are compared with experimental results from [119]. The influence of the  $KC$  number on hydrodynamic coefficients is investigated.

### 5.3.1 Description of the case

The geometry used in the experimental campaign [119] is described in Figure 5.1b. It is composed of a vertical cylinder of radius  $R_c = 0.044$  m and a circular heave plate of radius  $R = 0.125$  m at the bottom of the cylinder. The thickness of the plate is  $e = 0.043$  m and the draft of the structure is  $d = 0.25$  m. The water depth is  $h = 0.7$  m. Thiagarajan et al. [119] carried out experiments on the structure in still water with  $KC$  varying between 0.05 ( $A = 0.002$  m) and 1.2 ( $A = 0.048$  m) at a period  $T = 1$  s. They also conducted experiments in waves but these results are not used in the present work. The numerical schemes for the CFD model selected in the disk only model have also been used in this case. A similar method is applied to mesh the fluid domain. The minimum amplitude of oscillation considered in the CFD analysis  $A_{min} = 0.008$  m ( $KC = 0.2$ ) is used to calibrate the mesh sizing. A minimum of 5 cells per  $A_{min}$  have been used in the refinement zones and a level 1 of refinement has been implemented close to the structure. The cells in the zone of interest are squared and the dimensions in the refined zones are  $\delta_x = \delta_z = 0.0016$  m.

### 5.3.2 Results

#### 5.3.2.1 Hydrodynamic coefficients

The hydrodynamic coefficients  $C_a$  and  $C_b$  have been computed using the method described in section 5.1.6 and made non-dimensional using equations (5.22-5.23). It should be noted that Thiagarajan et al. [119] used a least squares method to compute the coefficients. Although the method used here is different, the results are expected to be similar. The comparisons of  $C_a$  and  $C_b$  for different values of  $KC$  are presented in Figure 5.20.

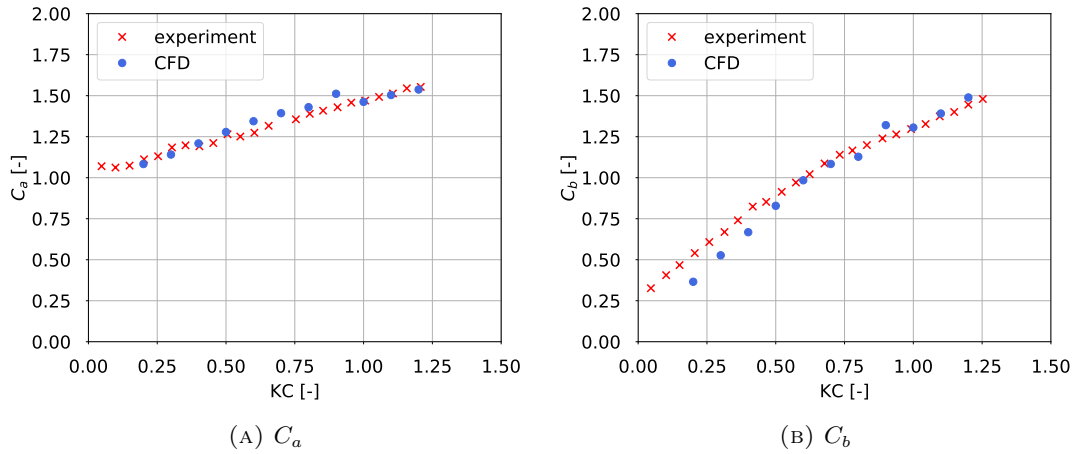


FIGURE 5.20: Hydrodynamic coefficients  $C_a$  (left) and  $C_b$  (right) for different  $KC$ . The red crosses are the experimental results and the blue dots are the CFD results.  $T = 1$  s ( $kR = 1.22$ )

The CFD results match well the experimental values, especially for the added mass coefficients. The added mass coefficient increases mostly linearly with  $KC$  with a small slope. Concerning the damping coefficient, agreement with experiments is also very good for  $KC$  greater than 0.6 but some discrepancies at lower  $KC$  can be noted. The damping coefficient also increases linearly with  $KC$ . At low  $KC$ , it seems that the slope is higher in the CFD model than in the experimental results. The intercept of the CFD models seems to be 0, whereas the intercept of the experimental results is around 0.25.

### 5.3.2.2 Vorticity

The vorticity magnitude around the  $y$ -axis near the structure is presented in figure 5.21 for a case at  $KC = 0.9$ , at different stages of a period of oscillation. Again, only half of the domain is computed, the other side is obtained by symmetry.  $t_0 + 0.2T$  corresponds to the highest position of the structure and  $t_0 + 0.7T$  corresponds to the lowest position.

The free surface is not represented in the figures. In this case, there are limited interactions between the vortices and the free surface. It can be observed that the vortex is dissipated rapidly before reaching the free surface. As the disk moves upward, a positive vortex is generated at the edge of the disk ( $t_0 + 0.7T$ ) and stays below it. When the disk reaches its highest position and starts going down, the positive vortex separates from the disk, travels upward and another vortex rotating in the opposite direction is generated at the edge above the disk. The positive vortex traveling upward interacts with the negative vortex and forms a vortex pair ( $t_0 + 0.4T$ ). This phenomenon was also observed in the mode 4 described in [138] when  $KC$  is large and the thickness of the disk small. This pattern is repeated at each period of oscillation.

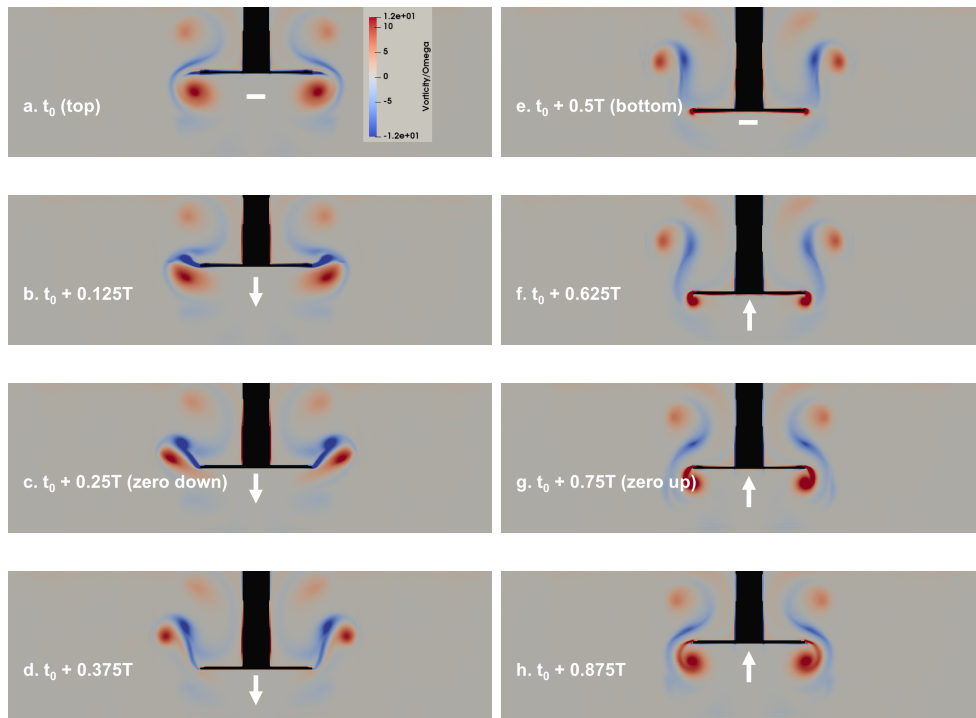


FIGURE 5.21: vorticity/ $\omega$  induced by the vertical motion of the disk+column (left : downward, right upward).  $A = 0.036$  m,  $T = 1$  s, ( $kR = 1.22$ ,  $KC = 0.9$ )

## 5.4 Conclusion

This paper has focused on validating a CFD model using the overset mesh method implemented in OpenFOAM® for the analysis of the vertical force acting on a heave damping plate in forced motion. The case of the disk only and the case of a disk at the bottom of a vertical cylinder have been investigated. A meshing method adapted to the overset mesh technique is proposed and a mesh convergence analysis is presented. The results have been compared with experimental data from the literature. The

comparison of the hydrodynamic coefficients  $C_a$  and  $C_b$  and the vorticity field near the plates have been investigated and have shown good agreement between the CFD model and the experimental results.

In the case of an isolated disk close to the free surface, the CFD model has also shown superior accuracy and a wider range of applicability in predicting the coefficients than a LPFM. It also succeeded in predicting the occurrence of negative added mass coefficients that were observed during the experiments. At larger submergence, the CFD model better predicts the added mass compared to the LPFM. Moreover, the results of the damping coefficients are similar when an empirical drag contribution is added to the LPFM. The numerical model can give a good representation of the vortex shedding around the plates. It has been shown that the vortices impact the free surface in the case of the disk only close to the free surface. Moreover, radiated waves and water jets are generated at specific time instants over the oscillation period. The vortices generated are large and occur at the edge of the disk, so a laminar flow assumption could be considered when computing the force on the disk. However, in future analysis, a turbulence model could be added to better estimate the dynamics and the dissipation of the vortices at the free surface.

In the case of the disk at the bottom of a cylinder, there is only some discrepancies of the slope and intercept of the damping coefficient at low  $KC$ , but overall the CFD and experimental results are in good agreement. The vortices generation could be observed at the heave plate location. It could be noticed that the vortices dissipate rapidly and have a low impact on the free surface dynamics.

This CFD method will be extended to a full platform with 6 degrees of freedom and will be used to better predict the flow around FOWT in realistic ocean wave conditions.



# 6 3D simulations of fixed FOWT in waves: the OC6 project

In this chapter, analyses of a fixed 3D FOWT subjected to incident regular and bichromatic waves are presented. The DeepCWind floater developed by NREL and described in section 1.4 is used. The floater is considered static and wave loads on the structure are investigated. The results are compared with experimental data, linear model results, and CFD results from other participants of the Offshore Code Comparison Collaboration, Continued, with Correlation, and unCertainty (OC6) project.

## 6.1 Introduction to the static analysis of the DeepCWind FOWT within the OC6 project

The Offshore Code Comparison Collaboration, Continued, with Correlation, and unCertainty (OC6) project started in January 2019 (<https://iea-wind.org/task30/>). It is a joint industry project, run under the IEAWind – Task 30 (OC4-OC6). This project is led by NREL. The main purpose of this project is to focus on the verification and validation of coupled offshore wind modeling tools. The objective is to validate these tools with measured data from a dedicated experimental campaign. It includes a large variety of engineering-level models and CFD codes. The CFD simulation will be used to improve the performance of engineering-level tools. Up to now, phase I of the project has almost been completed. This first phase aimed to assess the wave loads on the DeepCWind FOWT. In this phase, the structure was considered fixed (no DoF allowed). The CFD models of the participants were first compared by analyzing a regular monochromatic wave condition. Then, bichromatic wave conditions were performed to assess the low-frequency loads caused by the 2<sup>nd</sup> order difference-frequency waves.

In the scope of this thesis, I participated actively in the OC6 group of CFD research, and most of the load cases results I obtained were shared with that OC6 group. The complete comparison and validation analysis will be published in 2021 in a journal paper. In this section, my own results are presented and partially compared to the results of other participants.

In order, to maintain consistency between the participants, a large number of imposed inputs and settings was proposed by NREL. These inputs vary slightly between the cases as they have been evolving based on the experience acquired during the project. These inputs will be emphasized for each load case in this section.

## 6.2 Monochromatic wave case

In this section, a monochromatic wave load case is presented (LC 31) with a fifth-order wave:  $T = 12.1$  s,  $A = 3.5$  m at full scale. The results of induced forces are compared with experimental measurements and CFD results from OC6 participants. Following several comparisons of the results and variations of numerical inputs, the

model has been improved to converge to an optimal solution. Two meshes of the NWT are presented here. The first one (section 6.2.1) follows the meshing method described in chapter 3. The second mesh has been proposed by NREL to facilitate the comparison of the numerical results between the participants.

## 6.2.1 Model 1 of the static DeepCWind FOWT

### 6.2.1.1 Description of the fluid domain

The fluid domain of this model is presented in figure 6.1. The generation/relaxation zone at the inlet of the NWT is 1 wavelength long, the propagation zone is 2 wavelengths long, and the relaxation zone at the outlet is 1 wavelength long, as shown in figure 6.1. As a first coarse model, the relaxation zone is deliberately shorter than the prescription from the convergence analysis of chapter 3 to reduce the simulation time. However, it was already shown to provide good results. The structure is located in the middle of the tank and its dimensions are shown in figure 1.10. The water depth is  $d = 120$  m, smaller than the experimental set-up but enough to ensure that the deepwater wave condition is verified. The resulting wavelength is  $\lambda = 233$  m. The structure and the flow are expected to be symmetrical with respect to the  $xz$  plane, so only half of the domain is modeled to reduce the computational cost, and a symmetry boundary condition is imposed, as described in figure 6.1. The width of the half NWT is 80 m. This model is run at full scale.

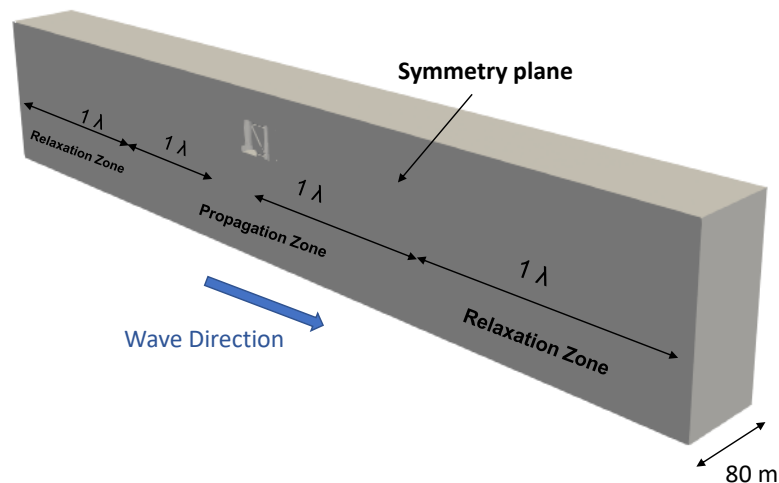


FIGURE 6.1: Description of the NWT of the model 1 for the static DeepCWind FOWT

### 6.2.1.2 Mesh description of the model

This mesh was generated using the commercial software Ansys Meshing (<https://www.ansys.com/>). This tool has shown a better ability in generating clean structured meshes with complex geometries than the OpenFOAM® meshing tools. The mesh is based on the prescription of chapter 3. 5 cells per  $\lambda$  are used in the refinement zone at the free surface (figure 6.2). The vicinity of the structure is also refined with 5 cells per  $\lambda$  with an extra refinement level near the sharp edges of the structure, especially at the

junction between the braces and the column, as shown in figure 6.2. The mesh is composed of 7.5 million cells.

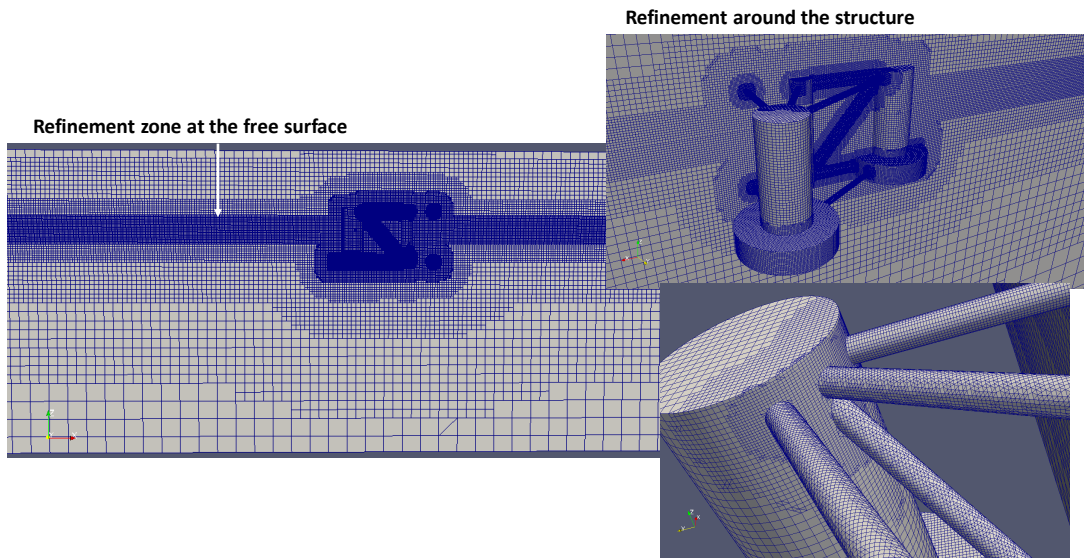


FIGURE 6.2: Description of the mesh of the model 1 of the static DeepCWind case

### 6.2.1.3 Physics and Solver of the model 1

The boundary conditions described in chapter 3 are used for the fluid domain. A wall condition is applied to the structure. The maximum CFL number is set to  $Co = 1$ . A laminar flow is considered, as turbulent effects are not expected to influence significantly the results. The PISO algorithm with 3 inner iterations is used for the pressure coupling-velocity coupling.

### 6.2.1.4 Results of model 1

In this section, the CFD results of the forces, and the run-up on the structure, obtained with the previously described model, are compared to experimental results, CFD results from two other OC6 participants (who also used OpenFOAM®), and results obtained with a linear potential flow model developed by Guillaume Dupont during his post-doc period at Centrale Marseille. The surge and heave forces on the global structure are presented in figure 6.3, the surge forces on the two parts of the upstream column are compared in figure 6.4, the forces on the central column are shown in figure 6.5, and the run-up on the upstream column is shown in figure 6.6.

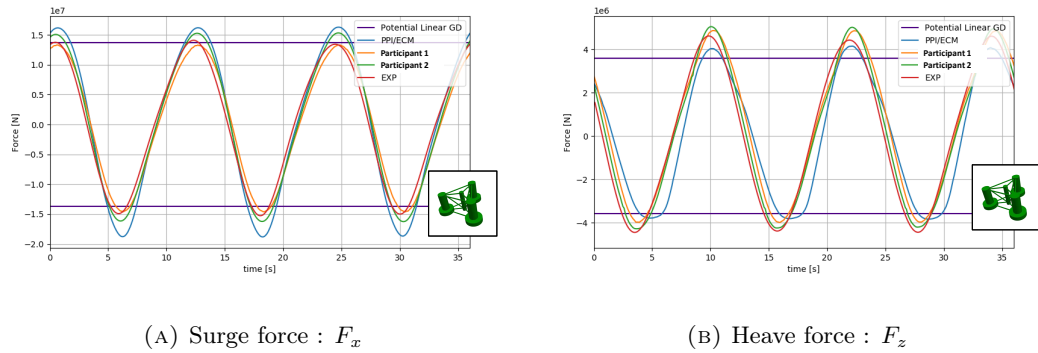


FIGURE 6.3: Time series of the forces acting on the global structure. The purple line is the amplitude of the linear model from G. Dupont. The red line are the experimental results from the OC6 project, The blue line are the CFD results of the present work. Model 1 - full scale:  $T = 12.1$  s,  $A = 3.5$  m

The surge force computed with the linear model is in good agreement with the experimental results, but the present CFD model predicts a slightly larger force amplitude of around 10% compared to experiments. A higher level of nonlinearity can be observed on the heave force where the linear model under-predicts the experimental results. The CFD model better predicts the amplitude of the force, but the results are also lower than measurements. Moreover, the pattern of the response is different for the negative forces. These differences might be explained by a too coarse mesh or by reflected waves that might occur at the outlet boundary of the NWT due to a too short relaxation zone.

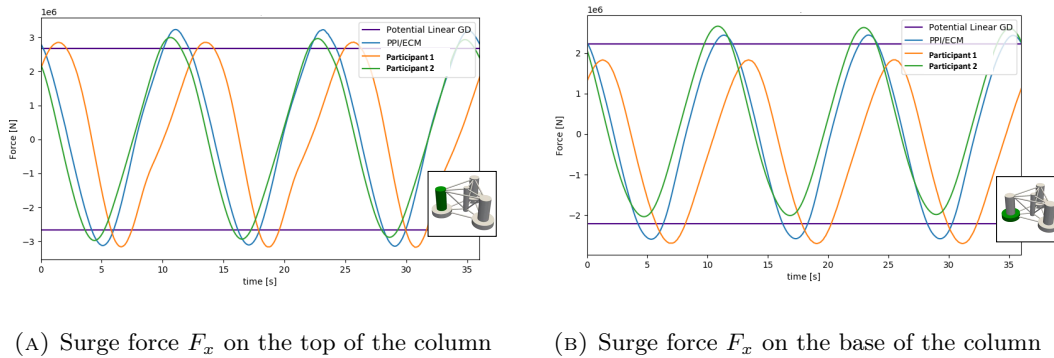


FIGURE 6.4: Time series of the forces acting on the upstream column. The purple line is the amplitude of the linear model from G. Dupont, the blue line are the CFD results of the present work. Model 1 - full scale:  $T = 12.1$  s,  $A = 3.5$  m

The CFD results predict relatively larger surge force amplitude on the two parts of the upstream column than the linear model. There was no experimental result available for these forces. It should be noted that the large nonlinearities observed on the 2D case of a vertical section of the column (figure 4.9 in chapter 4) do not appear here in 3D.

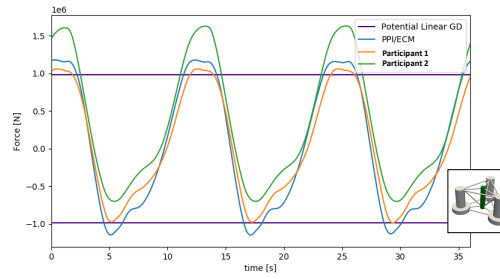


FIGURE 6.5: Time series of the forces acting on the central column. The purple line is the amplitude of the linear model from G. Dupont, the blue line are the CFD results of the present work. Model 1 - full scale:  $T = 12.1$  s,  $A = 3.5$  m

The CFD surge force results on the central column show a highly nonlinear pattern, However, the amplitude of the force remains relatively close to the linear amplitude.

The time series of the run-up on the upstream column at 3 different angles are presented in figure 6.6. The amplitudes of CFD run-ups are relatively close to the linear amplitude. However, time profiles show highly nonlinear patterns.

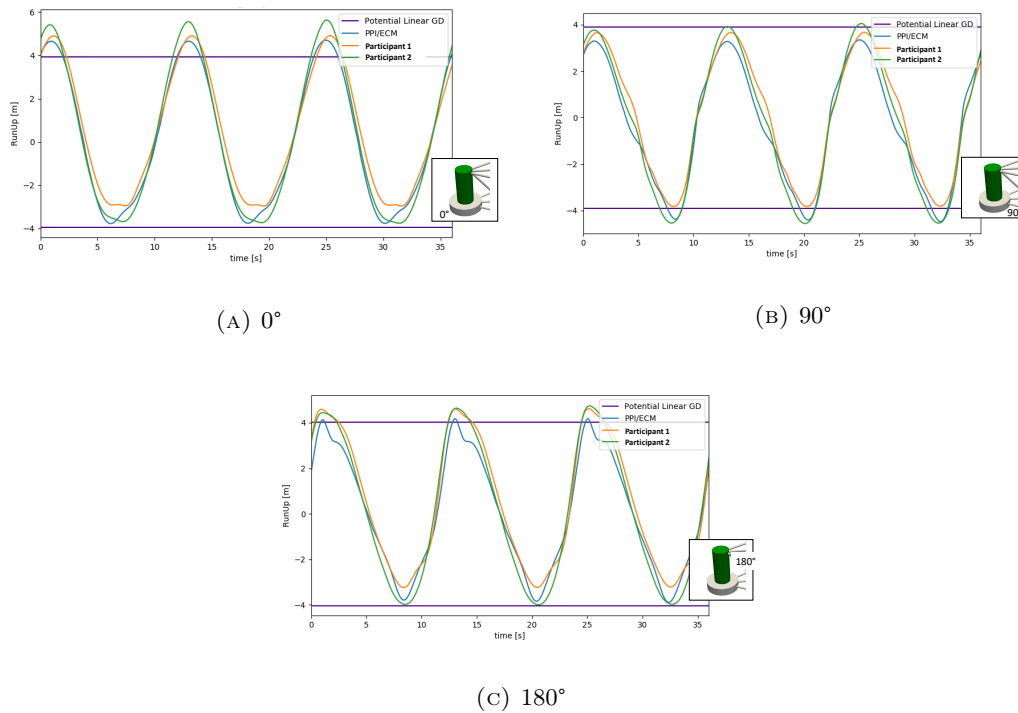


FIGURE 6.6: Time series of the run-up acting on the upstream column. The purple line is the amplitude of the linear model from G. Dupont, the blue line are the CFD results of the present work. Model 1 - full scale:  $T = 12.1$  s,  $A = 3.5$  m

### 6.2.2 Model 2 of the DeepCWind FOWT based on OC6 project

Based on analyses of initial results of the Load case 31 such as the results presented above, prescriptions of the numerical model parameters and mesh characteristics were

proposed by NREL to the OC6 project, to improve the comparison between the different participants. The prescriptions are summarized in this section and the updated results are presented.

### 6.2.2.1 Imposed numerical inputs and mesh

The global domain of the model is presented on figure 6.7. The simulation was run at  $1/50^{\text{th}}$  model scale. The domain length is extended compared to model 1. The generation/relaxation zone at the inlet is  $1.5$  wavelength long and the relaxation zone at the outlet is  $3$  wavelengths long. The full fluid domain is modeled (no use of symmetry plane) and the water depth is  $3.6$  m ( $180$  m at full scale).

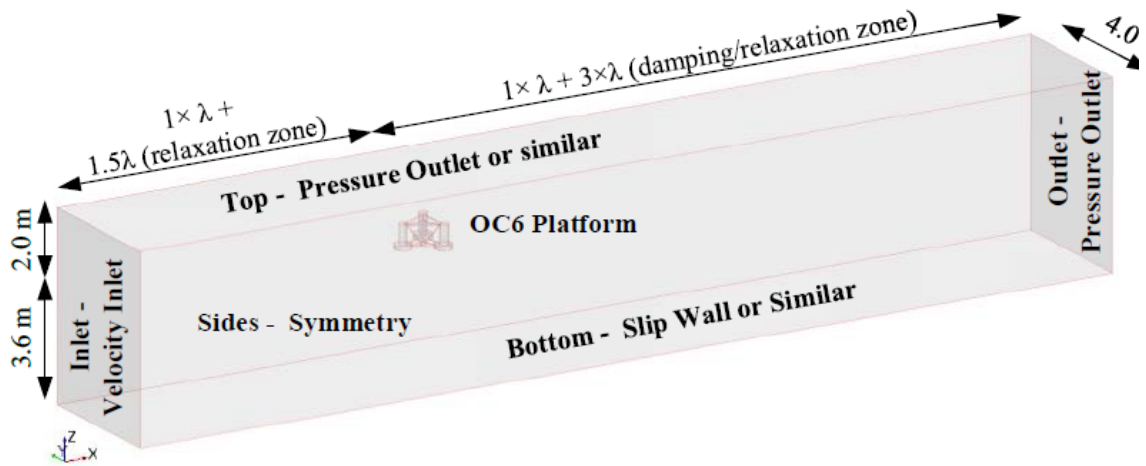


FIGURE 6.7: Domain description of the model 2 prescribed by the OC6 project

The mesh is also different from model 1. Precise cell dimensions were imposed and are presented in table 6.1 and on figure 6.8. The mesh file has been provided by another participant of the project. Nevertheless, the global meshing method is similar to model 1. The mesh is refined near the free surface and in the vicinity of the structure. The largest difference is that the aspect ratio is different from 1 in the refined boxes (table 6.1) increasing the number of cells per wave amplitude.

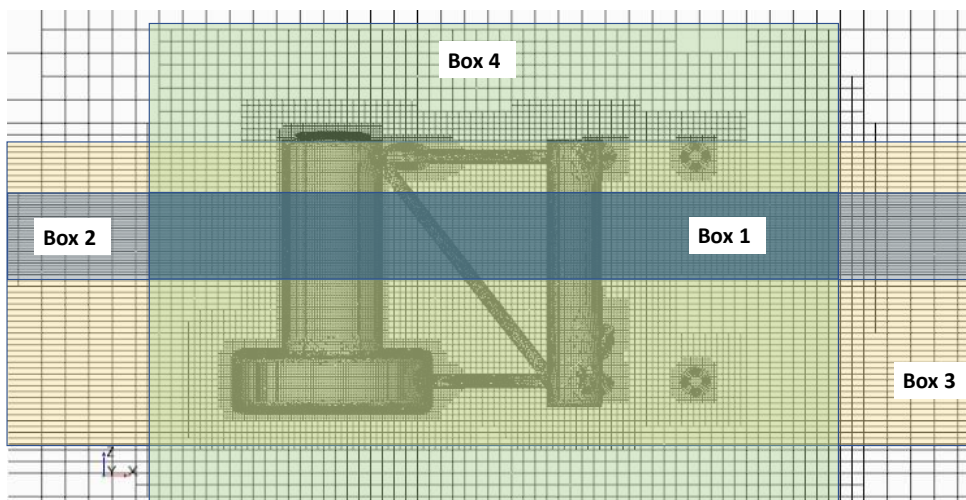


FIGURE 6.8: Vertical slice of the mesh prescribed by the OC6 project

Refinement Box	Aspect ratio	Cells per wave Amplitude
Box 1	$\Delta x/\Delta z = \Delta y/\Delta z = 2$	$\Delta z = A/10$ (m)
Box 2	$\Delta x/\Delta z = 8; \Delta y/\Delta z = 16$	$\Delta z = A/10$ (m)
Box 3	$\Delta x/\Delta z = 8; \Delta y/\Delta z = 8$	$\Delta z = A/5$ (m)
Box 4	$\Delta x = \Delta y = \Delta z$	$\Delta z = A/2.5$ (m)

TABLE 6.1: Cell dimensions for the mesh imposed in the OC6 project

Numerical settings were also imposed and are summarized in table 6.2. In this case, the use of a turbulence model was advocated. The  $k - \omega$  SST-stabilized model described in chapter 2 was used.

Implicit Unsteady	Yes
Time Discretization	Second-order or similar
Discretization of Gradient, Momentum, Transport Equations.	Second-order or similar
Wave Model	Fifth Order (5 <sup>th</sup> Order)
Time Step Size ( $\Delta t$ )	$T/850$
Turbulence Model	$k - \omega$ SST
Water Density	$998.6 \text{ kg/m}^3$
Turbulence Kinetic Energy ( $k$ )	$1e-5 \text{ (m}^2/\text{s}^2)$
Turbulence Dissipation ( $\omega$ )	$1.0 \text{ (1/s)}$
Relaxation zones at Inlet & Outlet BC	$1.5\lambda$ and $3.0\lambda$

TABLE 6.2: Numerical parameters and settings for CFD solver imposed in OC6 project

### 6.2.2.2 Results

The time series and amplitude of the RAO of the forces and moment on the global structure are presented in this section. A comparison is made between the present CFD results, experimental measurements, and CFD results from other participants of the OC6 project.

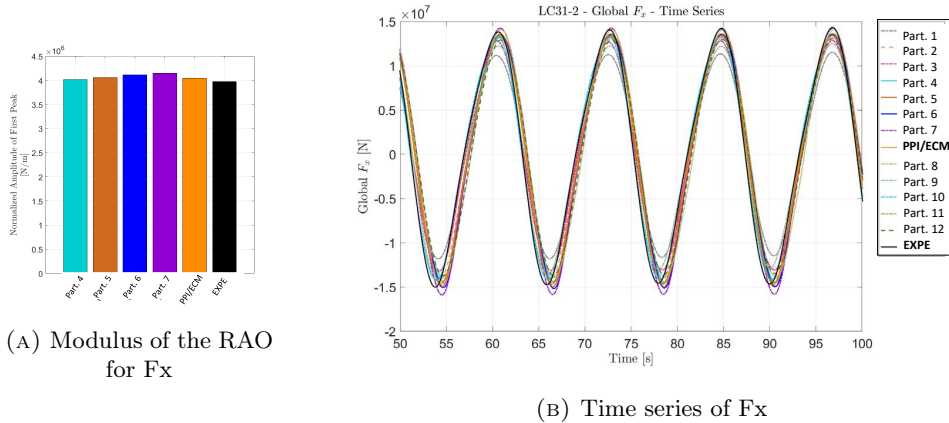


FIGURE 6.9: Vertical force ( $F_x$ ) acting on the global structure. Comparison between the present work (in orange), experimental measurements (in black), and CFD results of other participants of the OC6 project. Model 2 - small scale:  $T = 12.1$  s,  $A = 3.5$  m

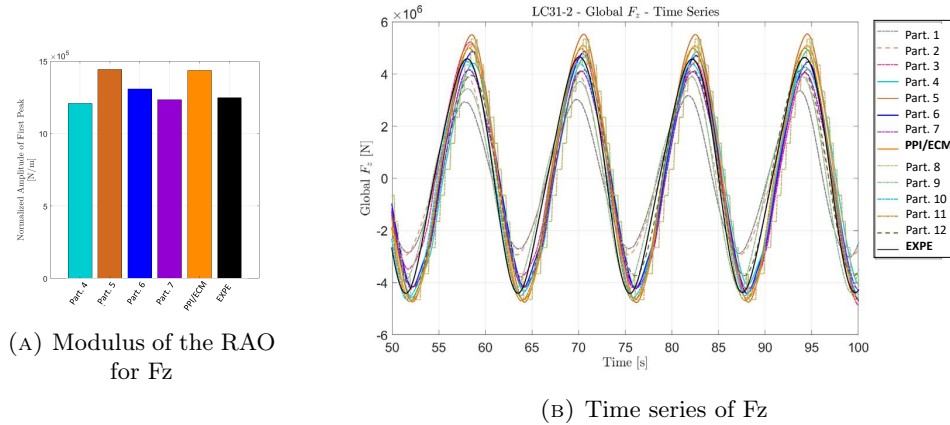


FIGURE 6.10: Horizontal force ( $F_z$ ) acting on the global structure. Comparison between the present work (in orange), experimental measurements (in black), and CFD results of other participants of the OC6 project. Model 2 - small scale:  $T = 12.1$  s,  $A = 3.5$  m

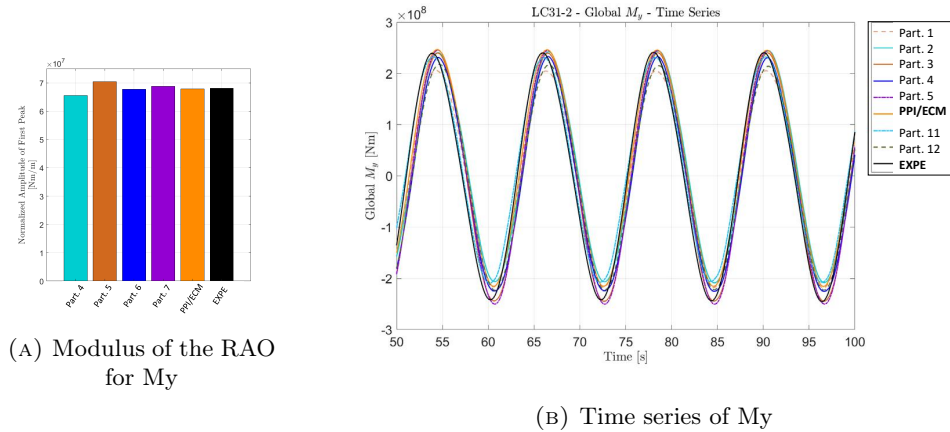


FIGURE 6.11: Pitch moment ( $M_y$ ) acting on the global structure. Comparison between the present work (in orange), experimental measurements (in black), and CFD results of other participants of the OC6 project. Model 2 - small scale:  $T = 12.1$  s,  $A = 3.5$  m

Results of forces and pitch moment from the present CFD model show good agreement with experimental measurements and results from other OC6 participants. More discrepancies are observed on the heave force between the present results and experiments. Nevertheless, it should be noted that there is a factor difference of 10 between surge and heave force magnitudes. Overall, numerical results were improved compared to Model 1. The main reasons for improvement were most likely, the refinement of the mesh and the decrease of the time step.

Simulations were also run without turbulence model and have shown similar results, which confirms that turbulence effects have a low impact on the global force on the structure, at least in this specific case.

### 6.3 Bichromatic wave cases

In this section, bichromatic wave conditions are presented to assess the low-frequency loads caused by the 2<sup>nd</sup> order difference-frequency waves. The induced 2<sup>nd</sup> order loads

have shown to be under-predicted by engineering-level models in the OC5 project [149]. However, it represents a major challenge in order to predict ultimate and fatigue loads accurately [150]. Indeed, semi-submersible platforms are designed to have low surge and pitch natural frequencies that can be excited by these 2<sup>nd</sup> order force components ([151], [152], [150]). Investigations of the 2<sup>nd</sup> order loads were previously performed using full quadratic transfer functions (QTFs) from the second-order potential-flow theory. Even though this method has shown significant improvement in the predictions of the 2<sup>nd</sup> order loads in irregular waves, these loads were still underestimated near surge and pitch resonance frequencies ([150], [149]).

Another method was also presented in ([149]) using the 2<sup>nd</sup> order potential flow theory completed with a strip theory method with large drag Morison coefficients. It has been shown that the low-frequency load predictions were improved but that the motion prediction of the platform was deteriorated [150]. In this chapter, the numerical setup and preliminary CFD results of the OC6 project are presented. The results are extracted from the conference paper [150]. More results and comparisons with experimental data should be published in a journal paper in the coming months, but cannot be presented in this thesis because of pending IP restrictions.

### 6.3.1 Set up of the numerical model

The numerical setup is different from the monochromatic case. In this model, only the 3 main columns are considered. The central column and the braces are removed from the structure, as shown in figure 6.12. The quantities are given here at full scale, but the simulations are run at model scale.

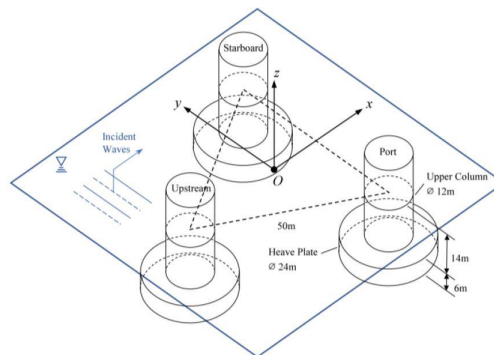


FIGURE 6.12: Geometry of the DeepCWind without braces and central column (dimensions are given at full scale)

Similar to the monochromatic case, mesh and domain prescriptions were provided by the OC6 project to guarantee consistency between the participants. The mesh, used in our analysis, was provided by another participant of the project (IFPEN). A mesh convergence analysis was performed by NREL and presented in [150]. The cell size at free surface is set as  $\delta_x = 0.018$  m (model scale) and the aspect ratios are defined as  $\delta_x/\delta_z = 4$  and  $\delta_y/\delta_z = 16$ . A slice of the mesh is shown in figure 6.13. The mesh is also refined near the walls of the structure. In the present study, no boundary layer was used but some participants included boundary layers. A complete description of the mesh sizing can be found in [150].

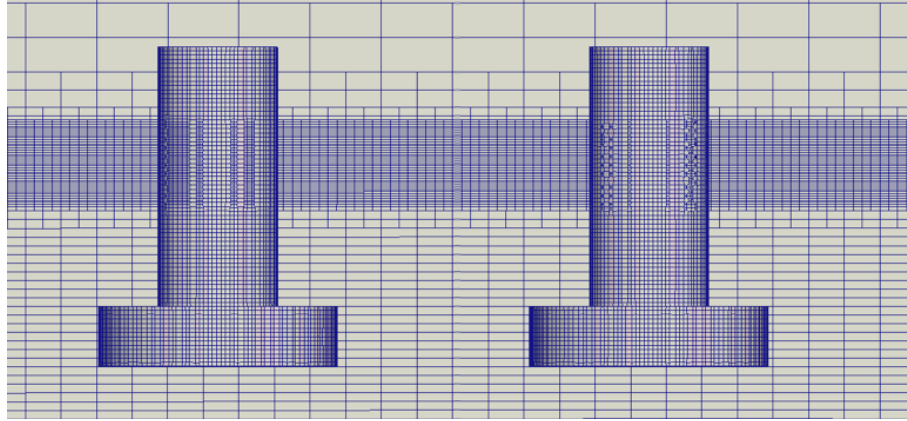


FIGURE 6.13: Mesh used for the bichromatic wave analysis. Credit for the mesh : Adria Borrás Nadal (IFPEN)

The domain dimensions and boundary conditions are summarized in figure 6.14. The deepwater wave hypothesis is verified. The length of the zones is defined as a function of the largest wavelength  $\lambda_2$ . Half of the domain is represented on the figure as several participants used the symmetry to model only half of the flow. However, in the present work, the full domain was considered. Table 6.3 summarizes the main numerical inputs imposed by the OC6 project. A more advanced description of the CFD settings used by all participants can be found in [150].

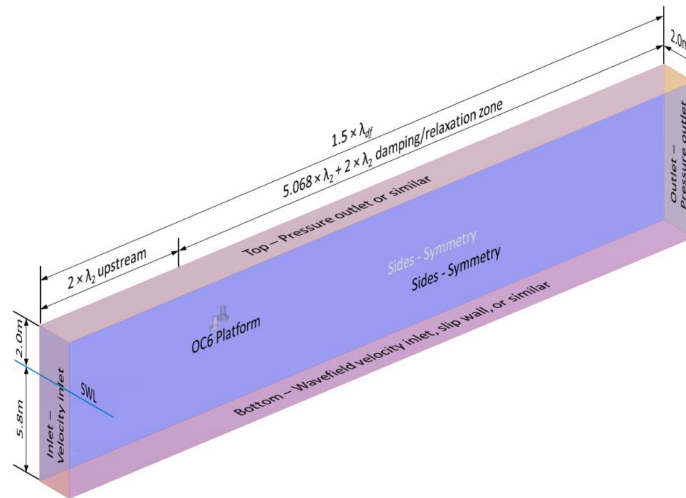


FIGURE 6.14: Dimensions of the NWT and boundary conditions for the bichromatic wave case of OC6

Implicit Unsteady	Yes
Time Discretization	Second-order or similar
Discretization of Gradient, Momentum, Transport Equations.	Second-order or similar
Wave Model	Fifth Order (5 <sup>th</sup> Order)
Time Step Size ( $\Delta t$ )	$T/1030$
Duration of Simulation	$2.5 \times \text{Repeat Period} = 88.35 \text{ s (model scale)}$
Turbulence Model	None
Water Density	$998.6 \text{ kg/m}^3$
Relaxation Zone at Inlet & Outlet BC	$1.5\lambda_2$ upstream and $2.0\lambda_2$ downstream

TABLE 6.3: Numerical settings for CFD solver imposed in OC6 project for the bichromatic wave case

One wave case is presented in this thesis and the wave characteristics are given in table 6.4.

Wave	Period	Frequency	Wavelength	Amplitude	Repeat period
1	$T_1 = 11.900$ s	$f_1 = 0.084$ Hz	$L_1 = 221$ m	$A_1 = 1.755$ m	249.9 s
2	$T_2 = 8.6172$ s	$f_2 = 0.116$ Hz	$L_2 = 116$ m	$A_2 = 1.745$ m	

TABLE 6.4: Description of the parameters of the bichromatic wave case

### 6.3.2 Wave Calibration

The first milestone of the validation process is to ensure the quality of the generated wave. So, first, the propagation of the wave in the NWT without the structure was analyzed in a 2D section of the tank. Wave gauges were located along the domain to follow the evolution of the wave amplitude in time and distance. Figure 6.15 compares the wave amplitude of the two primary waves computed along the NWT with the targets (with the blue scale on the left). The amplitude of the difference-frequency wave component is also represented (with the orange scale on the right). The amplitudes are extracted from a FFT analysis of the free surface time series at each wave probe. An overall good correlation between the two wave components is observed with the target values. Though the amplitude of the longest wave ( $T = 11.9$  s) slowly decreases along the tank and the decay rate is accelerated after  $x = 600$  m. This position corresponds to an increase of the cell size  $\delta_x$  in the mesh and could explain the diffusion of the wave. The difference-frequency wave component amplitude shows a very small amplitude oscillation along the tank probably caused by reflection at the outlet boundary. However, this reflection is very small when considering the scale difference with primary waves.

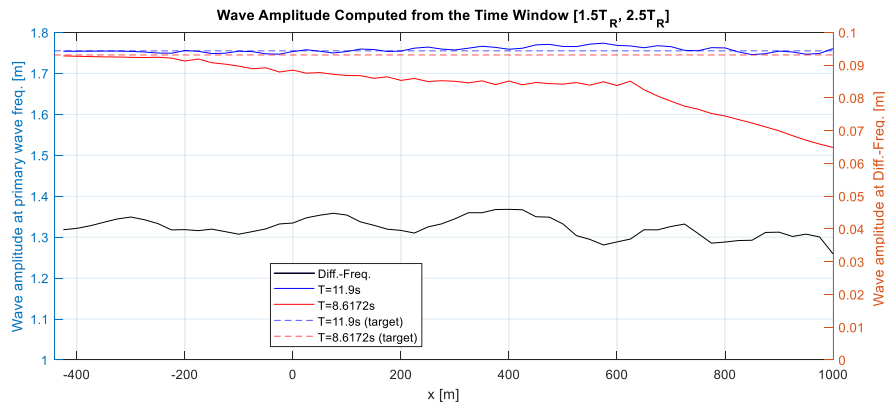


FIGURE 6.15: Amplitude of the primary waves (left scale) and the difference-frequency wave (right scale) along the NWT

A Fourier analysis with a sliding window was also performed to compute the evolution of the free surface elevation at  $x = 0$  m, the position where the center of the structure should be placed. Figure 6.16 shows the evolution of the amplitude over time. The two primary waves are compared to the target amplitude. At  $x = 0$  m the wave amplitude of both components is globally well captured by the model over time. As shown on figure 6.15, the longest wave amplitude is slightly under-predicted. The amplitude of the difference-frequency wave is constant over time. The results before 50 s correspond to the ramp time.

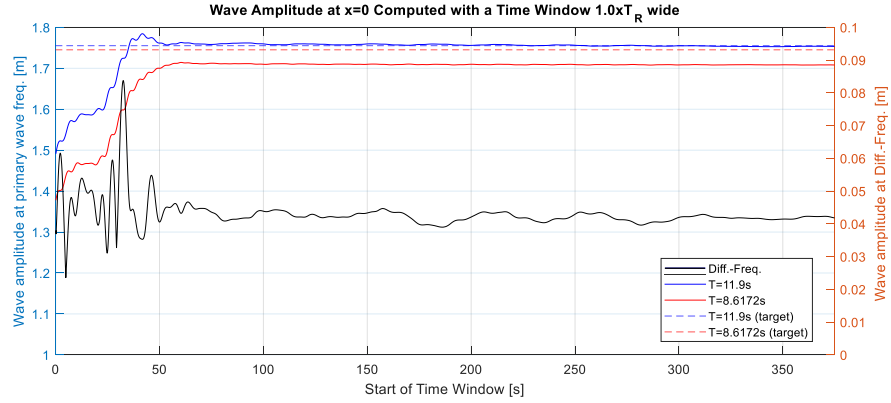


FIGURE 6.16: Amplitude of the primary waves (left scale) and the difference-frequency wave (right scale) at  $x = 0$  m over time.

Overall, waves2Foam appears capable of generating high-quality bichromatic waves. The second-order bichromatic wave model described in [50] has shown to reduce reflection of the difference-frequency component both in time and space. When the first order bichromatic wave model is used, a large variation of the difference-frequency wave amplitude is observed. According to Wang et al. [150], these variations are caused by imperfections in the incident waves that are the source of incident-free waves at the difference-frequency. These free waves have a very low frequency and so, cannot be damped in the relaxation zone, resulting in reflected free waves. A wave-splitting method was used by NREL to extract the amplitudes of the free wave components. The decomposition method is described in [150]. As mentioned in chapter 2, the Courant number correction in the absorption zone reduced significantly the reflection of the two main components of the wave.

### 6.3.3 Results of the bichromatic wave loads on the structure

In this section, the force amplitudes in the  $x$  (figure 6.17) and  $z$  (figure 6.18) directions and the moment around the  $y$ -axis (figure 6.19) are presented for the two primary waves and the difference-frequency wave. The results computed in the scope of this thesis are compared to those from other participants of the OC6 project and a QTF calculation from the second-order potential-flow theory computed by NREL using WAMIT. A description of the method is presented in the WAMIT theory manual [17]. The force contributions of the difference-frequency free waves are subtracted from the results. The loads computed for this thesis are represented in dark blue for the difference-frequency loads and in dark green for the primary wave loads and are labeled "PPI". When compared to the results shown in [150], the PPI results were updated after improvements of the model. The loads are normalized by the coefficients given in table 6.5 where  $A_{wp}$  is the water-plane area and  $L$  is the distance between the centers of two columns. The black bars on the figures are uncertainties computed by NREL. The uncertainty computation method is described in [150].

	Difference Freq. ( $f_d$ )	1 <sup>st</sup> Wave Freq. ( $f_1$ )	2 <sup>nd</sup> Wave Freq. ( $f_2$ )
$F_x$	$\rho g A_{wp} A_1 A_2 (k_1 - k_2)$	$2\rho g A_{wp} A_1$	$2\rho g A_{wp} A_2$
$F_z$	$0.5\rho g A_{wp} A_1 A_2 (k_1 - k_2)$	$\rho g A_{wp} A_1$	$\rho g A_{wp} A_2$
$M_y$	$0.5\rho g L A_{wp} A_1 A_2 (k_1 - k_2)$	$\rho g L A_{wp} A_1$	$\rho g L A_{wp} A_2$

TABLE 6.5: Normalization factors for the wave loads [150]

Overall, the results of the present thesis agree well with those from other participants of the project. The surge force from the primary waves is very consistent between participants and with the potential-flow model, showing a low impact of the viscous effect on the surge force at these wave frequencies. For the difference-frequency surge load, the present results are in the error margin computed by NREL as well as most of the participants. However, it can be observed that the difference-frequency loads predicted with CFD are much higher than the potential flow results, suggesting an important impact of the viscous effects on the nonlinear difference-frequency loads.

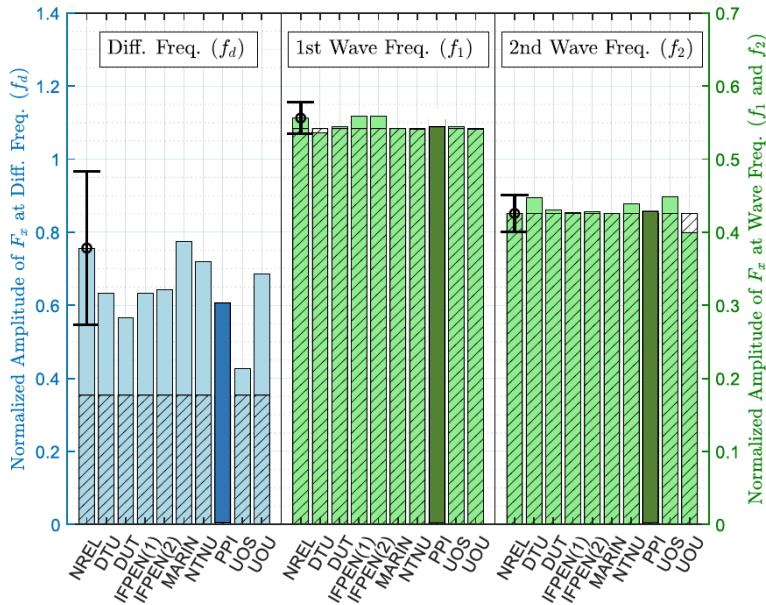


FIGURE 6.17: Amplitude of the surge force ( $F_x$ ) at difference-frequency ( $f_d$ ) and primary wave frequencies ( $f_1$  and  $f_2$ ). The darkest bars are the results from the present thesis, the hatched bars are the results from QTF method [150]

In the case of the heave force, the present results also show good agreement with other models. Unlike the surge force, more discrepancies can be observed for the primary wave loads between CFD and potential models, especially for the lowest wave frequency. All CFD models predict a larger force than the potential one, suggesting that viscous effects have a significant impact on the heave plates of the platform. According to [150], the discrepancies between participants are related to the difficulties to capture the flow separation at the corners of the plate. Also, the force amplitude is lower than the surge force amplitude. Again, the difference-frequency loads are larger in the CFD models than in the potential model.

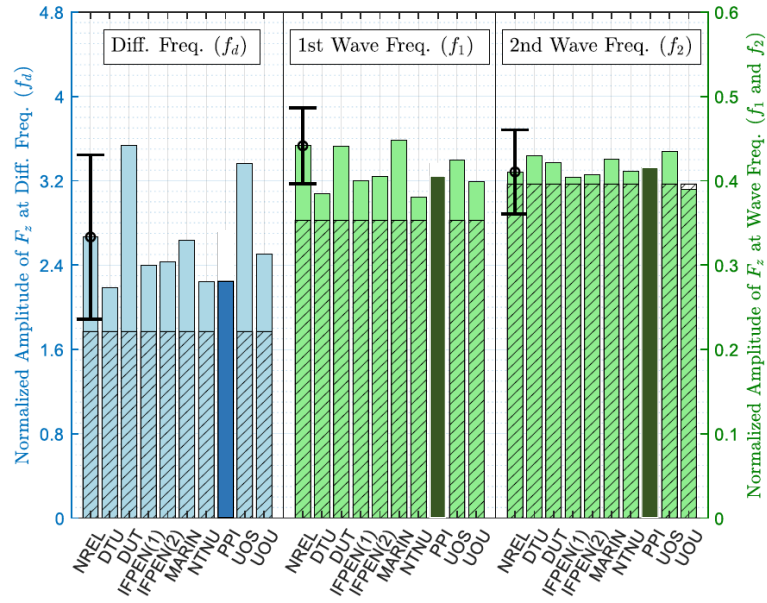


FIGURE 6.18: Amplitude of the heave force ( $F_z$ ) at difference-frequency ( $f_d$ ) and primary wave frequencies ( $f_1$  and  $f_2$ ). The darkest bars are the results from the present thesis, the hatched bars are the results from QTF method [150]

Finally, the pitch moment on the platform shows that the CFD predicts larger primary wave loads compared to the potential model, but the difference is small and close to the uncertainty margin. However, once again, the difference-frequency loads are much larger in the CFD results than in the potential model.

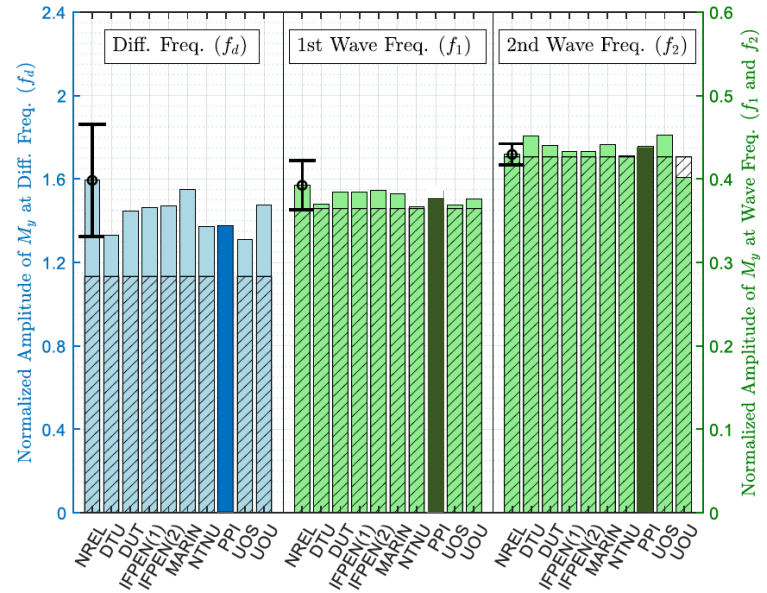


FIGURE 6.19: Amplitude of the pitch moment ( $M_y$ ) at difference-frequency ( $f_d$ ) and primary wave frequencies ( $f_1$  and  $f_2$ ). The darkest bars are the results from the present thesis, the hatched bars are the results from QTF method [150]

In conclusion, the good consistency between the participants shows promising

results for predicting second-order wave loads with this NWT. It should be noted that the difference-frequency wave load amplitudes are small, making the prediction and the comparison between models more difficult. For the three load components, CFD results predict larger difference-frequency load amplitudes than the QTF method. This difference suggests that viscous effects might have an impact on these second-order wave loads. These results will be compared to experimental data to enforce trust in the CFD model results.

## 6.4 Conclusions

In this chapter, the hydrodynamic behavior of the DeepCWind FOWT was investigated. The floater was considered fixed, which means that no DoF was allowed (i.e. so-called diffraction problem). The wave forces and moments on the structure were computed and the results were compared with experimental data and with results from other participants of the OC6 project. Both monochromatic and bichromatic wave cases were presented.

A wave-only analysis in a 2D NWT has shown the ability of the solver `waves2foam` to model high-quality bichromatic waves. Overall, the comparison of the present results with those from other participants of OC6 project has shown good agreement.

The second-order forces of the bichromatic wave computed with the CFD model are larger than the potential flow amplitudes. It emphasizes the contribution of nonlinear viscous effects in the global force. These results will be compared to experimental data to enforce trust in the CFD model results. Overall, the good consistency between the participants shows promising results for predicting second-order wave loads with this NWT.

In the scope of the OC6 project, simulations were done considering either a laminar flow approach or a turbulence model using the stabilized  $k-\omega$  SST turbulence model from [107]. The latter approach was shown to have a negligible impact on the quality of the results regarding the loads on the structure. This observation has also been made by the other participants of the OC6 project using different turbulence models [150]. Therefore no turbulence model was used in the majority of the cases.



## 7 3D simulations of freely-floating FOWT

In this chapter, we consider wave-interaction of freely-floating FOWT in three dimensions (3D). First, the overset mesh method is tested on a 3D simple cylinder. Free-decay tests of this structure are presented and compared with both experimental results and numerical simulations from the literature. Then, the freely-floating DeepCWind FOWT is studied. Free-decay test results in heave and pitch are shown, as well as wave-induced motions and forces for different regular wave conditions. Effects of nonlinearity of the incident wave field are assessed and discussed.

### 7.1 Validation of the overset mesh method using free-decay tests of floating offshore wind turbines

Free-decay tests provide crucial information on the natural frequencies and damping terms of FOWT. These tests are usually performed at the earliest stage of the design process of such structures. In this section, two cases of free-decay test analysis are presented. First, a vertical cylinder is considered to validate the model with a simple geometry. Then, the FOWT technology DeepCWind developed by NREL is analyzed. Results are compared with experimental results from the literature. This section was presented at the Thirtieth International Ocean and Polar Engineering Conference (virtual conf.), in 2020.

#### 7.1.1 Case of a vertical cylinder

The first validation case is based on the experimental tests carried out by Moura Paredes et al. [153] and presented by Palm et al. [74]. A 3D vertical truncated cylinder of circular cross-section is considered. Free-decay tests of the body with and without moorings are presented. In their study, Palm et al. [74] also presented numerical results but using a mesh morphing technique. Similar results, based on the same experimental data, are also presented in the work of Rivera-Arreba et al. [56].

##### 7.1.1.1 Settings of the case

###### 7.1.1.1.1 Geometry

The floating object is a cylinder of diameter  $D = 0.515$  m, height  $H = 0.401$  m and mass  $M = 35.85$  kg. According to Palm et al. [74], the draft of the free floating body is set to 0.172 m. However, the water density is not specified in [74]. In order to achieve hydrostatic equilibrium with this draft, the water density was set to  $\rho = 1000.59$  kg/m<sup>3</sup>. The CoG is located 0.0758 m above the bottom of the cylinder and the moments of inertia around the CoG are  $I_{xx} = I_{yy} = 0.9$  kg.m<sup>2</sup>,  $I_{zz} = 1.18$  kg.m<sup>2</sup>. The NWT has the same dimensions as the experimental tank. The length is  $L = 15$  m, the width is  $l = 5$  m, and the water depth is  $d = 0.9$  m.

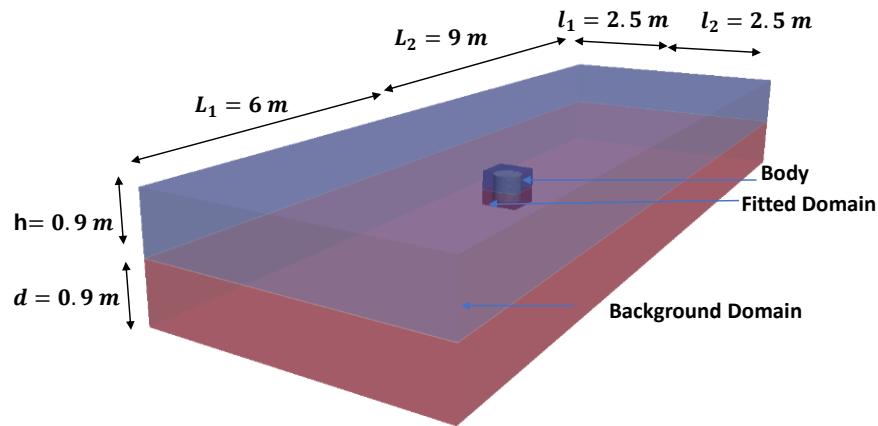


FIGURE 7.1: Overview of the computational domain for the vertical cylinder case

#### 7.1.1.1.2 Mesh

In this study, the OpenFOAM® meshing tools BlockMesh and SnappyHexMesh are used. As described above, two meshes are generated independently before being merged. The background mesh, which represents the NWT, is composed of squared cells of side length 0.08 m. The mesh is refined near the free surface using the level tool of snappyHexMesh. A level 3 is used around the free surface, which gives a cell size of 0.01 m. Based on the convergence analysis from chapter 4, the size of the cells on the sides of the fitted mesh is the same as the size of the cells in the nearby zone of the background mesh. So, another refined zone is set in the area where the floating body is expected to move. The same level of discretization is used for the free surface zone as shown in Figure 7.2.

The fitted mesh is generated using the following criteria: the cells near the sides have the same size as the refined zone of the background mesh as shown in Figure 7.2, and the mesh is refined near the wall of the body with a level 4 to better represent the structure and capture the nearby flow.

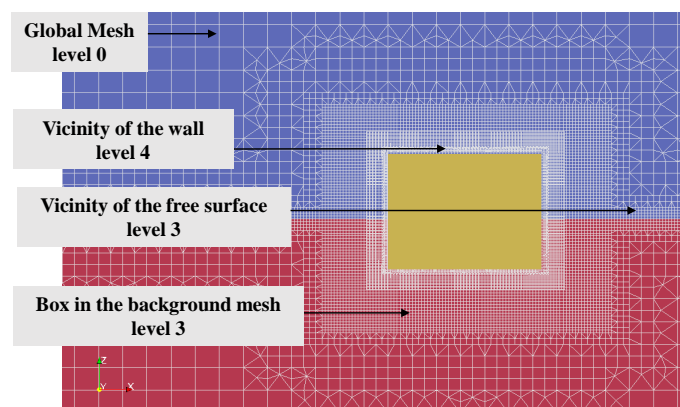


FIGURE 7.2: Description of the mesh sizing for the vertical cylinder case

The refinement level of the mesh is chosen based on the experience of previous internal studies. However, a mesh convergence study could be carried out to optimize the model in future work. The total number of cells is 8.2 million. It is not necessary to use such a large domain for free-decay tests. However, this case has been built respecting the experimental wave tank dimensions and with the future objective to study the interaction with waves (which requires these dimensions for comparisons with experiments to ensure the damping of the waves at the boundaries of the domain). As a preliminary work, the size of the box in the background mesh (figure 7.2) must be chosen according to the prediction of the motion of the structure to be sure that the fitted mesh stays in the box over time.

#### 7.1.1.1.3 Boundary conditions

The set of boundary conditions is defined in table 7.1.

	Alpha ( $\alpha$ )	Pressure (p)	Velocity (U)
<b>Atmosphere</b>	inletOutlet	totalPressure	Pressure Inlet Outlet Velocity
<b>Bottom</b>	zeroGradient	fixedFluxPressure	Fixed Value 0
<b>Front/back</b>	zeroGradient	fixedFluxPressure	Fixed Value 0
<b>Inlet</b>	zeroGradient	fixedFluxPressure	Fixed Value 0
<b>Outlet</b>	zeroGradient	fixedFluxPressure	Fixed Value 0
<b>Cylinder</b>	zeroGradient	fixedFluxPressure	Moving wall velocity
<b>Sides</b>	overset	overset	overset

TABLE 7.1: Description of the boundary conditions for volume fraction, pressure and velocity

More information on the boundary conditions can be found in the OpenFOAM® user guide. The main difference with a non-overset case is the use of the overset boundary condition for the sides of the fitted mesh. A moving wall velocity boundary condition is used for the wall of the floating cylinder. A point displacement variable is also initialized; it is the difference between the initial point location and the current location. The zone ID is a variable that defines whether a cell is in the fitted mesh or in the background mesh, which is specific to overset models.

#### 7.1.1.1.4 Numerical methods

In the following section, a description of the main numerical inputs is presented. These parameters and options are the same for all the presented cases.

#### 7.1.1.1.5 Numerical schemes

The numerical schemes described in table 7.2 are specified in all cases.

Time scheme	Backward Euler: first order
Gradient scheme	Gauss linear
Divergence scheme	$\rho \underline{u} \cdot \nabla \cdot \underline{u}$ : Gauss linear $\nabla \cdot (u\alpha)$ : Gauss van Leer $\nabla \cdot (u_r \alpha (1 - \alpha))$ : Gauss linear
Laplacian scheme	Gauss linear corrected
Overset Interpolation	Inverse Distance

TABLE 7.2: Numerical schemes used in the CFD model for the vertical cylinder case

Any other scheme is set as “default” in OpenFOAM®. The inverse distance interpolation scheme is used for the interpolation between the two meshes of the overset mesh method. A description of the numerical schemes can be found in the work of Guerrero [154]. The dynamic solver allows using the relaxation of the acceleration. It improves the stability of the solver. For more information about the relaxation method of this solver, one can refer to the work of Bruinsma et al. [53]. In our study, an acceleration relaxation coefficient of 0.6 was used in all the simulations.

The time step is adjusted to maintain a Courant number  $Co$  below 1. Choosing a lower Courant number when using overset simulation is recommended. However, this increases the computational time and, the results have been found accurate enough with  $Co = 1$ . The motion of the floater is small, and the velocity magnitude remains low, so the turbulence effects are expected to have a small influence on the results. A laminar flow is considered to avoid adding unwanted numerical damping.

#### 7.1.1.1.6 Mooring system

The mooring system used in the simulations is based on the system used in the experiment of Moura Paredes et al. [153] as shown in Figure 7.3.

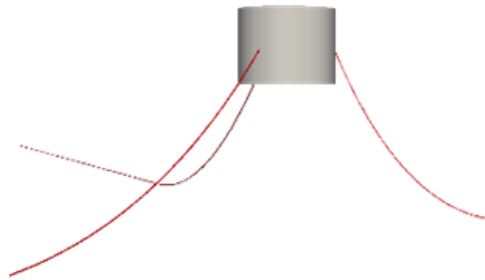


FIGURE 7.3: Sketch of the catenary mooring lines of the cylinder

The mooring system is composed of three catenary lines spaced  $120^\circ$  one from each other. For each line, the resting state defined above is used. The mass per unit length of the mooring is  $0.1267 \text{ kg/m}$ , each line has a length of  $6.733 \text{ m}$ . This length has been slightly modified compared to the length used by Moura Paredes et al. [153]. A calibration step of the mooring model is carried out to get a mean pre-tension in the lines in the rest position of  $3\text{N}$  as defined in the experiments of Moura Paredes et al. [153]. The coordinates of the fairleads and the anchors are given in table 7.3.

	<b>ML1</b>	<b>ML2</b>	<b>ML3</b>
<b>Anchor</b>	(6.66, 0.0, -0.9)	(-3.33, 5.77, -0.9)	(-3.33, -5.77, -0.9)
<b>Fairlead</b>	(0.371, 0.0, 0.0)	(-0.015, 0.223, 0.0)	(-0.015, -0.223, 0.0)

TABLE 7.3: Position of the anchors and the fairleads of the mooring lines (in meters)

#### 7.1.1.1.7 Computational resource and CPU time

The time step is adaptive to keep the Courant number below the prescribed limit. However, it stabilizes around  $0.001 \text{ s}$ . Each simulation is run in parallel on 96 cores using the Scotch decomposition. About 10 hours 30 min are needed for the simulation of  $5 \text{ s}$  of physical time. This execution time could be lowered by reducing the size of the domain in the case of free-decay tests.

### 7.1.1.2 Results

This section presents the results of free-decay tests of the simple vertical cylinder described above using an overset mesh method. In all simulations, the six DoF are enabled. The results of the decay tests in heave, pitch and surge motion are presented and compared with the experiments carried out by Moura Paredes et al. [153]. The time series of these experimental results are presented by Palm et al. [74] as well as CFD results. In their work, Palm et al. [74] also use OpenFOAM®; however, they used the grid deformation method to capture the dynamics of the floating body. For the mooring system, Palm et al. [74] used an in-house mooring module named MooDy which is different and more detailed than the mooring tool used in the present study. The numerical results of Palm et al. [74] are also compared with the overset results. Free-decay results in heave and pitch motion of a CFD model using the dynamic mesh solver of OpenFOAM® and the mooring system presented above can also be found in the work of Rivera-Arreba [55].

#### 7.1.1.2.1 Free-decay test in heave motion

A heave decay test was computed first to validate the CFD model. The fitted mesh of the floating body is initially moved 0.075 m from its theoretical equilibrium position to initiate a decay motion. This displacement is the same as the displacement used in the experimental results of Palm et al. [74]. No mooring system was used in the experiments of Moura Paredes et al. [153], nor in the models. The catenary mooring system does not significantly influence the heave motion of a floating body as seen in the results of Palm et al. [74].

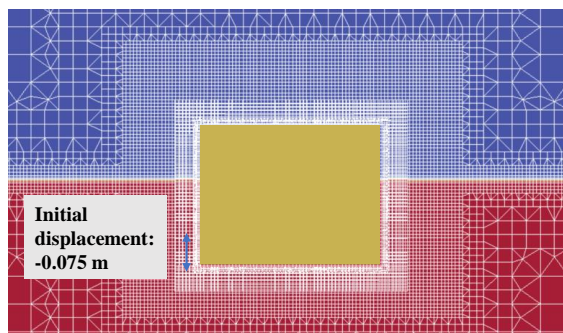


FIGURE 7.4: Initial vertical displacement of the floating cylinder for the heave decay test

The time series of the comparison between the experimental results, the numerical results of Palm et al. [74] and the results of the overset mesh method are presented in figure 7.5.

The overset mesh method shows good agreement with the experimental results. The period of the oscillation is found to be 1.1 s. It corresponds to the natural frequency in heave of the floating cylinder. This period is a key value for the design of any floating body subjected to waves. As described previously, the water density was adjusted to get the hydrostatic equilibrium of the floater. Knowing the exact value of the water density used in the experimental tests would provide more accurate results. Indeed, the physical behavior of the heave decay test is mainly influenced by the geometry, the mass of the body, and the density of the water. The choice of the numerical inputs such as time step, mesh discretization, or numerical schemes can also have an impact on the numerical solution and so, the natural period and the damping of the oscillation of the body.

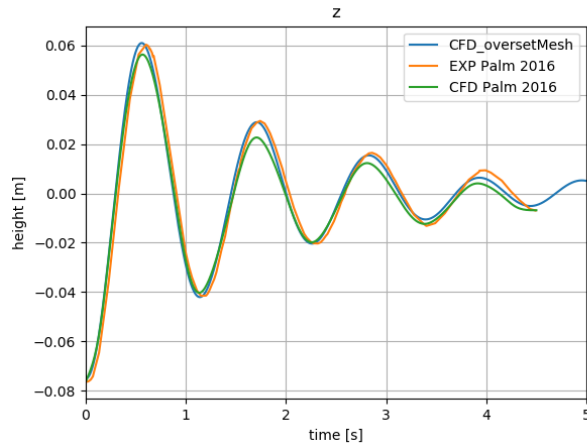


FIGURE 7.5: Comparison of the time series for the heave decay test of the simple cylinder

#### 7.1.1.2.2 Free-decay test in pitch motion

Similarly, a free-decay test in pitch motion was computed. The fitted mesh of the floating body was initially rotated by an angle of  $8.8^\circ$  to match the initial rotation of the results presented by Palm et al. [74]. Again, no mooring model was used in the experiment and in the models. Moorings have a small influence on the pitch motion as seen in the results of Palm et al. [74].

The CFD results using the overset mesh method are in good agreement with the experimental results (7.6). The period of oscillation in pitch motion is sensitive to the position of the COG of the body and its moments of inertia. However, these values are not easy to measure with precision experimentally. In the model of Palm et al. [74], the position of the CoG and the moments of inertia were slightly modified from the data of Moura Paredes et al. [153] to optimize the pitch decay results. The COG was moved 3 mm up to 0.0788 m above the bottom of the cylinder and the inertia was increased by  $0.05 \text{ kg}\cdot\text{m}^2$ . The same modifications were adopted in the present study.

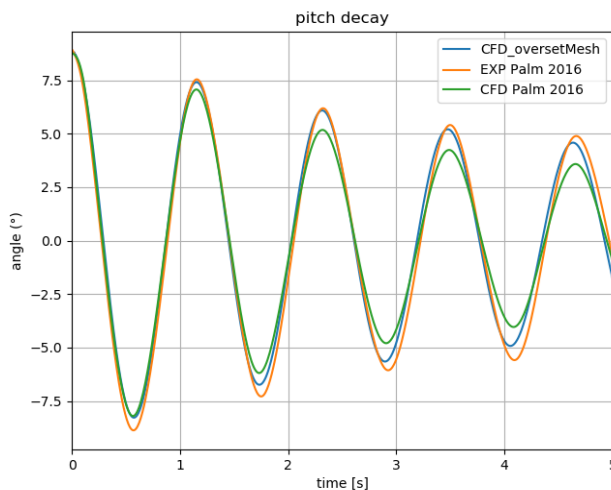


FIGURE 7.6: Comparison of the time series for the pitch decay test of the simple cylinder

### 7.1.1.2.3 Free-decay test in surge motion

Finally, a surge decay test was computed. Similarly, to heave and pitch decay tests, the floating body and its fitted mesh were initially translated horizontally from their original position. In this case, the mooring system model described above is implemented. Indeed, the surge natural period is mainly governed by restoring action from the mooring system. The goal of this test is to validate the mooring model used in this study. 7.7 shows the comparison of the time series of the overset mesh method with the results of Palm et al. [74].

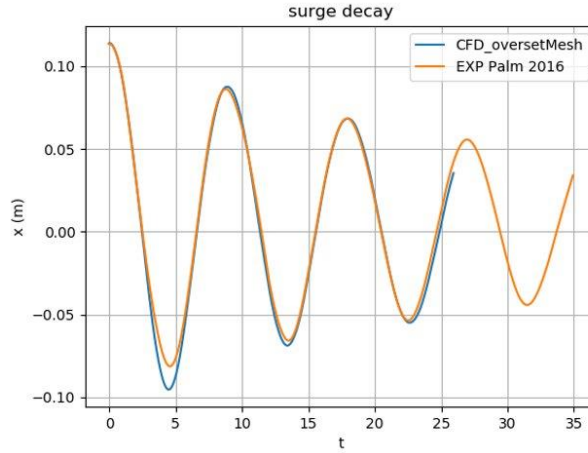


FIGURE 7.7: Comparison of the time series for the surge decay test of the simple cylinder

### 7.1.1.2.4 Estimation of natural periods and damping coefficients

In order to estimate the numerical values of the natural periods and damping coefficients, the equation of a freely vibrating system with damping is considered:

$$x(t) = X e^{-\xi \omega_0 t} \cos(\omega_0 \sqrt{1 - \xi^2} t - \phi) \quad (7.1)$$

where  $x$  is the coordinate of interest ( $x$ ,  $z$  or  $\alpha$  in this study),  $X$  is the amplitude,  $\xi$  the damping coefficient,  $\omega_0$  the natural frequency, and  $\phi$  the phase. The damping coefficient is computed as:

$$\xi = \frac{\delta}{\sqrt{4\pi^2 + \delta^2}} \quad (7.2)$$

where  $\delta$  is the logarithmic decrement:

$$\delta = \frac{1}{p} \ln \frac{X_n}{X_{n+p}} \quad (7.3)$$

The  $X_n$  are the local maxima distanced by  $pT$ . The natural periods and the damping coefficients in heave, pitch, and surge of the vertical cylinder are obtained from three successive positive peaks ( $p=3$ ), and shown in table 7.4.

	Natural period (s)			Damping coef. (-)		
	Overset	Exp	Rel. error (%)	Overset	Exp	Rel. error (%)
Heave	1.110	1.112	-0.1	0.127	0.098	29.6
Pitch	1.158	1.170	-1	0.028	0.026	7.69
Surge	9.097	9.137	-0.4	0.039	0.039	0

TABLE 7.4: Natural periods and damping coefficients of the free-decay tests of the vertical cylinder

From table 7.4, it can be observed that the overset mesh model predicts well the natural periods of the system for the three motions with a relative error of less than 1%. However, the damping coefficients of the decay tests in heave and pitch are over predicted in the CFD model compared to experiments. This difference might be caused by the difficulty in measuring pitch motion experimentally. On the contrary, the relative error of the surge damping coefficient is null. It shows that the mooring model used in this thesis performs well.

### 7.1.2 Case of the DeepCWind FOWT

The model is then applied to a more realistic FOWT. The floater presented in the study is based on the open-source DeepCwind concept. This semi-submersible platform was designed by NREL for the OC5 research project, which focused on verifying and validating numerical tools for offshore wind energy [155]. In parallel to the OC5 work, the ‘TO2 Floating Wind’ research project focused on the simulation and the testing of FOWT including a test campaign at MARIN [54]. Experimental measurements, CFD results at small scale [54], and CFD results at full scale [55] are available.

The characteristics of the platform were slightly different from the original OC5 phase II project design due to experimental constraints, but the geometry remains the same. Details are presented in the following section. The OC5 simulations were conducted at full scale using engineering-level models. CFD has the capability to simulate the flow physics directly at model scale and so, to be as close as possible to the experimental conditions. In the present study, a small-scale CFD model was developed based on the ‘TO2 Floating Wind’ experiments. The results are compared to this experimental data and the small scale CFD results of Bruinsma et al. [53].

#### 7.1.2.1 Settings of the case

##### 7.1.2.1.1 Geometry of floater

The floater is a semi-submersible platform with three main columns that ensure stability and a central column on which the turbine is installed. The experimental tests and the CFD models were conducted at  $1/50^{\text{th}}$  scale. The geometry of the platform is presented in Figure 1.10. The main properties of the platform are presented in table 7.5.

<b>Total mass</b>	111.66 kg
<b>Ixx</b>	49.77 kg.m <sup>2</sup>
<b>Iyy</b>	47.56 kg.m <sup>2</sup>
<b>Izz</b>	43.81 kg.m <sup>2</sup>
<b>Draft</b>	0.4 m
<b>Water density</b>	998.6 kg/m <sup>3</sup>

TABLE 7.5: Main characteristics of the FOWT at model scale [53]

In the simulation, the length of the tank is reduced compared to the experimental setup to reduce the computational time. The consequences on the results are weak in the case of free-decay tests. The width of the tank  $W = 3.2$  m and the water depth  $d = 4$  m are the same as the experimental values. The origin of the coordinate system is located at the mean water level and the center of the central column.

#### 7.1.2.1.2 Mesh of the FOWT for free-decay tests

As for the simple cylinder case, an overset mesh method is used to model the motion of the body. As before, two meshes are generated: a background mesh and a fitted mesh around the FOWT. The meshes can be seen in figures 7.8 and 7.9.

The OpenFOAM® meshing tools blockMesh and snappyHexMesh are used to generate both meshes. The background mesh is composed of squared cells of side length  $l = 0.42$  m far from the zone of interest. The level tool of snappyHexMesh is used to refine the mesh near the free surface and in the zone where the floating body is expected to move. In both regions, a level 4 discretization is used, leading to squared cells of length  $l_{refined} = 0.026$  m. The background mesh can be seen on figure 7.8.

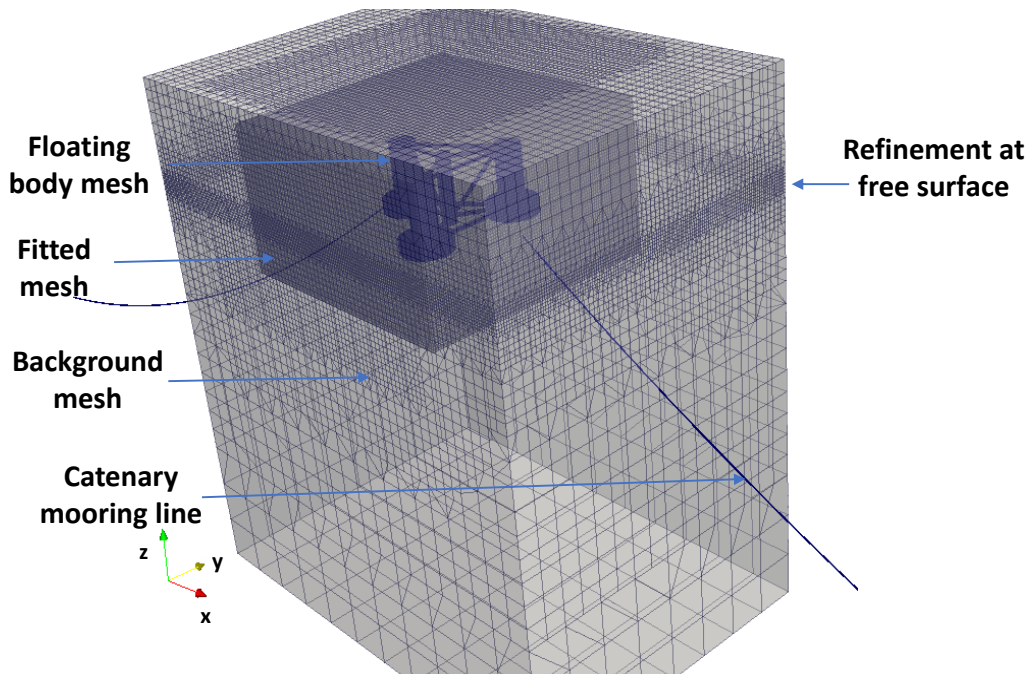


FIGURE 7.8: Overall mesh of the model for the free-decay tests of the deepCWind FOWT

The fitted mesh is generated around the FOWT. As required by overset mesh models. A global mesh is generated with cells size equal to the cell of the refined zone of the background mesh  $l_{refined} = 0.026$  m. The floater geometry is integrated into the mesh using the SnappyHexmesh module. The mesh is refined near the wall of the body and more precisely near the edges, as can be seen in figure 7.9.

The total number of cells is 4.2 million. This mesh might be considered too coarse to well capture the waves generated by the motion of the body, but it is large enough to get first good results in decay tests. A mesh convergence analysis will be carried out in future works.

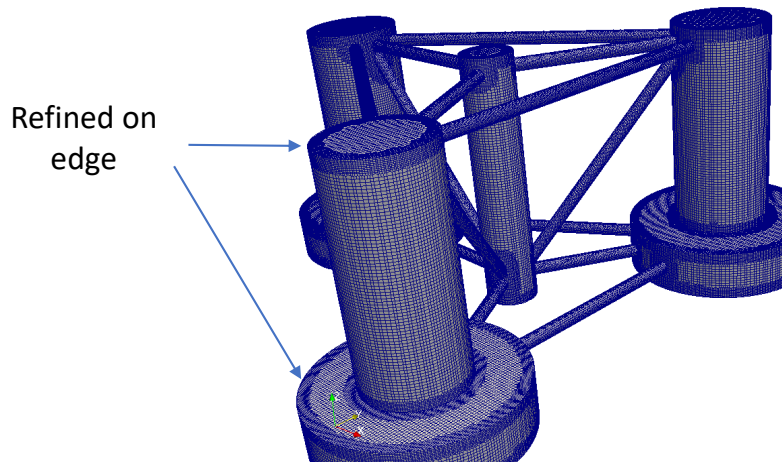


FIGURE 7.9: Mesh on the boundaries of the deepCWind FOWT

#### 7.1.2.1.3 Mooring system

The mooring system implemented in this model is based on the mooring system presented by Bruinsma et al. [156]. The experimental wave tank was not wide enough to install three catenary lines as in the OC5 project. Instead, the authors used 2 catenary lines in the  $x$  direction and two linear springs in the  $y$  direction. The properties of the overall mooring system are set up to get similar restoring forces as the OC5 system [54]. The positions of the anchor points and the fairleads are defined in table 7.6. In the case of catenary lines, the submerged weight is indicated whereas the stiffness is defined for the springs.

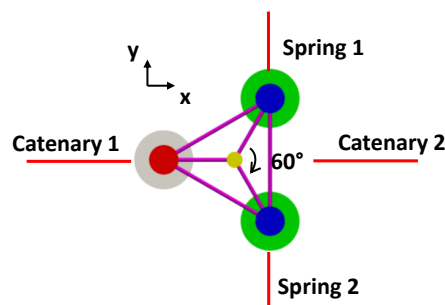


FIGURE 7.10: Mooring distribution for the DeepCWind FOWT based on the experimental model presented in [56]

	Catenary 1	Catenary 2	Spring 1 and 2
Submerged weight (N/m)/ Stiffness (N/m)	0.04348	0.04348	$k = 1.519$
Unstretched length (m)	18.38	16.71	-
Anchor (m)	(18.43, 0, -4.0)	(-16.76, 0, -4.0)	(-0.408, $\pm 2$ , 0.2)
Fairlead (m)	(0.818, 0, -0.28)	(-0.818, 0, -0.28)	(-0.408, $\pm 0.62$ , 0.2)

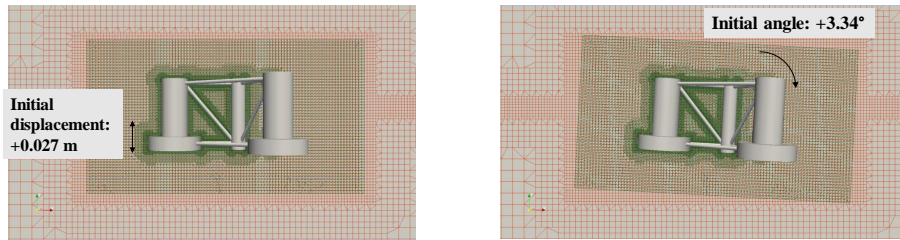
TABLE 7.6: Mooring characteristics for the DeepCWind FOWT based on the experimental model presented in [56]

#### 7.1.2.1.4 Boundary conditions

The boundary conditions of the FOWT case are similar to the boundary conditions of the floating cylinder case (cf. table 7.1).

#### 7.1.2.2 Results

This section presents the results in free-decay test of the previously described FOWT. The CFD results are computed using the overset mesh technique and are compared with the experimental results and numerical results of Bruinsma et al. [53]. In their work, the mesh morphing technique, also available in OpenFOAM®, is used. In all simulations, the six DoF are enabled.



(A) Heave initial position : +0.027 m

(B) Pitch initial position : +3.34°

FIGURE 7.11: Initial position of the free-decay tests. The orange mesh is the background mesh, the green mesh is the overset mesh

#### 7.1.2.2.1 Free-decay test in heave motion

A free-decay test in heave was first carried out. The FOWT was initially displaced 0.027 m up from its theoretical equilibrium position (figure 7.11a). However, the numerical draft was found to be larger than the theoretical draft when using the parameters of the experimental data of Bruinsma et al. [53]. This can be explained by a lack of mesh refinement. To be in line with the reference results, the mean vertical position has been set to 0 for the overset results presented. Figure 7.12 shows the comparison of the time series of the overset case with the results of Bruinsma et al. [53]. The time is normalized by the experimental natural period  $T = 2.47$  s. The amplitude is normalized by the initial displacement.

The period of the overset mesh simulation is in good agreement with the experimental results. The damping of the oscillation is similar to the damping of the results from the mesh morphing method used by Bruinsma et al. [53]. However, it is higher than the experimental damping (table 7.7). In the case of overset mesh, it can be explained by a mesh too coarse or a time step too large. The choice of a first-order temporal discretization scheme might also lead to higher numerical damping. Mesh

and time step convergence studies should be done to fully validate this case. Higher-order schemes could also be used.

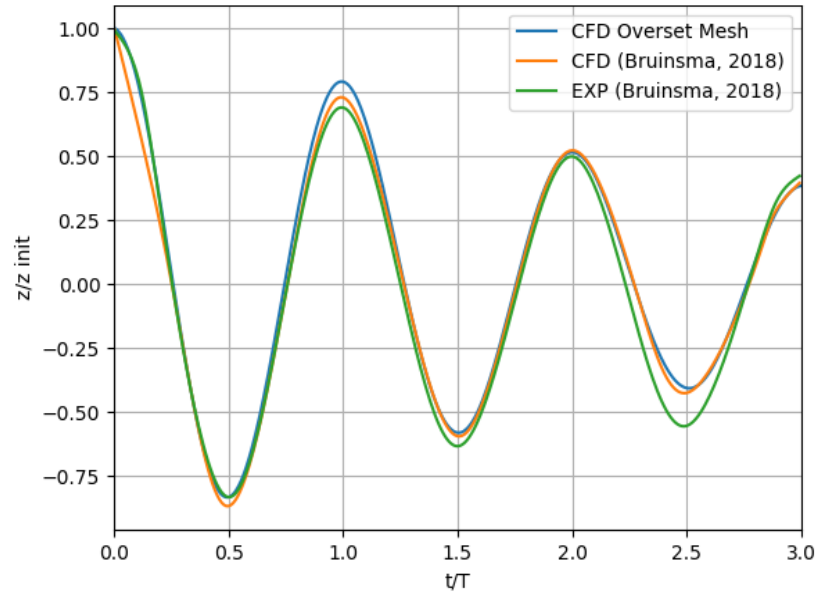


FIGURE 7.12: Comparison of the time series for the heave decay test of the FOWT normalized in time by the experimental natural period  $T = 2.47$  s and by the initial displacement  $z_{init} = 0.027$  m

#### 7.1.2.2.2 Free-decay test in pitch motion

Then, a free-decay test in pitch was computed for the FOWT. The platform was initially tilted  $3.34^\circ$  around  $y$ -axis from its theoretical equilibrium position (figure 7.11b). Figure 7.13 shows a comparison of the tilt angle time series of the overset mesh case with the results of Bruinsma et al. [53]. The time is normalized by the experimental natural period  $T = 4.68$  s. The pitch angle is normalized by the initial tilt angle.

The period of the overset mesh simulation is also in good agreement with the experimental results. However, the damping of the oscillations is smaller than the experimental damping and the numerical damping of Bruinsma et al. [53]. This discrepancy can be due to the difference in water density, mass, or CoG position with the experimental setup. The friction between the mooring and the basin bottom is not modeled in this work and this might also be a source of discrepancies. The absence of a turbulence model could be another source of differences. Vortex shedding may appear around the heave plates or near the braces and have not been considered here.

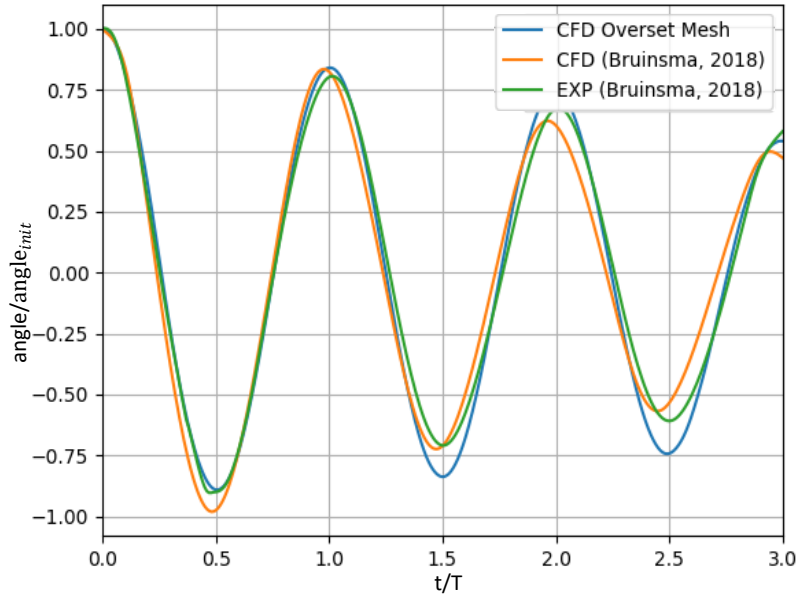


FIGURE 7.13: Comparison of the time series for the pitch decay test of the FOWT normalized in time by the experimental natural period  $T = 4.68$  s and by the initial tilt angle  $angle_{init} = 3.34^\circ$

The natural periods and the damping coefficients in heave and pitch of the DeepCWind platform (table 7.7) are obtained from three successive positive peaks using the method described in paragraph 7.1.1.2.4.

	Natural period (s)			Damping coef. (-)		
	Overset	Exp	Rel. error (%)	Overset	Exp	Rel. error (%)
Heave	2.47	2.47	0	0.055	0.052	5.8
Pitch	4.67	4.68	-0.2	0.023	0.031	-25.8

TABLE 7.7: Natural periods and damping coefficients of the free-decay tests for the DeepCWind cases

From table 7.7, it can be observed again that the overset mesh model predicts well the natural periods of the FOWT for the heave and pitch motions with a relative error of less than 1%. The damping coefficient of the decay test in heave is slightly over-predicted in the CFD case whereas the damping coefficient in pitch is largely under-predicted. Disturbances in the experimental set-up could be a cause of discrepancies as mentioned in [56].

## 7.2 Wave Induced Motion

### 7.2.1 Validation with a small scale model

The numerical tool and the meshing process described in chapters 2 and 3 are used to model a FOWT structure with the overWaveDyMFoam solver. The geometry of the DeepCWind described in section 7.1.2 with the mooring system is used. Experimental data of the motions of the structure in waves are available in [53] and [56]. In this

study, a 3D 1/50<sup>th</sup> lab-scale model is presented. A fifth-order Stokes regular wave of period  $T = 1.71$  s and height  $H = 0.14$  m is generated.

### 7.2.1.1 Description of the case

The DeepCWind floater is considered in this section with the same characteristics as presented in the free decay analysis. The dimensions of the structure are presented in figure 1.10. In the simulation, the waves are propagating along the positive  $x$ -axis, so the red column in figure 1.10 is the upstream column. Moreover, there is a plane of symmetry of the structure perpendicular to the  $y$ -axis, so the motions of the structure are mainly the heave (translation along  $z$ -axis), the pitch (rotation around  $y$ -axis) and the surge (translation around  $x$ -axis) motions. The simulation is carried out only on one half of the domain to reduce the computational cost (figure 7.14). The rotations around the  $x$ -axis (roll) and  $z$ -axis (yaw) and the translation along the  $y$ -axis (sway) are constrained. Again, no turbulence closure model is used in this model. The global characteristics of the model are described in table 7.8. The mass and the moments of inertia around the CoG of the numerical model replicate the experimental setup. However, a difference of 3% of the draft is observed between the two models. A similar difference was observed in [53] and [56]. This difference might be explained by experimental uncertainties or mesh refinement. The water depth of the NWT (2.4 m) was reduced compared to the depth of experimental facility (4 m) to reduce the computational cost. The numerical water depth was chosen to respect the deep-water regime, so the impact on the results can be neglected.

<b>Total mass</b>	111.66 kg
<b>Iyy around CoG</b>	47.56 kg.m <sup>2</sup>
<b>Targeted draft (experimental)</b>	0.4 m
<b>Computed draft (numerical)</b>	0.412 m
<b>Water density</b>	998.6 kg/m <sup>3</sup>
<b>Distance from keel to COG</b>	0.2386 m
<b>Numerical water depth</b>	2.4 m

TABLE 7.8: Main characteristics of the FOWT at model scale [53]

The numerical input and boundary conditions are similar to the ones presented in the 2D case presented in chapter 4, and in accordance with the convergence analysis of chapter 3. The acceleration relaxation method with a coefficient  $f_a = 0.6$  was used and showed a good convergence of the body acceleration. The maximum time step is set to  $\delta_t = T/1700 = 0.001$  s. In the numerical model, the mass and the moments of inertia were divided by 2 compared to the data from table 7.8 because of the use of a plane of symmetry. The generation zone is one wavelength long, the propagation zone is 2 wavelength long, and the absorption zone is 2 wavelength long. The mooring system is the same as for the free-decay test (cf. section 7.1.2). Due to the use of a symmetry plane, only one spring line is represented in the NWT. Moreover, the masses of the catenary lines located in the symmetry plane are divided by 2.

#### 7.2.1.1.1 Computational Meshes

Similar to the free-decay case, two meshes are generated: a background mesh (in blue in figure 7.14) and an overset mesh around the structure (in red). The meshing process described in chapter 2 is implemented. In the free surface vicinity, 5 cells per wave amplitude are used (figure 7.15). Far from the structure, the cell size of the overset mesh is the same as the size of the refined box of the background mesh as

shown in figure 7.15. The overset mesh is refined near the edges of the structure to better capture the sharp angles (figure 7.15). The aspect ratio is 1 in the propagation zone. There is no cell contraction used in the  $y$ -direction. The cells far from the floater in the overset mesh have the same size as the cells in the free surface vicinity and in the refined box of the background mesh where  $\delta x = \delta y = \delta z = 0.014$  m.

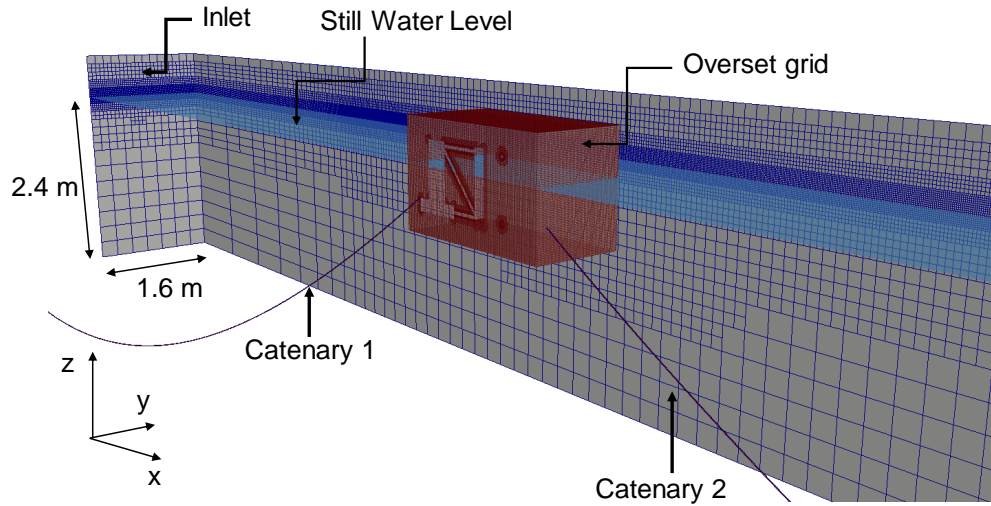


FIGURE 7.14: Global mesh of the FOWT numerical wave tank. The red cells are the overset mesh and the dark blue cells are in the background mesh. The light blue represents the free surface

A vertical slice of the grids, in the plane of symmetry, is shown in figure 7.15. The blue cells are the cells of the background mesh and the red cells are the cells of the overset mesh. The dimensions of the overset mesh are chosen to guarantee that there are at least 10 cells between the wall of the structures and the side of the overset mesh. Similar to the 2D case, the size of the refined box in the background mesh ensures that the overset mesh will remain in that refined zone. The dimensions are shown in figure 7.14. The refined zone in the free surface vicinity is  $2H$  high.

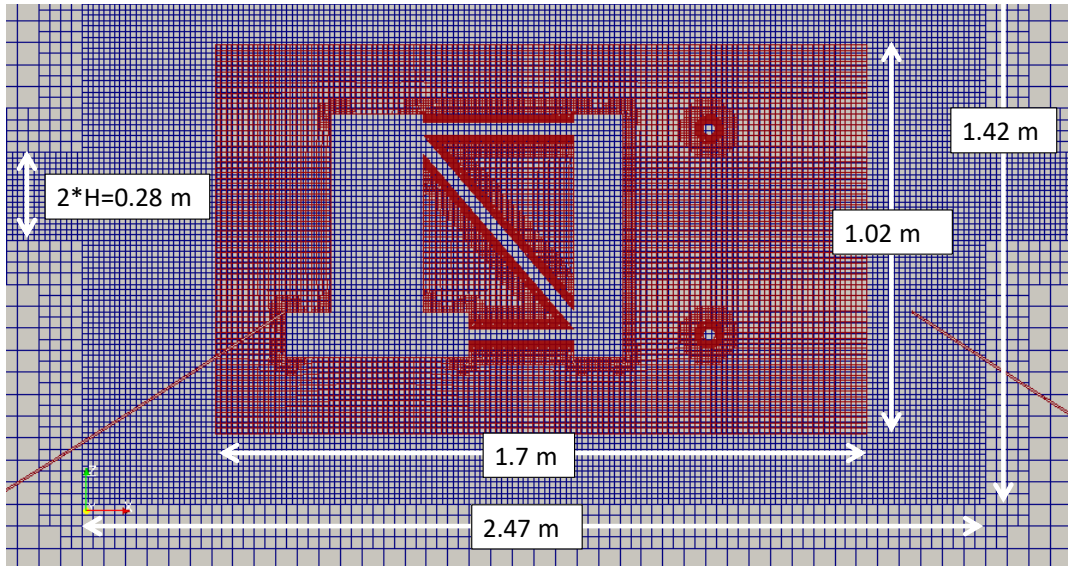


FIGURE 7.15: Vertical slice of the mesh of the FOWT. Blue cells are in the background mesh and red cells are in the overset mesh. The red lines are the catenary mooring lines

The background mesh is composed of 4.3 million cells and the overset mesh is composed of 1 million cells. So, the total number of cells for this model is 5.3 million. It should be noted that the wave conditions of this 3D case are less steep than the conditions previously presented in the 2D model in section 4.2. So, even if a refinement of 5 cells per wave amplitude has shown some discrepancies in the 2D model, this refinement shows good results in 3D for an acceptable computational cost (compared to 10 cells per amplitude, for instance).

#### 7.2.1.1.2 Wave calibration

As done previously, a wave only case is carried out to verify the quality of the wave generated in the NWT. However, it has been observed that the quality of the generated wave with the `overWaveDyMFoam` solver deteriorates as waves propagate along the domain. The wave amplitude at the structure location is constantly lower than the expected amplitude as shown in figure 7.16, leading to an error of around 10%. At this stage of the research, the reason for these discrepancies has not been found and should be investigated in future developments of the solver. The first investigation track concerns the boundary conditions at the inlet. Indeed, `overWaveDyMFoam` does not support the "wave velocity" boundary conditions that were used with the `waveFoam` solver. In place, a "fixed 0 value" condition was imposed at the inlet for overset mesh analyses.

To counteract this issue, the wave is first generated with the expected wave amplitude, then the gap between the computed amplitude and the target one is assessed and the input of the wave amplitude imposed at the boundary is tuned accordingly. As shown in figure 7.16, the tuned wave height matches the targeted one.

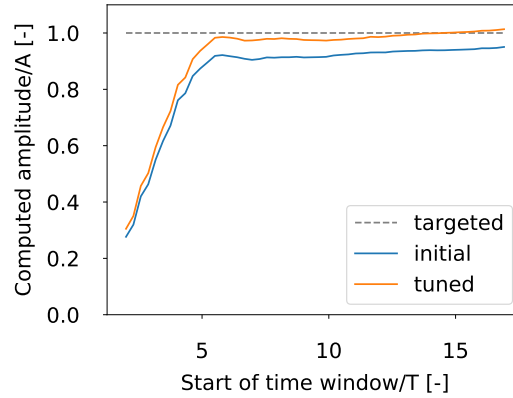


FIGURE 7.16: First order wave amplitude of the Fourier analysis on a sliding time window using overWaveDyMFoam solver

## 7.2.1.2 Results

### 7.2.1.2.1 Position

The free surface elevation at the center of the platform when there is no structure is presented on top of figure 7.17. The heave, pitch, and surge motions are also presented in the subsequent panels of this figure. The free surface elevation, the heave, and the surge positions are normalized by the wave amplitude. The time is normalized by the wave period. The results are compared with the experimental results extracted from [56]. There is no experimental result available for surge motion.

To balance a difference in wave tank length and ramp time, the experimental results of free surface elevation, heave, and pitch motions are shifted to get the free surface elevation time series in phase with numerical results. The relative phase difference is then maintained and applied to all time-series. The measured and computed wave elevation time series are in good agreement. The phases of the heave and pitch motions are in good agreement with the experimental phases as well. The amplitudes of both motions are slightly under-predicted in the numerical model. A low-frequency component can also be observed in the pitch response of the numerical model. Rivera et al. [56] also observed a similar low-frequency component and suggested that the floater is excited at its natural frequency by the third harmonic of the incident wave. The influence of the natural frequencies of the wave tank could also be investigated.

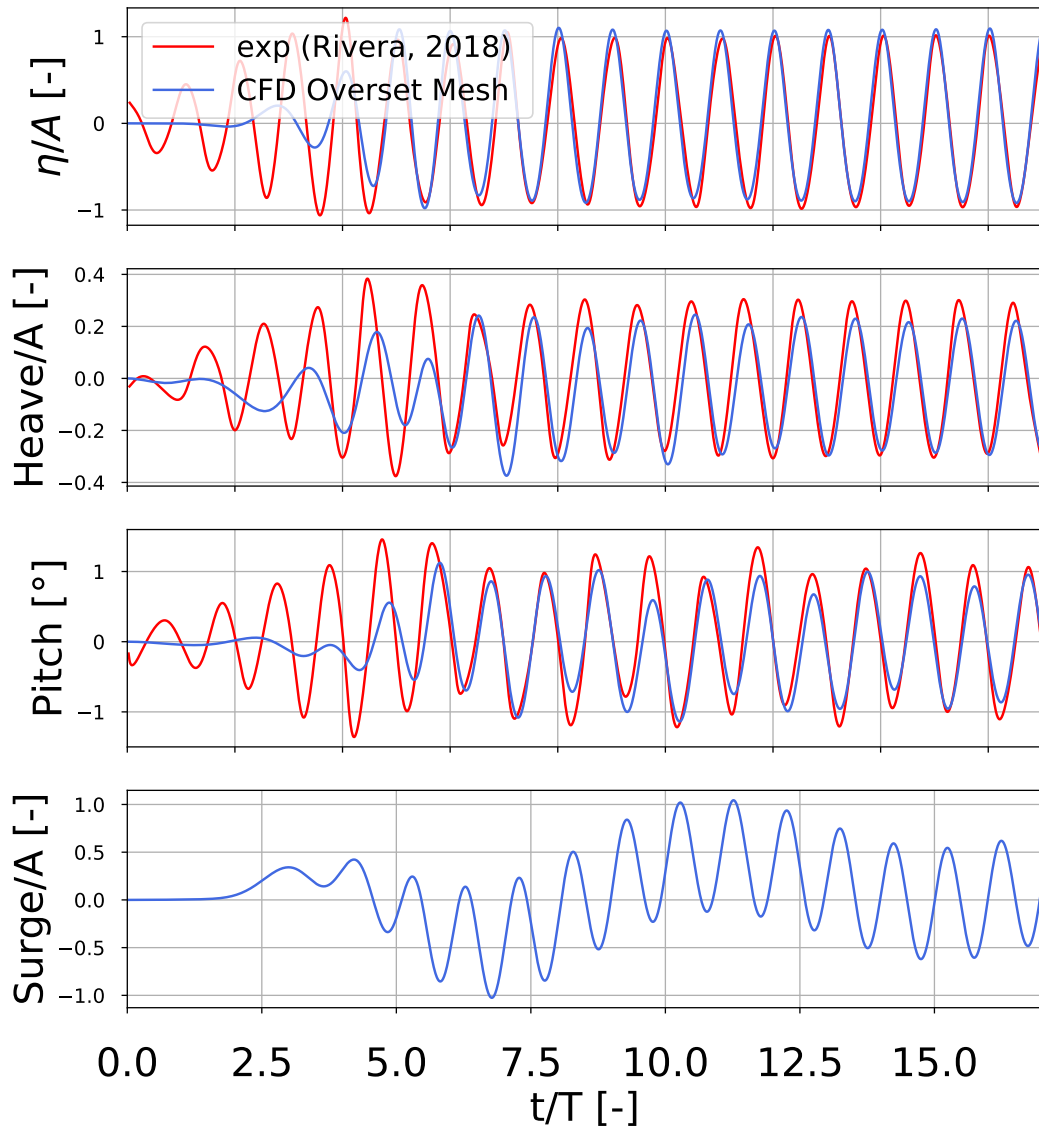


FIGURE 7.17: Time series of free surface elevation, heave pitch and surge positions. The blue lines are the results from the present CFD model, the red lines are the experimental results from [56]. Small scale:  
 $T = 1.71$  s  $A = 0.07$  m

The amplitudes of the RAOs of motion normalized by the incident wave amplitude are presented in figure 7.18. The CFD results slightly under-predict the experimental measurements, but overall the results are in good agreement.

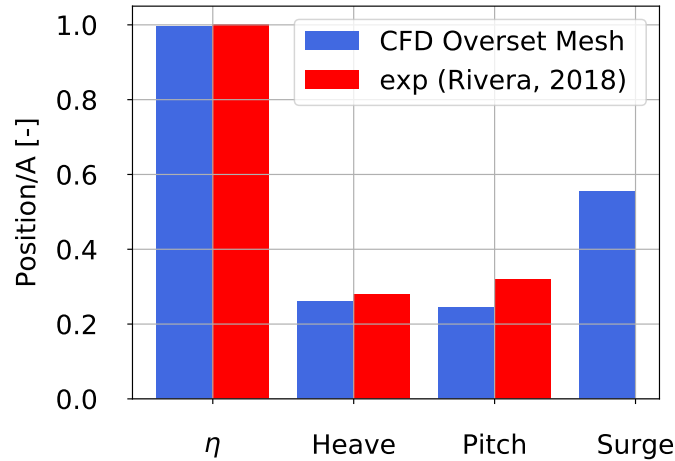


FIGURE 7.18: Modulus of the RAO for free surface elevation, heave, pitch, and surge motions. The blue bars correspond to the present CFD model and the red bars correspond to the experimental results from [56]. Small scale:  $T = 1.71$  s  $A = 0.07$  m

### 7.2.1.2.2 Run-up of the upstream column of the FOWT

Another important piece of information for the design of FOWT is the assessment of the run-up on the structure to calibrate the minimum air gap between the SWL and the top side of the platform. The run-up on the upstream column over one wave period is presented in figures 7.19 and 7.20 from the fore and the port sides respectively.

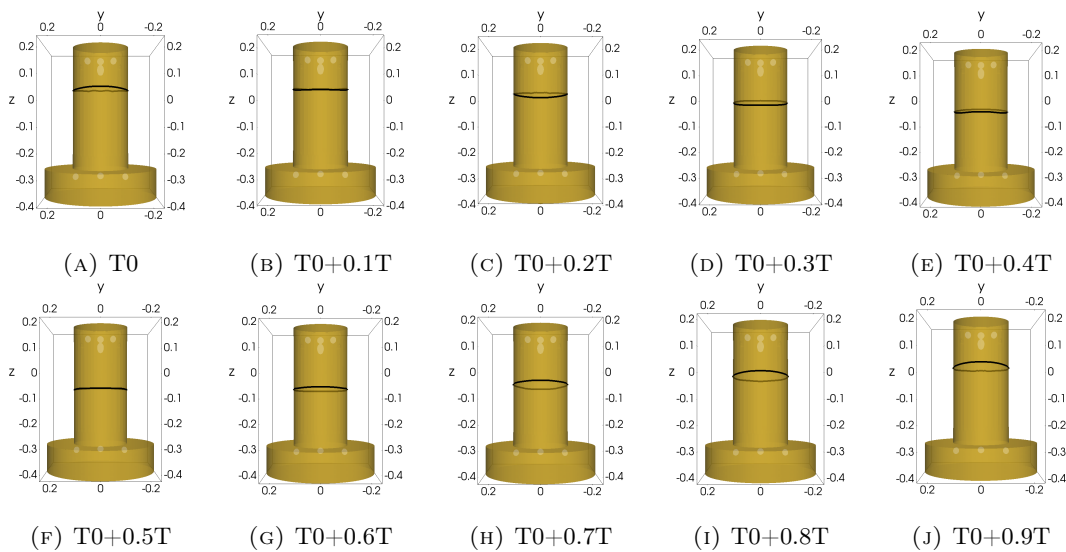


FIGURE 7.19: Run-up around the upstream column during one wave period. Fore side view. Small scale:  $T = 1.71$  s  $A = 0.07$  m

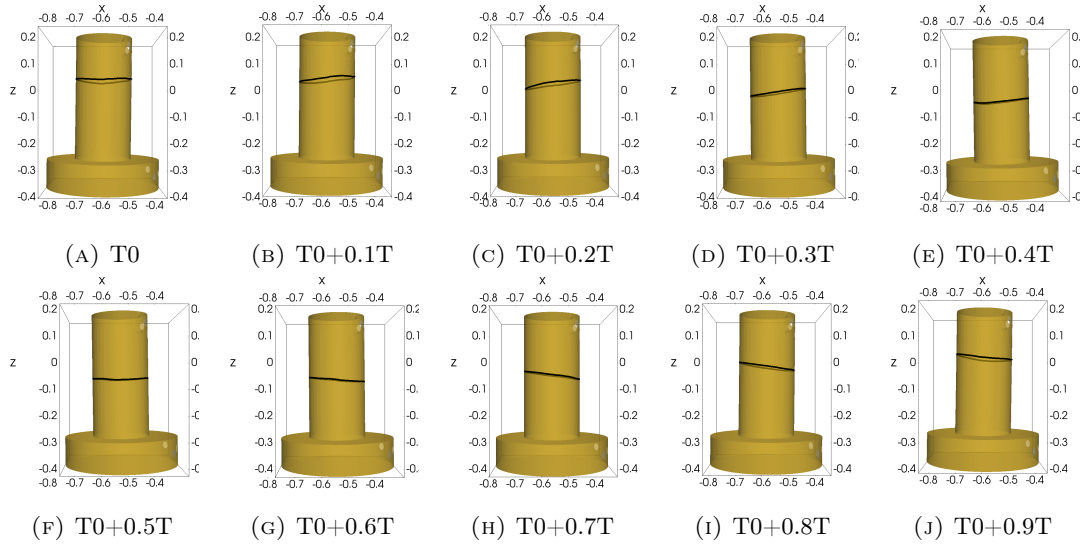


FIGURE 7.20: Run up around the upstream column during one wave period. Port side view. Small scale:  $T = 1.71$  s  $A = 0.07$  m

### 7.2.1.2.3 Interaction between the free surface and the structure

The propagation of the wave near the structure is shown in figure 7.21 during one wave period. The colour scale represents the velocity magnitude on the free-surface. As a reminder, only half of the flow was modeled, the other half is obtained by the symmetry of the results. The boundaries between the background and the fitted mesh can be observed in transparency. Overall, good continuity of the velocity field is observed at these boundaries. The wave elevation is not impacted by the boundaries of the overset mesh. On figure 7.21d or 7.21e, it can be observed that the flow is accelerated on the starboard and port sides of the column and that a wake appears at the fore and aft of the columns.

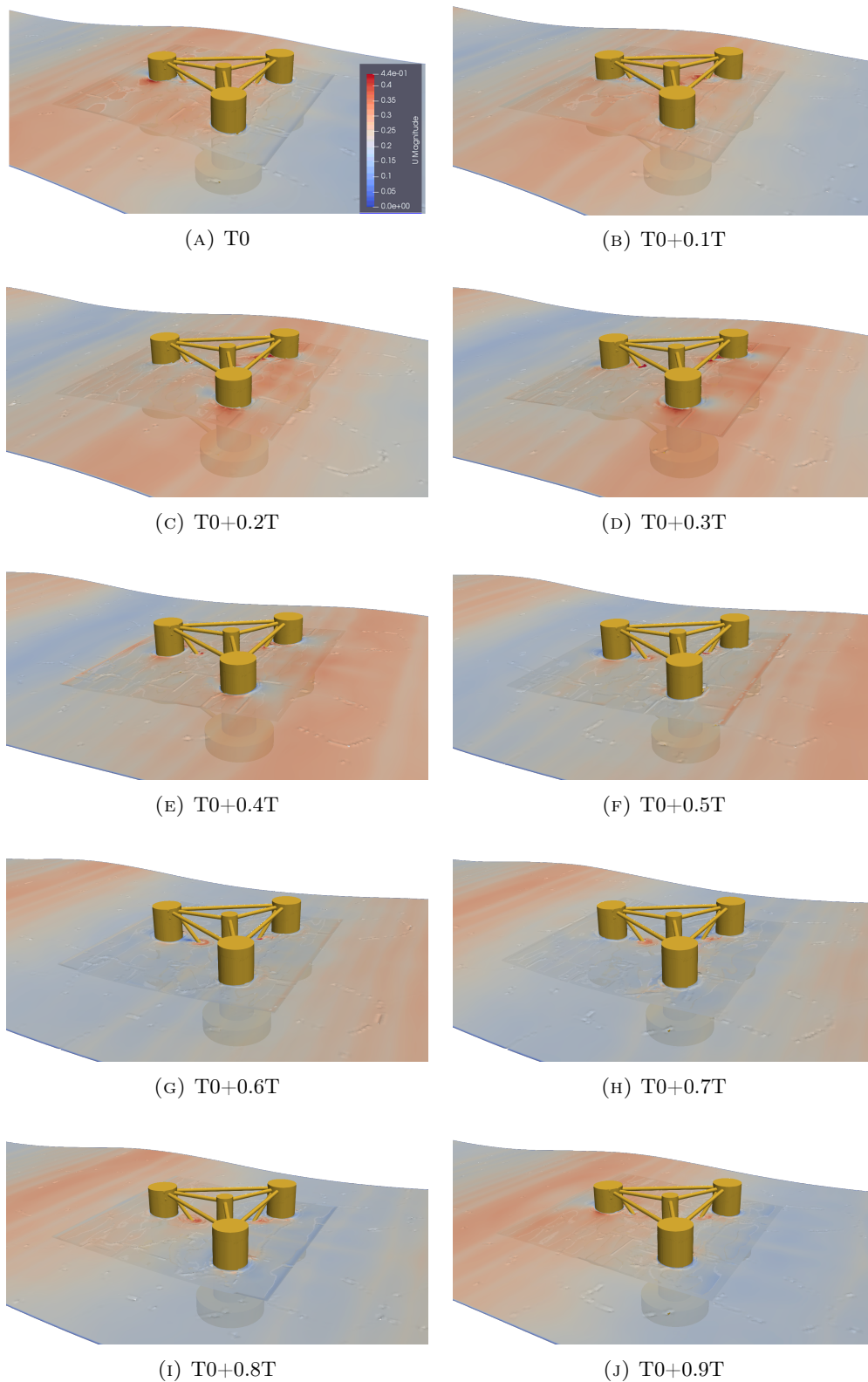


FIGURE 7.21: Velocity magnitude of the flow at the free surface near the structure. Small scale:  $T = 1.71$  s  $A = 0.07$  m

## 7.2.2 Hydrodynamic response of FOWT in regular waves for different values of wave steepness

In this section, the response of the DeepCWind platform to regular waves is investigated for several wave conditions. Three wave periods are considered, namely 12.1 s, 14.3 s, and 20 s (at full scale). For each period, different wave amplitudes are considered to investigate the effect of nonlinearities. The CFD results are compared with experimental and potential-flow model results from [98]. WAMIT and FAST codes were used by Coulling et al. [98] to compute the diffraction/radiation wave forces. A quadratic drag model is also implemented in the FAST model. A more detailed description of the method can be found in [98]. The same cases were also investigated with a CFD model in [65] and [94]. Liu et al. [65] used OpenFOAM with a sliding mesh technique to deal with the moving body. Tran et al. [94] also used the overset mesh technique, but with the software StarCCM+. Masciola et al. [99] also investigated these wave cases and compared the experimental results with a model based on a coupling between FAST and OrcaFlex.

### 7.2.2.1 Description of the case

In these cases, the floater is modeled at full scale. The geometry of the structure is the same as the one used in the previous section and described in figure 1.10. However, the characteristics of the platform are slightly different. These properties are extracted from [65] and are summarized in table 7.9. The origin of the referential is at the intersection between the SWL and the center-line of the platform.

<b>Total mass of the system</b>	14,143,400 kg
<b>System CM location below SWL along platform center-line</b>	10.21 m
<b>Pitch moment of inertia about system CM</b>	1,316,571,010 kg.m <sup>2</sup>

TABLE 7.9: General characteristics of the FOWT [65]

The mooring system is also different in this model. Three catenary lines are connected to the three columns of the platform, as shown in figure 7.22. The characteristics of the lines are summarized in table 7.10.

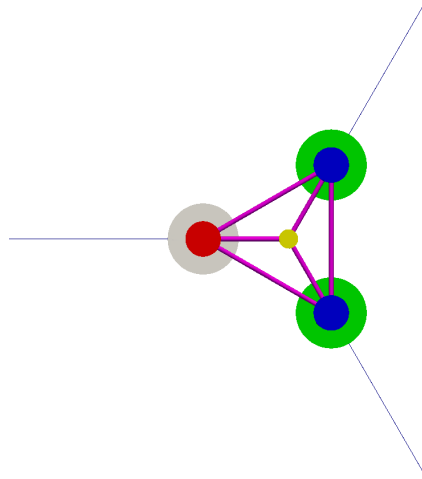


FIGURE 7.22: Catenary mooring positions on the floater based on the experimental campaign of [98]

<b>Number of mooring lines</b>	3
<b>Angle between adjacent lines</b>	120°
<b>Depth to anchors below SWL</b>	200 m
<b>Depth to fairleads below SWL</b>	14 m
<b>Unstretched mooring line length</b>	835.5 m

TABLE 7.10: Mooring lines characteristics [65]

The domain and the mesh of the model follow the method described in chapter 3. In all simulations of this section, 5 cells per wave amplitude are used in the refinement zone of the free surface and the refined box of the background mesh. The aspect ratio in the propagation zone is set to 1. The mesh is refined in the vicinity of the structure. The generation zone is 1 wavelength long, and the relaxation zone is 2 wavelengths long. The PISO algorithm is used with 3 inner iterations, and a laminar flow assumption is considered. As in the previous model, only half of the domain is considered, and the symmetry of the flow is used. So, 3 DoF are investigated: the surge, the heave, and the pitch motion. The other motions are constrained.

### 7.2.2.2 Wave Calibration

Table 7.11 summarizes the wave characteristics of the cases presented in this section. It includes the wave amplitude  $A$ , the wave period  $T$ , the wavelength  $\lambda$ , and the steepness of the wave ( $H/\lambda$ ). The period  $T = 20$  s is close to the natural period of heave motion. These wave conditions are the ones presented in the experimental analysis of [98], except for case 3 with the largest steepness, added here for the investigation of high steepness waves.

	<b>A (m)</b>	<b>T (s)</b>	<b><math>\lambda</math> (m)</b>	<b>steepness (%)</b>
<b>case 1</b>	3.79	12.1	233.0	3.25
<b>case 2</b>	5.15	12.1	233.0	4.42
<b>case 3</b>	6.9	12.1	233.0	5.92
<b>case 4</b>	3.57	14.3	320.2	2.22
<b>case 5</b>	5.37	14.3	320.2	3.36
<b>case 6</b>	3.79	20	605.7	1.26
<b>case 7</b>	5.56	20	605.7	1.84

TABLE 7.11: Parameters of the simulated wave cases

The method for wave calibration described in section 7.2.1.1.2 is also used in this analysis to ensure the quality of the generated waves. Again, the waves modeled with the solver `overWaveDyMFoam` have a lower amplitude than imposed. So the waves are tuned to match the targeted amplitude in the 2D NWT. Figure 7.23 shows the first-order amplitude of the wave over time at the location of the platform but without structure for cases 4, 5, 6, and 7. The same method was used for cases 1 to 3. The tuned waves are imposed in the 3D models of the next section.

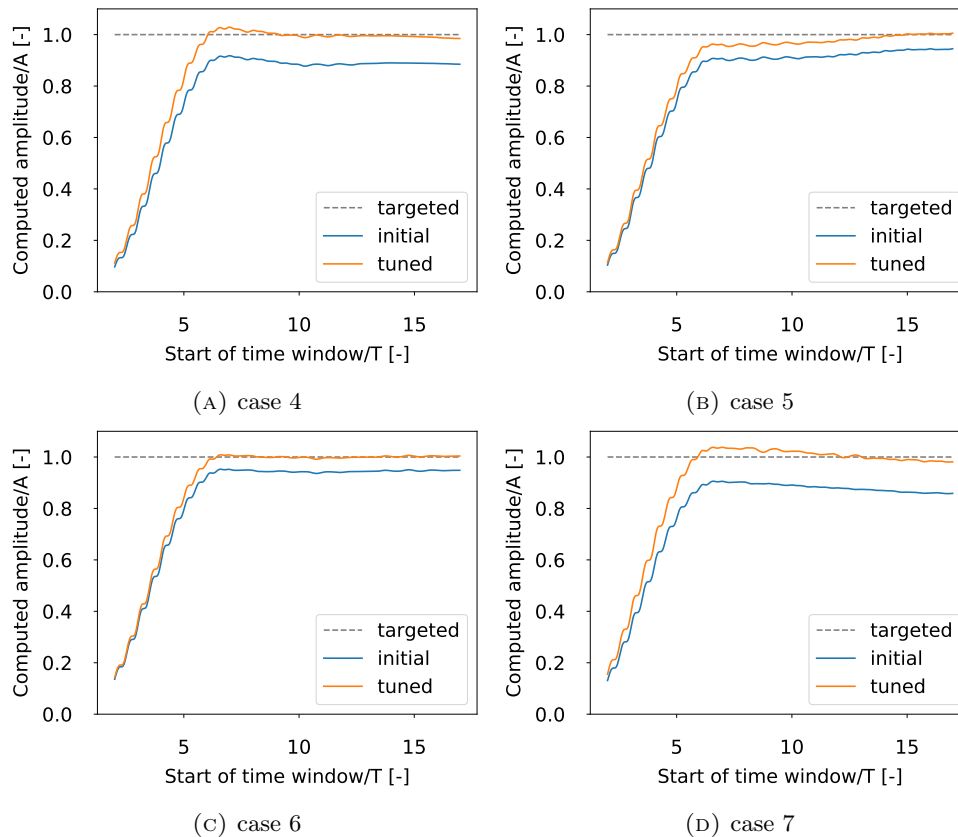


FIGURE 7.23: First order wave amplitude of the Fourier analysis on a sliding time window using `overWaveDyMFoam` solver. Initial and tuned wave conditions

### 7.2.2.3 Results of motions of the FOWT

The RAO amplitudes for surge, heave, and pitch motions are computed with the CFD model and compared with the experimental measurements and the FAST potential flow results of Coulling et al. [98]. The purpose of this analysis is to investigate

the nonlinearities of the floater response. The results of the wave cases 1 to 7 are presented in figure 7.24. The amplitude of motion is normalized by the incident wave amplitude. There are no experimental or FAST results for the case 3 in [98]. In figure 7.25, the amplitudes of RAOs of the CFD model are compared to a continuous distribution of the RAO amplitudes measured with irregular waves of significant wave height  $H_s = 11.3$  m and a broad-band, white noise spectrum, during experimental tests of Coulling et al. [98]. FAST simulation results from [98] of this irregular wave case are also presented. This comparison aims to have a qualitative idea of the RAOs amplitude on a broad wave spectrum. However, it should be noted that the regular waves modeled in CFD have a different steepness from the irregular wave model. The results should not be compared quantitatively. Amplitudes of the RAOs of the forces and moments on the global structure can also be found in appendix B.

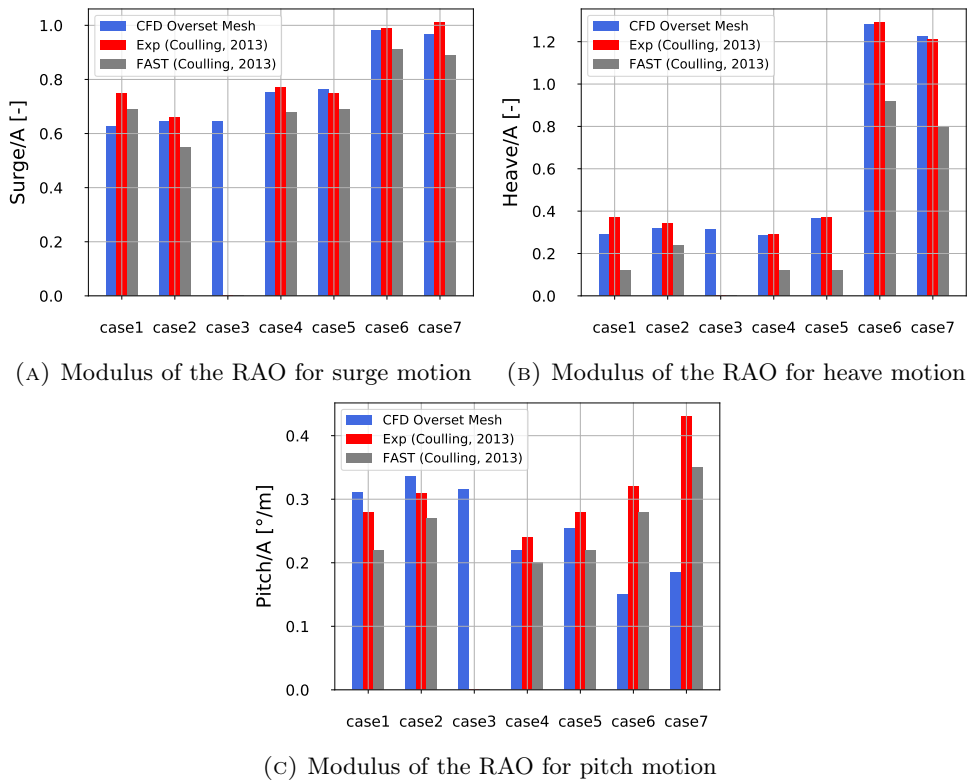


FIGURE 7.24: Modulus of the RAO for surge, heave, and pitch motions. The blue bars correspond to the present CFD model, the red and grey bars correspond to the experimental and FAST results respectively, taken from [98].

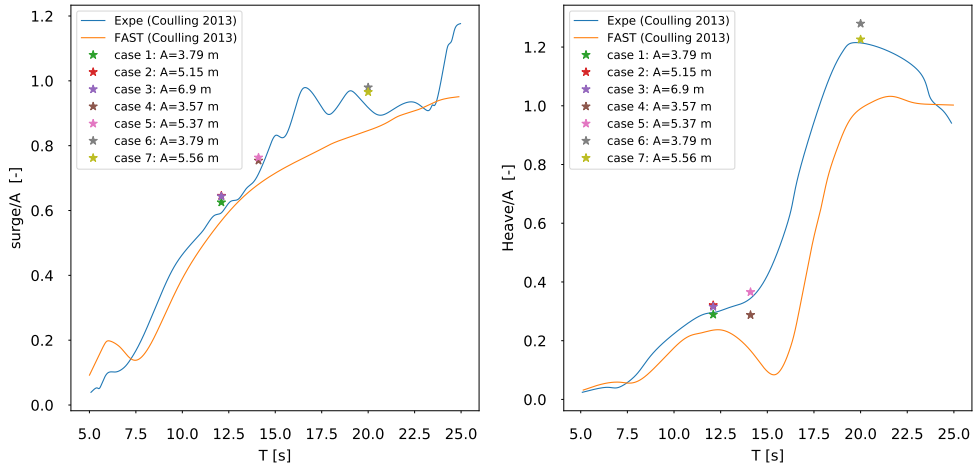
Overall, the CFD results are in good agreement with the experimental measurements and can better predict the platform motions than FAST, except for the pitch motion of cases 6 and 7.

The surge motion computed with CFD shows good agreement with experimental data for all cases, even though CFD tends to slightly under-predict the surge amplitude of the experimental measurements. The surge motion is mostly driven by the mooring system. So, the simplified quasi-static mooring model used in this analysis is sufficient in these load cases. It plausible that a more complex mooring model could improve even more the results. Few nonlinearities can be observed when comparing the normalized amplitude of two cases with the same wave period. The surge motion

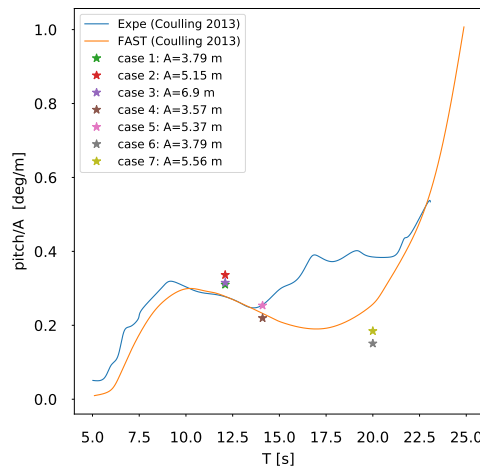
amplitude is increasing linearly with the wave period as shown in figure 7.25. The periods investigated in this analysis are far from the resonance period of the system (estimated at 107 s in [98]).

In heave motion, the CFD results also predict well the amplitude for all the cases. The CFD results are closer to the experimental measurements than the FAST results of Coulling et al. [98]. For the periods  $T = 12.1$  s and  $T = 14.3$  s, the heave amplitude is low (between 20% and 40% of the wave amplitude). These structures (columns with thick damping plates) are designed to have a "cancellation period", where the vertical diffraction forces are canceled. This period is usually chosen to be the dominant wave period of the sea state considered for the design of structure. This phenomenon has already been highlighted in 2D (see chapter 4). In 3D the "cancellation period" can be observed around 16 s on the RAO of heave motion of the potential-flow results from FAST presented in figure 7.25b. Near this "cancellation period", the viscous forces dominate over the diffraction forces. In figure 7.25b, the amplitude of RAO for the FAST results is smaller than the experimental data. It seems that the empirical drag coefficients imposed in the model were overestimated. In the CFD model, there is no need to add empirical data and the viscous contribution seems well captured. The simulation of cases 1 to 5 have periods close to this cancellation period, and so the response amplitude in heave is low. On the contrary, for  $T = 20$  s, the amplitude of heave motion is very large. This period is closer to the heave natural frequency (17.5 s according to [98]). So the amplitude of the RAO is large (around 120% of the wave amplitude). In this case, the diffraction/radiation forces dominate over the viscous contribution.

Finally, the pitch motion amplitude is investigated. The CFD results of the 2 lowest wave periods ( $T = 12.1$  s and  $T = 14.3$  s) are in relatively good agreement with the experimental data. The pitch amplitudes for the cases for  $T = 12.1$  s are slightly over-predicted whereas, for  $T = 14.3$  s, the measured amplitudes are slightly under-predicted. In the case of  $T = 20$  s, the CFD results are largely lower than both the measurements and the potential-flow results. This large difference is somewhat surprising, considering that the 4 other cases show good predictions in pitch and that the predictions for the other motions at this period are good. This discrepancy might be caused by a difference between the position of the CoG in the experimental case and the numerical model resulting in a difference in pitch motion, amplified at this wave period.



(A) Modulus of the RAO for surge motion (B) Modulus of the RAO for heave motion



(c) Modulus of the RAO for pitch motion

FIGURE 7.25: Modulus of the RAO for surge, heave, and pitch motions. the stars correspond to the regular wave cases, the blue and orange lines are the experimental and FAST results of Coulling [98] from an irregular wave spectrum.

The time series for each wave period with different wave amplitudes are presented in figure 7.26 for  $T = 12.1$  s, figure 7.27 for  $T = 14.3$  s and figure 7.27 for  $T = 20$  s to emphasize the nonlinearities. On these figures, the time is normalized by the wave period and the amplitude of motion is normalized by the wave amplitude. Time series of the forces and moment on the global structure can be found in appendix B.

In the case of  $T = 12.1$  s, it can be observed, in figure 7.26, that the mean surge position of case 2 is larger than those for case 1 or 3. This result is unexpected as the drift force and so the mean position is expected to increase with wave amplitude. This difference seems to be reduced after the 18<sup>th</sup> wave period. So, it is likely that this mean position is only observed in the transient state and converges toward the mean position of the two other cases in the steady-state regime. The simulation should be run on more wave periods to confirm this hypothesis. It should be noted the the pitch moment of this same wave case shows lower mean value than the other cases at the beginning of the simulation (figure B.3). This mean values also converges toward the mean value of the other cases. These two phenomena might be linked. In all three cases, the platform is excited at a low frequency in surge motion. Again, a longer

run should be carried out to investigate this excitation frequency. However, it can be noted that the surge period and amplitude, at the wave frequency, are mostly constant with wave amplitude increase. It confirms what was observed in figure 7.25a, namely that the steepness increase has only a limited impact on the surge motion.

Concerning the heave position, nonlinearities can be observed for the 2 lowest wave period cases (middle graph of figures 7.27 and B.4). In both cases, the heave response increases mildly with wave amplitude. However, for  $T = 20$  s, the time-series of cases 6 and 7 are perfectly superimposed (figure 7.28). It shows that, for this period, the response is linear with wave amplitude. It confirms what was explained before: the nonlinear drag forces dominate for  $T = 12.1$  s and  $T = 14.3$  s, whereas linear diffraction/radiation heave forces dominate for  $T = 20$  s.

For the three periods, the pitch response shows nonlinearities (bottom graph of figures 7.28, 7.27 and 7.28). The amplitude of heave motion increases with wave amplitude.

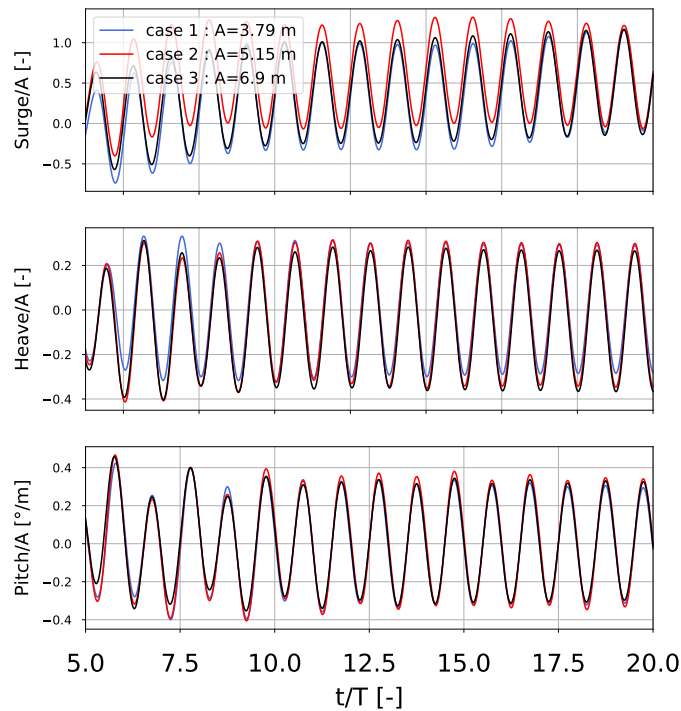


FIGURE 7.26: Time series of surge heave and pitch positions for 3 wave amplitudes.  $T = 12.1$  s

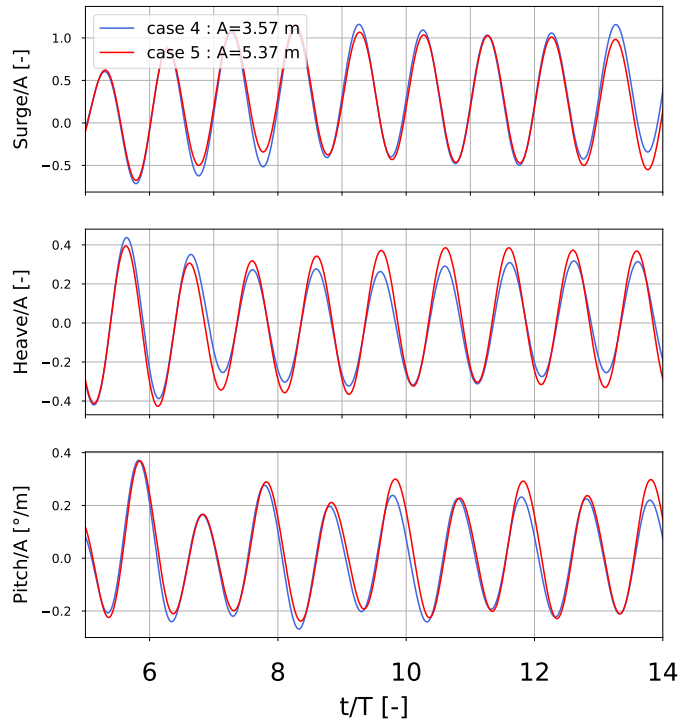


FIGURE 7.27: Time series of surge heave and pitch positions for the 2 wave amplitudes.  $T = 14.1$  s

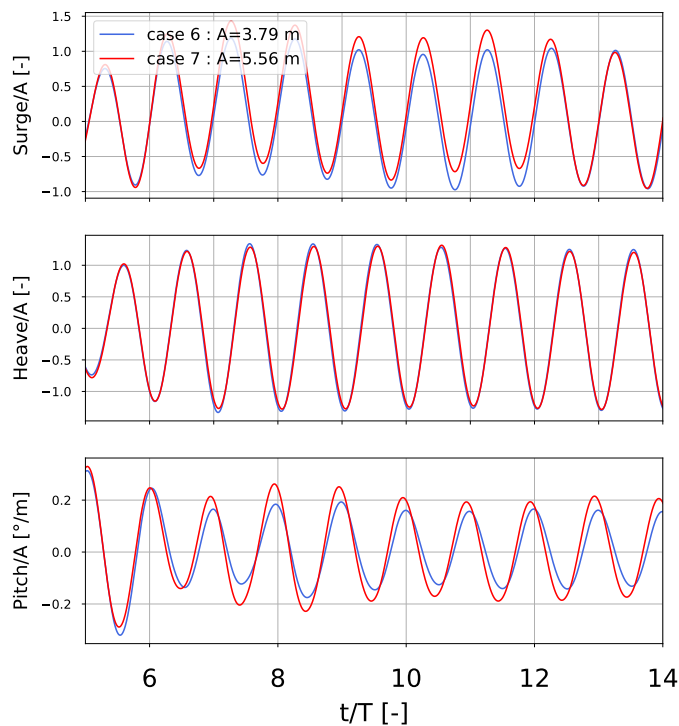


FIGURE 7.28: Time series of surge heave and pitch positions for the 2 wave amplitudes.  $T = 20.0$  s

### 7.2.2.3.1 Run-up on the upstream column

The run-ups on the upstream column from a port side view, during one wave period, for the cases 4 and 5 are presented on figures 7.29 and 7.30 respectively. As the wave amplitude increases, the run-up on the column increases. The air gap between the free surface and the top of the structure is significantly lower in the largest wave amplitude case as observed in figure 7.30j.

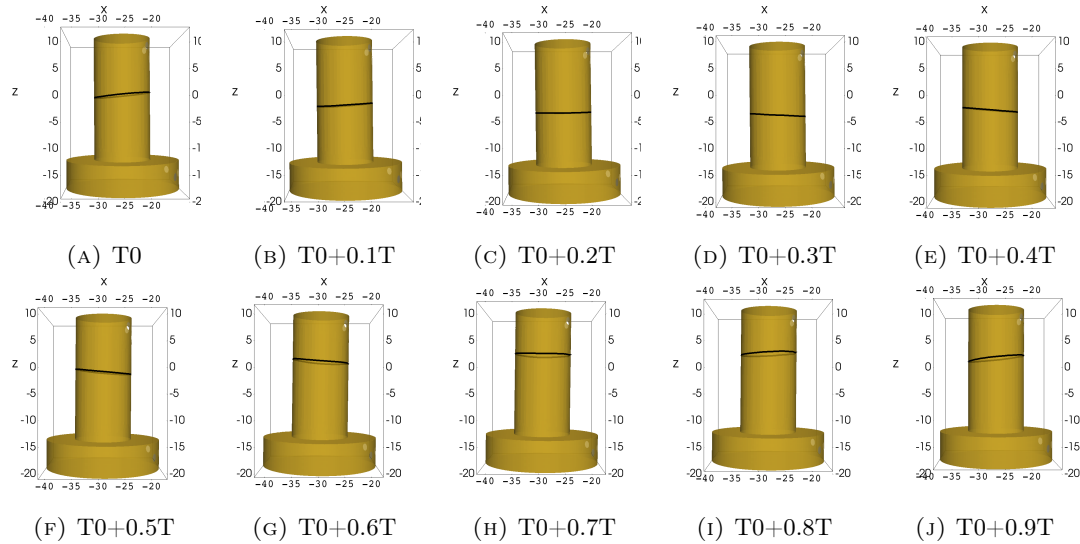


FIGURE 7.29: Run-up around the upstream column during one wave period. Port side view. Case 4:  $T = 14.3$  s  $A = 3.57$  m

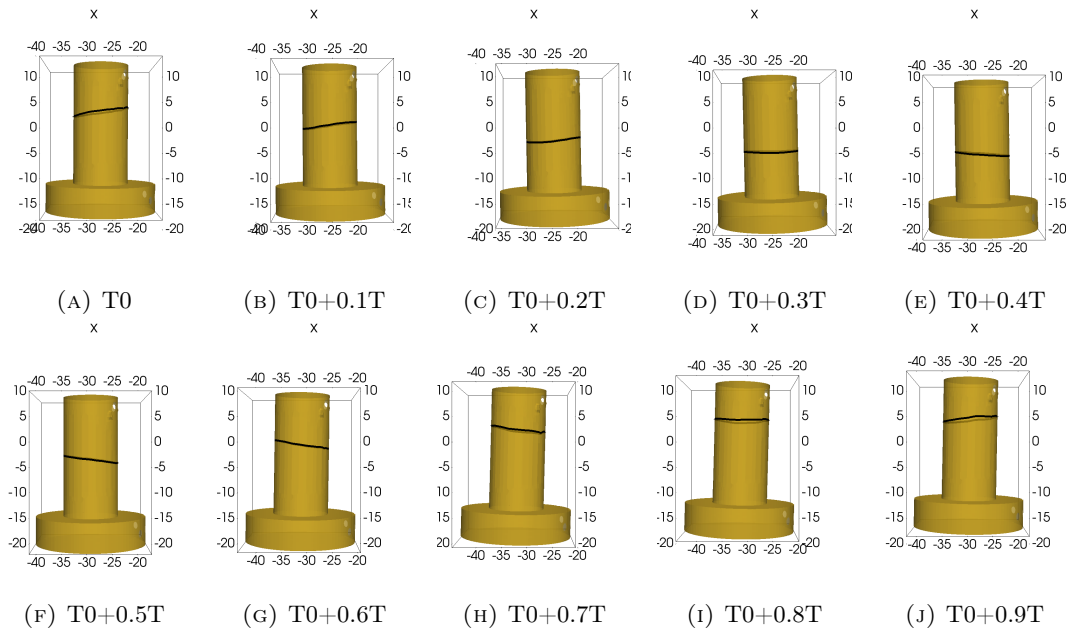


FIGURE 7.30: Run-up around the upstream column during one wave period. Port side view. Case 5:  $T = 14.3$  s  $A = 5.37$  m

### 7.3 Conclusions

In this chapter, the overset mesh method was tested on moving 3D structures. Free-decay tests of a floating cylinder and the DeepCWind FOWT were first presented.

A laminar flow approach was considered in all cases. The free-decay simulations in heave and pitch of the vertical truncated cylinder showed good agreement with the experimental measurements for both the damping rates and the natural periods. The surge decay showed that the catenary mooring model was able to reproduce the forces measured in the experiments.

The simulation of free-decay tests of the DeepCWind FOWT was carried out based on the numerical settings used in the simple cylinder case. The numerical results showed good agreement with the experimental measurements for the natural periods in heave and pitch. However, the damping of the oscillations was more difficult to reproduce. The scales of fluid motions below the scale of the mesh grid are not properly resolved because of the lack of a turbulence model in these simulations. Uncertainties related to the experimental set-up could also be a source of differences.

The response of the FOWT in regular waves was finally presented. To reduce the number of mesh cells, half of the domain was modeled and the flow and platform motions were supposed symmetrical. The meshing method presented in chapter 2 and applied in section 4.2 was used to mesh the NWT and the FOWT. Two slightly different models were presented based on two different experimental campaigns. For both models, CFD results of wave-induced motions were compared with experimental data and showed good agreement.

Nonlinear effects in these motion responses were investigated by considering increasing values of wave steepness. The overset mesh solver coupled with waves2Foam has proven to be able to predict relatively well the motion of a complex platform in nonlinear waves within a reasonable computational time (between 2h and 4h of CPU time per wave period using 96 cores on the following machine: aRyzen Threadripper 2990WX - AMD 32-core processor, operating at a base frequency of 3 GHz).



# 8 General conclusions and perspectives

## 8.1 Summary of the main results

The objective of this PhD thesis was to assess the capabilities of a CFD software in modeling a NWT for FOWT in realistic wave conditions. One part of the research focused on analyzing the modeling of diffraction wave loads and run-up on fixed structures to investigate the effects of nonlinearities and to emphasize the added value of CFD for accurately predicting these crucial design constraints. The other part of the project was to test and validate the overset mesh method to model the dynamics of floating structures, and in particular FOWT. The overset mesh solver implemented in the open-source software OpenFOAM was coupled with the wave generation and absorption module waves2Foam. It should be noted that the objective of this work was to elaborate methods to make the use of CFD for FOWT modeling accessible for industrial purposes in a fast and effective way. The purpose was not to get perfectly accurate results but rather to improve the predictions of nonlinear phenomena compared to potential theory and Morison's equation-based models, currently in use in the industry. The choice of the overset meshing technique for modeling the structure motions makes the CFD model process easier, considering that the mesh of the structure can be defined just once, and the NWT, which depends on the wave parameters, can be automatically generated. The main results of the work presented in this thesis are summarized in this section.

A CFD numerical model of a NWT with a meshing process was proposed and a convergence analysis on key numerical and meshing parameters was discussed. The aim of this analysis was to set up criteria for meshing the NWT so that the mesh can be automatically generated based on a combination of Three aspects: i. pre-defined incident wave conditions, ii. level of accuracy needed, and iii. computational resource available. Ocean waves of good quality were successfully modeled, with an acceptable computational cost. The waves2Foam solver has proved its efficiency to generate and absorb nonlinear waves.

Analysis of 2D cases of wave-structure interaction was first performed for a static and a freely-moving inverted T-section. The fixed case corresponds to a planar vertical slice of a column of the deepCWind FOWT investigated in 3D. The CFD results were compared to linear and nonlinear potential flow models. Higher-order harmonics and viscous effects were shown to have a significant impact on the force results even for low wave steepness. As expected, the nonlinear contributions increase with wave steepness. The main differences with the linear model are noted for heave force predictions, in cases of high viscous contribution due to the flow separation at the sharp corners of the structure. These structures can be designed to have a cancellation period for which the diffraction loads vanish (according to linear potential wave theory). The wave period investigated in this work was chosen close to the cancellation period,

so the viscous forces were dominant.

The overset mesh method coupled with waves2Foam was then tested on a 2D inverted T-section structure moving in response to incident waves, and a convergence analysis was presented to guarantee the quality of both the mesh and the numerical inputs. The wave considered in this analysis was highly nonlinear with green water breaking on the deck of the structure. The coupled solver has shown to accurately predict the motion of the structure, compared to experimental measurements.

The forces acting on a heave damping plate in forced motions were analyzed using the overset mesh solver of OpenFOAM. The cases modeled were, first, a disk itself and then a disk at the bottom of a cylinder. Results obtained are matching experimental measurements and showed good agreement, even in situations where the disk was close to the mean water level. The overset method accurately predicts the hydrodynamic coefficients and the vorticity field near the plates. Compared to a linear potential flow model, those results are improved. When using the CFD model, there is no need to add empirical drag contribution, unlike currently used engineering models. This opens a wider range of possibilities in the design of complex shapes of heave plates, without the necessity to do experimental campaigns. In this thesis, simple symmetrical structures were considered to test the method in 2D. However, the model can easily be extended in 3D and model non-symmetrical shapes of these damping plates.

As part of the OC6 joint industry research project, the DeepCWind FOWT subjected to waves was modeled. In this project, the structure was considered fixed. First, the interaction between a monochromatic wave and the structure was investigated. A comparison of the present CFD results with results from CFD models of other participants of the project and experimental measurements showed that the model was able to predict the forces on the platform. Two meshes were presented, one using the meshing method detailed in this thesis with coarse criteria and one imposed by the OC6 project to all participants. The first mesh showed more discrepancies with the experimental results but a lower computational cost than the imposed mesh. Then, bichromatic wave cases were carried out to assess the difference-frequency wave forces. The waves2Foam module was able to generate high-quality bichromatic waves. The comparison of the CFD results with second-order potential flow models showed that the difference-frequency force amplitudes computed in CFD are larger. It suggests that viscous effects contribute to the second-order wave loads and that CFD could be a valuable tool to assess these wave loads, usually under-predicted.

Free-decay tests of 3D freely floating bodies were analyzed. The overset mesh method was first used on a simple vertical cylinder piercing the free surface and then with the deepCWind FOWT. The natural periods and damping rates in heave, pitch, and surge motion computed for the simple cylinder showed good agreement with experimental data. It confirmed the ability of the overset mesh method to predict the structure motion in 3D. The quasi-static mooring system was used and showed to be sufficient in modeling restraint forces in the surge decay. The method was extended to compute free decay tests in heave and pitch for the deepCWind FOWT. The natural periods were again well captured but the damping rate appeared slightly more difficult to reproduce, which might be caused by the lack of a turbulence model in the current settings of the CFD model. However, overall satisfactory results were found.

The freely floating DeepCWind floater subjected to regular waves was also investigated. A wave only analysis carried out with the coupled solver between overset and Waves2Foam has shown to constantly underpredict the wave amplitude at the location of the FOWT. To counter this discrepancy, the input value of wave amplitude was initially tuned to match the target one at the FOWT location. Three DoF were considered to take advantage of the symmetry of the flow. The results of several wave conditions were compared to experimental measurements from two different experimental campaigns and showed satisfactory results. It has been shown that the largest nonlinearities appear for heave forces when the period is close to the cancellation period of the structure. Close to this period, viscous effects become dominant over the diffraction/radiation loads. The overset mesh model coupled with waves2Foam has been shown to successfully predict the motion of a complex floater of FOWT for a wide range of wave periods and heights, including steep waves and long waves close to the heave resonance period.

## 8.2 Main achievements of the thesis

The main achievements fulfilled during this PhD thesis are summarized in this section.

- A literature review of the published work on CFD modeling of FOWT in waves was carried out and presented.
- A meshing process and refinement criteria were proposed for modeling NWT using the waves2Foam solver. Preprocessing scripts were developed to automatically generate the mesh based on wave characteristics.
- The CFD NWT was validated for modeling static structures in monochromatic and bichromatic wave cases.
- The waves2Foam solver was coupled with the overset mesh module of OpenFOAM and the resulting solver, called overWaveDyMFoam, was tested and validated in 2D and 3D cases with moving bodies.
- The ability of the overset mesh solver to capture the flow around thin heave plate and compute accurately hydrodynamic coefficients was proven.
- Free decay tests and wave-induced motion of freely floating platforms were successfully performed with satisfactory results.
- The interest of the overset mesh technique to ensure the quality of the mesh and to reduce the pre-processing time to build a CFD NWT was emphasized.

## 8.3 Perspectives and future work

To continue with the work presented in this thesis, several research perspectives are listed in this section to improve the NWT quality, to optimize the computational cost and to increase the confidence in the model's results for industrial purposes.

- **Carry out in-depth mesh convergence analyses in 3D.** In the thesis, the convergence analyses were mostly performed on 2D models as it is computationally cheaper, and the criteria were subsequently extended to 3D. However, 3D phenomena can have significant impacts on the results and might require a dedicated 3D convergence analysis.

- **Assess the influence of the turbulence models.** In most of the cases presented in this thesis, a laminar flow was considered to avoid too excessive dissipation from existing turbulence models. This hypothesis seems valid for fixed FOWT structures as the Reynolds number is quite low. However, turbulence effects are expected to have more influence near sharp angles of the heave plates. To model these effects without dissipate too much the wave, the stabilized  $k-\omega$  SST turbulence model developed by Larsen and Fuhrman [107] and partially used in this thesis should be extended to the freely floating cases. Other solution such as the buoyancy-modified  $k-\omega$  SST turbulence model presented by Devolder et al. [157] could be investigated, as recently discussed in the PhD thesis of Fabien Robaux [44].
- **Compare with other dynamic solvers.** The overset mesh solver has the great advantage to allow large body motions of complex geometries while maintaining the same mesh quality all along the simulation. However, the interpolation step between the two meshes is time-consuming. It can also result in a loss of information. To better assess the advantages and limitations of the overset method, the results should be compared to other dynamic meshing methods.
- **Estimate the uncertainty in the results.** An uncertainty analysis should be applied to the results obtained in the thesis to increase confidence in the model. The work of Burmester et al. [60] could serve as a reference to quantify the uncertainty of this model.
- **Improve the wave quality of the coupled solver overWaveDyMFoam.** The quality of the generated wave of the coupled solver was deteriorated compared to the waves2Foam solver. These discrepancies should be investigated by looking more deeply into the code. A track could be to look at the wave velocity inlet boundary conditions which are not compatible with the overWaveDyMFoam solver. It should be noted that the OpenFOAM version 1712 was used in these overset mesh models. Improvements may have already been integrated into the latest versions.
- **Use more complex mooring models.** In this work, the quasi-static mooring model developed by Niels Jacobsen in the waves2Foam toolkit was used. This tool approximates the catenary mooring lines with restoring forces. It does not take into account the interactions between the fluid and the mooring. These interactions might have a significant impact on the platform motions in certain conditions. More complex mooring models have been developed for OpenFOAM, such as MooDy presented in the work of Palm et al. [74], and could be used in this model.
- **Integrate the turbine and model the coupled effects between aerodynamics and hydrodynamics.** This work aims to model FOWT, so it seems essential in a next step to assess the interactions between the turbine and the platform. The overset mesh method could also be an ideal tool to model the motion of the rotor as performed in the work of Tran and Kim [95]. However, such simulations are expensive and should be used only for specific extreme load cases.
- **Couple the CFD overset mesh solver with a potential flow NWT.** Most of the time, far from the structure, the flow is accurately predicted by potential flow solvers, so the CFD software has a limited added value and a much larger

computational cost. Considering a method similar to the one presented in this thesis, a solution could be to implement a potential flow model in the background mesh and use CFD only in the overset mesh with interpolation between the two models. This method was investigated in the PhD thesis of Fabien Robaux [44]. Other recent references in this direction include the work of Paulsen et al. [158], Kemper et al. [159] or Di Paolo et al. [160], among many others.

- **Couple the CFD model with a servo-aero-elastic model.** The modeling of the full wind turbine in CFD might remain too costly for industrial purposes. A solution could be to couple the CFD NWT with a servo-aero-elastic model such as FAST [24], to model the entire response of the wind turbine. The CFD NWT would replace the hydrodynamic solver currently used in global analyses. This high-fidelity coupled model could then be used to model extreme events. The SOWFA software developed by NREL uses this concept.



# A Comparison of the free surface of the experimental tests with the surface computed in CFD for forced oscillations of a disk

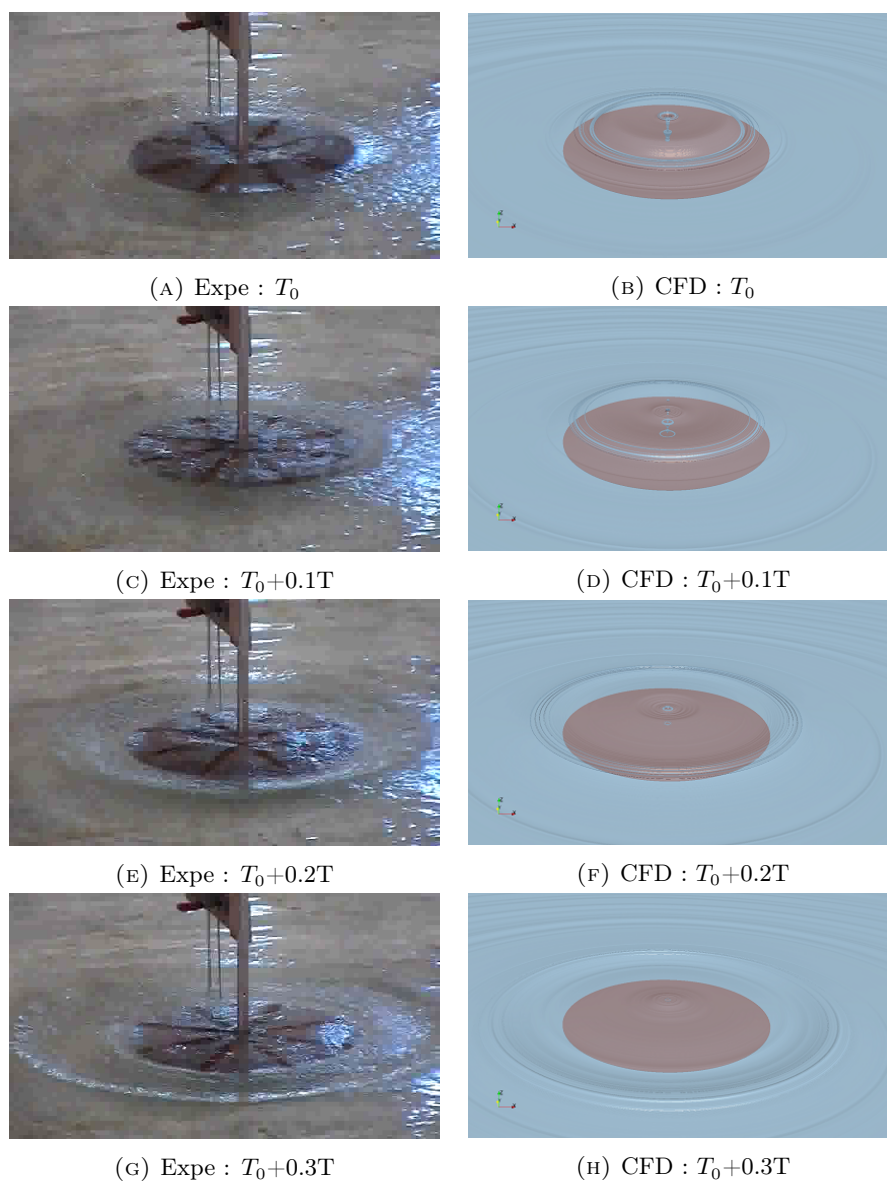


FIGURE A.1: Comparison of the free surface of the experimental tests (left [118]) and the 3D projection of the 2D CFD results  $A = 0.015$  m,  $T = 1.6$  s,  $d = 0.05$  m,  $KC = 0.157$ . part 1/2

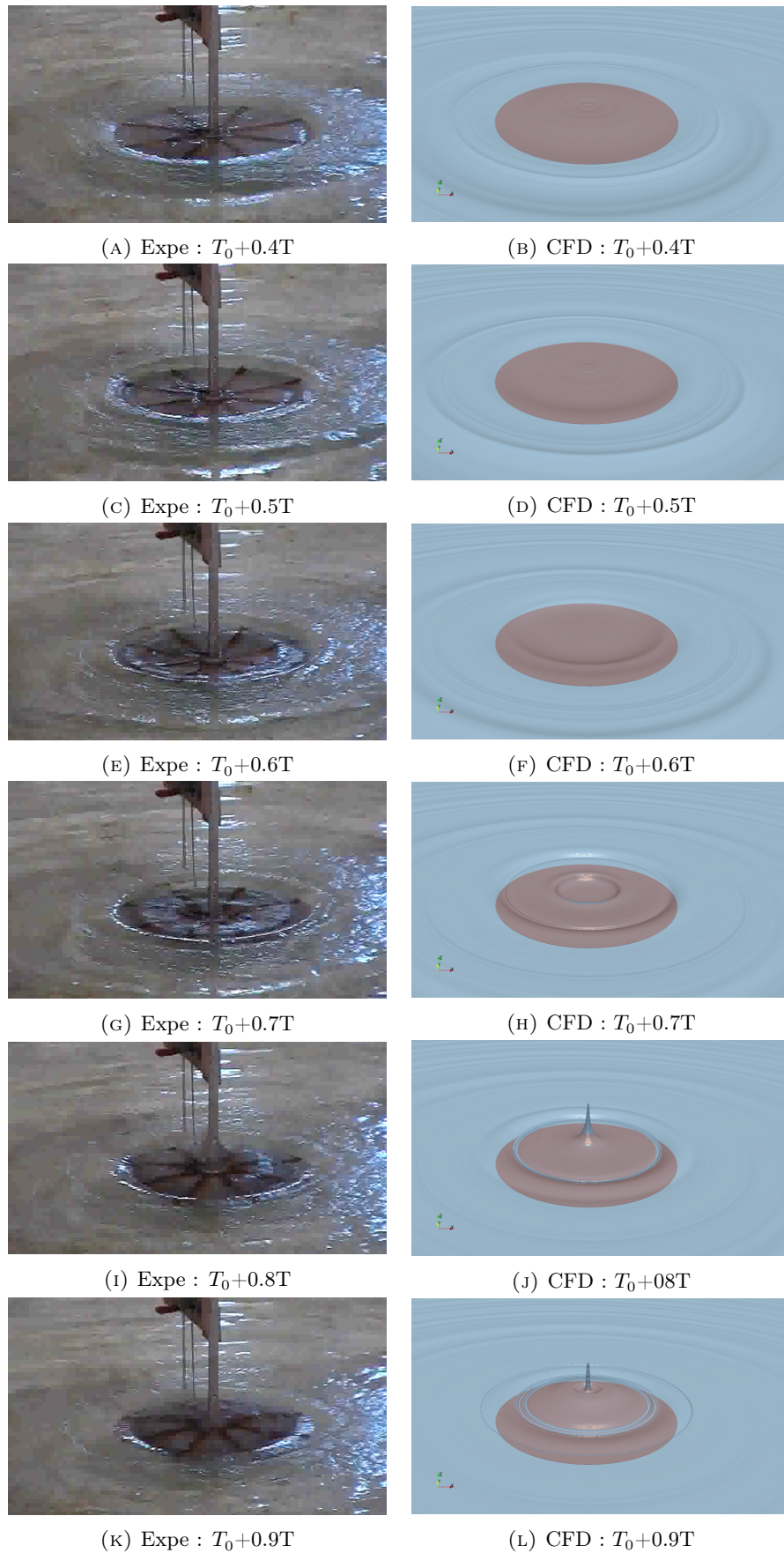


FIGURE A.2: Comparison of the free surface of the experimental tests (left) [118] and the 3D projection of the 2D CFD results (right)  $A = 0.015$  m,  $T = 1.6$  s,  $d = 0.05$  m,  $KC = 0.157$ . part 2/2

## B Wave loads on the freely-floating DeepCwind FOWT

### B.1 Forces and moment from the small scale model based on the experimental results presented in the work of Rivera-Arreba et al. [56]

Figure B.1 compares the time series of forces and moment on the front column, the starboard column, and on the entire structure. Figure B.2 shows the three first harmonics of the Force and moment in log scale on the entire structure and on each column. It can be observed that the surge force amplitude is larger on the front column than on the rear columns. However, the heave force amplitude is similar on both columns. As expected, there is a phase lag of the force acting on the rear column compared to the front column. However, it is interesting to observe that a phase lag also occurs on the heave force.

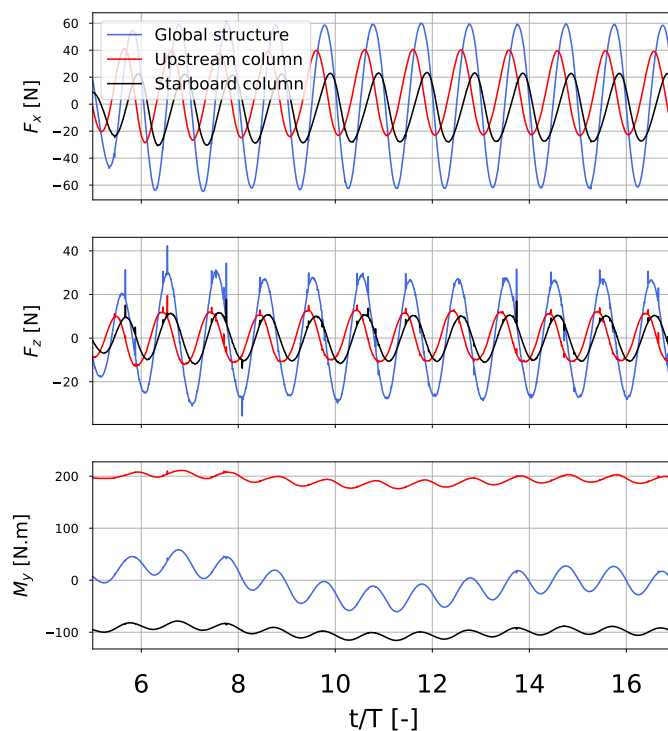


FIGURE B.1: Time series of the horizontal and vertical forces and the moment. The blue lines correspond to the global structure, the red and black lines to the upstream and starboard columns respectively.

Small scale:  $T = 1.71$  s  $A = 0.07$  m

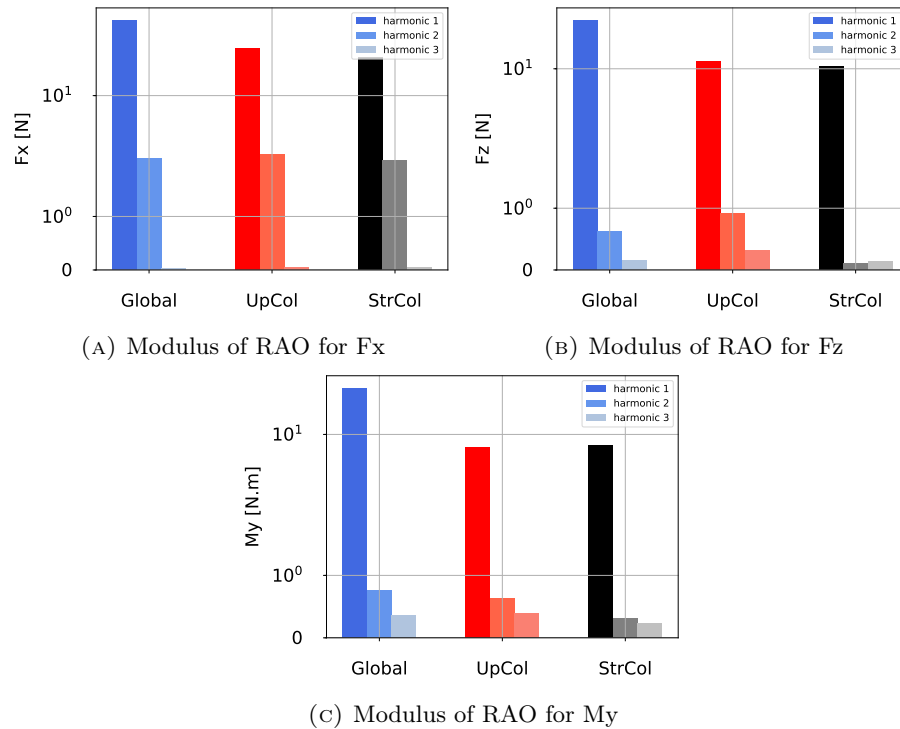


FIGURE B.2: Modulus of the RAO for the horizontal and vertical forces and the CoG moment. The blue lines correspond to the global structure, the red and black lines to the upstream and starboard columns respectively. Small scale:  $T = 1.71$  s  $A = 0.07$  m

#### B.1.0.0.1 Forces and moment for different wave conditions from the large scale model based on the experimental results presented in the work of Coulling et al. [98]

Figures B.3, B.4 and B.5 shows the time series of forces and moment on the entire structure for the 3 wave periods considered. The loads for the different wave amplitudes are compared. Figure B.6 shows a comparison of the amplitude of the three first harmonics of the loads for each case.

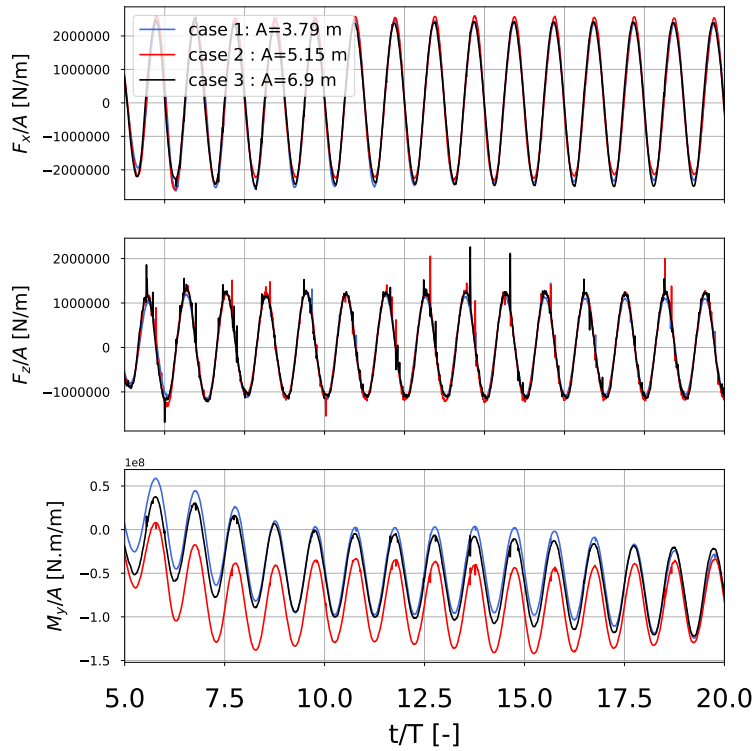


FIGURE B.3: Time series of the horizontal and vertical forces and the CoG moment on the whole structure for the cases 1, 2 and 3

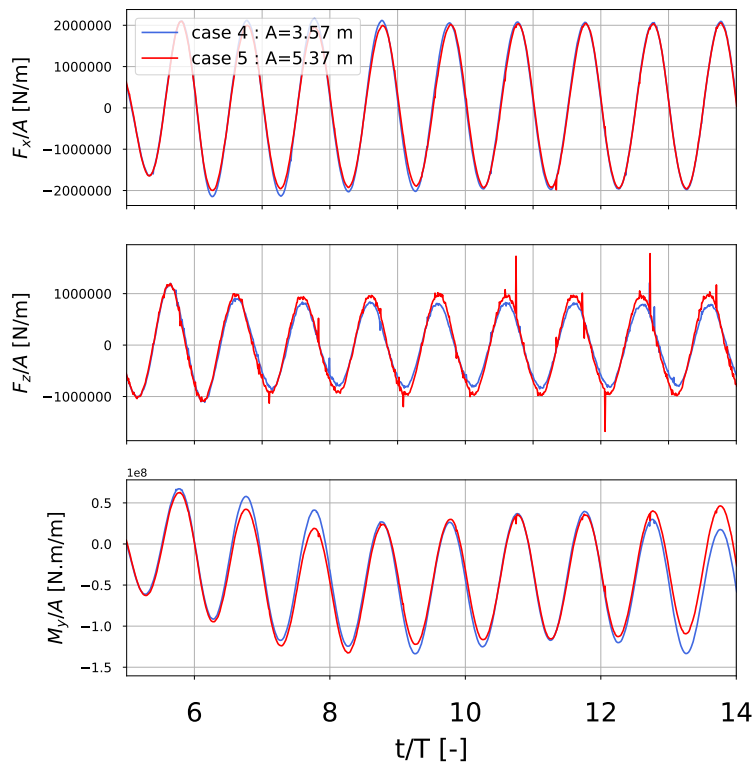


FIGURE B.4: Time series of the horizontal and vertical forces and the CoG moment on the whole structure for the cases 4 and 5

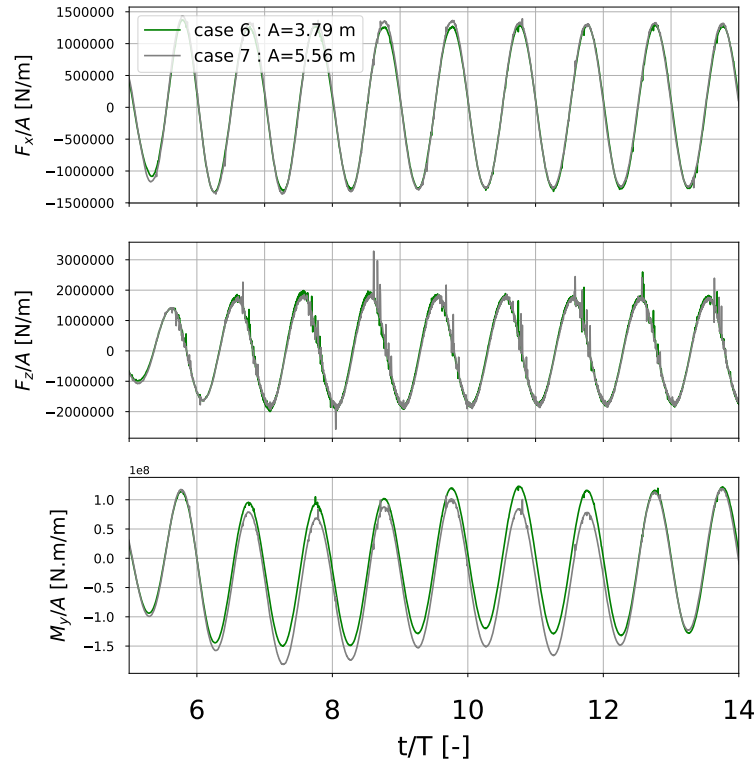
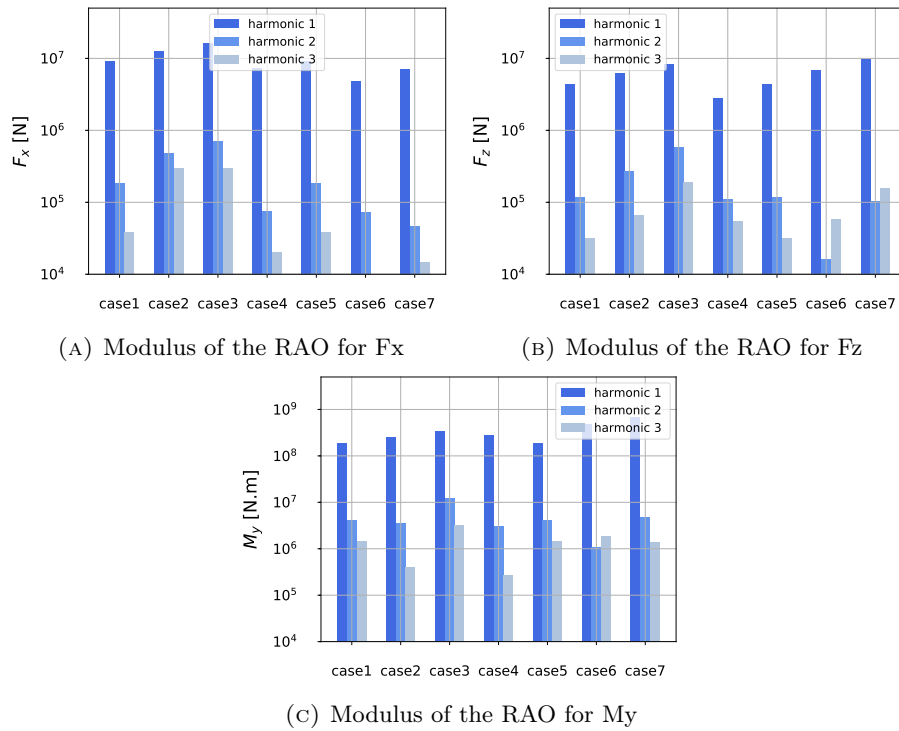


FIGURE B.5: Time series of the horizontal and vertical forces and the CoG moment on the whole structure for the cases 6 and 7



(A) Modulus of the RAO for  $F_x$

(B) Modulus of the RAO for  $F_z$

(C) Modulus of the RAO for  $M_y$

FIGURE B.6: Modulus of the RAO for the horizontal and vertical forces and the CoG moment on the whole structure for the 7 cases

# Bibliography

- [1] IRENA. *Renewable energy: A key climate solution*. Tech. rep. International Renewable Energy Agency (IRENA), 2017, p. 8.
- [2] EIA. *Levelized Cost and Levelized Avoided Cost of New Generation Resources in the Annual Energy Outlook 2020*. Tech. rep. U.S. Energy Information Administration (EIA), 2020, p. 22.
- [3] Laura Cozzi, Brent Wanner, and et al. *Offshore Wind Outlook 2019: World Energy Outlook Special Report*. Tech. rep. International Energy Agency (IEA), 2019, p. 98.
- [4] James Rhodri and Marc Costa Ros. *Floating Offshore Wind: Market and Technology Review*. Tech. rep. UK: The Carbon Trust, 2015, p. 167.
- [5] Laura Castro-Santos and Vicente Diaz-Casas, eds. *Floating Offshore Wind Farms*. Green Energy and Technology. Cham: Springer International Publishing, 2016. DOI: [10.1007/978-3-319-27972-5](https://doi.org/10.1007/978-3-319-27972-5).
- [6] Bjørn Skaare, Finn Gunnar Nielsen, Tor David Hanson, Rune Yttervik, Ole Havmøller, and Arne Rekdal. “Analysis of measurements and simulations from the Hywind Demo floating wind turbine: Dynamic analysis of the Hywind Demo floating wind turbine”. In: *Wind Energy* 18.6 (June 2015), pp. 1105–1122. DOI: [10.1002/we.1750](https://doi.org/10.1002/we.1750).
- [7] T Choisnet, E Rogier, Y Percher, A Courbois, I Le Crom, and R Mariani. “Performance and mooring qualification in Floatgen : the first french offshore wind turbine project”. In: *16èmes Journée de l’Hydrodynamique*. Marseille, France, 2018, p. 10.
- [8] Guillaume Bonnaffoux, Bauduin Christian, Bertolotti Christine, Melis Cecile, and Poirette Yann. “Design and Performance of a TLP Type Floating Support Structure for a 6MW Offshore Wind Turbine”. In: *Offshore Technology Conference*. Houston, Texas, USA, 2019, p. 13.
- [9] Fons Huijs, Rogier de Bruijn, and Feike Savenije. “Concept Design Verification of a Semi-submersible Floating Wind Turbine Using Coupled Simulations”. In: *Energy Procedia* 53 (2014), pp. 2–12. DOI: [10.1016/j.egypro.2014.07.210](https://doi.org/10.1016/j.egypro.2014.07.210).
- [10] Anthony M. Viselli, Andrew J. Goupee, and Habib J. Dagher. “Model Test of a 1:8-Scale Floating Wind Turbine Offshore in the Gulf of Maine”. In: *Journal of Offshore Mechanics and Arctic Engineering* 134(4) (2015). DOI: <https://doi.org/10.1115/1.4030381>.
- [11] Christian Cermelli, Alexia Aubault, Dominique Roddier, and Timothy McCoy. “Qualification of a Semi-Submersible Floating Foundation for Multi-Megawatt Wind Turbines”. In: *Offshore Technology Conference*. Houston, Texas, USA: Offshore Technology Conference, 2010. DOI: [10.4043/20674-MS](https://doi.org/10.4043/20674-MS).
- [12] Thomas Chapalain, Cyrille Moiret, and Joël Grignoux. “Semi-submersible float, in particular for a wind turbine”. US 2020/0198741 A1. June 2020.

- [13] Thierry Delahaye, Paul Franc, Christophe Colmard, and Frédéric Gentil. “New pendular floater for offshore wind commercial”. In: *Offshore Mediterranean Conference*. Ravenna, Italy, 2019, p. 13.
- [14] Michael Borg, Morten Walkusch Jensen, Scott Urquhart, Morten Thøtt Andersen, Jonas Bjerg Thomsen, and Henrik Stiesdal. “Technical Definition of the TetraSpar Demonstrator Floating Wind Turbine Foundation”. In: *Energies* 13.18 (Sept. 2020), p. 4911. DOI: [10.3390/en13184911](https://doi.org/10.3390/en13184911).
- [15] Arthur Pecher and Jens Peter Kofoed, eds. *Handbook of Ocean Wave Energy*. Vol. 7. Ocean Engineering & Oceanography. Cham: Springer International Publishing, 2017. DOI: [10.1007/978-3-319-39889-1](https://doi.org/10.1007/978-3-319-39889-1).
- [16] Bernard Molin. *Hydrodynamique des structures offshore*. Editions Technip, 2002.
- [17] Lee. *WAMIT Theory Manual*. Tech. rep. Massachusetts Institute of Technology, Oct. 1995.
- [18] A L Defoy, J M Heurtier, C Le Cunff, R Antonutti, and P Weyne. “Comparison of three hydro-structure coupling approaches for the design of floating platforms”. In: *16èmes Journée de l’Hydrodynamique*. Marseille, France, 2018, p. 15.
- [19] Aurélien Babarit and Gerard Delhommeau. “Theoretical and numerical aspects of the open source BEM solver NEMOH”. In: *Proc. of the 11th European Wave and Tidal Energy Conference (EWTEC)*. Nantes, France, 2015.
- [20] Inc. ANSYS. *AQWA Reference Manual*. Tech. rep. 2012, p. 268.
- [21] J.R. Morison, J.W. Johnson, and S.A. Schaaf. “The Force Exerted by Surface Waves on Piles”. In: *Journal of Petroleum Technology* 2.05 (May 1950), pp. 149–154. DOI: [10.2118/950149-G](https://doi.org/10.2118/950149-G).
- [22] Turgut Sarpkaya. *Wave Forces on Offshore Structures*. New York, NY: Cambridge University Press, 1981.
- [23] Orcina Ltd. *OrcaFlex Version 9.7c*. Tech. rep. 2014.
- [24] J M Jonkman and Jr. Buhl. *FAST User’s Guide*. User guide. National Renewable Energy Laboratory, 2005.
- [25] National Renewable Energy Laboratory. *HydroDyn User’s Guide and Theory*. Tech. rep. 2013.
- [26] Daewoong Son, Romain Pinguet, and Dominique Roddier. “Global Sizing of the WindFloat for a 10 MW Generic Wind Turbine”. In: *ASME 2018 1st International Offshore Wind Technical Conference*. San Francisco, California, USA: American Society of Mechanical Engineers, Nov. 2018, V001T01A035. DOI: [10.1115/IOWTC2018-1104](https://doi.org/10.1115/IOWTC2018-1104).
- [27] M. Hall. *MoorDyn User’s Guide*. Tech. rep. School of Sustainable Design Engineering, University of Prince Edward Island, 2017.
- [28] A Cordle and J Jonkman. “State of the Art in Floating Wind Turbine Design Tools”. In: *21st International Offshore and Polar Engineering Conference*. Maui, Hawaii, 2011, p. 11.
- [29] Stéphan T. Grilli and Juan Horrillo. “Numerical Generation and Absorption of Fully Nonlinear Periodic Waves”. In: *Journal of Engineering Mechanics* 123.10 (Oct. 1997), pp. 1060–1069. DOI: [10.1061/\(ASCE\)0733-9399\(1997\)123:10\(1060\)](https://doi.org/10.1061/(ASCE)0733-9399(1997)123:10(1060)).

- [30] Stephan T Grilli, Philippe Guyenne, and Frederic Dias. “A fully non-linear model for three-dimensional overturning waves over an arbitrary bottom”. In: *International Journal for Numerical Methods in Fluids* 35 (2001), pp. 829–867.
- [31] C.H. Kim, A.H. Clément, and K. Tanizawa. “Recent Research And Development of Numerical Wave Tanks - A Review”. In: *Int. J. Offshore Polar Eng.* 9.4 (1999).
- [32] Etienne Guerber, Michel Benoit, Stephan T. Grilli, and Clément Buvat. “A fully nonlinear implicit model for wave interactions with submerged structures in forced or free motion”. In: *Engineering Analysis with Boundary Elements* 36.7 (July 2012), pp. 1151–1163. DOI: [10.1016/j.enganabound.2012.02.005](https://doi.org/10.1016/j.enganabound.2012.02.005).
- [33] E. Dombre, J.C. Harris, M. Benoit, D. Violeau, and C. Peyrard. “A 3D parallel boundary element method on unstructured triangular grids for fully nonlinear wave-body interactions”. In: *Ocean Engineering* 171 (Jan. 2019), pp. 505–518. DOI: [10.1016/j.oceaneng.2018.09.044](https://doi.org/10.1016/j.oceaneng.2018.09.044).
- [34] C.H. Hague and C. Swan. “A multiple flux boundary element method applied to the description of surface water waves”. In: *Journal of Computational Physics* 228.14 (Aug. 2009), pp. 5111–5128. DOI: [10.1016/j.jcp.2009.04.012](https://doi.org/10.1016/j.jcp.2009.04.012).
- [35] Q.W. Ma and S. Yan. “Quasi ALE finite element method for nonlinear water waves”. In: *Journal of Computational Physics* 212.1 (Feb. 2006), pp. 52–72. DOI: [10.1016/j.jcp.2005.06.014](https://doi.org/10.1016/j.jcp.2005.06.014).
- [36] S. Yan and Q.W. Ma. “Numerical simulation of fully nonlinear interaction between steep waves and 2D floating bodies using the QALE-FEM method”. In: *Journal of Computational Physics* 221.2 (Feb. 2007), pp. 666–692. DOI: [10.1016/j.jcp.2006.06.046](https://doi.org/10.1016/j.jcp.2006.06.046).
- [37] A.P. Engsig-Karup, C. Eskilsson, and D. Bigoni. “A stabilised nodal spectral element method for fully nonlinear water waves”. In: *Journal of Computational Physics* 318 (Aug. 2016), pp. 1–21. DOI: [10.1016/j.jcp.2016.04.060](https://doi.org/10.1016/j.jcp.2016.04.060).
- [38] Allan P. Engsig-Karup, Carlos Monteserin, and Claes Eskilsson. “A Mixed Eulerian–Lagrangian Spectral Element Method for Nonlinear Wave Interaction with Fixed Structures”. In: *Water Waves* 1.2 (Nov. 2019), pp. 315–342. DOI: [10.1007/s42286-019-00018-5](https://doi.org/10.1007/s42286-019-00018-5).
- [39] Armin Tavassoli and M.H. Kim. “Interactions of Fully Nonlinear Waves With Submerged Bodies By a 2D Viscous NWT”. In: *The Eleventh International Offshore and Polar Engineering Conference*. Stavanger, Norway, 2001.
- [40] A.P. Engsig-Karup, H.B. Bingham, and O. Lindberg. “An efficient flexible-order model for 3D nonlinear water waves”. In: *Journal of Computational Physics* 228.6 (Apr. 2009), pp. 2100–2118. DOI: [10.1016/j.jcp.2008.11.028](https://doi.org/10.1016/j.jcp.2008.11.028).
- [41] Zaibin Lin, Ling Qian, Wei Bai, Zhihua Ma, Hao Chen, Jian-Guo Zhou, and Hanbin Gu. “A Finite Volume Based Fully Nonlinear Potential Flow Model for Water Wave Problems”. In: *Applied Ocean Research* 106 (Jan. 2021), p. 102445. DOI: [10.1016/j.apor.2020.102445](https://doi.org/10.1016/j.apor.2020.102445).
- [42] Yan-Lin Shao and Odd M. Faltinsen. “Fully-Nonlinear Wave-Current-Body Interaction Analysis by a Harmonic Polynomial Cell Method”. In: *Journal of Offshore Mechanics and Arctic Engineering* 136.3 (Aug. 2014), p. 031301. DOI: [10.1115/1.4026960](https://doi.org/10.1115/1.4026960).

- [43] Fabien Robaux and Michel Benoit. “Development and validation of a numerical wave tank based on the Harmonic Polynomial Cell and Immersed Boundary methods to model nonlinear wave-structure interaction”. In: *arXiv:2009.08937 [physics]* (Sept. 2020). arXiv: 2009.08937.
- [44] Fabien Robaux. “Numerical simulation of wave-body interaction: development of a fully nonlinear potential flow solver and assessment of two local coupling strategies with a CFD solver”. Ph.D. Thesis. Aix Marseille University, 2020.
- [45] Guilherme Vaz, Frederick Jaouen, and Martin Hoekstra. “Free-Surface Viscous Flow Computations: Validation of URANS Code FreSCo”. In: *Volume 5: Polar and Arctic Sciences and Technology; CFD and VIV*. Honolulu, Hawaii, USA: ASMEDC, Jan. 2009, pp. 425–437. DOI: [10.1115/OMAE2009-79398](https://doi.org/10.1115/OMAE2009-79398).
- [46] Jian-hua Wang, Wei-wen Zhao, and De-cheng Wan. “Development of nao-FOAM-SJTU solver based on OpenFOAM for marine hydrodynamics”. In: *Journal of Hydrodynamics* 31 (2019), p. 20. DOI: <https://doi.org/10.1007/s42241-019-0020-6>.
- [47] Tristan de Lataillade, Aggelos Dimakopoulos, Christopher Kees, Lars Johanning, David Ingram, and Tahsin Tezdogan. “CFD Modelling coupled with Floating Structures and Mooring Dynamics for Offshore Renewable Energy Devices using the Proteus Simulation Toolkit”. In: *12th European Wave and Tidal Energy Conference*. Ireland, 2017, p. 11.
- [48] Pablo Higuera, Javier L. Lara, and Inigo J. Losada. “Realistic wave generation and active wave absorption for Navier–Stokes models”. In: *Coastal Engineering* 71 (Jan. 2013), pp. 102–118. DOI: [10.1016/j.coastaleng.2012.07.002](https://doi.org/10.1016/j.coastaleng.2012.07.002).
- [49] Niels G. Jacobsen, David R. Fuhrman, and Jørgen Fredsøe. “A wave generation toolbox for the open-source CFD library: OpenFoam®”. In: *International Journal for Numerical Methods in Fluids* 70.9 (2012), pp. 1073–1088. DOI: [10.1002/flid.2726](https://doi.org/10.1002/flid.2726).
- [50] Niels G. Jacobsen. *waves2Foam Manual*. 2017.
- [51] M A Benitz, D P Schmidt, M A Lackner, and G M Stewart. “Comparison of Hydrodynamic Load Predictions Between Engineering Models and Computational Fluid Dynamics for the OC4-DeepCwind Semi-Submersible: Preprint”. In: *ASME 2014 33rd International Conference on Ocean, Offshore and Arctic Engineering*. San Francisco, California, 2014, p. 13.
- [52] Maija Benitz. “Simulating the Hydrodynamics of Offshore Floating Wind Turbine Platforms in a Finite Volume Framework”. PhD thesis. University of Massachusetts - Amherst, July 2016.
- [53] N. Bruinsma, B.T. Paulsen, and N.G. Jacobsen. “Validation and application of a fully nonlinear numerical wave tank for simulating floating offshore wind turbines”. In: *Ocean Engineering* 147 (Jan. 2018), pp. 647–658. DOI: [10.1016/j.oceaneng.2017.09.054](https://doi.org/10.1016/j.oceaneng.2017.09.054).
- [54] N Bruinsma. “Validation and Application of a Fully Nonlinear Numerical Wave Tank”. PhD thesis. Delft University of Technology, Mar. 2016.
- [55] I Rivera-Arreba. “Computation of Nonlinear Wave Loads on Floating Structures”. PhD thesis. Delft University of Technology & Norwegian University of Science and Technology., Aug. 2017.

- [56] I. Rivera-Arreba, N. Bruinsma, E. E. Bachynski, A. Viré, B. T. Paulsen, and N. G. Jacobsen. “Modeling of a Semisubmersible Floating Wind Platform in Severe Waves”. In: *Volume 9: Offshore Geotechnics; Honoring Symposium for Professor Bernard Molin on Marine and Offshore Hydrodynamics*. Madrid, Spain: American Society of Mechanical Engineers, June 2018, V009T13A002. DOI: [10.1115/OMAE2018-77680](https://doi.org/10.1115/OMAE2018-77680).
- [57] Yang Zhou, Qing Xiao, Yuanchuan Liu, Atilla Incecik, and Christophe Peyrard. “Investigation of focused wave impact on floating platform for offshore floating wind turbine - A CFD study”. In: *ASME 2019 38th International Conference on Ocean, Offshore and Arctic Engineering*. Glasgow, Scotland, 2019, p. 11.
- [58] Alexander J Dunbar. “Development and validation of a tightly coupled CFD/6-DOF solver for simulating floating offshore wind turbine platforms”. In: *Ocean Engineering* (2015), p. 8.
- [59] Simon Burmester, Guilherme Vaz, Sebastien Gueydon, and Ould el Moctar. “Investigation of a semi-submersible floating wind turbine in surge decay using CFD”. In: *Ship Technology Research* (Dec. 2018), pp. 1–13. DOI: [10.1080/09377255.2018.1555987](https://doi.org/10.1080/09377255.2018.1555987).
- [60] Simon Burmester. “Towards credible CFD simulations for floating offshore wind turbines”. In: *Ocean Engineering* 209 (2020).
- [61] Yu Wang, Hamn-Ching Chen, Guilherme Vaz, and Simon Burmester. “CFD Simulation of Semi-Submersible Floating Offshore Wind Turbine Under Pitch Decay Motion”. In: *ASME 2019 2nd International Offshore Wind Technical Conference*. St. Julian’s, Malta: American Society of Mechanical Engineers, Nov. 2019, V001T01A002. DOI: [10.1115/IOWTC2019-7515](https://doi.org/10.1115/IOWTC2019-7515).
- [62] Yang Huang, Yuan Zhuang, and Decheng Wan. “Hydrodynamic Study and Performance Analysis of the OC4-Deepcwind Platform by CFD Method”. In: *International Journal of Computational Methods* (Mar. 2020), S0219876220500206. DOI: [10.1142/S0219876220500206](https://doi.org/10.1142/S0219876220500206).
- [63] Ping Cheng, Yang Huang, and Decheng Wan. “A numerical model for fully coupled aero-hydrodynamic analysis of floating offshore wind turbine”. In: *Ocean Engineering* 173 (Feb. 2019), pp. 183–196. DOI: [10.1016/j.oceaneng.2018.12.021](https://doi.org/10.1016/j.oceaneng.2018.12.021).
- [64] Cheng Liu and Changhong Hu. “CFD Simulation of a Floating Wind Turbine Platform in Rough Sea Conditions”. In: *Twenty-fourth (2014) International Ocean and Polar Engineering Conference*. Busan, Korea, 2014.
- [65] Yuanchuan Liu, Qing Xiao, Atilla Incecik, Christophe Peyrard, and Decheng Wan. “Establishing a fully coupled CFD analysis tool for floating offshore wind turbines”. In: *Renewable Energy* 112 (Nov. 2017), pp. 280–301. DOI: [10.1016/j.renene.2017.04.052](https://doi.org/10.1016/j.renene.2017.04.052).
- [66] Yuanchuan Liu and Qing Xiao. “Development of a fully coupled aero-hydro-mooring-elastic tool for floating offshore wind turbines”. In: *Journal of Hydrodynamics* 31.1 (Feb. 2019), pp. 21–33. DOI: [10.1007/s42241-019-0012-6](https://doi.org/10.1007/s42241-019-0012-6).
- [67] Yin Zhang and Bumsuk Kim. “A Fully Coupled Computational Fluid Dynamics Method for Analysis of Semi-Submersible Floating Offshore Wind Turbines Under Wind-Wave Excitation Conditions Based on OC5 Data”. In: *Applied Sciences* 8.11 (Nov. 2018), p. 2314. DOI: [10.3390/app8112314](https://doi.org/10.3390/app8112314).

- [68] Sean Quallen, Tao Xing, Pablo Carrica, Yuwei Li, and Jun Xu. “CFD Simulation of a Floating Offshore Wind Turbine System Using a Quasi-Static Crow-foot Mooring-Line Model”. In: *Twenty-third (2013) International Offshore and Polar Engineering*. Anchorage, Alaska, USA, 2013.
- [69] Sean Quallen. “CFD simulation of a floating offshore wind turbine system using a variable-speed generator-torque controller”. In: *Renewable Energy* (2016), p. 13.
- [70] Friedemann Beyer, Thomas Choisnet, Matthias Kretschmer, and Po Wen Cheng. “Coupled MBS-CFD Simulation of the IDEOL Floating Offshore Wind Turbine Foundation Compared to Wave Tank Model Test Data”. In: *Twenty-fifth (2015) International Ocean and Polar Engineering Conference*. Kona, Big Island, Hawaii, 2015, p. 8.
- [71] Josh Davidson, Marie Cathelain, and Louise Guillemet. “Implementation of an OpenFOAM Numerical Wave Tank for Wave Energy Experiments”. In: *11th European Wave and Tidal Energy Conference*. Nantes, France, 2015, p. 10.
- [72] H. Islam, S.C. Mohapatra, J. Gadelho, and C. Guedes Soares. “OpenFOAM analysis of the wave radiation by a box-type floating structure”. In: *Ocean Engineering* 193 (Dec. 2019), p. 106532. DOI: [10.1016/j.oceaneng.2019.106532](https://doi.org/10.1016/j.oceaneng.2019.106532).
- [73] Adrien Courbois, Emmanuel Tcheuko, Benjamin Bouscasse, Youngmyung Choi, Olivier Kimmoun, and Riccardo Mariani. “Study of Viscous Effects on Wave Drift Forces on a Rectangular Pontoon With a Damping Plate by Using CFD Code OpenFOAM”. In: *Volume 9: Offshore Geotechnics; Honoring Symposium for Professor Bernard Molin on Marine and Offshore Hydrodynamics*. Madrid, Spain: American Society of Mechanical Engineers, June 2018, V009T13A003. DOI: [10.1115/OMAE2018-78053](https://doi.org/10.1115/OMAE2018-78053).
- [74] Johannes Palm, Claes Eskilsson, Guilherme Moura Paredes, and Lars Bergdahl. “Coupled mooring analysis for floating wave energy converters using CFD: Formulation and validation”. In: *International Journal of Marine Energy* 16 (Dec. 2016), pp. 83–99. DOI: [10.1016/j.ijome.2016.05.003](https://doi.org/10.1016/j.ijome.2016.05.003).
- [75] Agnese Paci, Maria Gabriella Gaeta, Alessandro Antonini, and Renata Archetti. “The proceedings of the Twenty-Sixth (2016) International Ocean and Polar Engineering Conference Rhodes, Greece, June 26-July 1, 2016: Volumes 1-4, 2016”. In: *Twenty-sixth (2016) International Ocean and Polar Engineering Conference*. OCLC: 954266853. Rhodes, Greece, 2016.
- [76] Zhirong Shen, Decheng Wan, and Pablo M Carrica. “RANS simulation of free maneuvers with moving rudders and propellers using overset grids in OpenFOAM”. In: *SIMMAN workshop on Verification and Validation of Ship Maneuvering Simulation Methods*. Lyngby, Denmark, 2014, p. 7.
- [77] Zhirong Shen, Pablo M. Carrica, and Decheng Wan. “Ship Motions of KCS in Head Waves With Rotating Propeller Using Overset Grid Method”. In: *Volume 2: CFD and VIV*. San Francisco, California, USA: American Society of Mechanical Engineers, June 2014, V002T08A043. DOI: [10.1115/OMAE2014-23657](https://doi.org/10.1115/OMAE2014-23657).
- [78] Zhirong Shen. “Dynamic overset grids in OpenFOAM with application to KCS self-propulsion and maneuvering”. In: *Ocean Engineering* 108 (2015), pp. 287–306.

- [79] Zhirong Shen, Yi-Fang Hsieh, Zhongfu Ge, Richard Korpus, and James Huan. “Slamming Load Prediction Using Overset CFD Methods”. In: *Offshore Technology Conference*. Houston, Texas, USA: Offshore Technology Conference, 2016. DOI: [10.4043/27254-MS](https://doi.org/10.4043/27254-MS).
- [80] Cong Liu, Jianhua Wang, and Decheng Wan. “CFD Computation of Wave Forces and Motions of DTC Ship in Oblique Waves”. In: *International Journal of Offshore and Polar Engineering* 28.2 (June 2018), pp. 154–163. DOI: [10.17736/ijope.2018.sh21](https://doi.org/10.17736/ijope.2018.sh21).
- [81] Yao Peng, Decheng Wan, Gang Chen, and Wenhua Huang. “Numerical Study of a Moving Object in Calm Water Using Overset and Non-overset Grids”. In: *Twenty-sixth (2016) International Ocean and Polar Engineering Conference*. Rhodes, Greece, 2016, p. 7.
- [82] Jianhua Wang. “Numerical simulations of zigzag maneuver of free running ship in waves by RANS-Overset grid method”. In: *Ocean Engineering* 162 (2018), pp. 55–79.
- [83] Ping Cheng and Decheng Wan. “Fully Coupled Aero-Hydrodynamic Simulation of Floating Offshore Wind Turbines with Overset Grid Technology”. In: *Proceedings of the Fourth International Conference in Ocean Engineering (ICOE2018)*. Ed. by K. Murali, V. Sriram, Abdus Samad, and Nilanjan Saha. Vol. 22. Series Title: Lecture Notes in Civil Engineering. Singapore: Springer Singapore, 2019, pp. 647–661. DOI: [10.1007/978-981-13-3119-0\\_42](https://doi.org/10.1007/978-981-13-3119-0_42).
- [84] Pablo M. Carrica, Robert V. Wilson, Ralph W. Noack, and Fred Stern. “Ship motions using single-phase level set with dynamic overset grids”. In: *Computers & Fluids* 36.9 (Nov. 2007), pp. 1415–1433. DOI: [10.1016/j.compfluid.2007.01.007](https://doi.org/10.1016/j.compfluid.2007.01.007).
- [85] Hao Chen, Ling Qian, Zhihua Ma, Wei Bai, Ye Li, Derek Causon, and Clive Mingham. “Application of an overset mesh based numerical wave tank for modelling realistic free-surface hydrodynamic problems”. In: *Ocean Engineering* 176 (Mar. 2019), pp. 97–117. DOI: [10.1016/j.oceaneng.2019.02.001](https://doi.org/10.1016/j.oceaneng.2019.02.001).
- [86] Z.H. Ma, L. Qian, P.J. Martínez-Ferrer, D.M. Causon, C.G. Mingham, and W. Bai. “An overset mesh based multiphase flow solver for water entry problems”. In: *Computers & Fluids* 172 (Aug. 2018), pp. 689–705. DOI: [10.1016/j.compfluid.2018.01.025](https://doi.org/10.1016/j.compfluid.2018.01.025).
- [87] Alok Khaware, Kvss Srikanth, and Vinay Kumar Gupta. “Numerical Simulation of Free Surface Flows Using Overset Mesh”. In: *Offshore Technology Conference Asia*. Kuala Lumpur, Malaysia: Offshore Technology Conference, 2018. DOI: [10.4043/28461-MS](https://doi.org/10.4043/28461-MS).
- [88] Benedetto Di Paolo, Javier L Lara, Gabriel Barajas, Agnese Paci, and Inigo J Losada. “Numerical Analysis of Wave and Current Interaction With Moored Floating Bodies Using Overset Method”. In: *ASME 2018 37th International Conference on Ocean, Offshore and Arctic Engineering*. Madrid, Spain, 2018.
- [89] Christian Windt, Josh Davidson, Benazzou Akram, and John V. Ringwood. “Performance Assessment of the Overset Grid Method for Numerical Wave Tank Experiments in the OpenFOAM Environment”. In: *Volume 10: Ocean Renewable Energy*. Madrid, Spain: American Society of Mechanical Engineers, June 2018, V010T09A006. DOI: [10.1115/OMAE2018-77564](https://doi.org/10.1115/OMAE2018-77564).

- [90] Christian Windt, Josh Davidson, Dominic D. J. Chandar, Nicolás Faedo, and John V. Ringwood. “Evaluation of the overset grid method for control studies of wave energy converters in OpenFOAM numerical wave tanks”. In: *Journal of Ocean Engineering and Marine Energy* 6.1 (Feb. 2020), pp. 55–70. DOI: [10.1007/s40722-019-00156-5](https://doi.org/10.1007/s40722-019-00156-5).
- [91] Nicolai F. Heilskov. *Structural Design of Wave Energy Converters 11804965 SD-WED Part II Implementation and Results - State-of-the-Art and Implementation of Design Tools for Floating Wave Energy Converters - Part 2: Implementation and Results*. Tech. rep. 11804965. DHI Business Management System, 2015, p. 43.
- [92] Tian-Cheng Yao, Yong-Sheng Zhao, Yan-Ping He, Yan-Lin Shao, Zhao-Long Han, and Lei Duan. “CFD-based Analysis of a 6MW Spar-type Floating Wind Turbine with Focus on Nonlinear Wave Loads”. In: *Thirtieth (2020) International Ocean and Polar Engineering Conference*. Shanghai, China, 2020.
- [93] Thanh Toan Tran and Dong Hyun Kim. “The aerodynamic interference effects of a floating offshore wind turbine experiencing platform pitching and yawing motions”. In: *Journal of Mechanical Science and Technology* 29.2 (Feb. 2015), pp. 549–561. DOI: [10.1007/s12206-015-0115-0](https://doi.org/10.1007/s12206-015-0115-0).
- [94] Thanh Toan Tran and Dong-Hyun Kim. “The coupled dynamic response computation for a semi-submersible platform of floating offshore wind turbine”. In: *Journal of Wind Engineering and Industrial Aerodynamics* 147 (Dec. 2015), pp. 104–119. DOI: [10.1016/j.jweia.2015.09.016](https://doi.org/10.1016/j.jweia.2015.09.016).
- [95] Thanh Toan Tran and Dong-Hyun Kim. “Fully coupled aero-hydrodynamic analysis of a semi-submersible FOWT using a dynamic fluid body interaction approach”. In: *Renewable Energy* 92 (July 2016), pp. 244–261. DOI: [10.1016/j.renene.2016.02.021](https://doi.org/10.1016/j.renene.2016.02.021).
- [96] Thanh Toan Tran and Dong-Hyun Kim. “A CFD study into the influence of unsteady aerodynamic interference on wind turbine surge motion”. In: *Renewable Energy* 90 (May 2016), pp. 204–228. DOI: [10.1016/j.renene.2015.12.013](https://doi.org/10.1016/j.renene.2015.12.013).
- [97] Thanh Toan Tran and Dong-Hyun Kim. “A CFD study of coupled aerodynamic-hydrodynamic loads on a semisubmersible floating offshore wind turbine”. In: *Wind Energy* 21.1 (Jan. 2018), pp. 70–85. DOI: [10.1002/we.2145](https://doi.org/10.1002/we.2145).
- [98] Alexander J Coulling, Andrew J Goupee, Amy N Robertson, Jason M Jonkman, and Habib J Dagher. “Validation of a FAST semi-submersible floating wind turbine numerical model with DeepCwind test data”. In: *J. Renewable Sustainable Energy* (2013), p. 31.
- [99] Marco Masciola, Amy Robertson, Jason Jonkman, Alexander Coulling, and Andrew Goupee. “Assessment of the Importance of Mooring Dynamics on the Global Response of the DeepCwind Floating Semisubmersible Offshore Wind Turbine”. In: *Twenty-third International Offshore and Polar Engineering Conference*. Anchorage, Alaska, 2013.
- [100] A Robertson, J Jonkman, M Masciola, H Song, and C Luan. *Definition of the Semisubmersible Floating O System for Phase II of OC4*. Technical Report NREL/TP-5000-60601. Denver, CO, USA: National Renewable Energy Laboratory, 2014, p. 44.
- [101] Jean-Baptiste Lacaze. “Etude expérimentale et numérique du couplage des phénomènes aérodynamiques et hydrodynamiques sur une éolienne offshore flottante”. Thèse de Doctorat. Marseille, France: Aix Marseille Université, 2015.

- [102] Maxime Philippe. “Couplages aéro-hydrodynamiques pour l’étude de la tenue à la mer des éoliennes offshore flottantes”. Thèse de Doctorat. Nantes, France: Centrale Nantes, 2012.
- [103] Vincent Arnal. “Modélisation expérimentale d’une éolienne flottante par une approche « software-in-the-loop ”. Thèse de Doctorat. Nantes, France: Centrale Nantes, 2020.
- [104] C.W Hirt and B.D Nichols. “Volume of fluid (VOF) method for the dynamics of free boundaries”. In: *Journal of Computational Physics* 39.1 (Jan. 1981), pp. 201–225. DOI: [10.1016/0021-9991\(81\)90145-5](https://doi.org/10.1016/0021-9991(81)90145-5).
- [105] Henrik Rusche. “Computational Fluid Dynamics of Dispersed Two-Phase Flows at High Phase Fractions”. PhD thesis. London: Imperial College of Science, Technology & Medicine, Dec. 2002.
- [106] Edin Berberović, Nils P. van Hinsberg, Suad Jakirlić, Ilia V. Roisman, and Cameron Tropea. “Drop impact onto a liquid layer of finite thickness: Dynamics of the cavity evolution”. In: *Physical Review E* 79.3 (Mar. 2009), p. 036306. DOI: [10.1103/PhysRevE.79.036306](https://doi.org/10.1103/PhysRevE.79.036306).
- [107] Bjarke Eltard Larsen and David R. Fuhrman. “On the over-production of turbulence beneath surface waves in Reynolds-averaged Navier–Stokes models”. In: *Journal of Fluid Mechanics* 853 (Oct. 2018), pp. 419–460. DOI: [10.1017/jfm.2018.577](https://doi.org/10.1017/jfm.2018.577).
- [108] David R. Fuhrman, Per A. Madsen, and Harry B. Bingham. “Numerical simulation of lowest-order short-crested wave instabilities”. In: *Journal of Fluid Mechanics* 563 (Sept. 2006), p. 415. DOI: [10.1017/S0022112006001236](https://doi.org/10.1017/S0022112006001236).
- [109] Allan Peter Engsig-Karup. “Unstructured nodal DG-FEM solution of high-order Boussinesq-type equations”. OCLC: 917964612. PhD thesis. Kongens Lyngby: Technical University of Denmark, Department of Mechanical Engineering, 2006.
- [110] Sopheak Seng. “Slamming And Whipping Analysis Of Ships”. Ph.D. Thesis. DTU Mechanical Engineering, 2012.
- [111] Nathan M Newmark. “A Method of Computation for Structural Dynamics”. In: *Journal of the Engineering Mechanics Division* 85.3 (July 1959), pp. 67–94.
- [112] Constance Clement, Pauline Bozonnet, Guillaume Vinay, Adria Borrás Nadal, Philippe Pagnier, and Julien Reveillon. “Numerical Wave Tank Including a Fixed Vertical Cylinder Subjected to Waves, Towards the Investigation of Floating Offshore Wind Turbine Hydrodynamics”. In: *ASME 2020 39th International Conference on Ocean, Offshore and Arctic Engineering*. Virtual, 2020, p. 10.
- [113] A Robertson, J Jonkman, F Wendt, A Goupee, and H Dagher. *Definition of the OC5 DeepCwind Semisubmersible Floating System*. Tech. rep. 2017.
- [114] S. Ma, F.-C. W. Hanssen, M. A. Siddiqui, M. Greco, and O. M. Faltinsen. “Local and global properties of the harmonic polynomial cell method: In-depth analysis in two dimensions”. In: *International Journal for Numerical Methods in Engineering* 113.4 (Jan. 2018), pp. 681–718. DOI: [10.1002/nme.5631](https://doi.org/10.1002/nme.5631).
- [115] V. E. Zakharov. “Stability of periodic waves of finite amplitude on the surface of a deep fluid”. In: *Journal of Applied Mechanics and Technical Physics* 9.2 (1968), pp. 86–94. DOI: [10.1007/BF00913182](https://doi.org/10.1007/BF00913182).

- [116] Xizeng Zhao and Changhong Hu. “Numerical and experimental study on a 2-D floating body under extreme wave conditions”. In: *Applied Ocean Research* 35 (Mar. 2012), pp. 1–13. DOI: [10.1016/j.apor.2012.01.001](https://doi.org/10.1016/j.apor.2012.01.001).
- [117] Christian A. Cermelli and Dominique G. Roddier. “Experimental and Numerical Investigation of the Stabilizing Effects of a Water-Entrapment Plate on a Deepwater Minimal Floating Platform”. In: *24th International Conference on Offshore Mechanics and Arctic Engineering: Volume 2*. Halkidiki, Greece: ASMEDC, Jan. 2005, pp. 517–525. DOI: [10.1115/OMAE2005-67077](https://doi.org/10.1115/OMAE2005-67077).
- [118] Bernard Molin, Fabien Remy, and Thierry Rippol. “Experimental study of the heave added mass and damping of solid and perforated disks close to the free surface”. In: *International Congress of International Maritime Association of the Mediterranean*. Varna, Bulgaria, 2007.
- [119] Krish Thiagarajan and Javier Moreno. “Wave Induced Effects on the Hydrodynamic Coefficients of an Oscillating Heave Plate in Offshore Wind Turbines”. In: *Journal of Marine Science and Engineering* 8.8 (Aug. 2020), p. 622. DOI: [10.3390/jmse8080622](https://doi.org/10.3390/jmse8080622).
- [120] Longbin Tao and Krish Thiagarajan. “Low KC flow regimes of oscillating sharp edges I. Vortex shedding observation”. In: *Applied Ocean Research* 25.1 (Feb. 2003), pp. 21–35. DOI: [10.1016/S0141-1187\(03\)00031-2](https://doi.org/10.1016/S0141-1187(03)00031-2).
- [121] Carlos A. Garrido-Mendoza, Krish P. Thiagarajan, Antonio Souto-Iglesias, Andrea Colagrossi, and Benjamin Bouscasse. “Computation of flow features and hydrodynamic coefficients around heave plates oscillating near a seabed”. In: *Journal of Fluids and Structures* 59 (Nov. 2015), pp. 406–431. DOI: [10.1016/j.jfluidstructs.2015.10.003](https://doi.org/10.1016/j.jfluidstructs.2015.10.003).
- [122] K. P. Thiagarajan and A. W. Troesch. “Effects of Appendages and Small Currents on the Hydrodynamic Heave Damping of TLP Columns”. In: *Journal of Offshore Mechanics and Arctic Engineering* 120.1 (Feb. 1998), pp. 37–42. DOI: [10.1115/1.2829518](https://doi.org/10.1115/1.2829518).
- [123] Elena Anglada-Revenga, Ana Bezunartea-Barrio, Adolfo Maron-Loureiro, Enrique Molinelli-Fernandez, Julio Oria-Escudero, Leandro Saavedra-Ynocente, Cristina Soriano-Gomez, Daniel Duque-Campayo, Jesus Gomez-Goni, and Antonio Souto-Iglesias. “Scale Effects in Heave Plates: PIV Investigation”. In: *Volume 9: Ocean Renewable Energy*. Virtual, Online: American Society of Mechanical Engineers, Aug. 2020. DOI: [10.1115/OMAE2020-18679](https://doi.org/10.1115/OMAE2020-18679).
- [124] Rodolfo Trentin Gonçalves. “Experimental Study on Vortex-Induced Motions of Floating Circular Single Cylinders with Low Aspect Ratio and Different Heave Plate Geometries”. In: *the Thirtieth (2020) International Ocean and Polar Engineering Conference*. Shanghai, China, 2020, pp. 2577–2587.
- [125] Jithin Jose, Sung-Jin Choi, and Ove Tobias Gudmestad. “Effect of heave plates on hydrodynamic response of a spar-type floating offshore wind turbine”. In: *the Twenty-ninth (2019) International Ocean and Polar Engineering Conference*. Honolulu, Hawaii USA, 2019.
- [126] Longbin Tao and Daniel Dray. “Hydrodynamic performance of solid and porous heave plates”. In: *Ocean Engineering* 35.10 (July 2008), pp. 1006–1014. DOI: [10.1016/j.oceaneng.2008.03.003](https://doi.org/10.1016/j.oceaneng.2008.03.003).

- [127] Hemlata Wadhwa, Balaji Krishnamoorthy, and Krish P. Thiagarajan. “Variation of Heave Added Mass and Damping Near Seabed”. In: *29th International Conference on Ocean, Offshore and Arctic Engineering: Volume 1*. Shanghai, China: ASMEDC, Jan. 2010, pp. 271–277. DOI: [10.1115/OMAE2010-20456](https://doi.org/10.1115/OMAE2010-20456).
- [128] Xinliang Tian, Jianmin Yang, Xin Li, and Tao Peng. “Experimental Investigations on the Hydrodynamic Characteristics of Heave Plate”. In: *Volume 5: Ocean Engineering*. Nantes, France: American Society of Mechanical Engineers, June 2013. DOI: [10.1115/OMAE2013-10437](https://doi.org/10.1115/OMAE2013-10437).
- [129] Nimmy Thankom Philip, S. Nallayarasu, and S. K. Bhattacharyya. “Experimental investigation and CFD simulation of heave damping effects due to circular plates attached to spar hull”. In: *Ships and Offshore Structures* 14.4 (May 2019), pp. 396–411. DOI: [10.1080/17445302.2013.835146](https://doi.org/10.1080/17445302.2013.835146).
- [130] Abuzar Abazari, Mehdi Behzad, and Krish P. Thiagarajan. “Hydrodynamic performance of multiple co-axial heave plates with different diameters”. In: *Ships and Offshore Structures* 15.4 (Apr. 2020), pp. 380–392. DOI: [10.1080/17445302.2019.1625109](https://doi.org/10.1080/17445302.2019.1625109).
- [131] L. Tao, B. Molin, Y.-M. Scolan, and K. Thiagarajan. “Spacing effects on hydrodynamics of heave plates on offshore structures”. In: *Journal of Fluids and Structures* 23.8 (Nov. 2007), pp. 1119–1136. DOI: [10.1016/j.jfluidstructs.2007.03.004](https://doi.org/10.1016/j.jfluidstructs.2007.03.004).
- [132] Shining Zhang and Takeshi Ishihara. “Numerical study of hydrodynamic coefficients of multiple heave plates by large eddy simulations with volume of fluid method”. In: *Ocean Engineering* 163 (Sept. 2018), pp. 583–598. DOI: [10.1016/j.oceaneng.2018.03.060](https://doi.org/10.1016/j.oceaneng.2018.03.060).
- [133] Matthew Lake, Haiping He, Armin W. Troesch, Marc Perlin, and Krish P. Thiagarajan. “Hydrodynamic Coefficient Estimation for TLP and Spar Structures”. In: *Journal of Offshore Mechanics and Arctic Engineering* 122.2 (May 2000), pp. 118–124. DOI: [10.1115/1.533733](https://doi.org/10.1115/1.533733).
- [134] Lixin Zhu and Hee-Chang Lim. “Hydrodynamic characteristics of a separated heave plate mounted at a vertical circular cylinder”. In: *Ocean Engineering* 131 (Feb. 2017), pp. 213–223. DOI: [10.1016/j.oceaneng.2017.01.007](https://doi.org/10.1016/j.oceaneng.2017.01.007).
- [135] Jinxuan Li, Shuxue Liu, Min Zhao, and Bin Teng. “Experimental investigation of the hydrodynamic characteristics of heave plates using forced oscillation”. In: *Ocean Engineering* 66 (July 2013), pp. 82–91. DOI: [10.1016/j.oceaneng.2013.04.012](https://doi.org/10.1016/j.oceaneng.2013.04.012).
- [136] Javier Moreno, Krish P. Thiagarajan, and Matthew Cameron. “Hydrodynamic Coefficients of Hexagonal Heave Plates for Floating Offshore Wind Turbine Platforms”. In: *Volume 6: Ocean Space Utilization; Ocean Renewable Energy*. Busan, South Korea: American Society of Mechanical Engineers, June 2016. DOI: [10.1115/OMAE2016-54139](https://doi.org/10.1115/OMAE2016-54139).
- [137] Song An and Odd M. Faltinsen. “An experimental and numerical study of heave added mass and damping of horizontally submerged and perforated rectangular plates”. In: *Journal of Fluids and Structures* 39 (May 2013), pp. 87–101. DOI: [10.1016/j.jfluidstructs.2013.03.004](https://doi.org/10.1016/j.jfluidstructs.2013.03.004).

- [138] Haiping He, Armin W. Troesch, and Marc Perlin. “Hydrodynamics of Damping Plates at Small KC Numbers”. In: *IUTAM Symposium on Fluid-Structure Interaction in Ocean Engineering*. Ed. by Edwin Kreuzer. Vol. 8. ISSN: 1875-3507 Series Title: Iutam Bookseries. Dordrecht: Springer Netherlands, 2008, pp. 93–104. DOI: [10.1007/978-1-4020-8630-4\\_9](https://doi.org/10.1007/978-1-4020-8630-4_9).
- [139] A Lavrov and C Guedes Soares. “Modelling the heave oscillations of vertical cylinders with damping plates”. In: *International Journal Maritime Engineering* 158 (2016), pp. 187–198. DOI: [10.3940/rina.ijme.2016.a3.365](https://doi.org/10.3940/rina.ijme.2016.a3.365).
- [140] Carlos Lopez-Pavon and Antonio Souto-Iglesias. “Hydrodynamic coefficients and pressure loads on heave plates for semi-submersible floating offshore wind turbines: A comparative analysis using large scale models”. In: *Renewable Energy* 81 (Sept. 2015), pp. 864–881. DOI: [10.1016/j.renene.2015.04.003](https://doi.org/10.1016/j.renene.2015.04.003).
- [141] Pauline Bozonnet and Adrien Emery. “CFD Simulations for the Design of Offshore Floating Wind Platforms Encompassing Heave Plates”. In: *the Twenty-fifth (2015) International Ocean and Polar Engineering Conference*. Kona, Big Island, Hawaii, USA, 2015.
- [142] T. Sarpkaya. “On the parameter  $\beta = \text{Re}/\text{KC} = D2/\sqrt{T}$ ”. In: *Journal of Fluids and Structures* 21.4 (Dec. 2005), pp. 435–440. DOI: [10.1016/j.jfluidstructs.2005.08.007](https://doi.org/10.1016/j.jfluidstructs.2005.08.007).
- [143] Ana Bezunartea-Barrio, Sergio Fernandez-Ruano, Adolfo Maron-Loureiro, Enrique Molinelli-Fernandez, Francisco Moreno-Buron, Julio Oria-Escudero, Jose Rios-Tubio, Cristina Soriano-Gomez, Alvaro Valea-Peces, Carlos Lopez-Pavon, and Antonio Souto-Iglesias. “Scale effects on heave plates for semi-submersible floating offshore wind turbines: case study with a solid plain plate”. In: *Journal of Offshore Mechanics and Arctic Engineering* (2019), pp. 1–14. DOI: [10.1115/1.4045374](https://doi.org/10.1115/1.4045374).
- [144] Romain Pinguet, Sam Kanner, Michel Benoit, and Bernard Molin. “Validation of Open-Source Overset Mesh Method using Free-Decay Tests of Floating Offshore Wind Turbine”. In: *the Thirtieth (2020) International Ocean and Polar Engineering Conference*. Virtual, 2020.
- [145] B. L. Jensen, B. M. Sumer, and J. Fredsøe. “Turbulent oscillatory boundary layers at high Reynolds numbers”. In: *Journal of Fluid Mechanics* 206 (Sept. 1989), pp. 265–297. DOI: [10.1017/S0022112089002302](https://doi.org/10.1017/S0022112089002302).
- [146] P. A. Martin and L. Farina. “Radiation of water waves by a heaving submerged horizontal disc”. In: *Journal of Fluid Mechanics* 337 (Apr. 1997), pp. 365–379. DOI: [10.1017/S0022112097004989](https://doi.org/10.1017/S0022112097004989).
- [147] John Nicholas Newman. “Added Mass and Damping of Rectangular Bodies Close to the Free Surface”. In: *Journal of Ship Research* (1984), pp. 219–225.
- [148] P. McIver and D. V. Evans. “The occurrence of negative added mass in free-surface problems involving submerged oscillating bodies”. In: *Journal of Engineering Mathematics* 18.1 (Mar. 1984), pp. 7–22. DOI: [10.1007/BF00042895](https://doi.org/10.1007/BF00042895).
- [149] A N Robertson, S Gueydon, E Bachynski, L Wang, J Jonkman, D Alarcón, E Amet, A Beardsell, P Bonnet, B Boudet, C Brun, Z Chen, M Féron, D Forbush, C Galinos, J Galvan, P Gilbert, J Gómez, V Harnois, F Haudin, Z Hu, J Le Dreff, M Leimeister, F Lemmer, H Li, G Mckinnon, I Mendikoa, A Moghtadaei, S Netzband, S Oh, A Pegalajar-Jurado, M Q Nguyen, K Ruehl, P Schünemann, W Shi, H Shin, Y Si, F Surmont, P Trubat, J Qwist, and S

- Wohlfahrt-Laymann. “OC6 Phase I: Investigating the underprediction of low-frequency hydrodynamic loads and responses of a floating wind turbine”. In: *Journal of Physics: Conference Series* 1618 (Sept. 2020), p. 032033. DOI: [10.1088/1742-6596/1618/3/032033](https://doi.org/10.1088/1742-6596/1618/3/032033).
- [150] Lu Wang, Amy Robertson, Jason Jonkman, Yi-Hsiang Yu, Arjen Koop, Adrià Borràs Nadal, Haoran Li, Wei Shi, Romain Pinguet, Yang Zhou, Qing Xiao, Rupesh Kumar, and Hamid Sarlak. “Investigation of nonlinear difference-frequency wave excitation on a semisubmersible offshore-wind platform with bichromatic-wave CFD simulations”. In: *ASME 2021 3rd International Offshore Wind Technical Conference*. Virtual, 2021.
- [151] Alexandre N. Simos, João V. Sparano, José A. P. Aranha, and Vinícius L. F. Matos. “2nd Order Hydrodynamic Effects on Resonant Heave, Pitch and Roll Motions of a Large-Volume Semi-Submersible Platform”. In: *Volume 6: Nick Newman Symposium on Marine Hydrodynamics; Yoshida and Maeda Special Symposium on Ocean Space Utilization; Special Symposium on Offshore Renewable Energy*. Estoril, Portugal: ASMEDC, Jan. 2008, pp. 229–237. DOI: [10.1115/OMAE2008-57430](https://doi.org/10.1115/OMAE2008-57430).
- [152] I Bayati, J Jonkman, A Robertson, and A Platt. “The effects of second-order hydrodynamics on a semisubmersible floating offshore wind turbine”. In: *Journal of Physics: Conference Series* 524 (June 2014), p. 012094. DOI: [10.1088/1742-6596/524/1/012094](https://doi.org/10.1088/1742-6596/524/1/012094).
- [153] Guilherme Moura Paredes, Johannes Palm, Claes Eskilsson, Lars Bergdahl, and Francisco Taveira-Pinto. “Experimental investigation of mooring configurations for wave energy converters”. In: *International Journal of Marine Energy* 15 (Sept. 2016), pp. 56–67. DOI: [10.1016/j.ijome.2016.04.009](https://doi.org/10.1016/j.ijome.2016.04.009).
- [154] Joel Guerrero. *Finite Volume Method : A crash introduction*. 2013.
- [155] Amy N. Robertson, Fabian Wendt, Jason M. Jonkman, Wojciech Popko, Habib Dagher, Sebastien Gueydon, Jacob Qvist, Felipe Vittori, José Azcona, Emre Uzunoglu, Carlos Guedes Soares, Rob Harries, Anders Yde, Christos Galinos, Koen Hermans, Jacobus Bernardus de Vaal, Pauline Bozonnet, Ludovic Bouy, Ilmas Bayati, Roger Bergua, Josean Galvan, Iñigo Mendikoa, Carlos Barrera Sanchez, Hyunkyung Shin, Sho Oh, Climent Molins, and Yannick Debruyne. “OC5 Project Phase II: Validation of Global Loads of the DeepCwind Floating Semisubmersible Wind Turbine”. In: *Energy Procedia* 137 (Oct. 2017), pp. 38–57. DOI: [10.1016/j.egypro.2017.10.333](https://doi.org/10.1016/j.egypro.2017.10.333).
- [156] N. Bruinsma, B.T. Paulsen, and N.G. Jacobsen. “Validation and application of a fully nonlinear numerical wave tank for simulating floating offshore wind turbines”. In: *Ocean Engineering* 147 (Jan. 2018), pp. 647–658. DOI: [10.1016/j.oceaneng.2017.09.054](https://doi.org/10.1016/j.oceaneng.2017.09.054).
- [157] Brecht Devolder, Pieter Rauwoens, and Peter Troch. “Application of a buoyancy-modified k- $\omega$  SST turbulence model to simulate wave run-up around a monopile subjected to regular waves using OpenFOAM®”. In: *Coastal Engineering* 125 (July 2017), pp. 81–94. DOI: [10.1016/j.coastaleng.2017.04.004](https://doi.org/10.1016/j.coastaleng.2017.04.004).
- [158] Bo Terp Paulsen, Henrik Bredmose, and Harry B. Bingham. “An efficient domain decomposition strategy for wave loads on surface piercing circular cylinders”. In: *Coastal Engineering* 86 (Apr. 2014), pp. 57–76. DOI: [10.1016/j.coastaleng.2014.01.006](https://doi.org/10.1016/j.coastaleng.2014.01.006).

- 
- [159] Jost Kemper, Christian Windt, Kai Graf, and John V Ringwood. “Development towards a nested hydrodynamic model for the numerical analysis of ocean wave energy systems”. In: *The 13th European Wave and Tidal Energy Conference*. Napoli, Italy, 2019, p. 11.
- [160] Benedetto Di Paolo, Javier L. Lara, Gabriel Barajas, and Íñigo J. Losada. “Wave and structure interaction using multi-domain couplings for Navier-Stokes solvers in OpenFOAM®. Part I: Implementation and validation”. In: *Coastal Engineering* 164 (Mar. 2021), p. 103799. DOI: [10.1016/j.coastaleng.2020.103799](https://doi.org/10.1016/j.coastaleng.2020.103799).

## Résumé

L'émergence rapide des éoliennes flottantes a entraîné une forte demande de méthodes numériques haute-fidélité afin de mieux prédire le comportement de telles structures dans des conditions météorologiques sévères. Dans ces scénarios, les standards de conception suggèrent des approches simplifiées, mais leur applicabilité est limitée, en particulier lorsque l'on considère des géométries complexes et / ou des événements non-linéaires. De plus, les campagnes expérimentales sont coûteuses et peu de données réelles sont disponibles. Ainsi, la Mécanique des Fluides Numérique (MFN) pourrait être un atout clé dans le processus de conception des éoliennes flottantes. Cette thèse vise à évaluer la capacité d'une approche de MFN à modéliser certains aspects hydrodynamiques critiques des éoliennes flottantes de type semi-submersible. La méthode des maillages superposés (overset), intégrée dans le logiciel open-source OpenFOAM®<sup>®</sup>, est utilisée pour modéliser les mouvements de la structure. La méthode numérique de génération et d'absorption de vagues de l'outil waves2Foam est couplée au solveur de maillages superposés pour modéliser les interactions entre les vagues et la structure. Les résultats sont validés par comparaison avec des données expérimentales et numériques issues de la littérature. Des analyses de convergence numérique sont réalisées, et les méthodologies de maillage d'un Canal à Houle Numérique 2D (CHN) sont analysées, pour des structures fixes ou flottantes soumises aux vagues. Les non-linéarités sont mises en évidence. Le CHN est ensuite étendu en 3D pour étudier la réponse hydrodynamique du flotteur semi-submersible DeepCWind, conçu par NREL. Les forces et le run-up le long des parois sont analysés pour des plateformes fixes ou flottantes. L'étude des mouvements de la structure dans les vagues, ainsi que des cas d'extinction libre, sont présentés. La méthode des maillages superposés est également utilisée pour étudier les coefficients hydrodynamiques résultant du mouvement forcé vertical de plaques d'amortissement en pilonnement, largement utilisées dans la conception d'éoliennes flottantes.

## Abstract

The rapid emergence of Floating Offshore Wind Turbines (FOWT) has brought a strong demand for high-fidelity numerical methods to better predict the response of such structures under severe metocean conditions. In these scenarios, design standards suggest simplified approaches, but their applicability is limited, especially when considering complex geometries and/or nonlinear events. Moreover, experimental campaigns are expensive, and few field data are available. So, Computational Fluid Dynamics (CFD) could be a key asset in the design process of FOWT. This thesis aims to assess the ability of a CFD approach to model critical hydrodynamic aspects of semi-submersible FOWT. The overset meshing method built in the open-source software OpenFOAM®<sup>®</sup> is used to handle the body motions. The wave generation and absorption toolbox waves2Foam is coupled with the overset solver to model the interaction between waves and the structure. The results are validated against experimental and numerical data from the literature. Convergence analysis and meshing methodologies of a 2D Numerical Wave Tank (NWT), with fixed and freely floating structures subjected to waves, are considered. Non-linearities are emphasized. The NWT is then extended in 3D to investigate the hydrodynamic response of the DeepCWind semi-submersible FOWT, designed by NREL. Forces and run-up are analyzed for fixed and anchored moving platforms. Wave induced motion and free decay tests are presented. The overset mesh method is also used to estimate the hydrodynamic coefficients resulting from the vertical forced motion of heave damping plate, widely used in FOWT designs.